frontiers | Research Topics

Quantum and semiclassical trajectories: Development and applications

Edited by
Yujun Zheng, Libin Fu, Craig Martens and Huan Yang

Published in
Frontiers in Physics

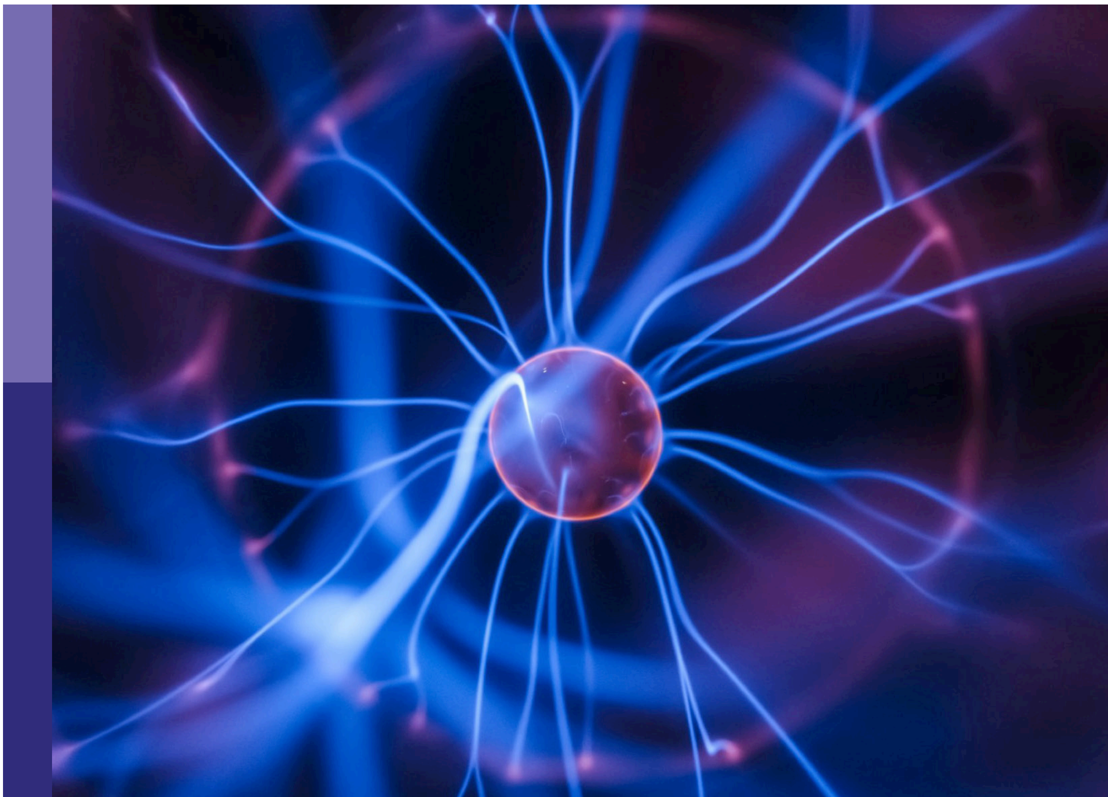

ISSN 1664-8714
ISBN 978-2-8325-3122-8
DOI 10.3389/978-2-8325-3122-8

About Frontiers

Frontiers is more than just an open access publisher of scholarly articles: it is a pioneering approach to the world of academia, radically improving the way scholarly research is managed. The grand vision of Frontiers is a world where all people have an equal opportunity to seek, share and generate knowledge. Frontiers provides immediate and permanent online open access to all its publications, but this alone is not enough to realize our grand goals.

Frontiers journal series

The Frontiers journal series is a multi-tier and interdisciplinary set of open-access, online journals, promising a paradigm shift from the current review, selection and dissemination processes in academic publishing. All Frontiers journals are driven by researchers for researchers; therefore, they constitute a service to the scholarly community. At the same time, the *Frontiers journal series* operates on a revolutionary invention, the tiered publishing system, initially addressing specific communities of scholars, and gradually climbing up to broader public understanding, thus serving the interests of the lay society, too.

Dedication to quality

Each Frontiers article is a landmark of the highest quality, thanks to genuinely collaborative interactions between authors and review editors, who include some of the world's best academicians. Research must be certified by peers before entering a stream of knowledge that may eventually reach the public - and shape society; therefore, Frontiers only applies the most rigorous and unbiased reviews. Frontiers revolutionizes research publishing by freely delivering the most outstanding research, evaluated with no bias from both the academic and social point of view. By applying the most advanced information technologies, Frontiers is catapulting scholarly publishing into a new generation.

What are Frontiers Research Topics?

Frontiers Research Topics are very popular trademarks of the *Frontiers journals series*: they are collections of at least ten articles, all centered on a particular subject. With their unique mix of varied contributions from Original Research to Review Articles, Frontiers Research Topics unify the most influential researchers, the latest key findings and historical advances in a hot research area.

Find out more on how to host your own Frontiers Research Topic or contribute to one as an author by contacting the Frontiers editorial office: frontiersin.org/about/contact

Quantum and semiclassical trajectories: Development and applications

Topic editors
Yujun Zheng — Shandong University, China
Libin Fu — Graduate School of China Academy of Engineering Physics, China
Craig Martens — University of California, Irvine, United States
Huan Yang — Shandong University, China

Citation
Zheng, Y., Fu, L., Martens, C., Yang, H., eds. (2023). *Quantum and semiclassical trajectories: Development and applications*. Lausanne: Frontiers Media SA.
doi: 10.3389/978-2-8325-3122-8

Table of contents

frontiers | Frontiers in Physics

TYPE Original Research
PUBLISHED 14 September 2022
DOI 10.3389/fphy.2022.1022222

EDITED BY
Yujun Zheng,
Shandong University, China

REVIEWED BY
Yongqing Li,
Liaoning University, China
Chuan-Lu Yang,
Ludong University, China

*CORRESPONDENCE
Maodu Chen,
mdchen@dlut.edu.cn

SPECIALTY SECTION
This article was submitted to Atomic and Molecular Physics,
a section of the journal
Frontiers in Physics

RECEIVED 18 August 2022
ACCEPTED 29 August 2022
PUBLISHED 14 September 2022

CITATION
Yang Z and Chen M (2022), A globally accurate potential energy surface and quantum dynamics calculations on the Be(^{1}S) + H$_2$(v_0 = 0, j_0 = 0) → BeH + H reaction.
Front. Phys. 10:1022222.
doi: 10.3389/fphy.2022.1022222

A globally accurate potential energy surface and quantum dynamics calculations on the Be(^{1}S) + H$_2$($v_0 = 0, j_0 = 0$) → BeH + H reaction

Zijiang Yang and Maodu Chen*

Key Laboratory of Materials Modification by Laser, Electron, and Ion Beams (Ministry of Education), School of Physics, Dalian University of Technology, Dalian, China

The reactive collision between Be atom and H$_2$ molecule has received great interest both experimentally and theoretically due to its significant role in hydrogen storage, astrophysics, quantum chemistry and other fields, but the corresponding dynamics calculations have not been reported. Herein, a globally accurate ground-state BeH$_2$ PES is represented using the neural network strategy based on 12371 high-level *ab initio* points. On this newly constructed PES, the quantum time-dependent wave packet calculations on the Be(^{1}S) + H$_2$(v_0 = 0, j_0 = 0) → BeH + H reaction are performed to study the microscopic dynamics mechanisms. The calculated results indicate that this reaction follows the complex-forming mechanism near the reactive threshold, whereas a direct H-abstraction process gradually plays the dominant role when the collision energy is large enough. The newly constructed PES can be used for further dynamics calculations on the BeH$_2$ reactive system, such as the rovibrational excitations and isotopic substitutions of the H$_2$ molecule, and the presented dynamics data would be of importance in experimental research at a finer level.

KEYWORDS

potential energy surface, quantum dynamics, neural network, *ab initio*, time-dependent wave packet, Be(^{1}S) + H$_2$ reaction

1 Introduction

In recent decades, the interactions between beryllium atom and hydrogen molecules have been of great attention because of their significance in astrophysics, hydrogen storage, quantum chemistry and other fields. On the one hand, the collision product BeH$_2$ molecule presents the fundamental and technological interest in potential applications, such as the nuclear materials and rocket fuel technology [1, 2], owing to its small mass and large hydrogen-to-metal mass ratios. Moreover, the molecular BeH$_2$, with a simple electronic structure, has become an excellent candidate for testing new computational methods for quantum chemistry [3–6]. On the other hand, the further product BeH molecule in the collision process of Be + H$_2$ is a popular testing target for the electronic structure calculations in open-shell systems [7, 8]. In addition, BeH is also an important interstellar molecule, which has been identified in stars and comets [9, 10].

Various experimental studies on the BeH_2 system have been implemented [11–18]. Tague and Andrews first detected the BeH_2 in molecular form by using infrared spectroscopy and the matrix isolation technique [11]. In their experiment, the pulsed laser evaporated Be atoms react with the hydrogen, and the primary product BeH and BeH_2 are largely favored compared with the other four more complex product molecules of Be_2H, HBeHBeH, $HBe(H)_2BeH$ and HBeBeH. [12] synthesized the gaseous BeH_2 molecule using an electrical discharge facility, which is verified by infrared emission spectroscopy. Their study concluded that the stable BeH_2 is a linearly symmetric molecule with the BeH bond length of 1.334 Å. The high-precision infrared emission spectra of the BeH_2 and BeD_2 molecules were measured by [14]. The antisymmetric stretching modes and some hot bands of the two molecules were studied and the spectroscopic data were accurately determined. In their later study [17], the new vibration-rotation hot bands of the BeH_2 molecule were analyzed, and an accurate value was obtained for the frequency of the bending vibrational mode.

In the theoretical aspect, numerous *ab initio* calculations on the BeH_2 molecule have also been performed [19–26]. Martin and Lee [19] accurately calculated the quartic force field of BeH_2 using the CCSD(T) method, and the obtained spectroscopic constants are consistent with the corresponding experimental measurements. Hrenar et al. reported the first potential energy surface (PES) of the BeH_2 molecule used for the vibrational configuration-interaction calculations by a multilevel scheme [23]. Their calculated results can reproduce the experimental values of the gas phase measurements and matrix isolation. The ground-state equilibrium structure and PES of BeH_2 were calculated utilizing the CCSD(T) method combined with the cc-pVTZ through cc-pV6Z basis sets by Koput and Peterson [24]. Furthermore, the rovibrational energy levels of BeH_2 and its isotopic variations of BeD_2 and BeHD were accurately calculated by a variational method. The newest PES of the BeH_2 system was constructed by Li and Roy [25] utilizing the three-dimensional spline interpolation over 6,864 energy points with the internally contracted multi-reference configuration interaction (icMRCI)/aug-cc-pV5Z level. On this PES, the spectral constants of the BeH_2 and BeD_2 molecules were accurately calculated and the corresponding data of the BeHD molecule were predicted.

Although the BeH_2 system has received great attention both experimentally and theoretically, most of those studies focused on its structural and spectral properties, and the dynamics mechanisms of the Be + H_2 reaction process have not been reported up to now. In theory, the most reliable approach for obtaining the accurate dynamics information of a chemical reaction is to implement rigorous quantum scattering calculations on a globally high-precision PES [27, 28]. The previous PESs of the BeH_2 system are extremely reliable and accurate for describing the BeH_2 complex, whereas they are not suitable for the reaction dynamics calculations since some key regions where the reaction could reach are not included. Therefore, constructing a global and accurate BeH_2 PES is a crucial premise for studying the microscopic dynamics mechanisms of this reactive system.

Herein, a high-fidelity ground-state BeH_2 PES is represented based on a mass of high-precision *ab initio* energy points and the permutation invariant polynomial-neural network (PIP-NN) scheme [29, 30]. Moreover, the quantum dynamics calculations at the state-resolved level for the $Be(^1S) + H_2(v_0 = 0, j_0 = 0) \rightarrow BeH + H$ reaction are carried out by the time-dependent wave packet (TDWP) method [31, 32] on this newly constructed PES. The computational details and the characteristics of the PES are given in Section 2. Section 3 displays the calculated dynamics results and the relevant discussion of the dynamics mechanisms for the title reaction and Section 4 concludes this work.

2 Ground-state BeH_2 potential energy surface

2.1 *Ab initio* calculations

The energy points of the BeH_2 system at the $1^1A'$ state are calculated using the icMRCI method [33, 34] with the Davidson correction (+Q). The molecular orbitals are optimized by the complete active space self-consistent field (CASSCF) method [35, 36] before the MRCI calculations are carried out. The CASSCF orbitals are determined by the state-averaged calculations with equal weight for the $1^1A'$, $2^1A'$, $1^1A''$ and $2^1A''$ states. The active space is composed of nine active orbitals ($8a' + 1a''$). The aug-cc-pV5Z basis set [37] is used for both the two different atoms. The energies calculated for the symmetrical configuration of Be-H_2 is defined by $0.8 \le R_{HH}/a_0 \le 8.0$, $0.1 \le R_{Be\text{-}HH}/a_0 \le 16.0$, $0 \le \theta \le \pi/2$, and the configuration of H-BeH is constructed by $2.0 \le R_{BeH}/a_0 \le 10.0$, $0.1 \le R_{H\text{-}BeH}/a_0 \le 16.0$, $0 \le \theta' \le \pi$, Here, the *ab initio* calculations are performed utilizing Molpro 2012 software [38].

2.2 Permutation invariant polynomial-neural network fitting

The ground-state BeH_2 PES can be expressed by the summing of the two-body potentials and three-body potential:

$$V(R_1, R_2, R_3) = \sum_{i=1}^{3} V_i^{(2)}(R_i) + V^{(3)}(R_1, R_2, R_3) \cdot f(\boldsymbol{R}) \quad (1)$$

where R_i ($i = 1, 2, 3$) are the bond length of Be-H_a, H_a-H_b and Be-H_b, respectively. A switch function $f(\boldsymbol{R})$ is used to get a better

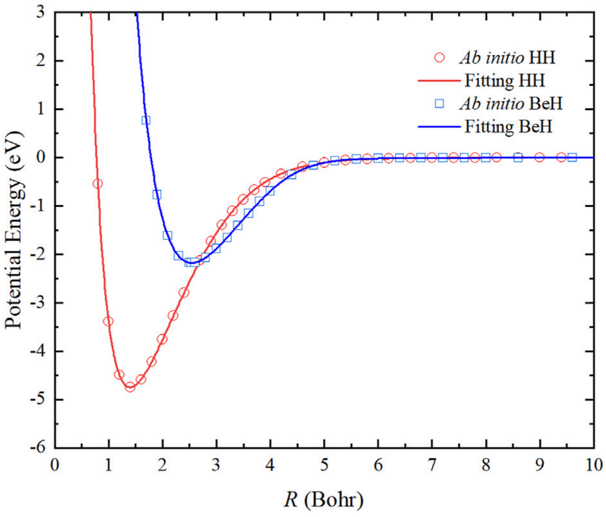

FIGURE 1
Comparison of the *ab initio* data and the NN fitting results of the PECs of $H_2(X^1\Sigma_g^+)$ and $BeH(X^1\Sigma^+)$.

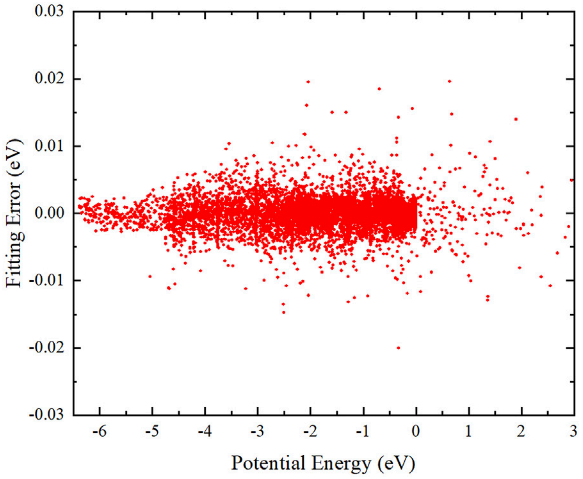

FIGURE. 2
Distribution of the PIP-NN fitting errors of the ground-state BeH_2 PES.

TABLE 1 Spectroscopic constants of $H_2(X^1\Sigma_g^+)$ and $BeH(X^1\Sigma^+)$.

	R_e (Bohr)	D_e (eV)	ω_e (cm^{-1})	$\omega_e x_e$ (cm^{-1})
$H_2(X^1\Sigma_g^+)$				
This work[a]	1.401	4.750	4400.9	124.6
Experiment[b]	1.401	4.747	4401.2	121.3
$BeH(X^1\Sigma^+)$				
This work[a]	2.544	2.176	2054.0	39.4
Experiment	2.537[c]	2.181[c]	2060.8[d]	36.3[d]

[a] Obtained on the analytical PECs.
[b] Ref. 39.
[c] Ref. 40.
[d] Ref. 41.

representation in the asymptotic areas of the PES, and its form is written as:

$$f(\boldsymbol{R}) = \prod_{n=1,2,3}\left(1-\frac{1}{2}\left(1+\tanh\left(\frac{R_n - R_d}{R_w}\right)\right)\right) \qquad (2)$$

where R_d and R_w are the central position and the constant of switch strength, respectively.

The two-body potentials are obtained by a feedforward NN structure, which consists of two hidden layers with five neurons. A total of 69 and 53 *ab initio* points are calculated to fit the potential energy curves (PECs) of HH and BeH, respectively, and the corresponding root mean square error (RMSE) are 0.036 and 0.385 meV. Figure 1 shows that the fitting PECs of $H_2(X^1\Sigma_g^+)$ and $BeH(X^1\Sigma^+)$ molecules can pass through the center of each *ab initio* point. To further demonstrate the accuracy of the two-body potentials, Table 1 displays that the spectroscopic constants of the two diatomic molecules determined on the analytical PECs are in good agreement with the corresponding experimental data [39–41], suggesting the presented PES are sufficiently accurate for representing the reactant and product channels when the dynamics calculations are carried out.

The global ground-state BeH_2 PES is represented by the PIP-NN strategy [29, 30], which can rigorously assure that the constructed PES satisfies the exchange symmetry of the two hydrogen atoms, and this scheme has been widely and successfully applied to lots of molecular systems [42–51]. First, the fundamental invariants can be expressed as:

$$P_i = \exp(-\alpha R_i) \quad (i = 1, 2, 3) \qquad (3)$$

where α is a constant between 0 and 1, and here the value of α is set as 0.2. Second, the symmetrized polynomial vector $\boldsymbol{G} = \{G_i\}$ is constructed as:

$$G_1 = (P_1 + P_3)/2 \qquad (4)$$

$$G_2 = P_1 \times P_3 \qquad (5)$$

$$G_3 = P_2 \qquad (6)$$

Finally, $\boldsymbol{G}$ is normalized as the input of the NN model:

$$I_i = \frac{2(G_i - G_{i,\min})}{(G_{i,\max} - G_{i,\min})} - 1, \ (i = 1, 2, 3) \qquad (7)$$

where $G_{i,\max}$ and $G_{i,\min}$ are the maximum and minimum values of G_i, respectively.

The NN model used for constructing the global CaH_2^+ PES consists of two hidden layers with 12 neurons. The hyperbolic tangent function and linear function are used as the transfer functions φ in the 1–2, 2–3 layers, and 3–4 layers, respectively.

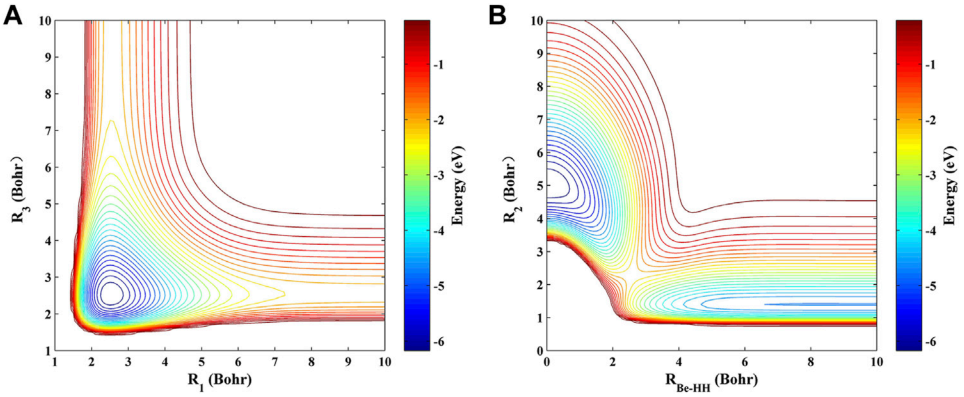

FIGURE 3
Contour plots of the ground-state BeH_2 PES at the **(A)** $D_{\infty h}$ and **(B)** C_{2v} symmetries.

TABLE 2 Structures, energies and vibrational frequencies of the GM and TS for the ground-state BeH_2.

	R_1 (a_0)	γ (degree)	E (eV)	ν_1 (cm^{-1})	ν_2 (cm^{-1})	ν_3 (cm^{-1})
GM ($D_{\infty h}$)						
This work[a]	2.515	180	−1.632	2042.9	705.1	2244.7
Ab initio[b]	2.507	180	−1.663	1991.8	711.8	2178.8
Experiment	2.507[c]	180[c]	—	—	711.5[d]	2178.9[c]
TS (C_{2v})						
This work[a]	2.801	47.8	2.594	937.4	2334.2*i*	1567.5
Ab initio[b]	2.822	42.1	2.587	—	—	—

[a] Obtained on the PIP-NN PES.
[b] Ref. 25. Calculated at the icMRCI/aug-cc-pCV5Z level and the core-electron correlation is included.
[c] Ref. 14.
[d] Ref. 17.

The finally analytical expansion of the final PES can be presented as:

$$y = \varphi^{(3)}\left(b_1^{(3)} + \sum_{i=1}^{12} w_{i1}^{(3)} \varphi^{(2)}\left(b_i^{(2)} + \sum_{j=1}^{12} w_{ji}^{(2)} \varphi^{(1)}\left(b_j^{(1)} + \sum_{k=1}^{3} w_{kj}^{(1)} I_k\right)\right)\right) \tag{8}$$

where y represents the normalized potential energy. The connecting weight w and bias b between the adjacent two layers are iteratively optimized by the Levenberg–Marquardt algorithm [52]. Here, a total of 12371 molecular configurations are picked out to take part in the PIP-NN fitting, which are randomly classified into 90% training data, 5% testing data, and 5% validation data to avoid over-fitting. The parameters of w and b of the analysis PES are determined by the training data; the testing data are used to evaluate the generalization performance of the trained PES and the training should stop immediately when the testing error starts to rise; the validation data can be used for the initial assessment and adjustment of the NN model. The distribution of the fitting errors of the ground-state BeH_2 PES is plotted in Figure 2. This figure shows that the constructed PES can keep small fitting errors in the whole energy area. The overall RMSE of the PIP-NN PES is only 1.972 meV, and the energy points with an absolutely fitting error less than 0.005 eV can reach 97.2% of all the selected configurations, implying the fitting PES is globally accurate and suitable for performing the reaction dynamics studies on the BeH_2 system.

2.3 Topographic characteristics of potential energy surface

Figures 3A,B display the contour plots of the PIP-NN PES at the $D_{\infty h}$ and C_{2v} symmetries, respectively. Excellent exchange symmetry of the PIP-PES is displayed in Figure 3A. There is a deep well with an energy minimum of −6.382 eV below the asymptotic H-Be-H at $R_1 = R_3 = 2.515\ a_0$, and it is also the global minimum (GM) of the ground-state BeH_2 PES, which has been demonstrated in the previous theoretical and experimental

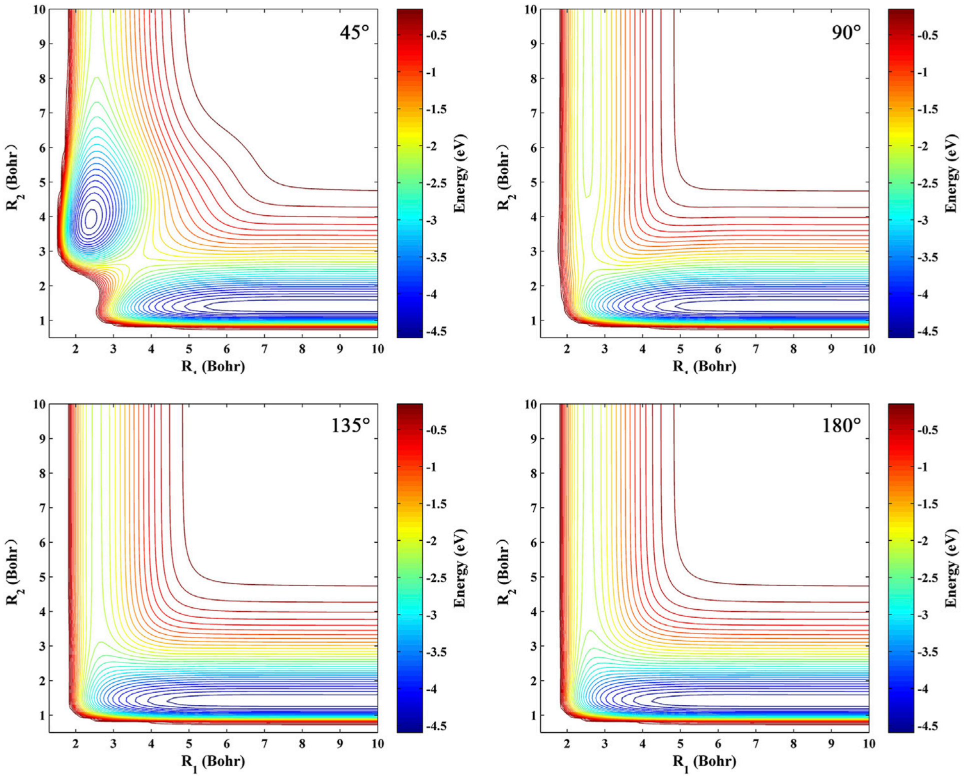

FIGURE 4
Contour plots of the ground-state BeH_2 PES at four Be-H-H angles (45°, 90°, 135°, and 180°).

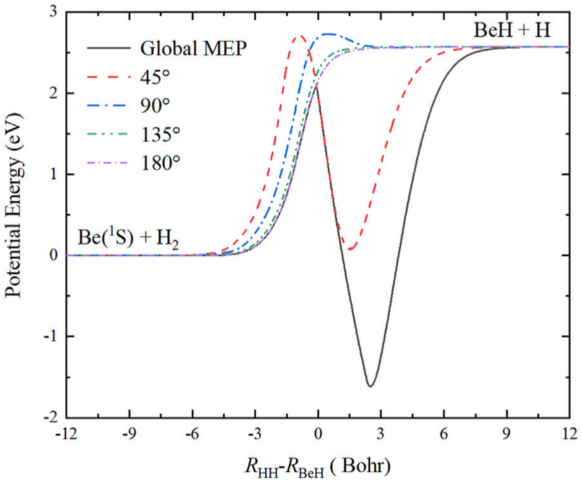

FIGURE 5
Global MEP and the MEPs at four Ca^+-H-H angles (45°, 90°, 135°, and 180°) of the $Be(^1S) + H_2 \rightarrow BeH + H$ reaction obtained on the ground-state BeH_2 PES.

studies [14, 25]. At the relatively low collision energy, the Be atom collides with the H_2 molecule with the remarkable elongation of the HH bond, and the BeH product is formed by the dissociation of the collinear BeH_2 molecule. For panel (B), a saddle point structure with the energy value of −2.156 eV is presented at $R_2 = 2.269\ a_0$, $R_{\text{Be-HH}} = 2.561\ a_0$, which is corresponding to the transition state (TS) of the BeH_2 system and dominates the collision process of the H- exchange path of $H_a + BeH_b \rightarrow H_b + BeH_a$. The valley at $R_2 = 1.401\ a_0$ corresponds to the $Be(^1S) + H_2$ channel, and the GM is also shown at $R_2 = 5.030\ a_0$, $R_{\text{Be-HH}} = 0\ a_0$ since the $D_{\infty h}$ configuration is a limitation of the C_{2v} symmetry.

Table 2 lists the structures, energy values and vibrational frequencies of the GM and TS for the ground-state BeH_2 calculated at the PIP-NN PES, and the available experimental and *ab initio* values are also presented. The energy values are relative to the $Be(^1S) + H_2$ asymptotic channel. The newly constructed PES can accurately reproduce the geometries and the corresponding energies of the two stationary points, and the vibrational frequency v_2 is consistent with the experimental [14, 17] and extremely high-precision *ab initio* data [25] well. There

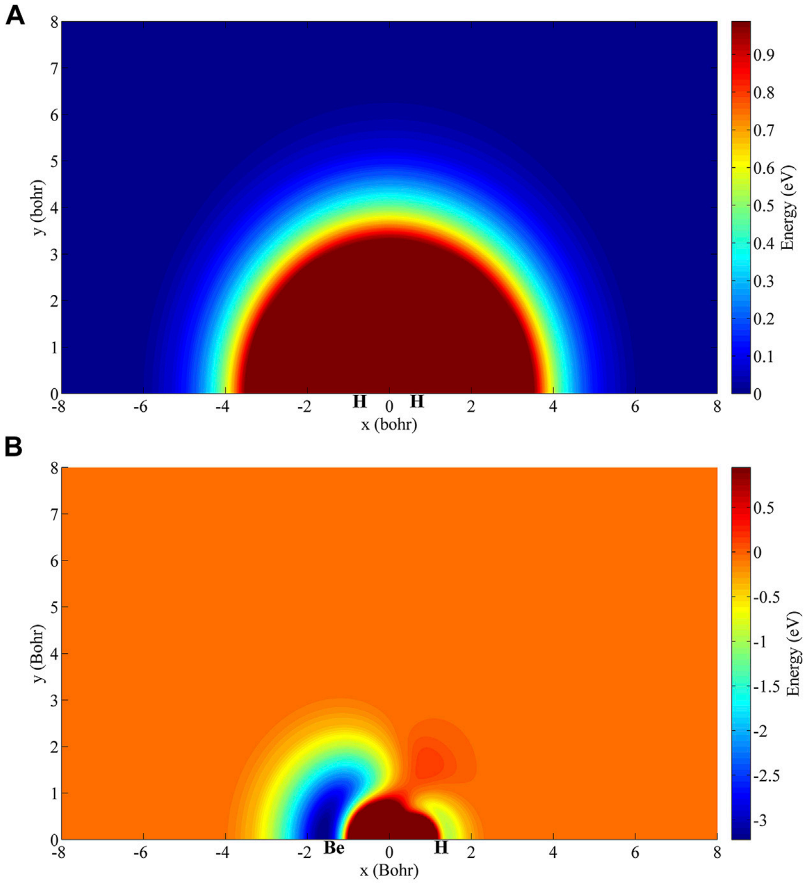

FIGURE 6
(A) Contour plot of the ground-state BeH_2 PES when the Be atom moves around the H_2 molecule with the fixed bond length at 1.401 a_0 **(B)** Contour plot of the ground-state BeH_2 PES when a H atom moves around the BeH molecule with the fixed bond length at 2.544 a_0.

exist some deviations for the values of v_1 and v_3 between the data calculated on the PIP-NN PES and the experimental or *ab initio* results, which are caused by the small fitting error because the harmonic frequencies are very sensitive to the small difference of PES, but they nearly do not affect the subsequent reaction dynamics results. In general, the PIP-NN PES can precisely represent the characteristics of the GM and TS of the ground-state BeH_2.

The contour maps of the ground-state BeH_2 PES at four fixed Be-H-H approaching angles (45°, 90°, 135°, and 180°) are presented in Figure 4. It is clear that the constructed PES is smooth in the entire configuration space, and there is no non-physical structure for each angle, suggesting the over-fitting behavior does not exist during the fitting PES. For the PES at every angle, the bottom valley is the $Be(^1S) + H_2$ channel, and the left valley is corresponding to the BeH + H channel. The energy of the bottom channel is lower than the left channel, indicating that the $Be(^1S) + H_2 \rightarrow BeH + H$ reaction is endothermic. For the angles of 45° and 90°, the reactant and product channels are connected by a barrier structure, which is generated by the avoid crossing behavior of the $2^1A'$ state. The energy value of the barrier is higher than the energy of the product channel, implying the larger collision energy is needed to initiate this reaction by the collision approach with a relatively small Be-H-H approaching angle. In addition, a potential well with the depth of 2.496 eV relative to the BeH + H asymptotic region is shown when the approaching angle is at 45°, and many bound states or quasi-bound states can be supported by this well. For the angles of 135° and 180°, no well or barrier exists in the PES, thus the title reaction proceeds via a direct H-abstraction process when the collision angle becomes larger enough.

Figure 5 shows the minimum energy paths (MEPs) of the $Be(^1S) + H_2 \rightarrow BeH + H$ reaction at four Be-H-H approaching angles (45°, 90°, 135°, 180°), calculated by scanning the ground-state BeH_2 PES with the fixed angle shown in Figure 4 at different coordinates to obtain the energy minimum. In addition, the global MEP generated by scanning the whole PES is also given in this plot, which plays the dominant role in

TABLE 3 Main numerical parameters in the TDWP calculations.

$Be(^1S) + H_2(v_0 = 0, j_0 = 0) \rightarrow BeH + H$

Grid/basis range and size	R (a_0)∈[0.1, 25], N_R = 299 (199 for interaction region) r (a_0)∈[0.01, 20], N_r = 239 (79 for asymptotic region) N_j = 99
Initial wave packet $\exp\left[-\frac{(R-R_c)^2}{2\Delta_R^2}\right]\cos k_0R$	R_c = 16 a_0, Δ_R = 0.20 a_0, $k_0 = (2E_0\mu_R)^{1/2}$ with E_0 = 4.0 eV
Total propagation time	20,000 a.u.

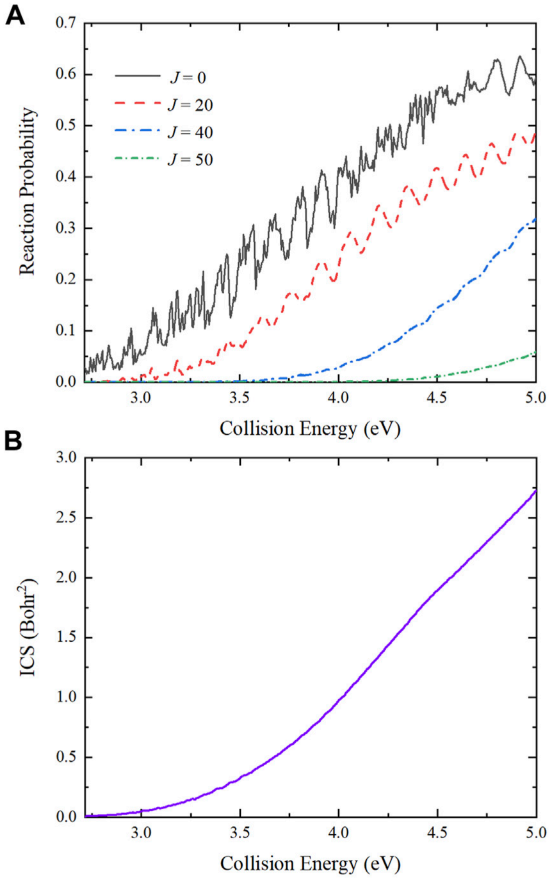

FIGURE 7
Collision energy dependence of **(A)** total reaction probabilities with four partial waves (J = 0, 20, 40 and 50) and **(B)** total ICS of the $Be(^1S) + H_2(v_0 = 0, j_0 = 0) \rightarrow BeH + H$ reaction calculated by the TDWP method on the ground-state BeH_2 PES.

determining the microscopic mechanisms of the title reaction, especially at relatively low energy. Under the action of collision energy, the reactants pass a barrier with the height of 2.096 eV relative to the reactant asymptotic region, and then a linear H-Be-H complex is formed on the well, which corresponds to the GM of the PES, finally, a Be-H bond is broken to generate the BeH molecule in the product channel. When the zero-point energies of the reactant and product molecules are taken into consideration, the endothermicity of the $Be(^1S) + H_2 \rightarrow BeH + H$ reaction calculated on this newly constructed PES is 2.716 eV.

Figure 6A displays the contour plot of the ground-state BeH_2 PES in the case of the Be atom moving around the H_2 molecule fixed at its equilibrium distance. It is clear that the Be atom is always repelled by the H_2 molecule, so initiating the title reaction is difficult when the HH bond is stabilized at its equilibrium structure. As shown in Figure 3A, when the HH bond is elongated 5.030 a_0, there exist the attractive interactions between the Be atom and the H_2 molecule, and a stable BeH_2 complex is formed. A similar map to Figure 6A but for a H atom moving around the BeH fixed at its equilibrium distance is displayed in Figure 6B. Different from the case of Figure 6A, it appears the attractive interactions between the H atom and BeH molecule, and the well around the Be atom is deeper than the well around another H atom, suggesting that this H atom prefers to get out from the side of H atom of BeH in the product region.

3 Quantum dynamics calculations

For most of the triatomic and some tetratomic reactive systems, the quantum TDWP method [31, 32, 53–55] is a high-efficiency and accurate tool for calculating the dynamics data. The full-dimensional quantum dynamics calculations of the $Be(^1S) + H_2(v_0 = 0, j_0 = 0) \rightarrow BeH + H$ reaction are carried out on this newly constructed PIP-NN PES by the TDWP method for understanding the state-resolved dynamics mechanisms. The Coriolis coupling effect is included in the quantum TDWP calculations. Here, only the main equations in the TDWP calculations are displayed below. The Hamiltonian of the title reaction can be expressed as:

$$\hat{H} = -\frac{\hbar^2}{2\mu_R}\frac{\partial^2}{\partial R^2} - \frac{\hbar^2}{2\mu_r}\frac{\partial^2}{\partial r^2} + \frac{\left(\hat{J} - \hat{j}\right)^2}{2\mu_R R^2} + \frac{\hat{j}^2}{2\mu_r r^2} + \hat{V} \tag{9}$$

where μ_r and μ_R are the reduced masses associated with r and R in the Jacobi coordinate, respectively. J and j express the total

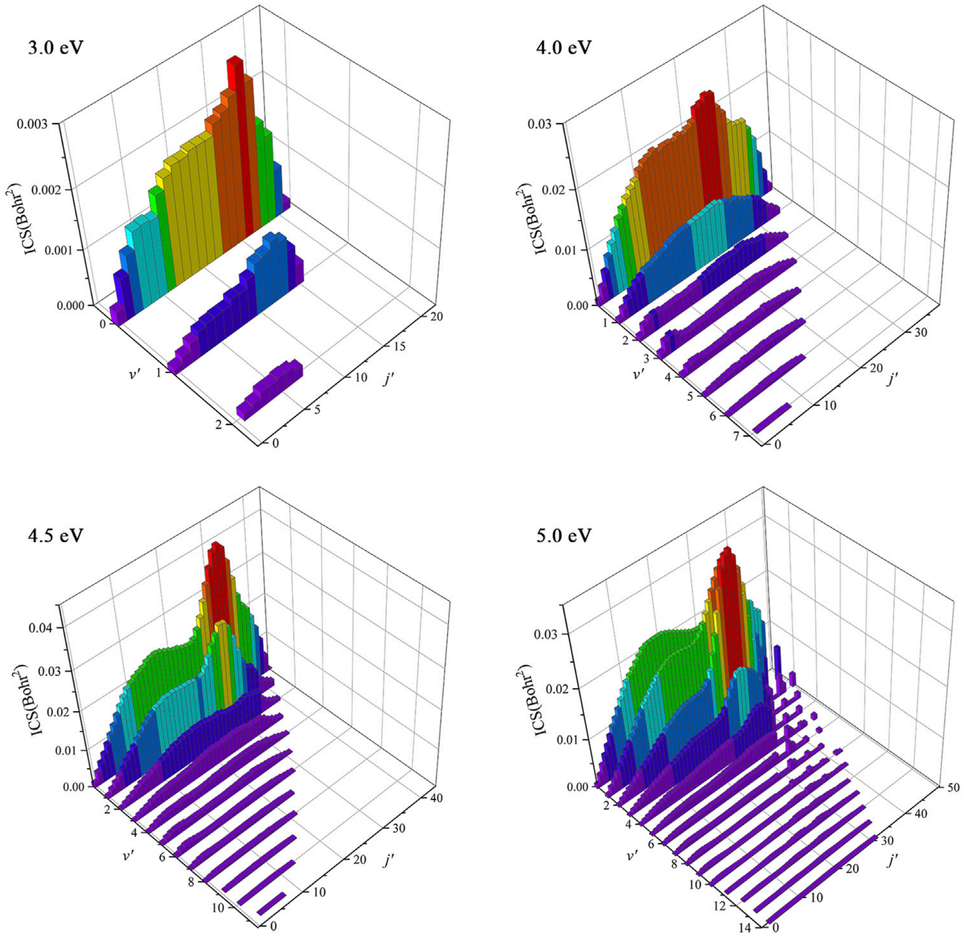

FIGURE 8
Rovibrationally state-resolved ICSs of the Be(^{1}S) + H_2(v_0 = 0, j_0 = 0) → BeH + H reaction at four collision energies (3.0, 4.0, 4.5, and 5.0 eV) calculated by the TDWP method on the ground-state BeH_2 PES.

angular momentum quantum number of BeH_2 and rotational angular momentum quantum number of H_2, respectively. The initial wave packet consists of a Gaussian type wave function, a rovibrational eigenfunction of H_2, and an eigenfunction of the total angular momentum, written as:

$$\Psi^{JM\varepsilon}_{\alpha v_0 j_0 l_0}(t=0) = G(R_\alpha)\phi_{v_0}(r_\alpha) j_0(\theta_\alpha)\left|JMj_0l_0\varepsilon\right\rangle \tag{10}$$

To avoid the reflection of wave packet at the grid edge, the absorption potential used in the TDWP calculations is defined as:

$$D(x) = \begin{cases} \exp\left[-\Delta_t \cdot C_a \cdot \left(\dfrac{x-x_a}{x_b-x_a}\right)^2\right], & x_a \le x \le x_b \\ \exp\left[-\Delta_t \cdot C_b \cdot \left(\dfrac{x-x_b}{x_{\text{end}}-x_b}\right)^2\right] \times \exp(-\Delta_t \cdot C_a), & x_b < x \le x_{\text{end}} \end{cases} \tag{11}$$

where C_i and x_i ($i = a, b$) represent the strength and positions of the absorption potential, respectively. Here, the time evolution of the wave packet is realized by the split operator scheme [56] and using the reactant coordinate-based method [57, 58] to extract the state-resolved *S*-matrix. The rovibrationally state-resolved reaction probability obtained by the *S*-matrix is expressed as:

$$P^J_{vj\leftarrow v_0j_0} = \frac{1}{2j_0+1}\sum_K\sum_{K_0}\left|S^J_{vjK\leftarrow v_0j_0K_0}\right|^2 \tag{12}$$

The state-resolved integral cross sections (ICSs) are calculated by summing the probabilities of all the calculated partial wave *J*:

$$\sigma_{vj\leftarrow v_0j_0} = \frac{\pi}{(2j_0+1)k^2_{v_0j_0}}\sum_K\sum_{K_0}\sum_J(2J+1)\left|S^J_{vjK\leftarrow v_0j_0K_0}\right|^2 \tag{13}$$

where $k_{v_0j_0}$ is the momenta in the entrance channel. The state-resolved differential cross sections (DCSs) can be obtained by the following equation:

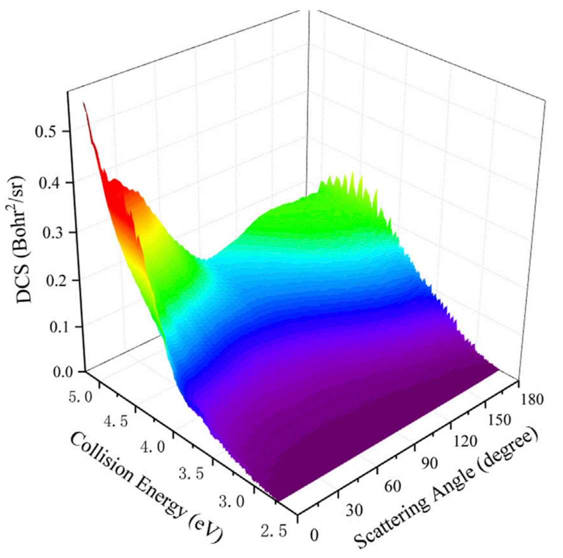

FIGURE 9
Total DCS of the Be(^{1}S) + $H_2(v_0 = 0, j_0 = 0) \rightarrow$ BeH + H reaction as a function of scattering angle and collision energy calculated by the TDWP method on the ground-state BeH_2 PES.

$$\frac{d\sigma_{vj\leftarrow v_0 j_0}(\vartheta, E)}{d\Omega} = \frac{1}{(2j_0+1)}\sum_{K}\sum_{K_0}\left|\frac{1}{2ik_{v_0 j_0}}\sum_{J}(2J+1)d^J_{KK_0}(\vartheta)S^J_{vjK\leftarrow v_0 j_0 K_0}\right|^2 \tag{14}$$

where$d^J_{KK_0}(\vartheta)$ represents the reduced Wigner matrix, andϑexpress the scattering angle.

In this work, the reactant H_2 molecule is set at its ground-rovibrational state of $v_0 = 0$, $j_0 = 0$, and the number of partial waves is calculated up to 65, which can obtain the convergent ICS and DCS up to the collision energy of 5.0 eV. In Table 3, the main parameters determined by many times tests of convergence in the TDWP calculations are listed.

The collision energy dependence of total reaction probabilities for the Be(^{1}S) + $H_2(v_0 = 0, j_0 = 0) \rightarrow$ BeH + H reaction with four partial waves (J = 0, 20, 40 and 50) are presented in Figure 7A. For $J = 0$, the curve exhibits relatively dense oscillation structures, which are attributed to the potential well on the reactive path. The title reaction is dominated by the global MEP and there is a well with the depth of 1.632 eV, resulting in obvious quantum resonances because numerous bound and quasi-bound states can be formed in the well. As the increase of J values, the reactive threshold becomes larger and the oscillations are gradually weakened. This is because the increasing centrifugal barrier reduces and even smooths the effective potential well, and the other collision channels shown in Figure 5 are opened, causing the amplitudes of oscillations on the reaction probability curves become less pronounced. Figure 7B shows the collision energy dependence of total ICS for the title reaction. The total ICS value increases monotonically with the increase of collision energy, which is consistent with the characteristic of an endothermic reaction. Compared to the reaction probabilities, there is no oscillation structures on the ICS curve due to the superposition of all the calculated partial waves.

To understand the dynamics mechanisms of the Be(^{1}S) + $H_2(v_0 = 0, j_0 = 0) \rightarrow$ BeH + H reaction at the state-to-state level, the rovibrationally state-resolved ICSs of the product BeH molecule at four collision energies (3.0, 4.0, 4.5, and 5.0 eV) are shown in Figure 8. For the collision energy of 3.0 eV, the BeH molecule only can be excited to the lowest three vibrational states, but the maximum of the rotational quantum number can reach $j' = 21$ at $v' = 0$, and the peak value of the rovibrationally state-resolved ICS is located at $v' = 0$, $j' = 16$. The presented vibrationally cold and rotationally hot distribution conforms to the complex-forming mechanism. More rovibrational states become available with the increase of collision energy, and there is a population inversion of the vibrational quantum number. For the collision energy of 5.0 eV, the product BeH molecule can populate at very high rovibrational states ($v' = 10$, $j' = 28$), suggesting more collision energy is effectively transformed into the internal energy of the product molecule. The contributions of high-order partial waves are larger and more reaction paths are gradually opened as the collision energy increases, thus the lifetime of the forming BeH_2 complex becomes shorter and the title reaction prefers a direct H-abstraction process when the collision energy is large enough.

To study the dynamics process of the Be(^{1}S) + $H_2(v_0 = 0, j_0 = 0) \rightarrow$ BeH + H reaction more intuitively by giving the angular distribution of the product molecule, Figure 9 presents the total DCSs varying with the scattering angle and collision energy. It is clear that the peak values of the angular distribution are located at the two extreme angles (0° and 180°) and the forward-backward symmetric DCSs are displayed when the collision energy is slightly larger than the reactive threshold, which is due to the forming of a BeH_2 complex supported by the potential well on the global MEP. With the increase of collision energy, the product BeH molecule increasingly prefers the forward scattering, showing an obviously non-statistical behavior. It also can be explained by the increasing contributions of the centrifugal barriers and more open reactive paths without a well at large collision energy. The calculated results of the total DCS further imply that the title reaction follows the complex-forming mechanism near the reactive threshold, whereas s direct H-abstraction process gradually plays a dominant role at high collision energy.

4 Conclusion

In this paper, a globally accurate ground-state BeH_2 PES is structured using the PIP-NN scheme based on 12371 *ab initio* points calculated at the icMRCI + Q/aug-cc-pCV5Z level. The PES can accurately reproduce the original *ab initio* data in each region, and the global fitting RMSE is only 1.972 meV. The molecular constants of $H_2(X^1\Sigma_g^+)$ and $BeH(X^1\Sigma^+)$ calculated on the PES are consistent with the corresponding experimental data, and the PES can reproduce the characteristics of stationary points well. The GM and TS of the ground-state BeH_2 correspond to the $D_{\infty h}$ and C_{2v} symmetries, respectively. The topographic features of the PES are described in detail. On this newly constructed PES, the dynamics calculations are performed on the $Be(^1S) + H_2(v_0 = 0, j_0 = 0) \rightarrow BeH + H$ reaction at the state-to-state level by the quantum TDWP method for understanding the microscopic mechanisms. The endothermicity of the title reaction determined by the PES is 2.716 eV. There exist obvious oscillation structures on the curves of reaction probabilities since the well on the global MEP can support numerous bound and quasi-bound states, and the total ICS increases monotonically with the increase of collision energy. The rovibrationally state-resolved ICSs present vibrationally cold and rotationally hot distribution at relatively low collision energy, and the product BeH molecule can populate at very high rovibrational states. The total DCSs are forward-backward symmetric when the collision energy is slightly larger than the reactive threshold, but only the forward scattering is presented at high collision energy. The dynamics results indicate that the title reaction follows the complex-forming mechanism near the reactive threshold, whereas a direct H-abstraction process gradually plays the dominant role at high collision energy. Further dynamics studies for this reaction system can be carried out on the presented PES, such as the effects of rovibrational excitations and isotopic substitutions of the H_2 molecule, and the dynamics data calculated in this paper would be of importance in the experimental studies on the title reaction.

Data availability statement

The original contributions presented in the study are included in the article/Supplementary Material, further inquiries can be directed to the corresponding author.

Author contributions

ZY wrote the original manuscript, constructed the theoretical models and performed the calculations. MC proposed the idea, supervised the research work and revised the manuscript. ZY and MC discussed and analysed the results.

Funding

This work was supported by the National Natural Science Foundation of China (Grant No. 11774043).

Conflict of interest

The authors declare that the research was conducted in the absence of any commercial or financial relationships that could be construed as a potential conflict of interest.

Publisher's note

References

1. Senin MD, Akhachinskii VV, Markushkin YE, Chirin NA, Kopytin LM, Mikhalenko IP, et al. The production, structure, and properties of beryllium hydride. *Inorg Mater* (1993) 29:1416–20.

2. Nechiporenko GN, Lempert DB. An analysis of energy potentialities of composite solid propellants containing beryllium or beryllium hydride as an energetic component. *Chem Phys Rep* (1998) 17:1927–47.

3. Szalay PG, Bartlett RJ. Approximately extensive modifications of the multireference configuration-interaction method: A theoretical and practical analysis. *J Chem Phys* (1995) 103:3600–12. doi:10.1063/1.470243

4. Mahapatra US, Datta B, Mukherjee D. A size-consistent state-specific multireference coupled cluster theory: Formal developments and molecular applications. *J Chem Phys* (1999) 110:6171–88. doi:10.1063/1.478523

5. Mazziotti DA. Comparison of contracted Schrödinger and coupled-cluster theories. *Phys Rev A (Coll Park)* (1999) 60:4396–408. doi:10.1103/physreva.60.4396

6. Baer R, Neuhauser D. Molecular electronic structure using auxiliary field Monte Carlo, plane-waves, and pseudopotentials. *J Chem Phys* (2000) 112:1679–84. doi:10.1063/1.480733

7. Meissner H, Paldus J. Direct iterative solution of the generalized bloch equation. IV. Application to H_2, LiH, BeH, and CH_2. *J Chem Phys* (2000) 113: 2622–37. doi:10.1063/1.1305323

8. Fülscher MP, Serrano-Andrés L. Quasi diabatic CASSCF state functions. *Mol Phys* (2002) 100:903–9. doi:10.1080/00268970110101590

9. Sauval AJ, Tatum JB. A set of partition-functions and equilibrium constants for 300 diatomic-molecules of astrophysical interest. *Astrophys J Suppl Ser* (1984) 56: 193–209. doi:10.1086/190980

10. Singh M. Thirty-one new diatomic-molecules in cosmic objects spectra. *Astrophys Space Sci* (1988) 140:421–7. doi:10.1007/BF00638995

11. Tague TJ, Andrews L. Reactions of beryllium atoms with hydrogen. Matrix infrared-spectra of novel product molecules. *J Am Chem Soc* (1993) 115:12111–6. doi:10.1021/ja00078a057

12. Bernath PF, Shayesteh A, Tereszchuk K, Colin R. The vibration-rotation emission spectrum of free BeH_2. *Science* (2002) 297:1323–4. doi:10.1126/science.1074580

13. Sampath S, Lantzky KM, Benmore CJ, Neuefeind J, Siewenie JE, Egelstaff PA, et al. Structural quantum isotope effects in amorphous beryllium hydride. *J Chem Phys* (2003) 119:12499–502. doi:10.1063/1.1626638

14. Shayesteh A, Tereszchuk K, Bernath PF, Colin R. Infrared emission spectra of BeH_2 and BeD_2. *J Chem Phys* (2003) 118:3622–7. doi:10.1063/1.1539850

15. Wang XF, Andrews L. One-dimensional BeH_2 polymers: Infrared spectra and theoretical calculations. *Inorg Chem* (2005) 44:610–4. doi:10.1021/ic048464b

16. Sampath S, Kolesnikov AI, Lantzky KM, Yarger JL. Vibrational dynamics of amorphous beryllium hydride and lithium beryllium hydrides. *J Chem Phys* (2008) 128:134512. doi:10.1063/1.2842079

17. Motallebipour MS, Shayesteh A. Determination of v_2 fundamental band origin for BeH_2 and BeD_2 from deperturbation analysis of hot bands. *J Chem Phys* (2016) 145:074310. doi:10.1063/1.4960551

18. Pépin CM, Loubeyre P. Layered structure and re-entrant disproportionation observed in crystalline BeH_2 under pressure. *Phys Rev B* (2016) 93:224104. doi:10.1103/PhysRevB.93.224104

19. Martin JML, Lee TJ. Accurate ab initio quartic force-fields for borane and BeH_2. *Chem Phys Lett* (1992) 200:502–10. doi:10.1016/0009-2614(92)80082-M

20. Ben Amor N, Maynau D. Size-consistent self-consistent configuration interaction from a complete active space. *Chem Phys Lett* (1998) 286:211–20. doi:10.1016/S0009-2614(98)00104-3

21. Hinze J, Friedrich O, Sundermann A. A study of some unusual hydrides: BeH_2, BeH_6^+ and SH_6. *Mol Phys* (1999) 96:711–8. doi:10.1080/00268979909483007

22. Hantsch U, Winkler B, Milman V. The isotypism of BeH_2 and SiO_2: An *ab initio* study. *Chem Phys Lett* (2003) 378:343–8. doi:10.1016/S0009-2614(03)01333-2

23. Hrenar T, Werner HJ, Rauhut G. Towards accurate *ab initio* calculations on the vibrational modes of the alkaline Earth metal hydrides. *Phys Chem Chem Phys* (2005) 7:3123–5. doi:10.1039/b508779a

24. Koput J, Peterson KA. *Ab initio* prediction of the potential energy surface and vibration-rotation energy levels of BeH_2. *J Chem Phys* (2006) 125:044306. doi:10.1063/1.2212932

25. Li H, Le Roy RJ. An accurate *ab initio* potential energy surface and calculated spectroscopic constants for BeH_2, BeD_2, and BeHD. *J Chem Phys* (2006) 125:044307. doi:10.1063/1.2212933

26. Vasiliu M, Peterson KA, Dixon DA. Benchmark-quality atomization energies for BeH and BeH_2. *J Chem Theor Comput* (2017) 13:649–53. doi:10.1021/acs.jctc.6b01154

27. Jiang B, Li J, Guo H. High-fidelity potential energy surfaces for gas-phase and gas-surface scattering processes from machine learning. *J Phys Chem Lett* (2020) 11:5120–31. doi:10.1021/acs.jpclett.0c00989

28. Li J, Zhao B, Xie DQ, Guo H. Advances and new challenges to bimolecular reaction dynamics theory. *J Phys Chem Lett* (2020) 11:8844–60. doi:10.1021/acs.jpclett.0c02501

29. Jiang B, Guo H. Permutation invariant polynomial neural network approach to fitting potential energy surfaces. *J Chem Phys* (2013) 139:054112. doi:10.1063/1.4817187

30. Jiang B, Li J, Guo H. Potential energy surfaces from high fidelity fitting of *ab initio* points: The permutation invariant polynomial - neural network approach. *Int Rev Phys Chem* (2016) 35:479–506. doi:10.1080/0144235X.2016.1200347

31. Sun ZG, Lee SY, Guo H, Zhang DH. Comparison of second-order split operator and Chebyshev propagator in wave packet based state-to-state reactive scattering calculations. *J Chem Phys* (2009) 130:174102. doi:10.1063/1.3126363

32. Sun ZG, Guo H, Zhang DH. Extraction of state-to-state reactive scattering attributes from wave packet in reactant Jacobi coordinates. *J Chem Phys* (2010) 132:084112. doi:10.1063/1.3328109

33. Werner HJ, Knowles PJ. An efficient internally contracted multiconfiguration reference configuration-interaction method. *J Chem Phys* (1988) 89:5803–14. doi:10.1063/1.455556

34. Knowles PJ, Werner HJ. An efficient method for the evaluation of coupling-coefficients in configuration-interaction calculations. *Chem Phys Lett* (1988) 145:514–22. doi:10.1016/0009-2614(88)87412-8

35. Werner HJ, Knowles PJ. A second order multiconfiguration SCF procedure with optimum convergence. *J Chem Phys* (1985) 82:5053–63. doi:10.1063/1.448627

36. Knowles PJ, Werner HJ. An efficient second-order MC SCF method for long configuration expansions. *Chem Phys Lett* (1985) 115:259–67. doi:10.1016/0009-2614(85)80025-7

37. Kendall RA, Dunning TH, Harrison RJ. Electron affinities of the first-row atoms revisited. Systematic basis sets and wave functions. *J Chem Phys* (1992) 96:6796–806. doi:10.1063/1.462569

38. Werner HJ, Knowles PJ, Knizia G, Manby FR, Schutz M. Molpro: A general-purpose quantum chemistry program package. *Wires Comput Mol Sci* (2012) 2:242–53. doi:10.1002/wcms.82

39. Huber KP, Herzberg G. *Molecular spectra and molecular structure, vol. 4,* Constants of diatomic molecules. New York: Van Nostrand Reinhold (1979).

40. Le Roy RJ, Appadoo DRT, Colin R, Bernath PF. On the $X^2\ \Sigma^+$, $A^2\Pi$, and $C^2\ \Sigma^+$ states of BeH, BeD, and BeT. *J Mol Spectrosc* (2006) 236:178–88. doi:10.1016/j.jms.2006.01.010

41. Horne R, Colin R. $A^2\Pi$-$X^2\Sigma^+$ band system of BeH and BeD in absorption. *B Soc Chim Belg* (1972) 81:93. doi:10.1002/bscb.19720810108

42. Yang ZJ, Chen HH, Chen MD. Representing globally accurate reactive potential energy surfaces with complex topography by combining Gaussian process regression and neural networks. *Phys Chem Chem Phys* (2022) 24:12827–36. doi:10.1039/d2cp00719c

43. Song KS, Song HW, Li J. Validating experiments for the reaction H_2 + NH_2^- by dynamical calculations on an accurate full-dimensional potential energy surface. *Phys Chem Chem Phys* (2022) 24:10160–7. doi:10.1039/d2cp00870j

44. Zuo JX, Croft JFE, Yao Q, Balakrishnan N, Guo H. Full-dimensional potential energy surface for ro-vibrationally inelastic scattering between H_2 molecules. *J Chem Theor Comput* (2021) 17:6747–56. doi:10.1021/acs.jctc.1c00882

45. Varga Z, Liu Y, Li J, Paukku Y, Guo H, Truhlar DG. Potential energy surfaces for high-energy N + O_2 collisions. *J Chem Phys* (2021) 154:084304. doi:10.1063/5.0039771

46. Yang ZJ, Wang SF, Yuan JC, Chen MD. Neural network potential energy surface and dynamical isotope effects for the $N^+(^3P) + H_2 \rightarrow$ NH+ + H reaction. *Phys Chem Chem Phys* (2019) 21:22203–14. doi:10.1039/c9cp02798j

47. Yuan JC, He D, Wang SF, Chen MD, Han KL. Diabatic potential energy surfaces of MgH_2^+ and dynamic studies for the $Mg^+(3p) + H_2 \rightarrow MgH^+ + H$ reaction. *Phys Chem Chem Phys* (2018) 20:6638–47. doi:10.1039/c7cp08679b

48. Yang TG, Li AY, Chen GK, Yao Q, Suits AG, Guo H, et al. Isomer-specific kinetics of the $C^+ + H_2O$ reaction at the temperature of interstellar clouds. *Sci Adv* (2021) 7:eabe4080. doi:10.1126/sciadv.abe4080

49. Yang DZ, Zuo JX, Huang J, Hu XX, Dawes R, Xie DQ, et al. A global full-dimensional potential energy surface for the K_2Rb_2 complex and its lifetime. *J Phys Chem Lett* (2020) 11:2605–10. doi:10.1021/acs.jpclett.0c00518

50. He D, Yuan JC, Li HX, Chen MD. A new potential energy surface of LiHCl system and dynamic studies for the $Li(^2S) + HCl(X^1\ \Sigma^+) \rightarrow LiCl(X^1\ \Sigma^+) + H(^2S)$ reaction. *J Chem Phys* (2016) 145:234312. doi:10.1063/1.4972229

51. Li J, Varga Z, Truhlar DG, Guo H. Many-body permutationally invariant polynomial neural network potential energy surface for N_4. *J Chem Theor Comput* (2020) 16:4822–32. doi:10.1021/acs.jctc.0c00430

52. Hagan MT, Menhaj MB. Training feedforward networks with the marquardt algorithm. *IEEE Trans Neural Netw* (1994) 5:989–93. doi:10.1109/72.329697

53. Huang JY, Liu S, Zhang DH, Krems RV. Time-dependent wave packet dynamics calculations of cross sections for ultracold scattering of molecules. *Phys Rev Lett* (2018) 120:143401. doi:10.1103/PhysRevLett.120.143401

54. Buren B, Chen MD, Sun ZG, Guo H. Quantum wave packet treatment of cold nonadiabatic reactive scattering at the state-to-state level. *J Phys Chem A* (2021) 125:10111–20. doi:10.1021/acs.jpca.1c08105

55. Buren B, Chen MD. Wave packet approach to adiabatic and nonadiabatic dynamics of cold inelastic scatterings. *Molecules* (2022) 27:2912. doi:10.3390/molecules27092912

56. Feit MD, Fleck JA, Steiger A. Solution of the Schrödinger equation by a spectral method. *J Comput Phys* (1982) 47:412–33. doi:10.1016/0021-9991(82)90091-2

57. Gómez-Carrasco S, Roncero O. Coordinate transformation methods to calculate state-to-state reaction probabilities with wave packet treatments. *J Chem Phys* (2006) 125:054102. doi:10.1063/1.2218337

58. Sun ZG, Lin X, Lee SY, Zhang DH. A reactant-coordinate-based time-dependent wave packet method for triatomic state-to-state reaction dynamics: Application to the H + O_2 reaction. *J Phys Chem A* (2009) 113:4145–54. doi:10.1021/jp810512j

frontiers | Frontiers in Physics

TYPE Original Research
PUBLISHED 28 October 2022
DOI 10.3389/fphy.2022.1026384

OPEN ACCESS

EDITED BY
Yujun Zheng,
Shandong University, China

REVIEWED BY
Chunlei Wang,
Shanghai Advanced Research Institute,
(CAS), China
Jijun Zhao,
Ministry of Education, China

*CORRESPONDENCE
Zhigang Wang,
wangzg@jlu.edu.cn

†These authors have contributed equally to this work and share first authorship

SPECIALTY SECTION
This article was submitted to Atomic and Molecular Physics,
a section of the journal
Frontiers in Physics

RECEIVED 23 August 2022
ACCEPTED 17 October 2022
PUBLISHED 28 October 2022

CITATION
Yang X, Jin L, Zhu Y, Zhang Z, Liu R and Wang Z (2022), The hydrogen bond rotation of confined water affected by quantum resonance tunnelling.
Front. Phys. 10:1026384.
doi: 10.3389/fphy.2022.1026384

The hydrogen bond rotation of confined water affected by quantum resonance tunnelling

Xinrui Yang[1†], Le Jin[1,2†], Yu Zhu[1], Zhiyuan Zhang[1], Rui Liu[1] and Zhigang Wang[1,3*]

[1]Institute of Atomic and Molecular Physics, Jilin University, Changchun, China, [2]Normal School, Shenyang University, Shenyang, China, [3]College of Physics, Jilin University, Changchun, China

In this work, we report quantum tunnelling effects on the confined water chain flipping, different from the spatial size and even electronic correlation effects of the confinement environment. First-principles calculations and analyses confirm that quantum tunnelling from the water chain itself enhances the hydrogen bond rotation. Importantly, the neglected resonant tunnelling can result in tunnelling rotation of hydrogen bonds with a probability close to 1 through the provided 0.6 eV energy, while the probability of generally recognized sequential tunnelling is only 10^{-6}. Not only that, compared to sequential tunnelling, resonant tunnelling leads to a 20 K higher flipping temperature of the water chain. Additionally, the ratio of the resonant tunnelling probability to the thermal disturbance probability at 200 K is at least ten times larger than that of sequential tunnelling, which further illustrates the enhancement of hydrogen bond rotation brought about by resonant tunnelling.

KEYWORDS

resonant tunnelling, quantum coherence, thermal disturbance, hydrogen bond, confinement, first-principles

Introduction

To achieve effective regulation of the water transport process, an important goal is to deeply understand the confined hydrogen bond (H-bond) rotation mechanism at the atomic level. Quantum effects have been reported to be essential and should be carefully considered on a microscopic scale [1–7], including quantum effects related to water, such as properties of electronic correlation [8–10], nuclear quantum effects [11, 12] and tunnelling [13, 14]. This suggests that quantum effects play an important role in understanding the nature of water and even regulating its behavior. More importantly, some studies show that the H-bond rotation of water is affected by quantum effects [8, 15]. As a microstructure, a hydrogen atom has a very small mass, which leads to the existence of tunnelling effects from the water chain itself during H-bond rotation. Moreover, a recent experiment revealed that quantum coherence can effectively improve the tunnelling effects [1]. This inspired us to explore the deep effect of the quantum properties of a water chain on the H-bond rotation.

Currently, many studies have been performed on the transport and H-bonds of confined water [16–23], including on the step-by-step rotation behavior of confined water and its intrinsic mechanism [24]. Many studies have shown that the flipping of confined water is affected by the spatial size [25–30]. For example, the transport of confined water has a high conductivity [28, 29], and the water flux through a carbon nanotube (CNT) has a linear relationship with the radius of the CNT when the length is much larger than the radius [30]. However, due to the inherent complexity of the molecular system, the understanding of the mechanism of water chain flipping under confinement is still unclear. The experimental technique has been greatly improved compared with the past, which has resulted in water chains formed in CNTs with diameters as small as 0.548 nm, and an extremely high freezing temperature has been detected [31, 32]. However, observing the details of the mechanism of water chain flipping in a short time, much less regulating the mechanism of water chain flipping, is still a great challenge. Considering that the tunnelling effects, especially the previously often neglected quantum coherence, have a more fundamental significance in quantum physics, studying the resonance effects caused by the coherence that exists when a water chain flips in a confined space from the perspective of the basic principles of tunnelling is necessary.

In this work, we study the possible flipping of a water chain under quasi-one-dimensional (1D) confinement and find that the quantum tunnelling cannot be ignored. Significantly, quantum resonant tunnelling brings different effects than generally recognized tunnelling and thermal processes. Here, the calculation results show that the H-bond rotation of the water chain in a 1D-CNT is obviously affected by tunnelling, especially resonant tunnelling. Compared with the tunnelling without considering quantum coherence, the resonant tunnelling with considering quantum coherence can achieve a higher probability with less provided energies, which leads to an increase of water chain flipping temperature by 20 K. Therefore, our work opens a new perspective for the quantum regulation of water chain flipping in channels.

Computational methods

For first-principles calculations, the empirical-dispersion-corrected hybrid Perdew-Burke-Ernzerhof (PBE0-D3) method of density functional theory was carried out in the Gaussian 09 package [33–35]. The basis sets 6-311+G (d, p) and 6-31G (d) were used for water and the CNT, respectively. The armchair-type single-walled (6, 6) CNT was employed, and the diameter and length were set to 8.20 Å and 20 Å, respectively. After CNT preoptimization, we froze all of the atoms of the CNT to ensure constant confinement effects on the water. In the CNT, three water molecules were selected to form the water chain. The water chain was along the tube axis, and the molecules were connected to each other by H-bonds. Based on the different initial geometries of the water chain, we searched the structures for extreme points (including equilibrium and transition states) in the rotation of water molecules in the CNT and traced the reaction paths of the flipping for the water chain according to the intrinsic reaction coordinate [36, 37]. The reduced masses are 1.0834 amu and 1.0955 amu for the water chain flipping along the path containing L-type and D-type defective intermediates.

For the formula without considering quantum coherence, the Wentzel-Kramers-Brillouin (WKB) approximation is used for calculating the tunnelling probability for a single barrier using the following formula [38, 39]:

$$P = Exp\left[-\frac{2}{\hbar}\int_{x_1}^{x_2}\sqrt{2m\left(V\left(x\right)-E\right)}\,dx\right] \tag{1}$$

where $\hbar$ is the reduced Planck constant, V(x) represents the potential energy surface (PES) function with the coordinate x as the variable, expressed by a Gaussian fitting function, and x_1 and x_2 are the two coordinates when V(x) and E are equal. The tunnelling probability for double barriers is obtained by multiplying the tunnelling probability of two single barriers.

For the formula considering quantum coherence, the steady-state Schrödinger equation of N multiple barriers is strictly solved. For the convenience of calculation, the equivalent square barrier is used to fit the PES. In detail, we first take the half-height width of the left-side barrier as the square barrier width to obtain the approximate equivalent square barrier. Then, the local minimum value is taken as the axis of symmetry to obtain the ideal double barrier model. This equivalent square barrier method is an approximation based on the principle that original barrier and approximate square barrier have the same tunnelling probability. The general expression of the Schrödinger equation can be written as follows:

$$\psi_j = C_{2j-1}\,exp\left(ik_jx\right) + C_{2j}\,exp\left(-ik_jx\right) \tag{2}$$

in which C_{2j-1} represents the transmission amplitude, C_{2j} is the reflection amplitude and k_j is the wavenumber. The tunnelling probability is defined as the ratio of the flow of particles out of the barrier to the flow of particles into the barrier as follows:

$$T = \frac{|C_{4N+1}|^2}{|C_1|^2} \tag{3}$$

For the thermodynamic model, the Boltzmann distribution is used to describe the probability of crossing the barrier from the classical perspective as follows:

$$P_{thermal} = Exp\left(-\frac{\Delta E}{kT}\right) \tag{4}$$

where k is the Boltzmann constant and T is the temperature. ΔE represents the relative energy between the initial provided energy and the barrier peak. Additionally, to compare the classical and

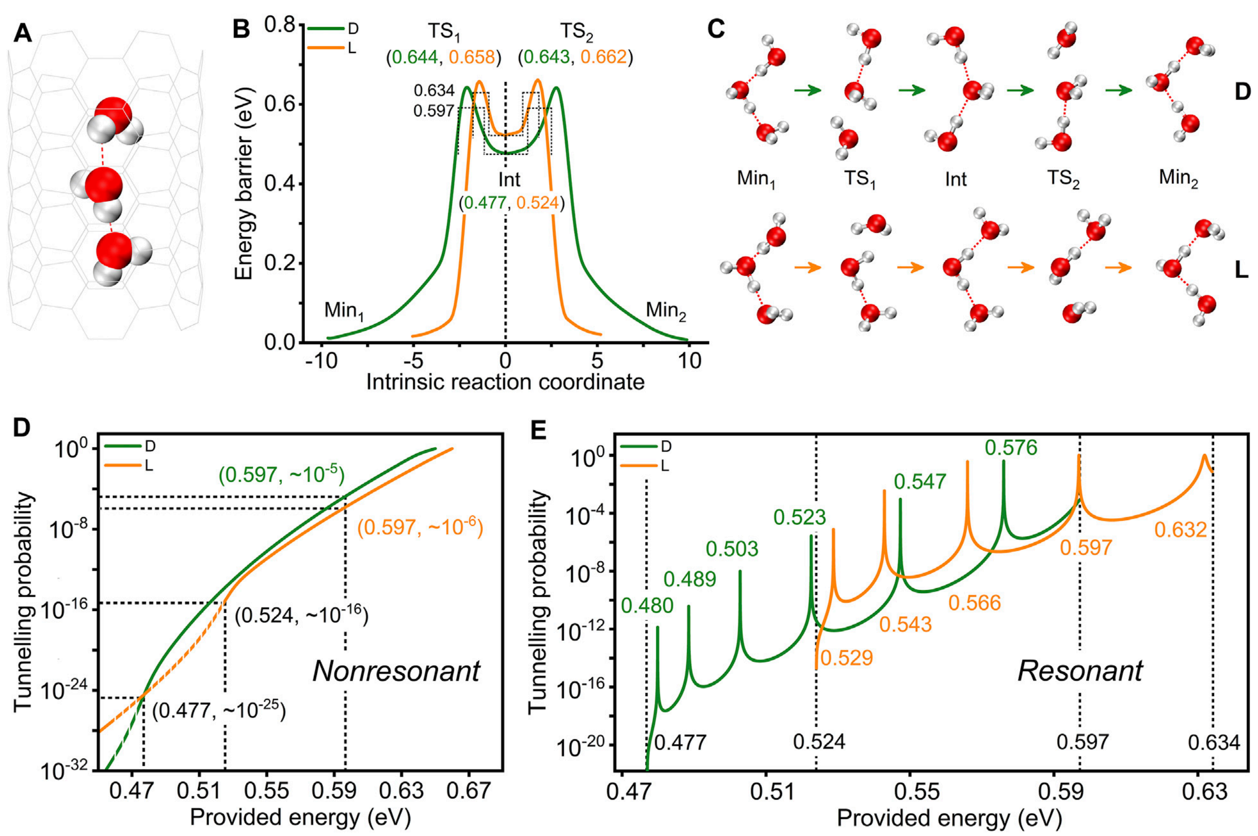

FIGURE 1
Different mechanisms by which the water chain with three water molecules in the CNT achieves reorientation. **(A)** Model of the confined water chain. **(B)** PESs of the water chain flipping. Dotted lines are the equivalent square energy barriers obtained by fitting the double barriers of the PESs. **(C)** Water chain structures corresponding to each extreme point on the PESs. **(D)** Variation in the quantum tunnelling probability with provided energy without considering coherence. The dotted and solid lines indicate the tunnelling probability at provided energies below and above the intermediate energies, respectively. **(E)** Variation in the quantum tunnelling probability with provided energy considering coherence. According to the square barriers, the energy height provided are 0.477–0.597 eV and 0.524–0.634 eV, corresponding to the two reaction paths. The dotted lines represent the provided energy at the start or end of the two reaction paths. Green and yellow represent the reaction paths containing D-type and L-type defective intermediates, respectively.

quantum methods of crossing the barrier, the ratio of the quantum tunnelling probability to the thermal disturbance probability is studied.

Results and discussion

To study the possible flipping of a water chain under confinement, the water molecules in a CNT that form a 1D chain are examined (Figure 1A). We give two reaction paths, and the corresponding PESs of flipping are shown in Figure 1B. There are five extreme points along each reaction path: two structures with lower energies (reactant and product, labelled Min1 and Min2), two transition state structures (labelled TS1 and TS2), and an intermediate structure (labelled Int). These structures are shown in Figure 1C. This suggests that the flipping of the water chain is a step-by-step process, and the formation of the intermediate is necessary, which is consistent with our previous study [24]. For the two reaction paths, the main difference lies in the structure of the intermediate. In detail, when the water chain flips along the nanotube axis in the opposite direction to the H-bonds, the heights of the energy barriers of the two transition states to be overcome are approximately 0.660 eV, and an intermediate with an energy of approximately 0.524 eV is formed. This structure has the two hydrogen atoms in the middle water molecule forming H-bonds with the oxygen atoms of the two adjacent water molecules. We call this the intermediate with an L-type defect [40]. The H-bonds are oriented towards the middle water molecule. When the water chain flips along the direction of the H-bond, it needs to overcome two energy barriers with

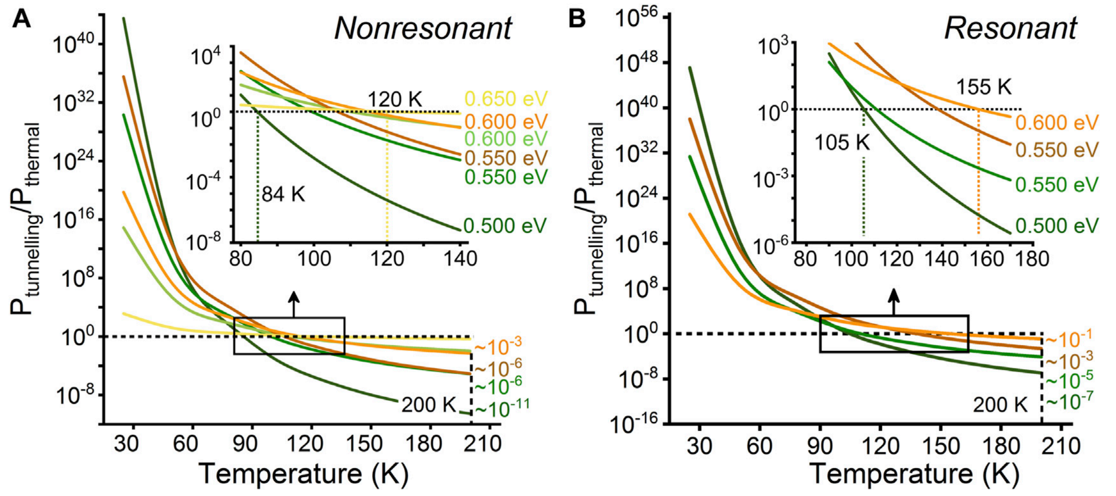

FIGURE 2
Ratio of the tunnelling probability to the thermal disturbance probability for the water chain in the CNT to achieve reorientation at certain provided energies and different temperatures. **(A)** Coherence is not considered in the tunnelling probability calculation. **(B)** Coherence is considered in the tunnelling probability calculation. The temperature range is 25–200 K, and the interval is 25 K "~" is the magnitude.

heights of approximately 0.640 eV. Additionally, the intermediate formed has an energy of approximately 0.477 eV. In this structure, the oxygen atom in the middle water molecule forms H-bonds with the hydrogen atoms of the two adjacent water molecules. The H-bonds are oriented towards both ends of the water molecules, which is called the intermediate with a D-type defect [40]. The energy of the intermediate with an L-type defect is approximately 10^{-2} eV higher than that of the intermediate with a D-type defect. This indicates that the water chain is more likely to flip along the path of the intermediate with a D-type defect.

Reorientation of the water chain can be achieved not only through step-by-step flipping by classical thermodynamic perturbations but also by quantum tunnelling. Here, to obtain the sequential tunnelling probability for double barriers without considering the quantum coherence, the WKB approximation is applied [39, 40]. We considered the difficulty of the water chain to achieve reorientation by quantum tunnelling at different provided energies. As shown in Figure 1D, with an increase in the provided energy, the tunnelling probability gradually increases. Taking the path containing the L-type defective intermediate as an example, the tunnelling probabilities are approximately 10^{-25}, 10^{-16} and 10^{-6} when the provided energies are approximately 0.477 eV, 0.524 eV and 0.597 eV, respectively. For the two paths containing L-type and D-type defective intermediates, when the provided energy is approximately 0.477 eV, the two tunnelling probabilities are almost equal. However, when the provided energy is larger than 0.477 eV, the tunnelling probability of the water chain along the path containing the L-type defective intermediate is less than that along the path containing the D-type defective intermediate. For example, at the provided energy of 0.597 eV, the tunnelling probabilities are approximately 10^{-6} and 10^{-5} for the reaction paths containing the L-type and D-type defective intermediates, respectively. When the provided energy is less than 0.477 eV, the tunnelling probability of the water chain along the path containing the L-type defective intermediate is greater than that along the path containing the D-type defective intermediate.

In addition to quantum tunnelling, thermal effects can also cause the water chain to flip. To clearly show the relationship between tunnelling and thermal disturbance with temperature and provided energy, we treat thermal disturbance and tunnelling as independent probability events. Under this condition, we compare the probabilities of the water chain achieving reorientation by quantum tunnelling and thermal disturbance (25–200 K). As shown in Figure 2A, when the provided energies at the double barriers of the two reaction paths are given, the probability of water chain flipping by thermal disturbance increases with the temperature. When the temperature is lower than 84 K, quantum tunnelling is more dominant than thermal disturbance. At temperatures above 120 K, thermal disturbance plays a dominant role, rather than quantum tunnelling. Therefore, we infer that at room temperature, thermal disturbance is more likely to cause the water chain to flip.

Remarkably, due to the narrow width (approximately 1.9 Å and 2.5 Å for the reaction paths containing the L-type defect and D-type defect, and the values are similar to the previous article predicting hydrogen atom resonance tunneling [41]) of the well between the double barriers along the reaction path, the quantum coherence should not be ignored. Therefore, a discussion of the quantum tunnelling effects while considering coherence, that is, resonant tunnelling, is necessary. The tunnelling probability is defined as the ratio of the flow of particles out of the barrier to the flow of particles into the barrier. As shown in Figure 1E, with an increase in the provided energy, the tunnelling probability increases and decreases at times, showing a nonlinear change. This is significantly different from the quantum tunnelling probability without considering coherence. In addition, according to the peaks in Figure 1E, compared with quantum tunnelling without coherence, quantum tunnelling with coherence can achieve a higher probability at smaller provided energy. Taking the path containing the L-type defective intermediate as an example, the probabilities of quantum tunnelling without and with consideration of coherence are approximately 10^{-15}, 10^{-12}, 10^{-10}, 10^{-6}, and 10^{-3} and 10^{-6}, 10^{-3}, 10^{-1}, 10^{0}, and 100 when the provided energies at the double barrier are approximately 0.529 eV, 0.543 eV, 0.566 eV, 0.597 eV and 0.632 eV, respectively. In a word, at some specific provided energies, such as about 0.6 eV (detailed value is 0.597 eV), the resonant tunnelling with consideration of coherence greatly improves the tunnelling probability compared with sequential tunnelling (see in Figures 1D,E), which means that neglected quantum coherence may play an important role in the process of water chain flipping.

Our previous study has demonstrated that the persistent time (t) of the H-bond alignment for the confined water chain was closely related to the PES of flipping [24]. It is negatively correlation with the probability that the water chain achieves flipping by overcoming energy barriers. And the relationship between the number of water molecules (n) and the persistent time is written:

$$\boldsymbol{Log}\ (\boldsymbol{t}) = \boldsymbol{a} \times \boldsymbol{n} + \boldsymbol{b} \tag{5}$$

where a is the dynamic parameter of thermodynamic flipping under the traditional perspective. In this work, we found that the quantum tunneling, especially resonant tunneling, from the water chain itself has a positive impact on its flipping. This means that the existence of quantum tunnelling effects will reduce the persistent time (i.e., reducing the value of a), thereby enhancing the effect of water chain flipping. It is reported that with the increase of water molecules [24], water chain rotation becomes more difficult, which is expected to lead to relatively weak quantum tunneling effects.

Furthermore, we compare the probabilities of the water chain achieving reorientation *via* two different mechanisms (quantum tunnelling considering coherence and thermal disturbance), as shown in Figure 2B. The results show that when the temperature is lower than 105 K, tunnelling is dominant compared with thermal disturbance. When the temperature is higher than 155 K, thermal disturbance gradually becomes dominant. This temperature is approximately 20 K higher than that without considering coherence, indicating that the neglect of quantum coherence could lead to underestimation of the tunnelling capability. In addition, the ratios of the tunnelling probability to the thermal disturbance probability at 200 K are analyzed (Figure 2). For example, the ratios with coherence and without coherence are approximately 10^{-11} and 10^{-7} when the provided energy is 0.5 eV for the reaction path containing the D defect, respectively. This further suggests that H-bond rotation is greater affected by quantum tunnelling than is generally recognized due to the presence of quantum coherence. Importantly, resonant tunnelling has been experimentally observed in hydrogen atom systems with an energy precision of 10^{-3} eV in previous report, which is equivalent to the resolution when considering resonant tunneling in this manuscript [1]. This suggests that there are opportunities for experimental observation and even regulation of water chain flipping in channels in the future, and our work is expected to provide theoretical guidance.

Although the approximation method in one-dimensional coordinates is widely used in the study of general tunnelling [42], it necessarily has some potential drawbacks in the study of resonant tunnelling. One of the problems neglected due to simplification is decoherence, i.e., the coherence breaking process caused by the interaction between the reaction coordinates and other coordinates under the influence of external environmental perturbations, which will correspondingly attenuate the effect of resonance tunnelling. However, it is well known that, the multidimensional quantum dynamics has remained difficult to describe properly with simulations up to now. We hope that our work will provide understanding of physical images and expect that further discussions on other factors can be performed in the future.

Conclusion

In summary, we shown the quantum tunnelling effects from the water chain itself under ideal conditions, which enhance the H-bond rotation. Importantly, compared with the generally recognized sequential tunnelling, the resonant tunnelling that considers quantum coherence can achieve a higher probability given less provided energy, which further enhances the rotation of the water chain. This work enriches the understanding of quantum tunneling effects on H-bonds and highlights the enhanced water chain rotation effect of previously neglected resonant tunneling due to quantum coherence, which is hoped to enable quantum regulation of the H-bond rotation mechanisms for confined water.

This paper is dedicated to the 70th anniversary of physics in Jilin University.

Data availability statement

The raw data supporting the conclusion of this article will be made available by the authors, without undue reservation.

Author contributions

XY and LJ performed the theoretical simulations. ZW supervised the work. XY, LJ, YZ, ZZ, RL, and ZW discussed the results. XY, LJ, and ZW wrote the article.

Funding

This work was supported by the 2020-JCJQ project (GFJQ2126-007) and the National Natural Science Foundation of China (under grant number 11974136).

Acknowledgments

ZW also acknowledges the assistance of the High-Performance Computing Center of Jilin University and National Supercomputing Center in Shanghai.

Conflict of interest

The authors declare that the research was conducted in the absence of any commercial or financial relationships that could be construed as a potential conflict of interest.

Publisher’s note

References

1. Yang T, Huang L, Xiao C, Chen J, Wang T, Dai D, et al. Enhanced reactivity of fluorine with para-hydrogen in cold interstellar clouds by resonance-induced quantum tunnelling. *Nat Chem* (2019) 11:744–9. doi:10.1038/s41557-019-0280-3

2. Meng X, Guo J, Peng J, Chen J, Wang Z, Shi JR, et al. Direct visualization of concerted proton tunnelling in a water nanocluster. *Nat Phys* (2015) 11:235–9. doi:10.1038/nphys3225

3. Benolt M, Marx D, Parrinello M. Tunnelling and zero-point motion in high-pressure ice. *Nature* (1998) 392:258–61. doi:10.1038/32609

4. Ranea VA, Michaelides A, Ramírez R, De Andres PL, Vergés JA, King DA. Water dimer diffusion on Pd{111} assisted by an H-bond donor-acceptor tunneling exchange. *Phys Rev Lett* (2004) 92:136104–4. doi:10.1103/PhysRevLett.92.136104

5. Zhang Q, Wahnström G, Björketun ME, Gao S, Wang E. Path integral treatment of proton transport processes inBaZrO3. *Phys Rev Lett* (2008) 101: 215902–4. doi:10.1103/PhysRevLett.101.215902

6. Quack M, Seyfang G. *Atomic and molecular tunneling processes in chemistry*. Amsterdam, Netherlands: Elsevier (2021). doi:10.1016/b978-0-12-817234-6.00012-x

7. Ryzhkin MI, Ryzhkin IA, Kashin AM, Zavorotnaya UM, Sinitsyn VV. Quantum protons in one-dimensional water. *J Phys Chem C* (2022) 126:8100–6. doi:10.1021/acs.jpcc.2c01140

8. Zhang D, Yang X, Jiang W, Jin L, Gao Y, Wang Z. Pauli repulsion enhances mobility of ultraconfined water. *ACS Nano* (2021) 15:2490–6. doi:10.1021/acsnano.0c06508

9. Li D, Zhang Z, Jiang W, Zhu Y, Gao Y, Wang Z. Uncooperative effect of hydrogen bond on water dimer. *Chin Phys Lett* (2021) 38:013101. doi:10.1088/0256-307X/38/1/013101

10. Liu R, Wang R, Li D, Zhu Y, Yang X, Wang Z. An *ab initio* study on boundaries for characterizing cooperative effect of hydrogen bonds by intermolecular compression. *Chin Chem Lett* (2022):107857. doi:10.1016/j.cclet.2022.107857

11. Zhou L, Wiebe J, Wiesendanger R, Gambardella P, Baxevanis B, Khajetoorians AA, et al. Nuclear quantum effects of hydrogen bonds probed by tip-enhanced inelastic electron tunneling. *Science* (2016) 352: 321–5. doi:10.1126/science.aaf2042

12. Ceriotti M, Fang W, Kusalik PG, McKenzie RH, Michaelides A, Morales MA, et al. Nuclear quantum effects in water and aqueous systems: Experiment, theory, and current challenges. *Chem Rev* (2016) 116:7529–50. doi:10.1021/acs.chemrev.5b00674

13. Kolesnikov AI, Anovitz LM, Mamontov E, Podlesnyak A, Ehlers G. Strong anisotropic dynamics of ultra-confined water. *J Phys Chem B* (2014) 118:13414–9. doi:10.1021/jp505355b

14. Gorshunov BP, Zhukova ES, Torgashev VI, Lebedev VV, Shakurov GS, Kremer RK, et al. Quantum behavior of water molecules confined to nanocavities in gemstones. *J Phys Chem Lett* (2013) 4:2015–20. doi:10.1021/jz400782j

15. Jeremy O, Richardson SCA, Lobsiger S, Reid AA, Temelso B, Shields GC, et al. Concerted hydrogen-bond breaking by quantum tunneling in the water hexamer prism. *Science* (2016) 351:1310–3. doi:10.1126/science.aae0012

16. Wang L, Zhao J, Li F, Fang H, Lu JP. First-principles study of water chains encapsulated in single-walled carbon nanotube. *J Phys Chem C* (2009) 113:5368–75. doi:10.1021/jp808873r

17. Hummer G, Rasaiah JC, Noworyta JP. Water conduction through the hydrophobic channel of a carbon nanotube. *Nature* (2001) 414:188–90. doi:10.1038/35102535

18. Joseph S, Aluru NR. Pumping of confined water in carbon nanotubes by rotation-translation coupling. *Phys Rev Lett* (2008) 101:064502–4. doi:10.1103/PhysRevLett.101.064502

19. Striolo A. The mechanism of water diffusion in narrow carbon nanotubes. *Nano Lett* (2006) 6:633–9. doi:10.1021/nl052254u

20. Kalra A, Garde S, Hummer G. Osmotic water transport through carbon nanotube membranes. *Proc Natl Acad Sci U S A* (2003) 100:10175–80. doi:10.1073/pnas.1633354100

21. Zhang D, Zhang Z, Jiang W, Gao Y, Wang Z. Effect of confinement on water rotation: Via quantum tunnelling. *Nanoscale* (2018) 10:18622–6. doi:10.1039/c8nr05137b

22. Liu X, Pang H, Liu X, Li Q, Zhang N, Mao L, et al. Orderly porous covalent organic frameworks-based materials: Superior adsorbents for pollutants removal from aqueous solutions. *Innovation (Camb)* (2021) 2:100076. doi:10.1016/j.xinn.2021.100076

23. Mondal D, Dandekar BR, Ahmad M, Mondal A, Mondal J, Talukdar P. Selective and rapid water transportation across a self-assembled peptide-diol channel via the formation of a dual water array. *Chem Sci* (2022) 13:9614–23. doi:10.1039/d2sc01737g

24. Jin L, Zhang D, Zhu Y, Yang X, Gao Y, Wang Z. A step-by-step process-induced unidirectional oriented water wire in the nanotube. *J Phys Chem Lett* (2021) 12:350–4. doi:10.1021/acs.jpclett.0c03340

25. Alexiadis A, Kassinos S. Molecular simulation of water in carbon nanotubes. *Chem Rev* (2008) 108:5014–34. doi:10.1021/cr078140f

26. Chen X, Cao G, Han A, Punyamurtula VK, Liu L, Culligan PJ, et al. Nanoscale fluid transport: Size and rate effects. *Nano Lett* (2008) 8:2988–92. doi:10.1021/nl802046b

27. Wang J, Zhu Y, Zhou J, Lu X-H. Diameter and helicity effects on static properties of water molecules confined in carbon nanotubes. *Phys Chem Chem Phys* (2004) 6:829–35. doi:10.1039/B313307A

28. Majumder M, Chopra N, Andrews R, Hinds BJ. Enhanced flow in carbon nanotubes. *Nature* (2005) 438:44. doi:10.1038/438044a

29. Joseph S, Aluru NR. Why are carbon nanotubes fast transporters of water? *Nano Lett* (2008) 8:452–8. doi:10.1021/nl072385q

30. Feng JW, Ding HM, Ren CL, Ma YQ. Pumping of water by rotating chiral carbon nanotube. *Nanoscale* (2014) 6:13606–12. doi:10.1039/c4nr03407d

31. Cambré S, Schoeters B, Luyckx S, Goovaerts E, Wenseleers W. Experimental observation of single-file water filling of thin single-wall carbon nanotubes down to chiral index (5, 3). *Phys Rev Lett* (2010) 104:207401–4. doi:10.1103/PhysRevLett.104.207401

32. Agrawal KV, Shimizu S, Drahushuk LW, Kilcoyne D, Strano MS. Observation of extreme phase transition temperatures of water confined inside isolated carbon nanotubes. *Nat Nanotechnol* (2017) 12:267–73. doi:10.1038/nnano.2016.254

33. Adamo C, Barone V. Toward reliable density functional methods without adjustable parameters: The PBE0 model. *J Chem Phys* (1999) 110:6158–70. doi:10.1063/1.478522

34. Frisch MJ, Trucks GW, Schlegel HB, Scuseria GE, Robb MA, Cheeseman JR, et al. *Gaussian 09, revision D.01.* (2016).

35. Grimme S, Antony J, Ehrlich S, Krieg H. A consistent and accurate *ab initio* parametrization of density functional dispersion correction (DFT-D) for the 94 elements H-Pu. *J Chem Phys* (2010) 132:154104. doi:10.1063/1.3382344

36. Fukui K. Formulation of the reaction coordinate. *J Phys Chem* (1970) 74:4161–3. doi:10.1021/j100717a029

37. Gonzalez C, Schlegel HB. Reaction path following in mass-weighted internal coordinates. *J Phys Chem* (1990) 94:5523–7. doi:10.1021/j100377a021

38. Kramers HA. Wellenmechanik und halbzahlige Quantisierung. *Z Physik* (1926) 39:828–40. doi:10.1007/BF01451751

39. Wentzel G. Eine Verallgemeinerung der Quantenbedingungen für die Zwecke der Wellenmechanik. *Z Physik* (1926) 38:518–29. doi:10.1007/BF01397171

40. Dellago C, Naor MM, Hummer G. Proton transport through water-filled carbon nanotubes. *Phys Rev Lett* (2003) 90:105902. doi:10.1103/PhysRevLett.90.105902

41. Bi C, Yang Y. Atomic resonant tunneling in the surface diffusion of H atoms on Pt(111). *J Phys Chem C* (2021) 125:464–80. doi:10.1021/acs.jpcc.0c08906

42. Schreiner PR. Quantum mechanical tunneling is essential to understanding chemical reactivity. *Trends Chem* (2020) 2:980–9. doi:10.1016/j.trechm.2020.08.006

Frontiers in Physics

TYPE Original Research
PUBLISHED 09 November 2022
DOI 10.3389/fphy.2022.1044959

EDITED BY
Huan Yang,
Shandong University, China

REVIEWED BY
Guangjiu Zhao,
Tianjin University, China
Maodu Chen,
Dalian University of Technology, China
Maikel Ballester,
Juiz de Fora Federal University, Brazil

*CORRESPONDENCE
Lulu Zhang,
yilutingyu@163.com

SPECIALTY SECTION
This article was submitted to Atomic and Molecular Physics,
a section of the journal
Frontiers in Physics

RECEIVED 15 September 2022
ACCEPTED 24 October 2022
PUBLISHED 09 November 2022

CITATION
Liu D, Zhao J, Wang W, Song Y, Meng Q and Zhang L (2022), State-to-state dynamics of the $\mathbf{C^+(^2P)}$ + $\mathbf{SH(X^2\Pi)}$ → $\mathbf{H(^2S)}$ + $\mathbf{CS^+(X^2\Sigma^+)}$ reaction using a time-dependent wave packet and quasi-classical trajectory methods.
Front. Phys. 10:1044959.
doi: 10.3389/fphy.2022.1044959

State-to-state dynamics of the $\mathbf{C^+(^2P)}$ + $\mathbf{SH(X^2\Pi)}$ → $\mathbf{H(^2S)}$ + $\mathbf{CS^+(X^2\Sigma^+)}$ reaction using a time-dependent wave packet and quasi-classical trajectory methods

Dong Liu[1], Juan Zhao[1], Wei Wang[1], Yuzhi Song[2], Qingtian Meng[2] and Lulu Zhang[1]*

[1]School of Science, Shandong Jiaotong University, Jinan, China, [2]School of Physics and Electronics, Shandong Normal University, Jinan, China

The time-dependent quantum wave packet (TDWP) and quasi-classical trajectory (QCT) are the basic research methods of reaction dynamics. Utilizing these two methods, the total reaction probability (J = 0), integral cross section (ICS), and rate parameter for the $C^+(^2P)$ + $SH(X^2\Pi)(v = 0, 1, 2, 3)$ → $H(^2S)$ + $CS^+(X^2\Sigma^+)$ reactions are calculated on an accurate potential energy surface [Zhang *et al.* Phys. Chem. Chem. Phys. 2022, **24**, 1007]. The results of QCT are slightly different from those of the TDWP in value, but the trend is consistent. They are also weakly dependent on the initial vibrational excitation of SH. The state-to-state reaction probability and ICS at fixed collision energies (0.1, 0.3, 0.5, and 0.7 eV) are first calculated using QCT methods. It is hoped that our work can attract experimentalists to study the dynamics of this interesting but rarely discussed system.

KEYWORDS

time-dependent quantum wave packet, quasi-classical trajectory, reaction probability, integral cross section, rate constant

1 Introduction

The ion-neutral collisions in the interstellar medium play essential roles in the field of molecular physics and astrophysics [1, 2]. Also, the interaction between the C^+ ion and SH radical is considered to be significant in the production of carbon monosulfide ions. The precise dynamics information on this reaction requires a full-dimensional analytical potential energy surface (PES) of high quality.

The research on $HCS^+(X^1\Sigma^+)$ could date back to 1978 when Bruna *et al.* [3] found that the global minimum HCS^+ is a linear structure with $CS^+ = 2.814\ a_0$ and $CH = 2.062\ a_0$, and one of its isomer, HSC^+, is located 4.770 eV above HCS^+. The equilibrium structure of HCS^+ was also calculated by Botschwina and Sebald [4], who reported the intensities of

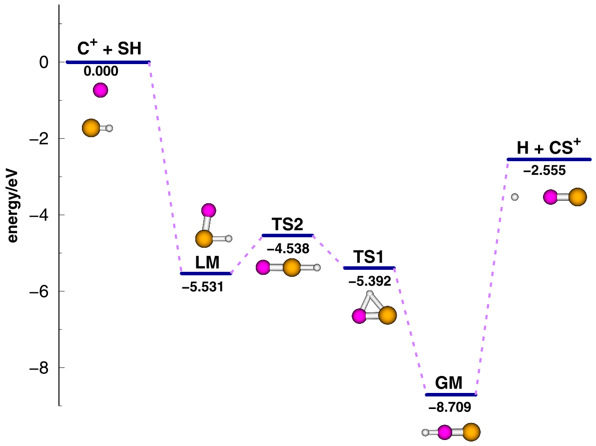

FIGURE 1
Energy diagram for the reaction pathway and relative stationary points of the C$^+$([2]*P*) + SH($X^2\Pi$) → H([2]*S*) + CS$^+$($X^2\Sigma^+$) reaction. Energies are given relative to the C$^+$([2]*P*) + SH($X^2\Pi$) asymptote with the unit of eV.

the stretching vibrations simultaneously. Wong *et al.* [5] found a tiny barrier (about 0.104 eV) between HCS$^+$ and HSC$^+$, and HSC$^+$ is 3.089 eV above HCS$^+$. Puzzarini [6] accurately investigated the structural and energetic characteristics of HCS$^+$ and HSC$^+$ using the coupled cluster method with single and double excitations with a perturbative treatment of the connected triples [CCSD(T)] method, and the results are in good agreement with the experimental results. Kaur and Kumar [7, 8] computed the various energy transfer channels of the collision between atomic H and CS$^+$ molecular ions and 3D *ab initio* PESs of the ground state and low-lying excited states of the HCS$^+$ system. Recently, the analytical global three-dimensional PES of HCS$^+$($X^1\Sigma^+$) for the C$^+$(^2P) + SH($X^2\Pi$) → H(^2S) + CS$^+$($X^2\Sigma^+$) reaction was first constructed by Zhang *et al.* [9]. This PES is fitted by a grid of 7,907 *ab initio* energy points computed at a multi-reference configuration interaction level plus the Davidson correction [MRCI(Q)] [10, 11] with aug-cc-pV(5 + d)Z basis sets [12, 13]. The MRCI method uses the full-valence complete active space self-consistent field (CASSCF) [14] wave function as a reference. By using this PES of high accuracy, with a final root mean square error of 0.0419 eV and a maximum error of 0.0251 eV, the structures and locations of the global minimum HCS$^+$, local minimum HSC$^+$, and transition states are obtained. Scrutiny of the HCS$^+$($X^1\Sigma^+$) PES shows that the isomeric HSC$^+$ is in a potential well, 3.178 eV above the most stable HCS$^+$ structure, but it is separated from HCS$^+$ only with a tiny barrier (0.139 eV). According to the PES, the most likely minimum energy path for the C$^+$(^2P) + SH($X^2\Pi$) → H(^2S) + CS$^+$($X^2\Sigma^+$) reaction and the energies of relative stationary points are displayed in Figure 1. The reaction is found to be exothermic (≈ 2.555 eV) and barrierless relative to the entrance channel.

The reaction probability and integral cross section (ICS) were first calculated by Zhang *et al.* [9] with a time-dependent quantum wave packet (TDWP) and quasi-classical trajectory (QCT) methods [9]. The calculated reaction probabilities for total angular momentum J = 0, 10, 60, and 120 by the TDWP and QCT are consistent with each other at high collision energies. Although the divergence in the ICSs obtained from the two methods is evident, the evolutional trend is consistent. Substantial dynamic information on the title reaction should be deduced with a more time-saving QCT method in the high-energy region in comparison with the time-consuming TDWP calculations. Finally, the type of the title reaction is given by using the QCT method. The complex with a long life easily formed in the title reaction is attributed to a distinct potential well in the path of reaction. Therefore, the indirect reaction is the primary mechanism for C$^+$(^2P) + SH($X^2\Pi$) → H(^2S) + CS$^+$($X^2\Sigma^+$).

In the present work, both the TDWP and QCT methods are applied to study the C$^+$(^2P) + SH($X^2\Pi$) → H(^2S) + CS$^+$($X^2\Sigma^+$) reaction on the PES of Zhang *et al.* [9] at the state-to-state level. The paper is structured as follows. Section 2 gives a brief survey of the TDWP and QCT theoretical methods used in this work. The results and discussion, and conclusions are explained in Section 3 and Section 4, respectively.

2 Theory

2.1 Time-dependent quantum wave packet

The TDWP [15–20] method is applied to calculate the accurate dynamic information on the C$^+$(^2P) + SH($X^2\Pi$) → H(^2S) + CS$^+$($X^2\Sigma^+$) reaction. The core idea is to get the numerical solution to the Schrödinger equation through the split-operator propagation scheme. The Hamiltonian is expressed in reactant Jacobi coordinates as follows:

$$H = -\frac{\hbar}{2\mu_R}\frac{\partial^2}{\partial R^2} + \frac{(\boldsymbol{J}-\boldsymbol{j})^2}{2\mu_R R^2} + \frac{\boldsymbol{j}^2}{2\mu_r r^2} + V(R, r, \gamma) + h(r), \qquad (1)$$

where r, R, and γ are the bond length of the reactant molecule, the distance from the atom to the center-of mass of the diatomic, and the angle between the $\boldsymbol{R}$ and $\boldsymbol{r}$ vectors, respectively. μ_R and μ_r are the reduced masses between the center-of-mass of the diatomic and atom and the reduced mass of the reactant molecule, respectively. $\boldsymbol{J}$ and $\boldsymbol{j}$ are the total angular momentum operators and the rotational angular momentum operator of BC, respectively. $V(R,\ r,$ and $\gamma)$ is the potential energy (total energy deducted from the diatomic potential energy), and $h(r)$ is the diatomic reference of Hamiltonian defined as follows:

$$h(r) = -\frac{\hbar}{2\mu_r}\frac{\partial^2}{\partial r^2} + V(r), \qquad (2)$$

where $V(r)$ is the diatomic reference potential usually used as an asymptotic diatomic potential.

TABLE 1 Numerical parameters used in the present quantum wavepacket calculations (atomic units unless the number of argument).

Scattering coordinate (R) range	**2.0–20**
Number of grid points in R (interaction region)	520 (170)
Diatomic coordinate (r) range	1.8–18.0
Number of grid points in r (interaction region)	270 (124)
Number of angular basis functions	120
Absorption region length in R (r)	3.0 (3.0)
Absorption strength in R (r)	0.03 (0.03)
Center of the initial wave packet R_0	16.1
Width of the wave packet	0.12
Time step for propagation	10
Total propagation time	80000

In this calculation, the initial wave packet is usually chosen as the product of a localized translational wave packet and a specific rovibrational eigenfunction [18, 21]. After the wave packet is propagated into the product region, the reaction probability and ICS can be calculated as follows:

$$P^J_{vjk}(E) = \frac{\hbar}{\mu_r}\mathrm{Im}\left[\langle\Psi(E)|\delta(r-r_0)\frac{\partial}{\partial r}|\Psi(E)\rangle\right], \tag{3}$$

$$\sigma_{vj}(E) = \frac{1}{2j_0+1}\frac{\pi}{k'^2}\sum_{Jk}(2J+1)P^J_{vjk}(E), \tag{4}$$

where v and j are the vibrational and rotational quantum numbers of the reactant, and k is the projection quantum number of j. $\Psi(E)$ can be derived from the Fourier transform of the time-dependent wave function $\Psi(t)$. $k' = \sqrt{2\mu_r E}$, with E being the collision energy. To get convergence results, a lot of test calculations are carried out for each parameter. Table 1 lists the parameters used in the quantum calculations of the $C^+(^2P)$ + $SH(X^2\Pi) \rightarrow H(^2S) + CS^+(X^2\Sigma^+)$ reaction.

The rate constant determined by the ICS $\sigma_{vj}(E)$ is as follows:

$$k_{vj}(T) = g_e(T)\left(\frac{8}{\pi\mu_R(k_BT)^3}\right)^{\frac{1}{2}}\int_0^\infty E\sigma_{vj}(E)e^{-E/k_BT}dE, \tag{5}$$

TABLE 2 Values of b_{max} (in Å) for the $C^+ + SH(v = 0 - 3, j = 0) \rightarrow H + CS^+$ reaction.

E_c	$b_{max,v}$			
	0	1	2	3
0.10	3.390	4.126	4.665	5.150
0.12	3.944	4.460	4.899	5.280
0.14	4.277	4.683	5.030	5.360
0.16	4.481	4.819	5.110	5.400
0.18	4.622	4.904	5.166	5.425
0.20	4.723	4.976	5.205	5.433
0.22	4.496	5.020	5.228	5.449
0.24	4.855	5.050	5.242	5.474
0.26	4.900	5.078	5.252	5.490
0.28	4.930	5.090	5.265	5.499
0.30	4.950	5.100	5.269	5.486
0.32	4.968	5.109	5.270	5.472
0.34	4.974	5.112	5.266	5.454
0.36	4.983	5.105	5.256	5.432
0.38	4.983	5.100	5.241	5.415
0.40	4.982	5.100	5.230	5.374
0.42	4.976	5.090	5.210	5.345
0.44	4.971	5.074	5.187	5.325
0.46	4.957	5.048	5.153	5.264
0.48	4.939	5.015	5.101	5.220
0.50	4.902	4.980	5.064	5.172
0.60	4.760	4.805	4.865	4.950
0.70	4.626	4.665	4.719	4.773
0.80	4.520	4.550	4.601	4.642

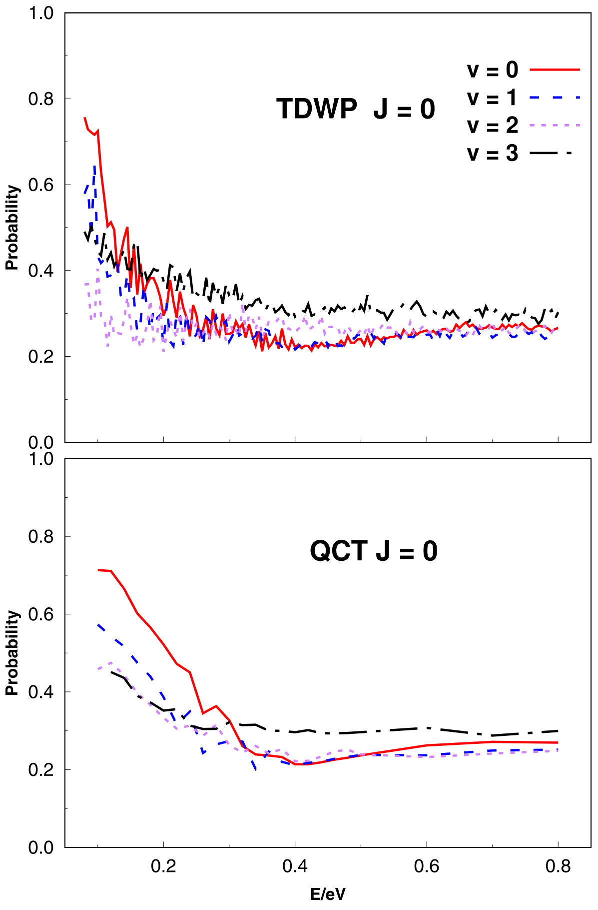

FIGURE 2
Total reaction probabilities at J = 0 as a function of collision energy calculated using the TDWP (top panel) and QCT (bottom panel) methods for various initial vibrational states of the SH for the title reaction.

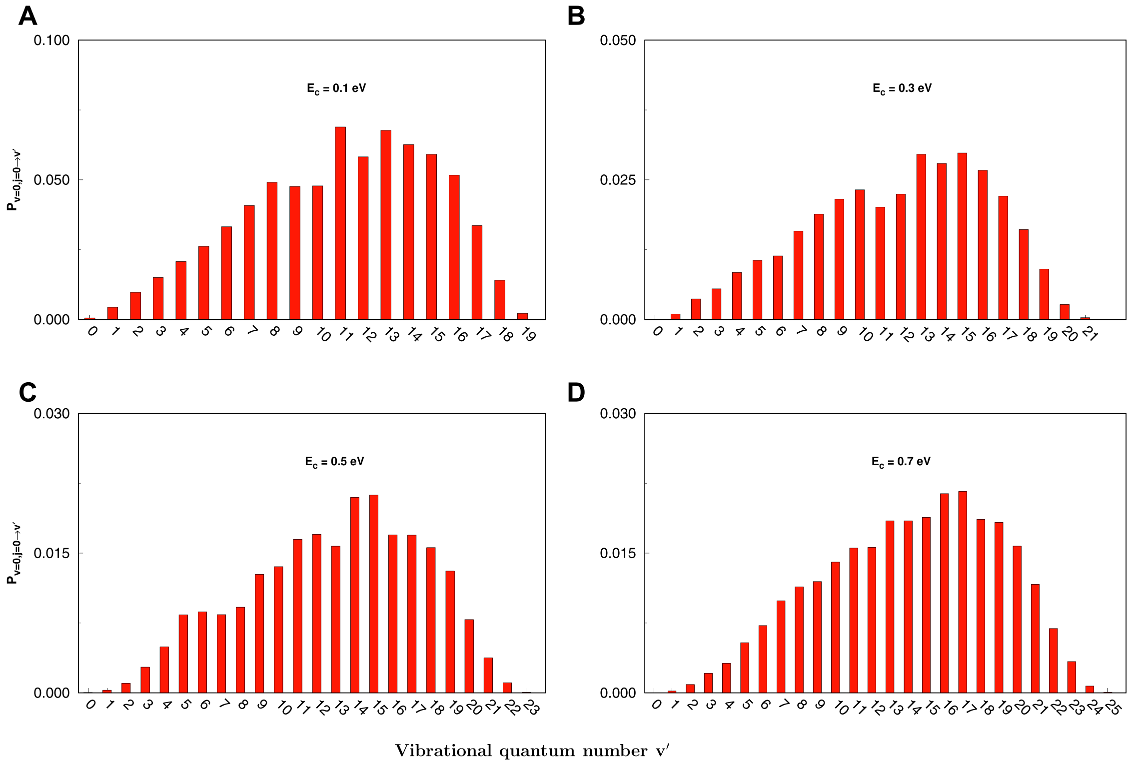

FIGURE 3
Final v' state-resolved reaction probabilities at $J = 0$ for the $C^+ + SH(v = 0, j = 0) \to H + CS^+(v')$ reaction at selected collision energies (0.1, 0.3, 0.5, and 0.7 eV) obtained with the QCT method. **(A)** for 0.1 eV, **(B)** for 0.3 eV, **(C)** for 0.5 eV, **(D)** for 0.7 eV.

where k_B is the Boltzmann constant and $g_e(T)$ is the electronic partition function with a form, which is as follows:

$$g_e(T) = \frac{1}{\left(2 + 4e^{-91.25/T}\right)\left(2 + 2e^{-542.36/T}\right)}. \quad (6)$$

2.2 Quasi-classical trajectory

The QCT method [22–27] has been widely applied to explore chemical reaction dynamics [28–33]. Here, only the details pertinent to the present work are summarized. In the QCT calculation [34–37], the distance from the atom C^+ to the center-of-mass of S and H is set to 20 Å for the conservation of total energy and angular momentum. The total 100,000 trajectories are introduced for the $C^+(^2P) + SH(X^2\Pi) \to H(^2S) + CS^+(X^2\Sigma^+)$ reaction, with the time step being 0.1 fs. The impact parameter $b_{\max,v}$ tabulated in Table 2 is simulated at each pair of E and v in the collision energy ranging from 0.1 eV to 0.8 eV and the initial vibrational quantum number ranges from 0 to 3. In the calculations, $b_{\max,v}$ is obtained by systematically increasing the value of the impact parameter, b, until no reaction trajectory is found for each trajectory at a given collision energy and initial vibrational quantum number. The ICS can be given as follows:

$$\sigma_v = \pi b^2_{\max,v} P_v, \quad (7)$$

where $P_v = \frac{N_r}{N}$ is the average reaction probability, with N being the total trajectory number and N_r the reactive trajectory number.

3 Results and discussion

3.1 Total and state-to-state reaction probabilities at J = 0

Figure 2 depicts the evolution of total reaction probability ($J = 0$) with collision energy obtained by employing the TDWP and QCT methods for $C^+ + SH(v = 0–3, j = 0)$ reactions. The reaction probabilities selected initially ($v = 0–3$; $j = 0$) illustrate that the title reaction is typically exothermic without threshold characteristics; in other words, the reaction is barrierless and the probability decreases with the increase of collision energy. A deep potential well in the reaction path makes the TDWP reaction probability in the upper panel a fluctuating decline. It is easily found that the reaction probability seems to decrease first with

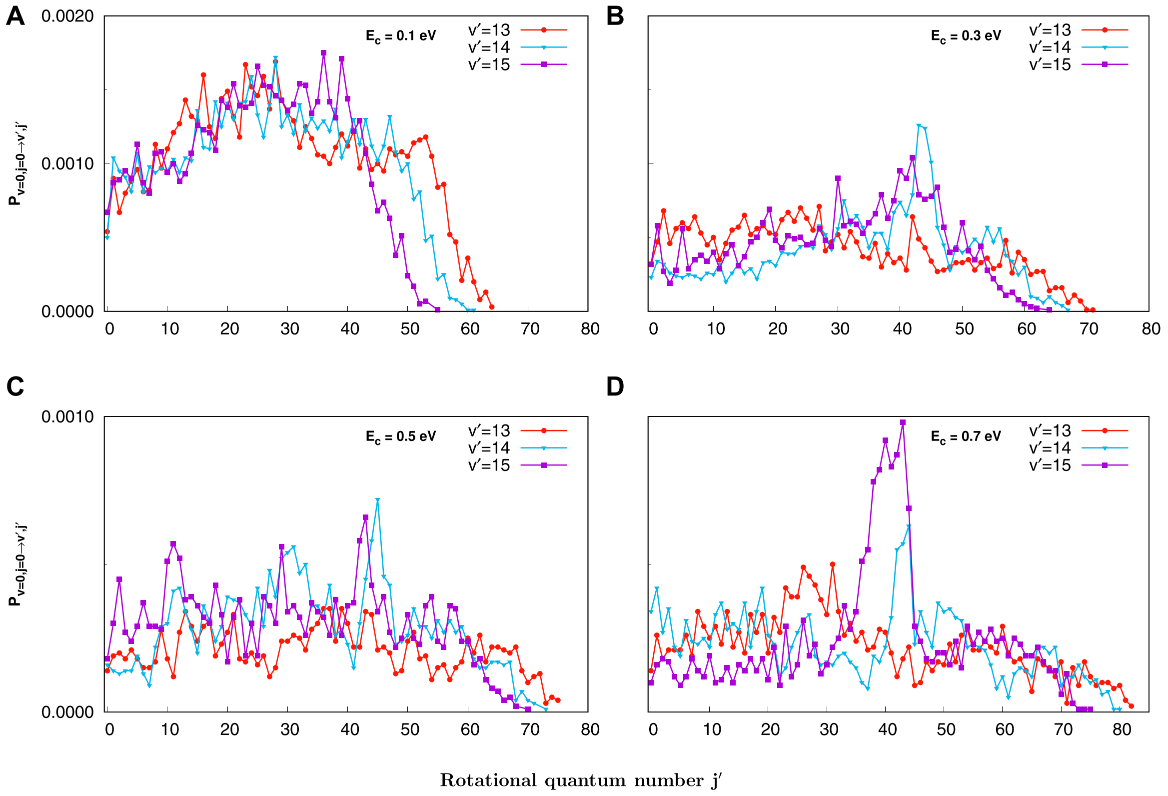

FIGURE 4
Final j' state-resolved reaction probabilities at $J = 0$ for the $C^+ + SH(v = 0, j = 0) \to H + CS^+(v' = 13, 14, 15)$ reaction at selected collision energies (0.1, 0.3, 0.5, and 0.7 eV) obtained with the QCT method. **(A)** for 0.1 eV, **(B)** for 0.3 eV, **(C)** for 0.5 eV, **(D)** for 0.7 eV.

initial v from 0 to 2 and then hardly changes with v at higher collision energies. With the increase in the vibrational energy level, the reaction probability becomes more and more gentle with the collision energy, and when $v = 3$, the probability is the most gentle. This is because, at higher vibration energy levels, the effect of the collision energy is weaker on the reaction probability. The QCT reaction probability (lower panel) perfectly reproduces the overall shape of the TDWP in the whole collision energy range (from $v = 0$ to 3).

Figure 3 reveals the QCT reaction probability of product vibrational distributions at $J = 0$ for the reaction of $C^+ + SH(v = 0, j = 0) \to H + CS^+(v')$ at certain collision energies (0.1, 0.3, 0.5, and 0.7 eV). It is easily found in a great number of vibrational excitation products with a distinguished population inversion. At $E_c = 0.1$ eV, the distribution is bimodal, peaking at $v' = 11$ and $v' = 13$ and the highest vibrational excitation product at $v' = 19$. The vibrational distributions get hotter and wider as the collision energy increases. Also, the v' state-resolved reaction probability decreases gradually when the collision energy increases, consistent with the total probability.

Figure 4 displays the final j' state-resolved reaction probabilities for the most populated product vibrational quantum states, i.e., $v' = 13$, 14, and 15, at the four selected collision energies. Similarly, the higher the collision energy, the higher the rotational energy level and the more obvious the population inversion are. Meanwhile, the shapes of probabilities for each v' state resemble each other as explained. On the whole, the QCT product rotational distribution shows a significant oscillatory behavior, particularly at the low collision energy for low final rotational quantum states. It clearly appears that the lower the vibrational excitation, the higher the rotational excitation of products with the same collision energy is. For instance, at 0.1eV, the maximum product rotational energy level j' is 64 when the vibrational energy level of the product $v' = 13$, while for $v' = 14$ and $v' = 15$, the maximum of j' is 61 and 55, respectively, which is consistent with the energy conservation.

QCT vibrational state-resolved reaction probabilities at the various collision energies for $C^+ + SH(v = 0–3, j = 0) \to H + CS^+$ are shown in Figure 5. The distinguishing feature of the vibrational distributions for the reaction is that because of the rise of v or collision energy, the distribution curve becomes wider and the peak value shifts rightward. The distributions are oscillatory, especially at lower collision energies. Moreover, the

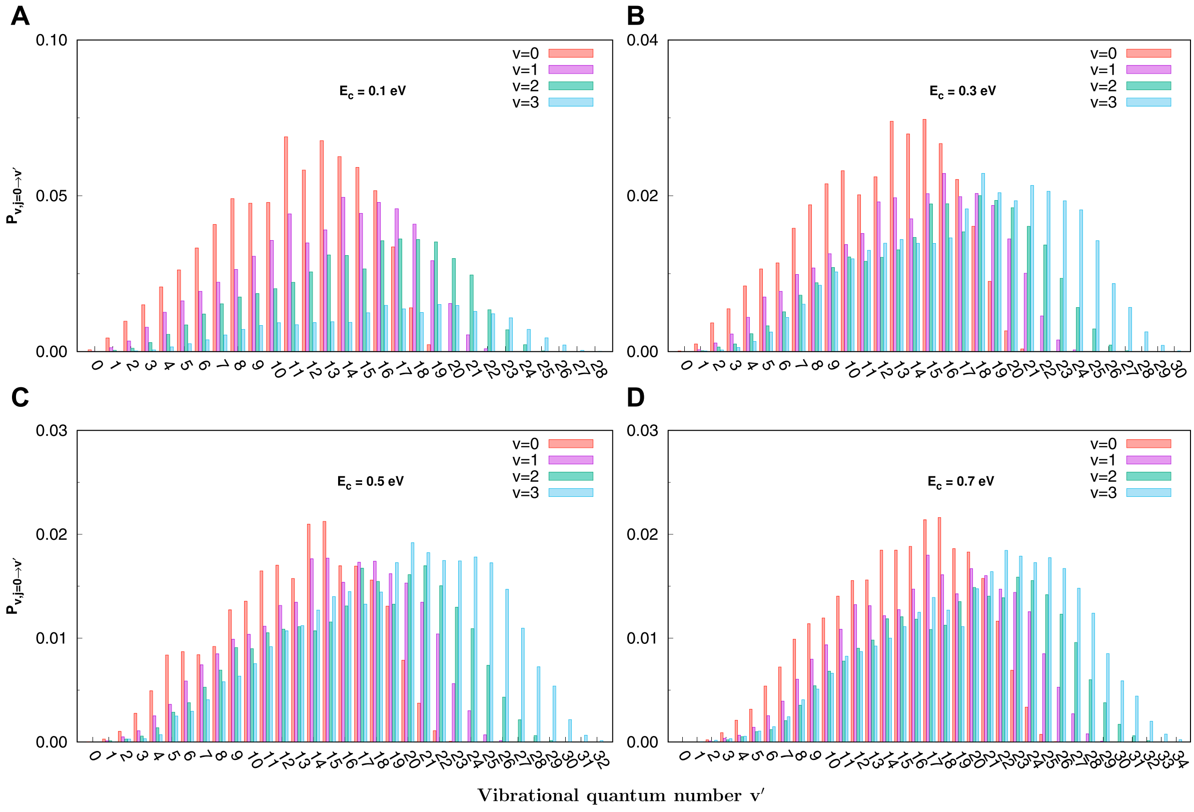

FIGURE 5

Final v' state-resolved reaction probabilities at $J = 0$ for the $C^+ + SH(v = 0-3, j = 0) \to H + CS^+(v')$ reaction at selected collision energies (0.1, 0.3, 0.5, and 0.7 eV) obtained with the QCT method. **(A)** for 0.1 eV, **(B)** for 0.3 eV, **(C)** for 0.5 eV, **(D)** for 0.7 eV.

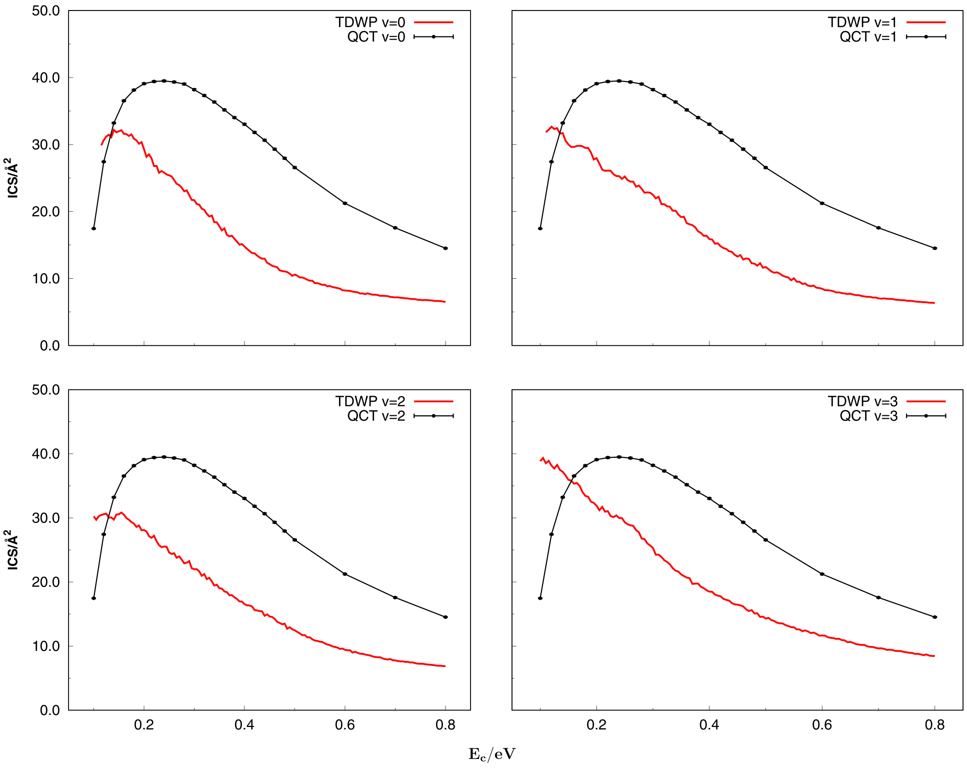

FIGURE 6

Integral cross sections as a function of collision energy for the $C^+ + SH(v = 0-3, j = 0) \to H + CS^+(v')$ reaction obtained with the TDWP and QCT methodologies.

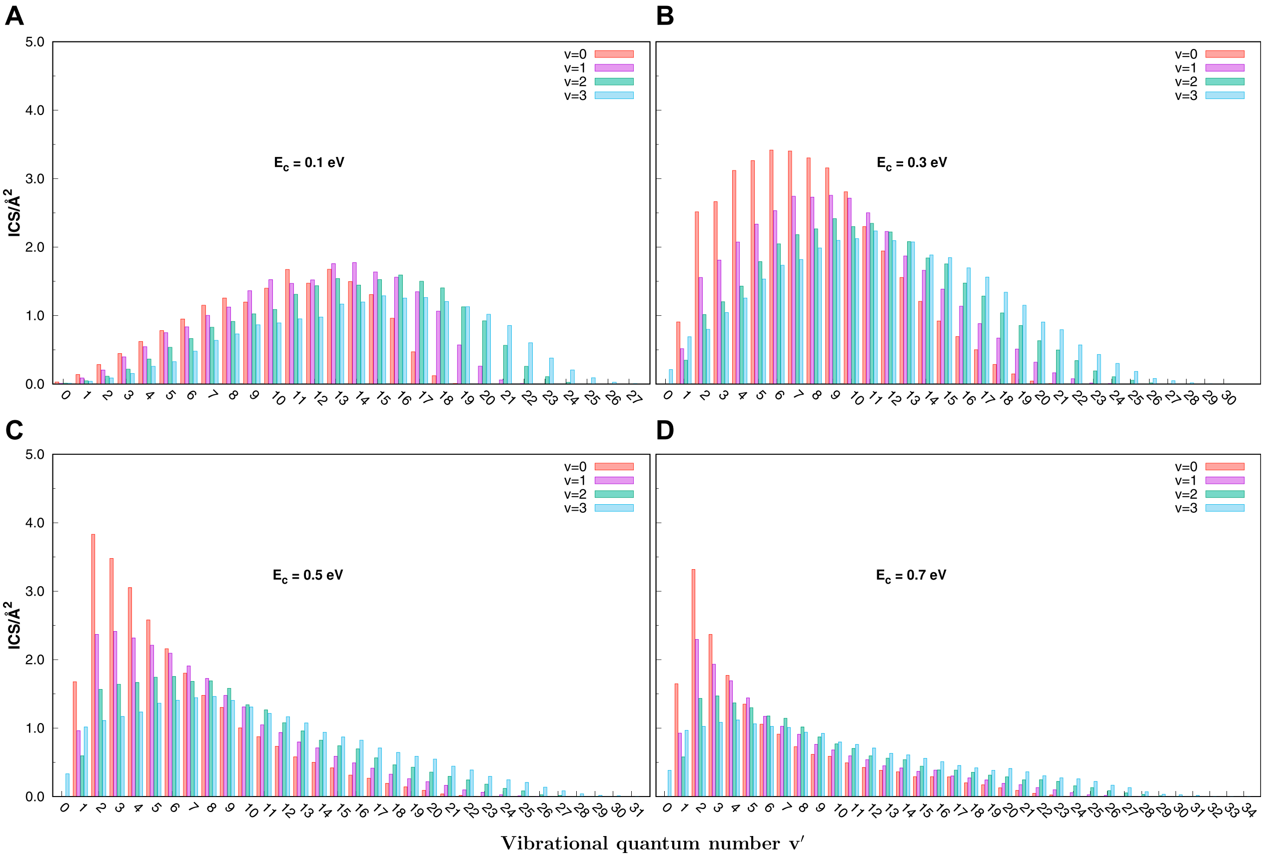

FIGURE 7
Final v' state-resolved integral cross sections for the $C^+ + SH(v = 0 - 3, j = 0) \rightarrow H + CS^+(v')$ reaction at selected collision energies (0.1, 0.3, 0.5, and 0.7 eV) obtained with the QCT method. **(A)** for 0.1 eV, **(B)** for 0.3 eV, **(C)** for 0.5 eV, **(D)** for 0.7 eV.

shapes of reaction probability curves for each v are similar to each other. Analogously, the reaction probability gradually decreases when the collision energy increases, consistent with the total probability.

3.2 Total and state-to-state integral cross sections

Figure 6 indicates the TDWP and QCT ICSs as a function of collision energy for $C^+ + SH(v = 0–3, j = 0) \rightarrow H + CS^+$. The ICSs calculated both with the TDWP and QCT methods climb over a mountain and gradually reach a plateau with increasing collision energy. The behavior is the common characteristic of barrierless exothermic reactions and similar to the same type reactions such as H + CH [38–40], $S^+ + H_2$ [41], and C + SH [30, 42]. First, we find that the shapes of ICSs for $C^+ + SH(v = 0–3, j = 0)$ are analogous in four panels obtained by the TDWP and QCT methods, indicating that the ICSs are insensitive to the vibrational quantum state of reactant SH. Then, it is distinguished that the QCT ICSs are slightly higher than the TDWP ICSs, particularly at low collision energies. The reason may be that in the present TDWP calculation, the zero-point energy (ZPE) is considered naturally, whereas in the QCT calculation, the ZPE is not taken into account, which leads to the larger ICS of the QCT than the TDWP calculation in the low energy range for such an exothermic reaction. In other words, the quantum effect cannot be ignored, especially at low collision energies. The error bars are calculated and added in Figure 6 for the QCT method. We find that the uncertainties of ICSs for the title reactions are very small in the entire collision energy ranges, so their accuracy can be warranted. Since the trend of the ICSs obtained by these two methods is consistent and as the two cases gradually approach the vibrational quantum state of SH increases, the QCT method can be used for further study due to the low time consumption.

The vibrational state-resolved ICSs computed by the QCT method at various collision energies (0.1, 0.3, 0.5, and 0.7 eV) for $C^+ + SH(v = 0–3, j = 0) \rightarrow H + CS^+$ are shown in Figure 7.

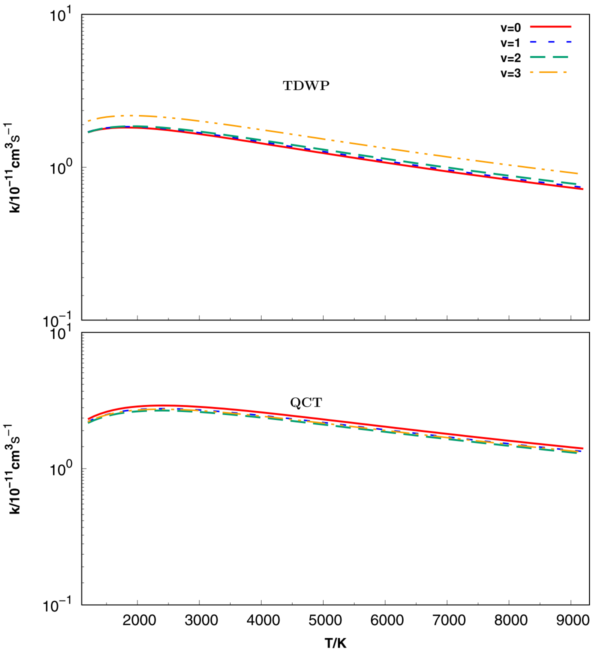

FIGURE 8
Vibrationally state-specific rate constants as a function of temperature for the $C^+ + SH(v = 0-3, j = 0) \rightarrow H + CS^+$ reaction calculated with the TDWP (top panel) and QCT (bottom panel) methods.

The most obvious feature is a population inversion of the vibrational distribution peak at a low value of v'. An increase in collision energy and the initial vibrational quantum number can make the ICS distributions wider. The distributions become hotter along with the enlargement of the initial vibrational quantum number. However, the distributions become colder as collision energy increases, at variance with the effect of the initial vibrational quantum number.

3.3 Rate constants

The initial state-selected rate constants shown in Figure 8 are calculated by the TDWP (in upper panel) and QCT (in lower panel) methods in a large temperature range from 1200 to 92000 K for $C^+ + SH(v = 0\text{–}3, j = 0) \rightarrow H + CS^+$. The current rate constants are calculated by numerical integration over the collision energy in the range of 0.10–0.80 eV. As revealed in Figure 8, both the TDWP and QCT rate constants rise slightly with increasing temperature until reaching a plateau. The increase in the QCT rate constants at a lower temperature is much faster than those of TDWP. In addition, the QCT rate constants are a little higher than the TDWP rate constants; meanwhile, the distributions are consistent with the TDWP and QCT ICSs as a function of collision energy. The TDWP state-selected rate constants are slightly positively correlated with the initial vibrational quantum number of the reagent molecule SH. Nevertheless, the QCT rate constants are insensitive to v, which is analogous to the cross-section results of Figure 6. In conclusion, the rate constants obtained by the TDWP and QCT methods are in essential agreement, especially in the high-temperature region.

In the present work, we provided a new and reliable rate constant for the $C^+ + SH(v = 0\text{–}3, j = 0) \rightarrow H + CS^+$ reaction. Although there are no other theoretical and experimental results for the title reaction on the $HCS^+(X^1\Sigma^+)$ PES, the vibrational distribution information is of deep value for further study of this system.

4 Conclusion

This study presents the initial state-selected reaction probabilities, ICSs, and rate constants calculated with both the QCT and TDWP methods. The QCT reaction probability perfectly reproduces the overall shape of the TDWP results in the whole collision energy region for $v = 0$ to 3. The ICSs obtained by the QCT are slightly higher than those obtained by the TDWP, and as the initial vibrational quantum state increases, the ICSs obtained by these two methods are in more substantial agreement. The QCT rate constants are slightly higher than those of the TDWP, and ICSs obtained from the two methods show a similar relationship. Overall, the aforementioned QCT results are consistent with those of the TDWP, both showing practical independence with the initial vibrational excitation. The QCT method is employed to obtain the state-to-state reaction probabilities and product state-resolved ICSs at fixed collision energies (0.1, 0.3, 0.5, and 0.7 eV). The probability distributions are hotter, wider, and peak at higher v' values at higher collision energy and a larger vibrational quantum number. An increase in collision energy and the initial vibrational quantum number can also make the ICS distributions wider. The ICS distributions become hotter along with the enlargement of v, while the collision energy has the opposite effect. Considering the time cost, the QCT method can well describe this reaction. We hope that our work can attract the attention of experimentalists to this fascinating but scarcely studied system.

Data availability statement

The original contributions presented in the study are included in the article/Supplementary Material; further inquiries can be directed to the corresponding author.

Author contributions

DL wrote the original manuscript and performed the QCT calculations. DL and JZ performed the TDWP calculations. YS and QM proposed the idea, supervised the research work, and revised the manuscript. DL, WW, QM, and LZ discussed and analyzed the results.

Funding

The present work was supported by the National Natural Science Foundation of China (Grant Nos. 12004216, 11904394, 12274265, and 11874241) and the Natural Science Foundation of Shandong Province, China (Grant Nos. ZR2020QA064, ZR2021MA069, and ZR2022MA006).

Conflict of interest

The authors declare that the research was conducted in the absence of any commercial or financial relationships that could be construed as a potential conflict of interest.

Publisher's note

References

1. Thaddeus P, Guelin M, Linke RA. Three new ″nonterrestrial″ molecules. *Astrophys J* (1981) 246:L41. doi:10.1086/183549

2. Marguès L, Lewen F, Winnewisser G, Botschwina P, Müller HSP. The rotational spectrum up to 1 THz and the molecular structure of thiomethylium, HCS$^+$. *Phys Chem Chem Phys* (2003) 5:2770–3. doi:10.1039/b303260d

3. Bruna PJ, Peyerimhoff SD, Buenker RJ. *Ab initio* SCF and CI study of the HCS$^+$ – CSH$^+$ system: Potential surfaces for hydrogen abstraction and internuclear bending for ground and excited states and vertical spectrum for HCS$^+$. *Chem Phys* (1978) 27:33–43. doi:10.1016/0301-0104(78)85159-3

4. Botschwina P, Sebald P. Spectroscopic properties of CS and HCS$^+$ from *ab initio* calculations. *J Mol Spectrosc* (1985) 110:1–18. doi:10.1016/0022-2852(85)90207-3

5. Wong MW, Nobes RH, Radom L. The [HCS]$^+$ and \mathrm{[H_2CS]}{2+} potential energy surfaces: Predictions of bridged equilibrium structures. *J Mol Struct THEOCHEM* (1988) 163:151–61. doi:10.1016/0166-1280(88)80387-7

6. Puzzarini C. The HCS/HSC and HCS$^+$/HSC$^+$ systems: Molecular properties, isomerization, and energetics. *J Chem Phys* (2005) 123:024313. doi:10.1063/1.1953367

7. Kaur R, Kumar TD. Nonadiabatic couplings and charge transfer study in H + CS$^+$ collision using time-dependent quantum dynamics. *Mol Phys* (2015) 113: 3271–81. doi:10.1080/00268976.2015.1017021

8. Kaur R, Dhilip Kumar T. *Ab initio* potential energy surfaces of HCS$^+$: A study of the ground and the low-lying excited electronic states. *Chem Phys* (2016) 479:36–41. doi:10.1016/j.chemphys.2016.09.015

9. Zhang LL, Zhao J, Liu D, Wang W, Yue DG, Song YZ, et al. A new global analytical *ab initio* potential energy surface for the dynamics of the C$^+$(^{2}P) + SH(X^{2}Π) reaction. *Phys Chem Chem Phys* (2022) 24:1007–15. doi:10.1039/d1cp04948h

10. Werner HJ, Knowles PJ. An efficient internally contracted multiconfiguration–reference configuration interaction method. *J Chem Phys* (1988) 89:5803–14. doi:10.1063/1.455556

11. Werner HJ, Knowles PJ. An efficient method for the evaluation of coupling coefficients in configuration interaction calculations. *Chem Phys Lett* (1988) 145: 514–22. doi:10.1016/0009-2614(88)87412-8

12. Dunning TH, Jr. Gaussian basis sets for use in correlated molecular calculations. I. The atoms boron through neon and hydrogen. *J Chem Phys* (1989) 90:1007–23. doi:10.1063/1.456153

13. Woon D, Dunning TH, Jr. Gaussian basis sets for use in correlated molecular calculations. III. The atoms aluminum through argon. *J Chem Phys* (1993) 98: 1358–71. doi:10.1063/1.464303

14. Knowles PJ, Werner HJ. An efficient second order MCSCF method for long configuration expansions. *Chem Phys Lett* (1985) 115:259–67. doi:10.1016/0009-2614(85)80025-7

15. Zhang DH, Zhang JZH. Full-dimensional time-dependent treatment for diatom-diatom reactions: The H$_2$ + *OH* reaction. *J Chem Phys* (1994) 101: 1146–56. doi:10.1063/1.467808

16. Varandas AJC, Chu TS, Han KL, Caridade PJ. Accurate rate constant and quantum effects for N(^{2}D) + H$_2$ reaction. *Chem Phys Lett* (2006) 421:415–20. doi:10.1016/j.cplett.2006.01.073

17. Chu TS, Han KL. Nonadiabatic time-dependent wave packet study of theD$^+$ + *H*$_2$ reaction system. *J Phys Chem A* (2005) 109:2050–6. doi:10.1021/jp0451391

18. Zhang Y, Cao E, Gao SB, Huang X, Meng QT, Song YZ. Exploring the reaction dynamics of O(^{3}P) + H$_2^+$ (X$^2\Sigma_g^+$) → OH$^+$ (X$^3\Sigma^-$) + H(^{2}S) reaction with time-dependent wave packet method. *Int J Quan Chem* (2017) 117:e25343. doi:10.1002/qua.25343

19. Mao Y, Buren B, Yang ZJ, Chen MD. Time-dependent wave packet dynamics study of the resonances in the H + LiH$^+$(v = 0, j = 0) → Li$^+$ + H$_2$ reaction at low collision energies. *Phys Chem Chem Phys* (2022) 24:15532–9. doi:10.1039/d1cp05601h

20. Zhang WY, Meng QT, Gao SB, Song YZ. Theoretical insight into the vibrational excitation effect of the S$^+$(^{4}S) + H$_2$(X$^1\Sigma_g^+$) reaction. *Chem Phys Lett* (2021) 764:138257. doi:10.1016/j.cplett.2020.138257

21. Gao SB, Zhang J, Song YZ, Meng QT. Cross sections for vibrational inhibition at low collision energies for the reaction H + Li$_2$(X$^1\Sigma_g^+$) → Li + LiH (X$^1\Sigma^+$). *Eur Phys J D* (2015) 69:111. doi:10.1140/epjd/e2015-50772-9

22. Han KL, Zheng XG, Sun BF, He GZ, Zhang RQ. Chemical reaction dynamics of barium atom with alkyl bromides. *Chem Phys Lett* (1991) 81:474–8. doi:10.1016/0009-2614(91)90383-k

23. Ju LP, Han KL, Zhang JZH. Global dynamics and transition state theories: Comparative study of reaction rate constants for gas-phase chemical reactions. *J Comput Chem* (2009) 30:305–16. doi:10.1002/jcc.21032

24. Chu TS, Han KL. Effect of Coriolis coupling in chemical reaction dynamics. *Phys Chem Chem Phys* (2008) 10:2431–41. doi:10.1039/b715180b

25. Lin SY, Han KL, Zhang JZH. Accurate quantum-mechanical calculation for O(^{1}D)+DCl reaction. *Chem Phys Lett* (2000) 324:122–6. doi:10.1016/s0009-2614(00)00590-x

26. Chu TS, Zhang Y, Han KL. The time-dependent quantum wave packet approach to the electronically nonadiabatic processes in chemical reactions. *Int Rev Phys Chem* (2006) 25:201–35. doi:10.1080/01442350600677929

27. Xin R, Xiang HP, Tian L, Rong L, Song HW. Kinetic and dynamic studies of the F(^{2}P) + ND$_3$ → DF + ND$_2$ reactio. *J Phys Chem A* (2021) 125:8025–32. doi:10.1021/acs.jpca.1c06515

28. Liu D, Zhang LL, Zhao J, Zhang Q, Song YZ, Meng QT. Quantum and quasiclassical dynamics of C(^{3}P) + H$_2$($^1\Sigma_g^+$) → H(^{2}S) + CH(^{2} Π). *Chin Phys B* (2022) 31:043102. doi:10.1088/1674-1056/ac3989

29. Yue DG, Zhang LL, Zhao J, Song YZ, Meng QT. Stereo-dynamics of the reaction C + SH(D, T)(v = 0, j = 0) → H(D, T) + CS based on a recent excited state potential energy surface. *Comput Theor Chem* (2019) 1155:82–9. doi:10.1016/j.comptc.2019.03.028

30. Zhang LL, Gao SB, Song YZ, Meng QT. The manifestation of vibrational excitation effect in reactions C + SH($v = 0 - 20$, $j = 0$) → H + CS, S + CH. *J Phys B: Mol Opt Phys* (2018) 51:065202. doi:10.1088/1361-6455/aaae2e

31. Wu H, Duan ZX, Yin SH, Zhao GJ. State-resolved dynamics study of the H + HS reaction on the $3A'$ and $3A''$states with time-dependent quantum wave packet method. *J Chem Phys* (2016) 145:124305. doi:10.1063/1.4962543

32. Yao CX, Zhao GJ. Energy-dependent stereodynamics for the H(^2S)+NH($X^3\Sigma$) → H2($X^1\Sigma_g^+$) + N(^4S) reaction on the improved ZH potential energy surface. *Can J Chem* (2013) 91:387–91. doi:10.1139/cjc-2012-0404

33. Yao CX, Zhao GJ. Quasiclassical trajectory theoretical study on the chemical stereodynamics of the O(^1D) +H2 → OH+H reaction and its isotopic variants (HD, D2). *Chin Phys B* (2013) 22:083403. doi:10.1088/1674-1056/22/8/083403

34. Wang ML, Han KL, He GZ. Product rotational polarization in the photoinitiated bimolecular reaction A+BC → AB+C on attractive, mixed and repulsive surfaces. *J Chem Phys* (1998) 109:5446–54. doi:10.1063/1.476522

35. Chen MD, Han KL, Lou NQ. Theoretical study of stereodynamics for the reactions Cl+H_2/HD/D_2. *J Chem Phys* (2003) 118:4463–70. doi:10.1063/1.1545112

36. Chen MD, Han KL, Lou NQ. Vector correlation in the H+D2 reaction and its isotopic variants: Isotope effect on stereodynamics. *Chem Phys Lett* (2002) 357: 483–90. doi:10.1016/s0009-2614(02)00585-7

37. Wang ML, Han KL, He GZ. Product rotational polarization in photo-initiated bimolecular reactions A+BC: Dependence on the character of the potential energy surface for different mass combinations. *J Phys Chem A* (1998) 102:10204–10. doi:10.1021/jp981738u

38. Zhang LL, Liu D, Yue DG, Song YZ, Meng QT. Dynamics of H(^{2}S) + $CH(X^2\Pi)$ reactions based on a new CH_2(X^3A'') surface via extrapolation to the complete basis set limit. *J Phys B: Mol Opt Phys* (2020) 53:095202. doi:10.1088/1361-6455/ab7641

39. Liu D, Zhao J, Wang LF, Song YZ, Meng QT, Zhang LL. Exploring reaction mechanism and vibrational excitation effect in H+CH(v, $j = 0$) reaction. *Chem Phys Lett* (2020) 749:137398. doi:10.1016/j.cplett.2020.137398

40. Zhang LL, Liu D, Song YZ, Gao F, Meng QT. Examining the isotope effect on CH decay and H exchange reactions: H(^2S) + CH (D/T)($^2\Pi$). *Phys Scr* (2020) 96: 015404. doi:10.1088/1402-4896/abc20d

41. Zhang LL, Gao SB, Meng QT, Pan J, Song YZ. Accurate potential energy surface of H_2S^+(X^2A'') via extrapolation to the complete basis set limit and its use in dynamics study of S^+(^{2}D)+H_2($X^1\Sigma_g^+$) reaction. *J Chem Phys* (2018) 149:154303. doi:10.1063/1.5046315

42. Zhang LL, Song YZ, Gao SB, Meng QT. Globally accurate potential energy surface for HCS(A^2A'') by extrapolation to the complete basis set limit. *J Phys Chem A* (2018) 122:4390–8. doi:10.1021/acs.jpca.8b02131

frontiers | Frontiers in Physics

TYPE Original Research
PUBLISHED 08 December 2022
DOI 10.3389/fphy.2022.1059968

OPEN ACCESS

EDITED BY
Yujun Zheng,
Shandong University, China

REVIEWED BY
Yabin Yu,
Hunan University, China
Kun Xun,
Retired, China

*CORRESPONDENCE
Huai-Yu Wang,
wanghuaiyu@mail.tsinghua.edu.cn

SPECIALTY SECTION
This article was submitted to Atomic and Molecular Physics, a section of the journal Frontiers in Physics

RECEIVED 02 October 2022
ACCEPTED 04 November 2022
PUBLISHED 08 December 2022

CITATION
Wang H-Y (2022), Exploring the implications of the uncertainty relationships in quantum mechanics. *Front. Phys.* 10:1059968.
doi: 10.3389/fphy.2022.1059968

Exploring the implications of the uncertainty relationships in quantum mechanics

Huai-Yu Wang*

Department of Physics, Tsinghua University, Beijing, China

Heisenberg guessed, after he established the matrix quantum mechanics, that the non-commutativity of the matrices of position and momentum implied that the position and momentum of a particle could not be precisely simultaneously determined. He consequently conjectured that time and energy should also have a similar relationship. Soon after, Robertson derived an inequality concerning the space coordinate and momentum, which was thought to be the mathematical expression of the uncertainty relation guessed by Heisenberg. Since then, people have tried various devices to prove the correctness of these two relations. However, no one conducted a careful analysis of Heisenberg's primary paper. In this work, we point out some serious problems in Heisenberg's paper and the literature talking about the uncertainty relationships: the physical concepts involved in the uncertainty relations are not clear; one physical concept had more than one explanation, i.e., switching concepts; there has never been measurement experiment to support the relations. The conclusions are that the so-called coordinate–momentum uncertainty relation has never been related to actual measurement and there does not exist a time–energy uncertainty relation.

KEYWORDS

coordinate–momentum uncertainty relation, time–energy uncertainty relation, measurement, dimension of a wave function in quantum mechanics, uncertainty, lifetime of energy level

1 Introduction

As soon as Heisenberg founded quantum mechanics (QM) in matrix form [1–3], he acutely perceived that the matrices of the position and momentum of a particle were non-commutative. He thought that this non-commutativity should have some physical meaning. In a later paper [4], he guessed that the physical meaning of the non-commutativity was that the position and momentum of a microscopic particle could not be precisely simultaneously determined by experimental measurement. He was unable to provide an explicit expression for that, but merely presented qualitative discussion, including the gedanken experiments. He inferred consequently that there was a similar relationship between time and energy.

Soon after that, Robertson [5] derived an inequality, which was believed the mathematical expression of the uncertainty relation guessed by Heisenberg. Thus, the guess of the uncertainty relationship proposed by Heisenberg was generally accepted by people, and this was set in stone. Almost all QM textbooks introduce the coordinate–momentum relation and time–energy relation [6–30]. The uncertainty relations are thought of as fundamental ones in QM. They have been frequently mentioned by researchers and were even promoted as a principle—uncertainty principle [6–12].

When the present author carefully read the introductions and explanations of the uncertainty relations in Heisenberg's primary paper [4] and the literature, questions emerged. A striking problem is that the uncertainty relations ought to be related to actual measurement, but it seems not to be so. Even in [4], Heisenberg merely talked about idealized experiments. The narrations connecting the uncertainty relations and the experiments are farfetched and specious. Confusions between different conceptions appear frequently. As a matter of fact, someone has been aware that there exist wrong explanations in the literature [31, 32]. We think that it is desirable to analyze in detail all the aspects involved in the uncertainty relations.

In the 1920s, Heisenberg, Schrödinger, Dirac *et al.* performed pioneering work in founding QM, which was a completely new field in physics. A series of new concepts merged. Some new concepts were formed. Among the new concepts, some were not very clear to people; they were not very clear even to these pioneers themselves, which should not be surprising. Hence, no one could guarantee that their works were flawless.

For example, when Schrödinger proposed his wave equation of QM, he unknowingly put down the negative kinetic energy (NKE) Schrödinger equation (33). However, this NKE Schrödinger equation was never realized by himself and others and was abandoned since then. We found that the NKE Schrödinger equation could be obtained by taking low-momentum approximation from relativistic quantum mechanics equations (RQMEs), and it was of explicit physical meanings [34, 35]. Dirac explained the NKE solutions of his RQME as representing antiparticles. Although people know that this explanation implied contradictions, no one could propose the right scenario to resolve the contradictions. We have given a correct explanation of the NKE solutions [35, 36].

There are two reasons that make people not aware of these pioneers' mistakes in some aspects. One is that due to their genius achievements, people think that what they said was right. The other is that the related mistakes have not brought perceivable affection up till now. For instance, if there is no so-called uncertainty relationship, the evaluations and measurements in QM are not affected. The new theories raised after the uncertainty relations had been established, such as RQMEs, quantum electrodynamics (QED), quantum field theory (QFT), and quantum information, did not resort to the uncertainty relations. The computation of the band structures in solid-state materials and of nuclear physics does not need uncertainty relations. Physical experiments have never been arranged under the guidance of uncertainty relations, in spite of that, they are called principles. The uncertainty relations are usually employed to provide explanatory notes to some known phenomena and results.

After almost one hundred years, as later generations, we have grasped knowledge much more and wider than the pioneers did. People nowadays ought to have more sophisticated and rigorous reasoning. We should be able to recognize what the problems left by these pioneers are and how to resolve them. With clearer distinguishing and understanding of physical concepts, we are able to solve some difficulties left in QM [34–42].

The study of physics obeys physical laws. The physical laws are represented by fundamental equations and statements. The conclusions in physics need to be verified by experiments, which means that quantitative results are necessary. Theoretically, quantitative results are obtained by mathematical derivation starting from the fundamental equations. Theoretical discussions observe rigorous logical reasoning. We believe that in order to avoid the flaws in physical discussions as far as possible, some principles related to the physical contents discussed should be obeyed besides the mathematical derivation. The principles are presently called the basic viewpoints of the author.

The basic viewpoints depended on the concrete contents under discussion. The author's previous papers [34–42] concerned some basic problems in QM. When we discussed one of these problems, certain viewpoints were based on [35, 42].

The uncertainty relationship is believed to be a fundamental topic in QM. In the present work, we are going to investigate this topic based on certain points of view. In the author's following work, more topics will be touched on, and corresponding basic viewpoints will be stemmed on.

All the basic viewpoints we have been aware of are listed in Supplementary Appendix SA. We think that only when these viewpoints are abided by can one guarantee logical rigorousness and validity of the conclusions in discussing physical problems. Or, conception confusion may occur, and subsequently, the problem may not be solved correctly.

Here we mention one of the basic points of view. In QM, we always deal with wave functions. Every wave function satisfies a fundamental QM equation. Explicitly, the fundamental QM equation is in the form of

$$\mathrm{i}\hbar\frac{\partial}{\partial t}\psi(t)=H\psi(t). \tag{1.1}$$

Here, the coordinate variables are not explicitly shown. In this paper, we always assume that (Eq. 1.1) is Schrödinger equation. If the Hamiltonian H is time-independent, the dependence of the wave function on time can be written as

$$\psi(t)=\mathrm{e}^{-\mathrm{i}Et/\hbar}\varphi. \tag{1.2}$$

Thus, the function φ meets the stationary equation

$$H\varphi=E\varphi. \tag{1.3}$$

Every wave function is necessarily the solution of Eq. 1.1. The wave functions of stationary states observe Eq. 1.3. In other words, when one discusses a wave function, he must be able to put down the corresponding Hamiltonian H. This is important. In textbooks, some functions are treated as wave functions because of their seemingly good behaviors. However, they are not the solutions of Eq. 1.1, i.e., there is no corresponding Hamiltonian. In Section 2, we will see two examples: the wave packet and wave train with the finite length for moving particles.

In Sections 2 and 3, we discuss coordinate–momentum and time–energy uncertainty relations, respectively. We will point out that physical conceptions are confused in the literature in discussing the two uncertainty relations. In [4], Heisenberg proposed the possible relations between the uncertainties of position and momentum, directed against single particles. Naturally, the similar relation between time and energy that he guessed was also for single particles. We stress this because in the literature, the problems of single-particles are confused with those of many-body systems. Section 4 is further discussion, and Section 5 contains the conclusions. Supplementary Appendix SA lists our basic viewpoints. Supplementary Appendix SB introduces the derivation of the so-called coordinate–momentum uncertainty relation.

2 Coordinate–momentum uncertainty relation

There are confusions of concepts when the coordinate–momentum uncertainty relation is discussed. The inequality derived by Robertson [5] was irrespective of experiments and Heisenberg's primary paper [4]. This section presents a detailed analysis.

In this paper, we always consider the case of one dimension.

2.1 Heisenberg's primary discussion

The paper [4] was the first one to talk about possible uncertainty relationships. The whole article did only qualitative discussion with no rigorous mathematical derivation. Heisenberg, based on his established QM in matrix form, found that the commutator of the two matrices q and p had the following result:

$$pq - qp = i\hbar. \tag{2.1}$$

The nonzero result meant that the two matrices could not exchange the order in their product. From this, he guessed that when a particle's position and momentum were measured, both had some uncertainties.

"Let q_1 be the precision with which the value q is known (q_1 is, say, the mean error of q); therefore, here, it is the wavelength of the light. Let p_1 be the precision with which the value p is determinable; that is, here, it is the discontinuous change of p in the Compton effect. Then, according to the elementary laws of the Compton effect, p_1 and q_1 stand in the relation

$$q_1 p_1 \sim \hbar.\text{"}[4]. \tag{2.2}$$

Here, the definition of the uncertainty of q was obvious: "q_1 be the precision with which the value q is known (q_1 is, say, the mean error of q)". q_1 is also the measurement precision of q. Then, its value must rely on the measurement equipment and measurement process. For instance, he mentioned a special case where photons were used to impinge a particle. Then, the uncertainty of the particle's position was the photon's wave length. This example showed that the measurement precision was indeed closely related to the measurement instrument chosen.

According to the basic viewpoint I.1 in Supplementary Appendix SA, every physical concept should have an explicit mathematical expression, or people would not clearly understand the conception.

First, in QM, a particle is described by its wave function. The wave function is the function of the spatial coordinate q, that is to say, q is an argument in a function, e.g., Eqs. 3, 12–(14) in [4]. In Heisenberg's words, "Let q_1 be the precision with which the value q is known". What is the meaning of the q in this sentence was not clear. In Eq. 2.1, q and p are matrices. It seems that Heisenberg unknowingly regarded them as numbers.

Next, we discuss the contents in the QM field. Following the viewpoint II.2, a wave function must be the solution of a fundamental QM equation. Heisenberg put down functions for discussion, but some of them were not the solutions of the Schrödinger equation for the system under consideration.

"If, for any definite state variable η, we determine the position q of the electron as q' with an uncertainty q_1, then we can express this fact by a probability amplitude $S(\eta, q)$, which differs appreciably from zero only in a region of spread q_1 near q'. For example, one can write

$$S(\eta, q) \propto \exp\left[-\left(q-q'\right)^2/2q_1^2 - ip'\left(q-q'\right)/\hbar\right]\text{".}[4]. \tag{2.3}$$

This should be a wave function in QM. Such a function was called a Gaussian wave packet and used in the literature [6, 13–16]. It is time independent. Only the stationary eigenfunctions of a harmonic oscillator are of the form of $\psi(x) \propto e^{-\alpha x^2}$, and the possible parameter is the location of the center of the oscillator. Otherwise, we do not know what the Hamiltonian of the wave function Eq. (2.3) is, while describing a moving particle we are talking about. When the Hamiltonian of a free particle is acted on this function,

$$-\frac{\hbar^2}{2m}\frac{\partial^2}{\partial q^2}\psi(q) = \frac{\hbar^2}{2m}\left[\frac{1}{2q_1^2} - \left(\frac{q}{2q_1^2} + \frac{ip'}{\hbar}\right)^2\right]\psi(q). \tag{2.4}$$

It is seen that the function (Eq. 2.3) is not a free particle. We do not know what a potential $V(q)$ enables us to put down the stationary equation for the wave function (2.3).

$$\left[-\frac{\hbar^2}{2m}\frac{\partial^2}{\partial q^2}+V(q)\right]\psi(q)=E\psi(q). \tag{2.5}$$

We are unable to write down a $V(q)$ other than the oscillator potential, and neither the expression of the corresponding Hamiltonian H.

In Eq. 2.3, q is the spatial coordinate of the wave function, but not the position of the electron. Heisenberg confused the concepts.

Eq. 18 in [4] was

$$S(t,p)=\mathrm{e}^{-\alpha t}\psi(E_2,p)\mathrm{e}^{-\mathrm{i}E_2 t/\hbar}+\left(1-\mathrm{e}^{-2\alpha t}\right)^{1/2}\psi(E_1,p)\mathrm{e}^{-\mathrm{i}E_1 t/\hbar}. \tag{2.6}$$

This was a time-dependent function. When it is substituted into the left-hand side of Eq. 1.1, the result is

$$\mathrm{i}\hbar\frac{\partial}{\partial t}S(t,p)=(-\alpha-\mathrm{i}E_2 t/\hbar)\mathrm{e}^{-\alpha t}\psi(E_2,p)\mathrm{e}^{-\mathrm{i}E_2 t/\hbar}+\left(\frac{\alpha\mathrm{e}^{-2\alpha t}}{1-\mathrm{e}^{-2\alpha t}}-\mathrm{i}E_1/\hbar\right)\left(1-\mathrm{e}^{-2\alpha t}\right)^{1/2}\psi(E_1,p)\mathrm{e}^{-\mathrm{i}E_1 t/\hbar}. \tag{2.7}$$

We are unable to find a time-dependent Hamiltonian $H(t)$ such that the function Eq. 2.6 satisfies Schrödinger Eq. 1.1:

$$\mathrm{i}\hbar\frac{\partial}{\partial t}S(t,p)=H(t)S(t,p). \tag{2.8}$$

Therefore Eq. 2.6 is not a wave function in QM.

For the wave function (22) in [4], one was unable to write a corresponding Hamiltonian as well, and so it was not a wave function in QM.

When writing down a function, one should first prove that it is the solution of a fundamental QM equation or has its corresponding Hamiltonian. Otherwise, it cannot be treated as a wave function in QM.

Third, Heisenberg did not present explicit expressions or rigorous mathematical derivations when he mentioned some physical conceptions.

For example, he mentioned "statistical error" more than once, but we do not know what he meant by it.

In Eq. 2.6, a concept of "radiation damping" was used. However, Heisenberg did not provide the mathematical derivation for the form in Eq. 2.6. In QM, a single particle does not have the concept of "radiation damping." This concept must belong to a many-body system.

In [4], the argument below Eq. 8 was questionable. A beam of electrons was arranged to run through two fields successively in two different manners. In the second manner, no derivation was presented. Therefore, one could not know how the result $Z_{nl}=\sum_m c_{nm}\bar{c}_{nm}d_{ml}\bar{d}_{ml}$ was reached.

Fourth, according to viewpoint I.3, when a gedanken experiment leads to a positive conclusion, it cannot explain anything. Such a conclusion could neither be proved nor be disproved.

In short, Heisenberg's primary paper [4] lacked rigorous mathematics, was not quantitatively related to real experiments, and was not very clear in some physical concepts.

Heisenberg's paper [4] just considered the measurement precisions of the position and the momentum of a single particle.

2.2 The analysis of the coordinate–momentum uncertainty relation

In 1929, Robertson [5] derived the famous mathematical inequality, see Supplementary Appendix SB. The conclusion was that the mean square errors of coordinate and momentum obeyed the following inequality:

$$\Delta x\Delta p\geq\hbar/2. \tag{2.9}$$

This inequality was believed to be the mathematical expression of the uncertainties of coordinate and momentum that Heisenberg guessed. So, (2.9) was called the Heisenberg uncertainty relation.

Here, we distinguish the concepts of the position of a particle and coordinate. Heisenberg discussed the uncertainties of the measured position and momentum of a particle, so that his assumed relation was called the position–momentum uncertainty relation. However, in QM, a particle at a state is described by a wave function, which is a function of coordinates. The Δx in (2.9) does not involve the meaning of a particle's position. Hereafter, (2.9) is called the coordinate–momentum uncertainty relation.

According to the current understanding, the Δx and Δp in (2.9) are two quantities related to measurement. We point out in Supplementary Appendix SB that (2.9) is irrespective to both measurement and the content in Ref. [4].

Now, we explain that it is not right to understand the Δx and Δp in (2.9) as measurement uncertainties of coordinate and momentum, and as a matter of fact, it is impossible to implement measurement in the way of (2.9).

Usually, the recognition of (2.9) is that if one measures the position x and momentum p of a particle, they cannot be precisely simultaneously measured, and the smaller the measuring deviation of one quantity is, the greater the other. This recognition is incorrect.

Since (2.9) is regarded as the relation between the ncertainties of position and momentum, it ought to be related to the statistics of measured quantities. This prompts us to explain the implication of the inequality and the way of statistics of measured quantities.

2.2.1 The implication of the coordinate–momentum uncertainty relation

The coordinate is expressed by x, and the momentum operator is $p=-\mathrm{i}\hbar\frac{\partial}{\partial x}$. Suppose a microscopic system's

Hamiltonian H is known, and its wave function ψ is solved from (1.1).

The inner product of any two functions ψ and φ is defined by

$$(\psi, \varphi) = \int dx\psi^{*}\varphi = (\varphi, \psi)^{*}. \tag{2.10}$$

We perform the following calculations:

$$\bar{x} = (\psi, x\psi), \tag{2.11}$$

$$\Delta x = \left(\psi, (x - \bar{x})^{2}\psi\right)^{1/2}. \tag{2.12}$$

$$\bar{p} = \left(\psi, -i\hbar\frac{\partial}{\partial x}\psi\right). \tag{2.13}$$

$$\Delta p = \left(\psi, \left(-i\hbar\frac{\partial}{\partial x} - \bar{p}\right)^{2}\psi\right)^{1/2}. \tag{2.14}$$

The four calculated quantities meet (2.9).

Because the forms of 2.11–2.14 seem the same as that of the definition of mean square error, people mistakenly believe that 2.11–2.14 are of the meanings of the mean square error in the sense of measurement.

When talking about 2.9, people usually think that the smaller the one of Δx and Δp, the larger the other. However, it is seen from 2.11–2.14 that Δx and Δp are uniquely determined by the given wave function, and their product necessarily meet (2.9). As a matter of fact, neither of Δx and Δp is variable.

For a one-dimensional harmonic oscillator, the nth stationary state wave function is denoted by ψ_n. It is evaluated [3, 7, 17] that in ψ_n, $\Delta x = \sqrt{n + 1/2}\ \frac{1}{\alpha}$ and $\Delta p = \sqrt{n + 1/2}\hbar\alpha$, so that $\Delta x\Delta p = (n + \frac{1}{2})\hbar$. Both Δx and Δp increase with the index n. For the wave functions of hydrogen, we have $\Delta x = \frac{a_0}{2\sqrt{3}}\sqrt{7n^2 + 5}$, which increases with energy level, and $\Delta p = \frac{\hbar}{\sqrt{3}a_0}$, remaining unchanged for all the energy levels [3].

We turn to look at the comparison between the ground states of different systems. A hydrogen atom and an atomic nucleus have different dimensions. Compared with the hydrogen atom, the dimension of the nucleus is smaller, and so, the uncertainty Δq seems smaller and that of momentum Δp seems larger. This is often used as an example showing that if one of Δq and Δp is smaller, the other is necessarily larger. However, such a comparison is incorrect. It is meaningless to compare the quantities in two different systems. Furthermore, in the comparison, one confuses the two conceptions: the dimension of a particle and the uncertainty of the particle's position, which will be made clear in Section 2.3.1 below.

Personally, Eq. 2.9 has only one usage: it can be used to judge if the wave function solved from (1.1) has some error. If the Δx and Δp calculated through (2.11–2.14) do not meet (2.9), then it is assured that the wave function is not a correct one in QM. What if (2.9) is satisfied? Nothing is explained because (2.9) is originally an inequality that every normalized function ought to satisfy.

2.2.2 There is no way to implement measurement according to the uncertainty relation

People usually say that (2.9) concerns measurement, and it shows that the position and momentum of a particle cannot be precisely simultaneously measured. We recall how the statistics of the measured results are made.

Suppose that there is a sample, Y. We measure its value. The ith measured value is denoted as y_i. After N times of the measurement, this sample's averaged value and mean square deviation are evaluated by

$$\bar{y} = \frac{1}{N}\sum_{i=1}^{N} y_i \tag{2.15}$$

and

$$\Delta y = \left[\frac{1}{N}\sum_{i=1}^{N}(y_i - \bar{y})^{2}\right]^{1/2}. \tag{2.16}$$

Now, we have a QM system, and a mechanical quantity F is to be measured. Suppose that an appropriate device is designed, and the value of F can be measured experimentally.

According to QM, the average of the mechanical quantity F in a state ψ is

$$\bar{F} = (\psi, F\psi). \tag{2.17}$$

The inner product is defined by (2.10). In order to evaluate the average (2.17), in principle, at any spatial coordinate x, the value of F should be measured. Actually, one has to check, if possible, the measurement at discrete x points. Hence, the integration is replaced with the form of summation

$$\bar{F} = \sum_{i=1}^{N} b_i F(x_i). \tag{2.18}$$

The coefficients b_is are related to the square of the absolute value of the wave function at point x_i, $|\psi(x_i)|^2$. If this can be done, one further measures the values of $F^2(x_i)$ at point x_is. After these manipulations, one calculates $\overline{F^2}$ by

$$\overline{F^2} = (\psi, F^2\psi) = \sum_{i=1}^{N} b_i F^2(x_i). \tag{2.19}$$

In this way, the mean square deviation $\Delta F = (\overline{F^2} - \bar{F}^2)^{1/2}$ can be obtained.

However, what is the meaning of $F(x_i)$ in (2.18)—measuring the value of a physical quantity at individual coordinates? How can this quantity be measured? The same questions also rise for $F^2(x_i)$ in (2.19).

In QM, the state of a particle is represented by its wave function. The wave function distributes in space at any time. One cannot say that the wave function is at a point at one instant and another point at the next instant. The physical quantity F belongs to the whole QM system and is not fixed to discrete spatial points.

We do not know how to experimentally measure $\bar{x}$, $\overline{x^2}$, $\bar{p}$, and $\overline{p^2}$ in the way of (2.18, 2.19). In short, Eq. 2.9 cannot correspond to practical measurement. As a matter of fact, people never apply (2.11–2.14) to perform measurements.

Furthermore, from Eq. 2.9 itself, we are unable to see the concepts of "position uncertainty" and "momentum uncertainty", since it is irrespective to measurement. That is to say, the uncertainty relation (2.9) itself does not contain the concepts of "position uncertainty" and "momentum uncertainty", since it does not contain the information related to measurement.

The relation (2.9) is sometimes called a principle. However, no one designs an experiment based on this so-called principle.

The conclusion is that Eq. 2.9 is irrespective to measurement.

2.3 The discussions of the uncertainty relation in the literature

We have pointed out above that in [4], there was no rigorous argument and mathematical derivation, and some concepts were confused. However, people *a priori* believed that the content in this paper was right and the mathematical expression was what Robertson [5] provided. Some textbooks presented (2.9) without explanation [8, 17, 18]. Some others tried various devices in order to explain that this uncertainty relation was correct.

Because the narration in [4] was not clear, when later people talked about the uncertainty relation, they did not have fixed rules, but depended on their own imaginative development. Different people had different explanations. Each explanation was unable to overturn others. Therefore, according to the basic viewpoint I.2, none of the explanations were right. The so-called examples, that were believed to support the uncertainty relation, were just farfetched ex-post explanations.

There are three typical examples giving farfetched explanations: finite-length wave train or a piece of truncated plane wave, single-slit diffraction, and the ground state of hydrogen atom. Before analyzing these examples, we distinguish between two concepts: a particle's dimension and the uncertainty of its position.

2.3.1 Distinguishing a particle's dimension and the uncertainty of its position

A particle's dimension and the uncertainty of its position are two different conceptions.

In QM, a particle at a state is described by a wave function. For each wave function, we are able to roughly define a range in space, outside which the wave function can be regarded as zero. This range is defined as the dimension of this particle at this state. For instance, in an infinitely deep square potential with width a, the dimension of a particle is just the potential width a. For a one-dimensional harmonic oscillator, the ground state wave function is $\psi_0 \propto \mathrm{e}^{-\alpha^2 x^2/2}$. We define the length of the interval $[-\frac{\sqrt{2}}{\alpha}, \frac{\sqrt{2}}{\alpha}]$ as the dimension of this particle in the ground state. In the case that Eq. 2.3 represents the wave packet of a particle, then the dimension of this particle is the length of the interval $[-\sqrt{2}\,q_1, \sqrt{2}\,q_1]$. As soon as a state is known, the dimension is definitely determined by its wave function.

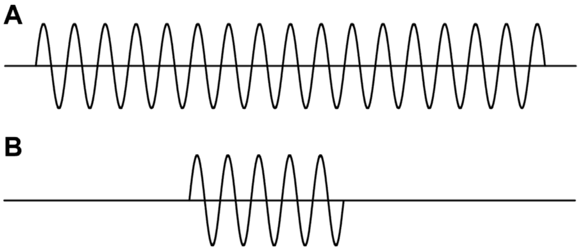

FIGURE 1
Two wave trains (interrupted sine waves) with finite lengths. **(A)** Longer length. **(B)** Shorter length.

The De Broglie relation tells us that as long as a particle's momentum is known, its dimension can be roughly estimated by

$$\lambda = h/p. \tag{2.20}$$

Here, we regard De Broglie wave length as the particle's dimension. The De Broglie relation tells us that the larger the momentum of a particle, the less its dimension. It is seen that Eq. 2.2 guessed by Heisenberg was more like the De Broglie relation.

The uncertainty of a particle's position can be roughly defined as the precision, or error range, of the measured position of the particle.

We stress that a particle's dimension and the uncertainty of a particle's position are two different concepts. The former is uniquely determined by the wave function, independent of measurement, whereas the latter depends on the measurement devices and measurement process.

For example, Heisenberg mentioned [4] that when a photon was employed to collide with a particle, "the highest attainable accuracy in the measurement of position is governed by the wavelength of the light." Thus, roughly speaking, when the light wavelength is λ, the measuring precision of the particle's position is λ; when the light wavelength is 2λ, the precision will be 2λ.

In literature, the two concepts were confused frequently.

In [4], Heisenberg put down a wave packet, Eq. 2.3, and said that the wave function "differs appreciably from zero only in a region of spread q_1 near q'." That is to say, $2q_1$ was the dimension of the wave packet. Then, he thought that the relation $p_1 q_1 = \hbar$ limited the precision of the wave packet, where q_1 is the precision of measuring the position of the wave packet. So, he equated the dimension and uncertainty. On one hand, the uncertainty q_1 ought to be given after measurement and might vary depending on the measurement. On the other hand, q_1 was the half dimension of the wave packet and was contained in the function already. In this case, the two concepts were confused.

The confusion of the two concepts, or concept stealing, also occurred later [14, 19].

2.3.2 Wave train with finite length

Figures 1A,B are often used to represent the two states of a moving particle. This picture is utilized to explain the coordinate–momentum uncertainty relation [9]. An intuitive understanding is that the shorter the particle's dimension or its position uncertainty, the greater its momentum uncertainty. Comparison of Figures 1A,B prompted such a recognition: "we can see very clearly that the better the position is defined, the more poorly is the momentum defined" [9].

Here, we are considering a particle with a mass. Figure 1 represents the wave functions of the particle. Following basic viewpoint II.2, the wave functions should be the solutions of Eq. 1.1.

The two pictures in Figure 1 are actually the stationary wave functions in two one-dimensional infinitely deep square potential wells with different widths. Because the widths are different, the two wells are of different Hamiltonians. The two wave functions are in different systems. Comparing the positions and momenta of the particles in the different systems is meaningless. Furthermore, the average of momentum in each state is exactly zero. In this case, discussing the momentum uncertainty is meaningless.

It can be certain that a particle which is marching is not represented by the functions in Figure 1. Thus, the two pictures in Figure 1 are not wave functions in QM for describing a moving particle.

Now, suppose that ψ_a and ψ_b are two real wave functions in QM, instead of those in Figure 1. Assume that the dimension of ψ_a is longer than that of ψ_b. In this situation, we make following discussion.

First, we should not say that the uncertainty of ψ_a is greater than that of ψ_b, because we have not arranged the measurement. The discussion of the uncertainties of the functions in Figure 1 actually confuses dimension and uncertainty, which is known as concept stealing.

Next, since ψ_a and ψ_b are two different wave functions, they may either belong to different Hamiltonians, i.e., different systems, or belong to one Hamiltonian but two different states. In either case, comparing the uncertainties of two different states is meaningless.

Another analysis commonly used is to write a function's Fourier transformation and inverse Fourier transformation [9].

$$\psi(x) = \int_{-\infty}^{\infty} \mathrm{d}p e^{\mathrm{i}px} A(p). \tag{2.21}$$

$$A(p) = \int_{-\infty}^{\infty} \mathrm{d}x e^{-\mathrm{i}px} \psi(x). \tag{2.22}$$

It was analyzed that the more localized the $\psi(x)$ in space, the more extended the $A(p)$ in momentum space. An illustration of it was Figure 4 in [13].

Equations 2.21 and 2.22 are Fourier transformation and its inverse of each other. This is a general mathematic property, not a unique property in QM. Furthermore, the localization and extension of the $\psi(x)$ refer to the dimension, not uncertainty. In the Fourier components, the ranges of momenta and the uncertainties of momenta are confused. Since the explicit form of 2.21 is not given, one does not know if it is a wave function in QM. If it is, the corresponding Hamiltonian should be given. This pair of functions should not be used to explain the uncertainty relation.

2.3.3 Single-slit diffraction

Single-slit experiment is often used to explain the uncertainty relation of a particle [9, 13, 14].

Let the width of a slit be d and the wavelength of particles be λ. The particles go through the slit and diffraction occurs as $\lambda > d$. At the moment when a particle just reaches the position of the slit, its wave function is confined within the slit. Then, the slit width d is regarded as the uncertainty Δx in (2.9).

$$\Delta x = d. \tag{2.23}$$

This is not correct. When a particle is within the slit, its wave function is zero outside of the slit. At this moment, the width d is the dimension of the particle, which is independent of measurement. However, Δx must be evaluated by the wave function following 2.12, not simply written in terms of the geometric dimension of the system. Eq 2.23 is again an example that a particle's dimension is confused with its position's uncertainty. This confusion also reflects that people subconsciously do not think of the Δx in 2.9 as a quantity related to measurement.

If the measurement precisions of the position and momentum of a particle obey the uncertainty relation, these precisions ought to be obtained in experimental measurements. In single-slit diffraction experiment, neither a single particle's position nor its momentum is measured. The energy of the incident particle is already known. Since the slit width d is known, the diffraction pattern, the distribution of the outgoing particles with diffraction angle, is determined, which can be evaluated by means of the diffraction law before the experiment. The diffraction pattern obtained experimentally is in agreement with the theoretical calculation, and is stable. The single-slit diffraction experiment just lets particles go through a slit, and all the information is known before the experiment. According to viewpoint I.3, this experiment is not a measurement.

The single-slit experiment is just an observation of a phenomenon, not a measuring manipulation. Every wave, when going through a region, the room of which is less than the wave length, yields diffraction. Water waves are the same, and no one would explain the water diffraction by uncertainty relation. The behavior of water waves is explained by the

Huygens–Fresnel principle. The wavelength of radio waves can be as long as kilometers, so that they can diffract in a larger room. The distribution of the electromagnetic field can be evaluated by Maxwell equations under specific boundary conditions. These diffractions are irrespective to uncertainty relation.

Suppose that there are two slits, with widths d_1 and d_2, respectively, and $d_1 > d_2$. People may say that the first order diffraction minimum from d_1 slit is less than that from d_2 slit, which seems to embody the uncertainty relation. Please note that the two slits with widths d_1 and d_2 are two different systems, because their Hamiltonians are different. Comparing the quantities in two different systems is meaningless. To verify the uncertainty relation, one should measure a particle's position and momentum simultaneously in one system, which implies that the slit width d remains unchanged,

In [4], Heisenberg considered using photons to probe electrons, a measurement of single particle. In the single-slit experiment, no physical quantity of a single particle is measured. The single-slit diffraction shows the angular distribution of a large number of particles after going through the slit. The distribution is stable, and there is no concept of uncertainty.

Single-slit diffraction is a collective effect of many particles. Trying to explain the uncertainty relation by the single-slit diffraction is a confusion of the single-particle system and many-particle system.

Figure 2.8 in [19] actually showed the distribution of a large number of particles, and not the uncertainty of a particle's position.

2.3.4 The ground state of hydrogen atom

There is a way of estimating the energy of the ground state of a hydrogen atom [6, 9, 20, 21], which is thought of as an application of the uncertainty relation. The energy of a hydrogen atom reads

$$E = \frac{p^2}{2m} - \frac{e^2}{r}. \tag{2.24}$$

The dimension of this system is very small, i.e., the r is very small and Δr is of the same order of magnitude as r. So, r is replaced by Δr. Because Δp is the same order of magnitude as p, p is replaced by Δp. Then, the relation

$$\Delta r \Delta p \sim \hbar \tag{2.25}$$

is used to express Δp by Δr. These replacements recast (2.24) to become

$$E \sim \frac{\hbar^2}{2m(\Delta r)^2} - \frac{e^2}{\Delta r}. \tag{2.26}$$

By taking the derivative of Δr, the energy minimum is estimated:

$$E_{\min} = -\frac{me^4}{2\hbar^2}. \tag{2.27}$$

In this course, it seems that the uncertainty relation (2.25) is employed. This method is also employed to estimate the ground state energy of a nucleus.

First, this example is irrespective to measurement. It is just an estimation of the energy minimum. Second, the above procedure can be simplified. Using $rp \sim \hbar$, which is actually the De Broglie relation, Eq. 2.24 can be recast to become $E \sim \frac{\hbar^2}{2mr^2} - \frac{e^2}{r}$. Then, taking the derivative of r leads to the same energy minimum. There is no need for replacing r by Δr and replacing p by Δp. That is to say, the so-called uncertainty relation (2.25) is actually not touched. Third, the r here is actually the dimension of the hydrogen atom. Replacing r by Δr is substantially again the confusion of a particle's dimension and its position uncertainty. Fourth, taking derivative with respect to Δr is ridiculous, because Δr is, in the sense of either (2.12) or the position uncertainty, not a variable. In the course of derivation, the uncertainty relation (2.25) is used, but a definite result is obtained. This is not a correct mathematical derivation because wrong logic is involved.

We stress once more that a particle's dimension is a definite quantity, whereas its position's uncertainty relies on measurement.

2.4 Real measurement experiments

Until now, when discussing the uncertainty relation, often idealized experiments have been concerned, which are irrelative to the experiment of measurement.

Actually, there is no such experiment in which the position and momentum of a particle are measured simultaneously, and their uncertainties are estimated from the measured information, so as to meet Eq. 2.9.

To gain the uncertainty of a particle's position, one first has to measure its position. Nevertheless, in QM, a particle is described by a wave function, and has a dimension as having been defined in Section 2.3.1. In QM, the concept of a particle's position is not clearly defined. Because of this fact, in experiments, no measurement of the so-called position of a particle is carried out.

People did measure a particle's momentum, and estimate the uncertainty from the information of the experiment. However, they did not measure the particle's position in the same experiment simultaneously. There are two examples [14].

One is that the momentum of a charged particle is measured by deflection in a constant magnetic field, the strength of which is denoted by B. An electron with a charge e enters the magnet after passing through a diaphragm with width d_1, and leaves it through another diaphragm with width d_2 after having suffered a 180-degree deflection. The trajectory of the electron in the magnet is a semicircle, the radius R of which is equal to half of the distance between the two diaphragms. When the momentum of the electron is measured to be p, the precision is estimated to be

$$\Delta p = \frac{p}{R}(d_1 + d_2). \tag{2.28}$$

At the instant at which the electron enters the magnet through the first diaphragm, it moves along the y axis. The uncertainty is estimated as

$$\Delta y \approx \frac{4\pi\hbar}{eBd_1}. \tag{2.29}$$

Thus, it seems that $\Delta y\Delta p \approx 4\pi\hbar(1 + \frac{d_2}{d_1})$, satisfying the coordinate–momentum uncertainty relation.

However, the right-hand side of Eq. 2.29 has been already known before the measurement. In the experiment, the position of the electron is not detected, and consequently, one is unable to estimate the precision of the position of the electron from measurement. This experiment does not need the knowledge of QM.

Another experiment measuring a particle's momentum is to let a photon collide with the particle. Before the collision, the photon's frequency ν is precisely known and the momentum of the particle is p. Let us suppose that before and after the collision, the photon and the particle move along a line, set as y axis. After the collision, the measured momentum and frequency are p' and ν', respectively. The precision $\Delta p'$ of the p' relies on the $\Delta\nu'$ of ν':

$$\Delta p' \approx mc\frac{\Delta\nu'}{\nu' + \nu}. \tag{2.30}$$

Assuming that the uncertainty at the time of the collision is Δt,

$$\Delta\nu'\Delta t \geq 1. \tag{2.31}$$

Within the time, the particle can go a distance of

$$\Delta y = \frac{|p - p'|}{m}\Delta t. \tag{2.32}$$

Substitution of (2.31) into (2.32) leads to the uncertainty of the position of the particle.

$$\Delta y \geq \frac{|p - p'|}{m\Delta\nu'} = \frac{2\pi\hbar}{mc}\frac{\nu + \nu'}{\Delta\nu'}. \tag{2.33}$$

It seems that $\Delta y\Delta p' \geq \hbar$, meeting the uncertainty relation.

This explanation is problematic. The relation 2.31 has neither rigorous mathematical derivation nor experimental verification. Eq. 2.32 assumes that within the time uncertainty Δt, the particle goes with the velocity of about p/m. Unfortunately, Δt is a part of the time period within which the collision occurs. In this period, the particle's momentum changes drastically, such that the particle's velocity cannot be estimated in the way of 2.32. This experiment does not involve the particle's wave function in QM, i.e., the particle is treated as a classical one.

The common features of these two examples are as follows: the measurement of a particle's position is out of question; the measured particles are actually treated as classical ones. Though the momentum is measured, the estimated Δp based on the measurements has nothing to do with Eq. 2.14. In conclusion, these two experiments do not embody the uncertainty relation.

3 Time–energy uncertainty relation

3.1 There is no way to derive the time–energy uncertainty relation

In Ref. [4], having discussed the possible uncertainty relation between the position and momentum, Heisenberg noticed that the product of the coordinate and momentum was of the dimension of angular momentum, and the result was proportional to the Planck constant. He associated the commutator of time and energy, and thus postulated the following commutator:

$$[t, E] = \mathrm{i}\hbar. \tag{3.1}$$

Then, imitating the discussion of position and momentum, he thought that the uncertainties of time and energy obeyed, similarly to (2.2), the relation

$$tE \sim \hbar. \tag{3.2}$$

Later, people accepted his postulation. Furthermore, imitating $\Delta x\Delta p \geq \hbar/2$, people guessed that there was a similar inequality,

$$\Delta t\Delta E \geq \hbar/2. \tag{3.3}$$

Since Δt and ΔE in 3.3 are uncertainties, they should be quantities related to measurement.

Eq. 3.3 is the so-called time–energy uncertainty, but it is even worse than the coordinate–momentum uncertainty relation.

Heisenberg put forth Eq. 3.1 without any derivation and proof. He did not even present the concrete form of the operator E. Hilgevoord [32] thought that "a relation like" (3.1) "does not occur in quantum mechanics". His reason was that "there is no Poisson bracket defined between t and H. Consequently, in quantum mechanics, one does not have a relation like" Eq. 3.3. "Accordingly, there is no natural analog for energy and time of the 'canonical' uncertainty relations" Eq. 2.9.

At the time when QM was established, Heisenberg himself did not know explicitly what the relation between time and energy was. The mathematical theory of QM had not been accomplished yet. In Heisenberg's paper [4], there was neither rigorous derivation nor an association with real experiments.

Thus, Heisenberg did not give a convincing conclusion, but people deemed that what he said was right. Later, many people tried to show that there was indeed the inequality (3.3). Everyone raised his own version, without rigorous derivation and experimental correspondence.

Until 1961, “there has been an erroneous interpretation of uncertainty relations of energy and time.” [31] Until 1990, “no general agreement has been reached. One finds physicists claiming that ‘there is no energy–time uncertainty relation at all,’ while others stress, for instance, that the relation is applied quite effectively to the analysis of individual short-lived elementary particles (resonances). Even among those who accept the validity of the relation, there is appreciable disagreement as to meanings of the relation.” [43] Until 1996, “It is generally thought desirable that quantum theory entail an uncertainty relation for time and energy similar to the one for position and momentum. Nevertheless, the existence of such a relation has still remained problematic” [32].

As a matter of fact, up to now, there has been no final verdict with respect to the time–energy uncertainty relation.

It should also be noted that Heisenberg discussed the measurement of individual particles, which can be inferred from his examples about the uncertainty relation (2.9). Subsequently, the discussion of time–energy uncertainty should be for individual particles. However, later, people often discuss many-particle systems.

Now we start to carefully analyze the so-called time–energy uncertainty relation.

First, let the two operators in Eq. (B1) be time and energy, respectively, $F = t$ and $G = H$. Nevertheless, the commutator

$$[t, H] \tag{3.4}$$

does not have a definite result. When the Hamiltonian H is independent of time, the result is zero.

$$[t, H] = 0, \text{when } H \text{ is independent of time.} \tag{3.5}$$

The key is that the coordinate and momentum operators on the left-hand side of (2.1) have explicit forms, no matter what function they act on. By contrast, the form of Hamiltonian H depends on the system under investigation. Hilgevoord noticed that “for a system of particles, one should not demand a communication relation between t and H as a complement to the ones between q and p, nor could there be such a commutation relation.” [32].

Time t is not an operator. According to Pauli, “the introduction of an operator t is basically forbidden, and the time t must necessarily be considered as an ordinary number (‘c-number’).” [12] The average of t in any normalized state is still the time itself, $\bar{t} = (\psi, t\psi) = t(\psi, \psi) = t$, which makes the average meaningless.

Therefore, there is no way to derive a time–energy uncertainty relation starting from (3.4) in the way in Supplementary Appendix SB.

People may think that although the Hamiltonian H in (3.4) depends on systems, the operator $\mathrm{i}\hbar\frac{\partial}{\partial t}$ on the left-hand side of (1.1) corresponds to Hamiltonian and is independent of systems. There is a definite commutator

$$\left[t, \mathrm{i}\hbar\frac{\partial}{\partial t}\right] = \mathrm{i}\hbar. \tag{3.6}$$

It seems, then, that imitating the procedure of deriving (2.9) can lead to (3.3). It is not so. Obviously, the averages of time t and its square t^2 in any normalized function are still t and t^2, so that $\Delta t = 0$. It is easily verified that $(\psi, \mathrm{i}\hbar\frac{\partial}{\partial t}\psi)^2 = (\psi, (\mathrm{i}\hbar\frac{\partial}{\partial t})^2\psi)$. Therefore, along this routine, one is unable to reach Eq. 3.3.

The conclusion is that there is no way to acquire (3.3) through the procedure in Supplementary Appendix SB. In [44], Eq. 3.3 was just a hypothesis.

3.2 The operator of taking a derivative with respect to time

Here we intend to clarify the implication of the operator $\mathrm{i}\hbar\frac{\partial}{\partial t}$. Someone thought it to be an energy operator and denoted it by [22]

$$\hat{E} = \mathrm{i}\hbar\frac{\partial}{\partial t}. \tag{3.7}$$

Following this definition, (3.1) could be understood as (3.5), but this problematic.

When we put down $\frac{\partial}{\partial t}$, it is just an operator taking a derivative with respect to time, without any other physical information. When we put down $\mathrm{i}\hbar\frac{\partial}{\partial t}$, we just let the dimension of the operator become that of energy and make it a Hermitian one, and no physical information is added yet.

An operator should have its eigenvalues and corresponding eigenfunctions under appropriate boundary conditions, such as a momentum operator. The operator $\mathrm{i}\hbar\frac{\partial}{\partial t}$ is not of this property. In [19], an attempt was made to define a time operator, but no eigenvalue and eigenfunction could be given. One may define an operator in some way, but it is meaningless if the operator does not have eigenvalues and eigenfunctions.

Then, why do people think of $\mathrm{i}\hbar\frac{\partial}{\partial t}$ as an energy operator? The reason is based on the fundamental QM equation. In Eq. 1.1, $\mathrm{i}\hbar\frac{\partial}{\partial t}$ is directly connected to Hamiltonian H. When, and only when, in this equation, the operator $\mathrm{i}\hbar\frac{\partial}{\partial t}$ represents the Hamiltonian on the right-hand side of this equation.

It is stressed that $\mathrm{i}\hbar\frac{\partial}{\partial t}$ should not be regarded as a Hamiltonian operator or energy operator carelessly except in the case of (1.1). The following two points are important: (i) according to Eq. (1.1), the operator $\mathrm{i}\hbar\frac{\partial}{\partial t}$ must be related to a specific Hamiltonian of the system under investigation; (ii) only when the operator $\mathrm{i}\hbar\frac{\partial}{\partial t}$ acts on the wave function ψ satisfying (1.1), can it show the meaning of energy, because this action is just that of this specific Hamiltonian on this wave function ψ.

When these two points are met, the result calculated through

$$\left(\psi, \mathrm{i}\hbar\frac{\partial}{\partial t}\psi\right) = (\psi, H\psi) = \bar{E} \tag{3.8}$$

is of the meaning of the energy average in this state.

For any function of φ not satisfying (1.1), $(\varphi, i\hbar \frac{\partial}{\partial t}\varphi)$ is not of the meaning of energy.

Since the implication of the operator $i\hbar \frac{\partial}{\partial t}$ is clarified, we are able to figure out the Pauli difficulty, which is as follows [12, 19].

Let Hamiltonian H be independent of time and its eigenfunction be denoted as ψ_E.

$$H\psi_E = E\psi_E. \tag{3.9}$$

We construct a wave function $e^{-i\alpha t/\hbar}\psi_E$, where α can be any real number. Let the Hamiltonian act on this function $He^{-i\alpha t/\hbar}\psi_E$, and make the Taylor expansion of the factor $e^{-i\alpha t/\hbar}$. It follows that

$$He^{-i\alpha t/\hbar}\psi_E = (E-\alpha)e^{-i\alpha t/\hbar}\psi_E. \tag{3.10}$$

This result shows that for any α, $E-\alpha$ is an eigenvalue of the H. That is to say, the eigenvalues of the H compose a continuous spectrum covering the whole real axis. However, the energy spectrum of the Schrödinger equation (1.1) must have a lower limit. This contradiction is the Pauli difficulty.

We explain how this difficulty is yielded. When taking the Taylor expansion of the factor $e^{-i\alpha t/\hbar}$ on the left-hand side of (3.10), the commutator $[t, H] = i\hbar$ is employed [19], which results on the right-hand side of (3.10). The reason of the Pauli difficulty is the employment of the relation $[t, H] = i\hbar$. We have pointed out above that there is no such relation. Eq. 3.8 is one for stationary states, i.e., H is independent of time. So, Eq. 3.5 has to be employed. Starting from the left-hand side of (3.10), one obtains

$$He^{-i\alpha t/\hbar}\psi_E = Ee^{-i\alpha t/\hbar}\psi_E, \tag{3.11}$$

instead of the right-hand side of (3.10). If

$$\psi = e^{-i\alpha t/\hbar}\psi_E \tag{3.12}$$

is still an eigenfunction of the H, it must meet (1.1).

$$i\hbar\frac{\partial}{\partial t}e^{-i\alpha t/\hbar}\psi_E = He^{-i\alpha t/\hbar}\psi_E. \tag{3.13}$$

Since ψ_E is independent of time,

$$i\hbar\frac{\partial}{\partial t}e^{-i\alpha t/\hbar}\psi_E = \alpha e^{-i\alpha t/\hbar}\psi_E. \tag{3.14}$$

The right-hand side of (3.11) and (3.14) should be equal. It is seen that $\alpha = E$; i.e., α must be an eigenvalue of the H, not an arbitrary number.

3.3 The derivations and explanations of the so-called time– energy uncertainty relation in the literature

In [4], the relation (3.3) between the uncertainties of time and energy was guessed without derivation, and the discussion was vague. People believed that what Heisenberg said was right. Some first assumed (3.3), resembling (3.3), and then, tried to derive it by supposing various scenarios. Different persons present the derivation based on their own understanding of the uncertainties of time and energy. Among different derivations, none of them could overturn the others. Therefore, according to viewpoint I.2, none was correct. In fact, every derivation was apparently right but actually wrong. Although it was noticed [31, 32] that some of the derivations were wrong, a thorough analysis is desired.

In the following, we list several derivations and present our comments. In each case, we extract the concepts of Δt and ΔE, demonstrating that the concepts differ from person to person. The common features are that almost every proof has concept stealing and that no one made the measurements that could match the formulas.

Before the introduction, we emphasize that in inequality (B14),

$$\Delta A\Delta E \geq \frac{1}{2}|\langle[H, A]\rangle|, \tag{3.15}$$

and ΔA is defined by

$$\Delta A = \sqrt{\overline{A^2} - \bar{A}^2} = \left[(\psi, A^2\psi) - (\psi, A\psi)^2\right]^{1/2}. \tag{3.16}$$

It is a definite quantity determined by the known wave function but not a variable. One more point should be stressed that ΔA is finite, meaning that it is neither infinitely small nor infinitely large.

1) Using the concept of wave packet [14, 15, 19]:

This is for a single particle. Suppose that the particle is a wave packet with width Δx, moving along the x axis with speed v. The time it passes one point in the x axis is not definitely determined, but has an uncertainty

$$\Delta t \approx \frac{\Delta x}{v}. \tag{3.17}$$

On the other hand, the wave packet has some extension in momentum space, so that the particle's energy has an uncertainty ΔE.

$$\Delta E \approx \frac{\partial E}{\partial p}\Delta p = v\Delta p. \tag{3.18}$$

The product of these two equations yields

$$\Delta t \cdot \Delta E \approx \Delta x \cdot \Delta p. \tag{3.19}$$

Then Eq. 2.9 is used to result in (3.3), "which limits the product of the spread ΔE of the energy spectrum of the wave packet and the accuracy Δt of the prediction of the time of passage at a given point" [19].

Comment:

Since the right-hand side of (3.19) is just (2.9), the Δx and Δp ought to be evaluated in the way of (3.16). However, the Δx from (3.17) is the dimension of the wave packet and the Δp from (3.18) is the increment of the momentum, both not being the meanings of uncertainties. The concept stealing is obvious.

The use of (3.19) means that Eqs. (2.9) and (3.3) ought to be compatible. However, the two relations were thought to express two different and incompatible viewpoints in [19].

Here, Δt is the time a wave packet needs to pass through a distance. The ΔE is the increment of energy irrespective to measurement.

2) Making use of the formulas in Supplementary Appendix SB [3, 14, 19, 21, 23]:

When a quantity A varies, the time it needs to change ΔA is

$$\Delta t = \frac{\Delta A}{|\mathrm{d}\langle A\rangle/\mathrm{d}t|}. \tag{3.20}$$

We make use of the formula

$$\frac{\mathrm{d}\langle A\rangle}{\mathrm{d}t} = \frac{1}{\hbar}|\langle [H, A]\rangle|. \tag{3.21}$$

Then, by (3.15)

$$\Delta A\Delta E \geq \frac{1}{2}|\langle [H, A]\rangle| = \frac{\hbar}{2}\frac{\mathrm{d}\langle A\rangle}{\mathrm{d}t}. \tag{3.22}$$

The combination of these three equations results in

$$\Delta t\Delta E \geq \frac{\hbar}{2}. \tag{3.23}$$

Comment:

We point out that Eq. 3.20 is strange. In the denominate and following equations, A is regarded as an operator, and the numerator should be written as $\Delta\langle A\rangle$. It is not clear from which fundamental formula (3.20) was derived.

In Eq. 3.20, the Δt is variable and is the time increment when A has an increment ΔA. In (3.22), both the ΔA and ΔE should be calculated by (3.16), and are not variable. The ΔA in (3.20) is different form that in (3.22). The concept confusion happens from (3.20) to (3.22). Furthermore, both the Δt and ΔE do not have the meanings of uncertainty.

The authors of [45] recast (3.22) to be the form $\Delta t\Delta E \geq \frac{\hbar}{2}\frac{\mathrm{d}\langle A\rangle}{\mathrm{d}A}$ by replacement of the ΔA by $\mathrm{d}A$ and of the $\mathrm{d}t$ by Δt, which seemed to be a smart way to obtain (3.23), but this was wrong. The $\mathrm{d}A$ was a variable and could be taken as infinitesimal, but the ΔA on the left-hand side of (3.22) is calculated by (3.16), so it is finite and not a variable. This distinction stands also for the $\mathrm{d}t$ and Δt. Therefore, the replacements were illegal. The authors of [45] addressed that the quantity A in (3.20) could be arbitrary: "its physical meaning depending thus on the choice of this quantity." However, the A could not be t.

Here, the Δt is a time increment when a quantity A changes ΔA, and the ΔE is calculated by (3.16), both being irrespective to measurement.

3) Making use of the difference of two energy levels [3, 14]:

Suppose that a particle had two energy levels, E_1 and E_2. Their difference is

$$\Delta E = |E_1 - E_2|. \tag{3.24}$$

When the two states superpose, the particle oscillates between the two states and the oscillation period is

$$\tau = \frac{\hbar}{\Delta E}. \tag{3.25}$$

Then, ΔE is explained as the uncertainty of the energy level, and τ is explained as the time one needs to observe the system's variation. Eq. 3.25 is recast to be

$$\tau\Delta E \approx \hbar, \tag{3.26}$$

which is explained as the time–energy uncertainty relation.

Comment:

Here, the τ is the oscillation period between two energies of the system, and the ΔE is the difference of the two energies, both being not of the meaning of uncertainty.

Eq. 3.26 is simply the copy of (3.25), but the concepts are endowed different connotations, i.e., concept stealing. In Eq. 3.26, the ΔE and τ are respectively said to be the uncertainties of energy and time, which are created out of nothing.

4) Using the concept of "time packet" [6]:

It was assumed that a particle's behavior was a pulse or 'time packet'.

"We consider the case such that $\psi(t)$ is a pulse or 'time packet', which is negligible except in a time interval Δt." This time packet can be expressed as a superposition of monochromatic waves of angular frequency ω by the Fourier integral

$$\psi(t) = \int_{-\infty}^{\infty} \mathrm{d}\omega G(\omega)\mathrm{e}^{-\mathrm{i}\omega t}, \tag{3.27}$$

where the function $G(\omega)$ is given by

$$G(\omega) = \frac{1}{\sqrt{2\pi}}\int_{-\infty}^{\infty} \mathrm{d}t\psi(t)\mathrm{e}^{\mathrm{i}\omega t}. \tag{3.28}$$

As the $\psi(t)$ takes only significant values for a duration Δt, it follows from the general properties of Fourier transformations that $G(\omega)$ is only significant for a range of angular frequencies such that

$$\Delta\omega\Delta t \geq 1. \tag{3.29}$$

Since

$$E = \hbar\omega, \tag{3.30}$$

the width of the distribution in energy, ΔE, satisfies the time–energy uncertainty relation

$$\Delta E \Delta t \geq \hbar.\text{"}[6]. \tag{3.31}$$

In this way, it seems that the uncertainty relation can be proved.

Comment:

Here, the Δt is the time the particle exists—from its appearance to its vanishing, and the ΔE is the width of the distribution of the particle's energy. Both the concepts are strange, because we cannot image what the system is and how its Hamiltonian is written.

It is well known that a light pulse can be produced experimentally. But what about a massive particle? This imagined pulse or 'time packet' of a massive particle is not possible. No one is able to find a Hamiltonian H such that the solution $\psi(t)$ of Eq. 1.1 is a 'time packet'. If someone knew such a Hamiltonian, he would have put it down.

5) Making use of the interaction between the measured system and measuring device [10, 24, 46]:

The measured system and measuring device are combined to become a larger system. In other words, the whole system is divided into two parts, measured system and measuring devices, the energies of which are E and ε, respectively. "We suppose that it is known that at some instant these parts have definite values of the energy, which we denote by E and ε, respectively." "The energies E, ε, on the other hand, can be measured to any degree of accuracy at any instant" [10].

Because of the interaction between the two parts, each time the measurement would cause the energy E to change, say, to be E'. It was treated as the transition between the energies E and E'. The transition probability for a system subject to a periodic perturbation was given by the formula (43.2) in [10]. By taking $\omega = 0$ in this formula, the transition probability was

$$\frac{\sin^2\left[\left(E' - E\right)t/2\hbar\right]}{\left(E' - E\right)^2}. \tag{3.32}$$

According to this formula, "The most probable value of $E' - E$ is of the order of the magnitude of $\hbar/t$." [10]. Subsequently, it was believed that

$$\left|E + \varepsilon - E' - \varepsilon'\right|\Delta t \sim \hbar. \tag{3.33}$$

This was called the "uncertainty relation for energy."

Comment:

According to this result, the energy conservation in QM was understood in an alternative way. "It shows that, in quantum mechanics, the law of conservation of energy can be verified by the means of two measurements only to an accuracy of the order of $\hbar/\Delta t$, where Δt is the time interval between the measurements." "The quantity $(E + \varepsilon) - (E' + \varepsilon')$ in (44.1) is the difference between two exactly measured values of the energy $E + \varepsilon$ at two different instants, and not the uncertainty in the value of the energy at a given instant" [10]. However, "the statement that the conservation law of energy may be violated by an amount δE during a time $\delta t \cong \hbar/\delta E\ldots\ldots$ confuses the energy of the actual system with the energy of the unperturbed system" [32].

It was believed that the relation $\Delta t \Delta E > \hbar$ "does not signify that the energy cannot be known exactly at a given time (for in that case the concept of energy would have no meaning), nor does it means that the energy cannot be measured with arbitrary accuracy within a short time" [10].

This scenario is totally different from the above ones. Here the energy of a system can be measured in any accuracy, which contradicts the uncertainty of energy.

According to [10, 46], because the measured system is interacted by the measuring device, its energy shifts after the measurement. The amount of the shift and the time interval between adjacent measurements form the time–energy uncertainty relation: "the smaller the time interval Δt, the greater the energy change that is observed" [10]. This brings a question that why the shorter the time interval, the greater the energy shift.

In the transition probability formula, the difference of two energy levels is used, which is not the energy uncertainty. Furthermore, in [10], Eq. (42.3) was valid under a condition of (42.1) which required that the frequency ω should not be zero. It is hard to understand the transition expressed by (3.32) without releasing or absorbing photons.

Equations (3.32) and (3.33) contradict each other. Eq. 3.32 means that there were two energy levels E and E' in the system. The existence of the two energy levels was determined by the Hamiltonian of the system, independent of whether the transition happened or not. What is more, it was thought that $\Delta(E - E') > \hbar/\Delta t$ [46], which meant both E and E' had some uncertainties. However, Eq. 3.33 reflected that there was only one energy level E, which, after the measurement, shifted to E'. That is to say, before the measurement, there was no energy level E', and after the measurement, there was no energy level E.

Here, the Δt is the lifetime of an energy level. The ΔE is the energy shift caused by the measurement, and meanwhile, it is the difference of two energy levels.

This scenario was criticized in [31].

In [10, 46], following the above content, momentum variation was discussed by collision as an example. Nevertheless, Eq. 3.32 was obtained by perturbation theory, while collision could not be treated by the perturbation theory.

The last part of Section 44 in [10] related the difference $E - E'$ to the lifetime of energy level. This recognition, also seen in other textbooks [6, 7], is going to be expounded in next subsection.

All in all, it is seen from the entries 1) – 5) that people presumed the relation (3.3) and then designed certain ideas to scrape it together. None of the above scenarios were connected to a real measurement. All of them are incorrect.

Different people had different explanations of the Δt and ΔE in (3.3). In one textbook, more than one explanation arose [3, 10, 14, 18]. This fully revealed the serious confusion regarding these concepts. Some other narrations are as follows.

In [13], the relation (3.3) was given without derivation. The explanation was that "an energy determination that has an accuracy ΔE must occupy at least a time interval $\Delta t \sim \hbar/\Delta E$; thus if a system maintains a particular state of motion not longer than a time Δt, the energy of the system in that state is uncertain by at least the amount $\Delta E \sim \hbar/\Delta t$, since Δt is the longest time interval available for the energy determination." Here the Δt had the implication of the lifetime of the state of the system.

In [14], the ΔE was regarded as the uncertainty of the measured energy or the change of the energy of the system, but meanwhile, the ΔE is the difference of two energy levels, which could be both measured precisely.

In [19], there were contradictory statements. One was that "the energy of a system can be determined with arbitrary precision at any time." The other was that Eq. 3.3, written as $\tau\Delta E \sim \hbar$, "is the lifetime–width relation for unstable systems, i.e., systems which are not stationary and do not correspond to a well-defined value of the energy but rather to an energy spectrum with a certain spread ΔE, called the *level width*. The mean lifetime τ of the stable (or metastable) state here plays the role of the characteristic time considered above". "In this case, the accuracy ΔE of the energy measurement is connected with the time Δt required for the measurement itself."

In [24], the Δt and ΔE were replaced by δt and δE, respectively. "The time–energy uncertainty relation relates the rate at which the state of a system changes to the uncertainty δE of its energy. If the state of the system changes appreciably during a time interval δt, then the time–energy uncertainty relation states that $\delta t \delta E \geq \hbar$. I have written δt and δE, rather than Δt and ΔE, to emphasize that these are not standard deviations." Here, the time interval δt was regarded as the lifetime of the system.

3.4 The concept of the lifetime of an energy level

One explanation of the Δt in (3.3) was the lifetime of an energy level [16, 31, 32], and correspondingly, one of explanations of the ΔE was the width of the energy level [14, 19, 31, 32]. It is necessary to clarify the concept of the lifetime of an energy level [47, 48].

In Eq. 3.3, the ΔE, as mentioned in Section 3.3, at least has three explanations: the energy shift, energy width, and difference of two energy levels. All the explanations concern the real part of the energy. Unfortunately, the lifetime of a state is irrelative to the real part of the energy of the state. Let us recall the definition of the lifetime of a state.

In a wave function, there is a factor containing energy E and time t, $\mathrm{e}^{-\mathrm{i}Et}$. If the energy is a complex number,

$$E = \varepsilon - \mathrm{i}\gamma, \tag{3.34}$$

then

$$\mathrm{e}^{-\mathrm{i}Et/\hbar} = \mathrm{e}^{-\mathrm{i}\varepsilon t/\hbar}\mathrm{e}^{-\gamma t/\hbar}. \tag{3.35}$$

The wave function decays with time exponentially. After a time period of about

$$\tau \sim \hbar/\gamma, \tag{3.36}$$

the wave function almost disappears. Due to this fact, we say that the lifetime of this state is about $\hbar/\gamma$.

Here, we emphasize the following points: (1) The lifetime τ of a state is determined by the imaginary part, not the real part, of the state's energy. (2) The lifetime is defined by (3.36). It is not the case that we have first the two quantities ΔE and τ, which then meet Eq. 3.3. (3) The lifetime of the state is determined by the state itself, irrespective of the measurement process. (4) The lifetime reflects the decay of the state wave function, but is not related to the shift of the energy. From the lifetime, one is unable to gain the information of energy shift. (5) The lifetime does not involve energy level broadening, which is a property of the real part of the energy. From the lifetime, one is unable to gain the information of the energy level broadening. (6) The energy (3.34) has an imaginary part. This fact shows that this is a many-particle system.

In a many-particle system, there are interactions between particles, such as electron–phonon interaction, collision, and so on. Due to the interactions, elementary excitations are formed, and they are of finite lifetimes. An elementary excitation's lifetime is determined by the imaginary part of its energy [47, 48].

A detailed analysis was given in [25]. The interactions inside a system result in transitions between energy levels. The transitions in turn cause an energy shift and broadening. Now we introduce the analysis.

Suppose that in a system there are two states denoted by a and b, respectively. When there is no interaction, both are stationary states, and their energies are E_a and E_b, respectively. When there are interactions, the transition between them can occur. Suppose that a and b are, respectively, the initial and final states of the transition. In the course of the transition, the initial state a will vary. The state after the change is denoted by a′ with energy $E_a^{'} - \mathrm{i}\Gamma$, i.e., energy changes,

$$E_a \to E_a^{'} - \mathrm{i}\Gamma. \tag{3.37}$$

The change yields not only a shift of the energy but also an imaginary part of the energy, the latter being determined by transition probability. This imaginary part determines the lifetime of the state a$'$. This is because the amplitude of the state a$'$ contains a factor

$$\mathrm{e}^{-\mathrm{i}\left(E_a'-\mathrm{i}\Gamma\right)t\big/\hbar} = \mathrm{e}^{-\mathrm{i}E_a't\big/\hbar}\mathrm{e}^{-\Gamma t/\hbar}. \tag{3.38}$$

It is seen that in about time Δt_a, where

$$\Gamma\Delta t_a \sim \hbar, \tag{3.39}$$

the state a$'$ will almost vanish. Therefore, $\Delta t_a \sim \hbar/\Gamma$ is the lifetime of the state a$'$.

Meanwhile, the energy of the final state b has a broadening with a Lorentz line shape, the half height width of which happens to be Γ, too. We denote this half height width by ΔE_b.

$$\Delta E_b = \Gamma. \tag{3.40}$$

Then,

$$\Delta E_b\Delta t_a \sim \hbar. \tag{3.41}$$

Equations (3.39) and (3.41) seem to be the form of the time–energy uncertainty relation, but they are not. The former is the definition of the Δt_a, the lifetime of state a$'$. The latter relates the lifetime of state a$'$ and the half height width of the energy of state b. Among these quantities, none has the physical meaning of uncertainty, and none is to be determined by measurement.

4 Discussion

People subjectively thought that what Heisenberg said in his paper [4] were certainly right, and the inequality that Robertson derived [5] was just what Heisenberg wanted to express. Under these presumptions, people tried their best to present explanations to the coordinate–momentum uncertainty relation, and to derive the so-called time–energy uncertainty relation. There is no uniform and standard explanation. Several scenarios were proposed. From the source, the discussions in Heisenberg's primary paper [4] were ambiguous. The explanations and derivations are of the following defects.

One mathematical symbol has different explanations, that is, concept stealing. In the coordinate–momentum uncertainty relation, the Δx should be the uncertainty of measuring a particle's position, but is often replaced by the dimension of that particle, the range that the particle's wave function is not zero; the Δp should be the uncertainty of measuring a particle's momentum, but is often replaced by the width of the momentum range of the Fourier component of a wave packet. In the so-called time–energy uncertainty relation, the Δt is explained as either the time that a wave packet goes through a space point, or the time needed for measuring an energy level, or the lifetime of an energy level; the ΔE is explained as energy shift, or the difference of two energies, or energy width.

A truncated plane wave with finite length for a moving particle is not the wave functions in QM.

All the derivations of the so-called time–energy uncertainty relation are not rigorous, but simply patchwork. The last words in [31], "energy can be measured reproducibly in an arbitrarily short time", utterly negated the so-called time–energy uncertainty relation.

No real measurement was touched. Gedanken experiments were assumed, which could not verify the uncertainty relations. The application of the coordinate–momentum uncertainty relation was just to make some ex-post explanations to well-known phenomena such as single-slit diffraction. Even in these explanations there were confusions of the concepts.

In discussion of the time–energy uncertainty relation, the problems in one-particle and many-particle systems were confused.

There is more than one explanation for an uncertainty relation. This fact itself illustrates that none of the explanations is right. If one explanation was right, the other would be no longer displayed.

We have mentioned in Introduction the reasons that people do not realize the problem of the uncertainty relations. The uncertainty relations have never been related to real measurements, and solving problems and establishing new theories in QM do not resort to the uncertainty relations.

Up to now, the quantum measurement problem, that what precisely happens when a quantum measurement is performed, is still in dispute [49, 50], but the so-called uncertainty principle for quantum measurement was proposed long before. That is strange!

5 Conclusion

Heisenberg's primary paper did not explicitly present an uncertainty relation.

Robertson derived the coordinate–momentum uncertainty relation $\Delta x\Delta p \geq \hbar/2$. In this relation, Δx and Δp are uniquely determined by the wave function, and are not variable. In this relation, there is no quantity that needs to be gained by measurement. This relation does not need any knowledge of Heisenberg's primary paper and of measurement. The conclusion is that the coordinate–momentum uncertainty relation is irrespective to measurement.

There is no definite result for the commutation of time and Hamiltonian $[t, H]$. This is because Hamiltonian depends on systems. The operator $\mathrm{i}\hbar\frac{\partial}{\partial t}$ can represent a concrete Hamiltonian H only when the $\mathrm{i}\hbar\frac{\partial}{\partial t}$ and H are connected in one quantum mechanics equation. The discussions of the time–energy uncertainty relation in the literature are incorrect. The conclusion is that there is no so-called time–energy relation.

Data availability statement

The original contributions presented in the study are included in the article/Supplementary Material; further inquiries can be directed to the corresponding author.

Author contributions

H-YW carried out the whole work of this article.

Funding

This work was supported by the National Natural Science Foundation of China (Grant no. 12234013).

Conflict of interest

The author declares that the research was conducted in the absence of any commercial or financial relationships that could be construed as a potential conflict of interest.

Publisher's note

Supplementary material

The Supplementary Material for this article can be found online at: https://www.frontiersin.org/articles/10.3389/fphy.2022.1059968/full#supplementary-material

References

1. Heisenberg W. Quantum-theoretical Re-interpretation of kinetic and mechanical relations. *Z Phys* (1925) 333: 879-893. In: Van Waerden BL, editor. Source of quantum mechanics, New York: Dover Publications Inc. (1968). p. 261–276.

2 Aitchison I. J. R., MacManus D. A., Snyder T. M. Understanding Heisenberg's "magical" paper of july 1925: A new look at the calculational details. *Am J Phys* (2004) 72:1370–9. doi:10.1119/1.1775243

3 Razavy M. *Heisenberg's quantum mechanics*. London, UK: World Scientific Publishing Co. Pte. Ltd. (2011).

4 Heisenberg W. Uber den anschaulichen Inhalt der quantentheoretischen Kinematik und Mechanik. *Zeitschrift fur Physik* (1927) 43: 172-198. "The Physical Content of Quantum Kinetics and Mechanics". In: Wheeler JA, Zurek WH, Editor. Quantum Theory and Measurement. Princeton: Princeton University Press (1983). 62-84.

5 Robertson H. P. The uncertainty principle. *Phys Rev* (1929) 34:163–4. doi:10.1103/PhysRev.34.163

6 Bransden B. H., Joachain C. J. *Quantum mechanics*. 2nd ed. London, UK: Pearson Education Limited (2000).

7 Bes D. R. *Quantum mechanics A modern and concise introductory course*. Berlin, Germany: Spinger-Verlag (2004).

8 Hameka H. F. *Quantum mechanics*. New York, NY, USA: John Wiley & Sons (1981). p. 55–6.

9 Wichmann E. H. *Quantum Physics Berkeley Physics Course*, 4. New York: McGraw-Hill (1971).

10 Landau L. D., Lifshitz F. M. *Quantum Mechanics*, Oxford, UK: Pergamon Press (1977). p. 2, 47, 157.

11 Weinberg S. *Lectures on quantum mechanics*. 2nd ed. Cambridge, UK: Cambridge University Press (2015).

12 Pauli W. *General principles of quantum mechanics*. Berlin, Germany: Springer-Verlag (1980). p. 63.

13 Schiff L. I. *Quantum mechanics*. New York, NY, USA: McGraw-Hill Book Company Inc. (1949).

14 Messiah A. *Quantum mechanics* Vol. I. Amsterdam: North-Holland Pub. Co. (1961).

15 Blinder S. M. *Foundations of quantum mechanics*. London, UK: Academic Press (1974).

16 Band Y. B., Avishai Y. *Quantum Mechanics with Application to Nanotechnology and Information Science*. Amsterdam: Elsivier Ltd (2013). p. 68, 297.

17 Bohm A. *Quantum mechanics: Foundations and applications*. 3rd ed. New York, NY, USA: Springer-Verlag (1993).

18 Zettili N. *Quantum mechanics: Concepts and applications*. New York, NY, USA: John Wiley & Sons (2001). p. 28.

19 Auletta G., Fortunato M., Parisi G. *Quantum Mechanics*. Cambridge, UK: Cambridge University Press (2009). p. 82–89, 130–40.

20 Scheck F. *Quantum physics*. 2nd ed. Berlin, Heidelberg: Springer-Verlag (2013). Chap. 1.

21 Ballentine L. E. *Quantum Mechanics A Modern Development*. 2nd ed., Singapore: World Scientific Publishing Co. Pte. Ltd. (2015). p. 223-227, 271, 345.

22 Liboff R. L. *Introductory quantum mechanics*. San Fransisco: Holden-Day, Inc. (1980).

23 Kroemer H. *Quantum mechanics for engineering, materials science, and applied physics*. Englewood Cliffs, NJ, USA: Prentice-Hall (1994). p. 249–50.

24 Mandl F. *Quantum mechanics*. New York, NY, USA: John Wiley & Sons (1992). p. 82–6.

25 Abers E. S. *Quantum mechanics*. Upper Saddle River, NJ, USA: Pearson Education, Inc. (2004).

26 Beck M. *Quantum mechanics theory and experiment*. New York, NY, USA: Oxford University Press (2012).

27 Manoukian E. B. *Quantum theory A wide spectrum. The netherland*. Dordrecht: Springer (2006).

28 Peres A. *Quantum theory: Concepts and methods*. New York, NY, USA: Kluwer Academic Publishers (2002).

29 Cohen-Tannoudji G., Diu B., Laloë F. *Quantum Mechanics*, 1. New York, NY, USA: John Wiley & Sons (1977). p. 250.

30 Hecht K. T. *Quantum mechanics*. New York, NY, USA: Springer-Verlag (2000). p. 24.

31 Ahronov Y., Bohm D. Time in the quantum theory and the uncertainty relation for time and energy. *Phys Rev* (1961) 122:1649–58. doi:10.1103/PhysRev.122.1649

32 Hilgevoord J. The uncertainty principle for energy and time. *Am J Phys* (1996) 64:1451–6. doi:10.1119/1.18410

33 Schrödinger E. *Ann Phys* (1926). 386 (18): 109–139.; Quantisation as a problem of proper values (Part IV). In: *Collected papers on wave mechanics*. London and Glasgow: Blackie & son Limited (1926). p. 102–123.

34 Wang H. Y. New results by low momentum approximation from relativistic quantum mechanics equations and suggestion of experiments. *J Phys Commun* (2020) 4:125004. doi:10.1088/2399-6528/abd00b

35 Wang H. Y. The modified fundamental equations of quantum mechanics. *Phys Essays* (2022) 35(2):152–64. doi:10.4006/0836-1398-35.2.152

36 Wang H. Y. Fundamental formalism of statistical mechanics and thermodynamics of negative kinetic energy systems. *J Phys Commun* (2021) 5:055012. doi:10.1088/2399-6528/abfe71

37 Wang H. Y. Solving Klein's paradox. *J Phys Commun* (2020) 4:125010. doi:10.1088/2399-6528/abd340

38 Wang H. Y. Macromechanics and two-body problems. *J Phys Commun* (2021) 5:055018. doi:10.1088/2399-6528/ac016b

39 Wang H. Y., Virial theorem and its symmetry. *J. North China Inst Sci Technology* (2021) 18(4):1–10. (in Chinese).

40 Wang H. Y. Resolving problems of one-dimensional potential barriers based on Dirac equation. *J North China Inst Sci Technology* (2022) 19(1):97–107. (in Chinese) doi:10.19956/j.cnki.ncist.2022.01.016

41 Wang H. Y. Evaluation of cross section of elastic scattering for non-relativistic and relativistic particles by means of fundamental scattering formulas. *astp* (2022) 16(3):131–63. doi:10.12988/astp.2022.91866

42 Wang H. Y. There is no vacuum zero-point energy in our universe for massive particles within the scope of relativistic quantum mechanics. *Phys Essays* (2022) 35(3):270–5. doi:10.4006/0836-1398-35.3.270

43 Busch P. On the energy-time uncertainty relation, Part I: Dynamical time and time indeterminacy. *Found Phys* (1990) 20(1):1–32. doi:10.1007/BF00732932

44 Busch P. On the energy-time uncertainty relation. Part II: Pragmatic time versus energy indeterminacy. *Found Phys* (1990) 20(1):33–43. doi:10.1007/BF00732933

45 Mandelstam L., Tamm I. The uncertainty relation between energy and time in nonrelativistic quantum mechanics. *J Phys (Ussr)* (1945) 9:249–54.

46 Landau L., Peierls R. Erweiterung des Unbestimmtheisprinzips fur die relativistische Quantentheorie. *Z Phys* (1931) 69: 56; translated into English: Lev Davidovich Landau and Rudolf Peierls, Extension of the uncertainty principle to relativistic quantum theory in Quantum Theory and Measurement. edited by John Archibald Wheeler and Wojciech Hubert Zurek. Princeton: Princeton University Press (1983). 465-472.

47 Mahan G. D. *Many-particle physics*. 2nd ed. New York, NY, USA: Plenum Press (1990).

48 Wang H. Y. *Green's function in condensed matter physics*. Beijing: Alpha Science International ltd. and Science Press (2012).

49 Mermin N. D. There is no quantum measurement problem. *Phys Today* (2022) 76(6):62–3. doi:10.1063/PT.3.5027

50 Carroll S. M. Addressing the quantum measurement problem. *Phys Today* (2022) 75(7):62–3. doi:10.1063/PT.3.5046

frontiers | Frontiers in Physics

TYPE Original Research
PUBLISHED 20 December 2022
DOI 10.3389/fphy.2022.1098551

OPEN ACCESS

EDITED BY
Huan Yang,
Shandong University, China

REVIEWED BY
Hai-Rui Wei,
University of Science and Technology
Beijing, China
Hongbin Yao,
Xinjiang Institute of Engineering, China

*CORRESPONDENCE
Huai-Yu Wang,
✉ wanghuaiyu@mail.tsinghua.edu.cn

SPECIALTY SECTION
This article was submitted to Atomic and Molecular Physics,
a section of the journal
Frontiers in Physics

RECEIVED 15 November 2022
ACCEPTED 02 December 2022
PUBLISHED 20 December 2022

CITATION
Zhai L-J, Hou L-L, Gao Q and Wang H-Y (2022), Kibble–Zurek scaling of the dynamical localization–skin effect phase transition in a non-Hermitian quasi-periodic system under the open boundary condition.
Front. Phys. 10:1098551.
doi: 10.3389/fphy.2022.1098551

Kibble–Zurek scaling of the dynamical localization–skin effect phase transition in a non-Hermitian quasi-periodic system under the open boundary condition

Liang-Jun Zhai[1,2], Li-Li Hou[2], Qi Gao[2] and Huai-Yu Wang[3]*

[1]Department of Physics, Nanjing University, Nanjing, China, [2]The School of Mathematics and Physics, Jiangsu University of Technology, Changzhou, China, [3]Department of Physics, Tsinghua University, Beijing, China

In the present study, the driven dynamics in a non-Hermitian Aubry–André (AA) model under the open boundary condition (OBC) are studied. For this model, non-Hermiticity is introduced by the non-reciprocal hopping, and this model undergoes a localization–skin effect phase transition depending on the strength of the quasi-periodic potential. Although the properties of non-Hermitian systems are very sensitive to the imposed boundary conditions, we find that the scaling behavior can also be described by the same set of the exponents under the periodic boundary condition (PBC). When the initial state is prepared deep in the localized phase and the potential strength is slowly driven through the critical point, we find that the driven dynamics of the localization length ξ and the inverse participation ratio (IPR) could be described by the Kibble–Zurek scaling (KZS). Then, we numerically verify these predictions for different initial states. Finally, the dynamical emergence of the skin effect state is found, and the dynamics can also be described by the Kibble–Zurek scaling with the same set of critical exponents.

KEYWORDS

non-Hermitian quasi-periodic system, Aubry–André model, localization–skin effect phase transition, driven dynamics, Kibble–Zurek scaling, Anderson localization

1 Introduction

In recent years, the Anderson localization transition in quasi-periodic systems has attracted increasing interest [1–4]. The quasi-periodic system lacks a translational invariance but shows a long-range order, leading to some peculiar properties in comparison with the disordered system. For instance, the one-dimensional (1D) quasi-periodic system can show the Anderson localization transition [1]. A typical quasi-periodic example is the Aubry–André (AA) model, which undergoes a localization transition with the change of the potential strength [1, 4–7].

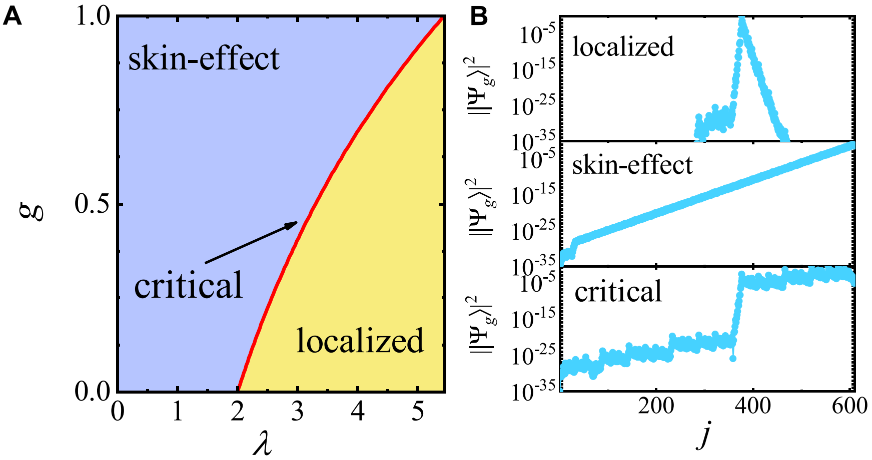

FIGURE 1
(A) Phase diagram of the non-Hermitian AA model under the OBC. **(B)** Typical spatial distributions of $\|\Psi_g\rangle|^2$ in the skin effect phase, localized phase, and critical phase under the OBC. The lattice size is $L = 610$ and $g = 0.5$ in **(B)**.

Many unusual characteristic features have been found in the AA model and generalized AA models [8–10], such as the self-similar energy spectra and non-trivial topological properties [1], the remarkable self-dual metal localization transition at a multifractal critical point [11], and many-body localization by including the interaction [6, 7, and 12–19]. Moreover, non-equilibrium dynamics in AA models have attracted increasing attention [20–25], and exotic properties, therein, have been discovered, e.g., the periodic driving can not only turn the localized eigenstates into extended eigenstates and *vice versa* [20 and 21] but also bring the system into the topological MBL phase [22]. For the driven dynamics in the AA model, it was shown that the driven dynamics from the initial state deep in the localized phase can be well described by the Kibble–Zurek scaling (KZS) [25].

On the other hand, the non-Hermitian systems have attracted enormous studies [26–40]. Due to the release of Hermiticity constraints, the non-Hermitian system exhibits rich phenomena without the Hermitian counterparts, e.g., the topological non-Hermitian skin effect under the open boundary condition (OBC), i.e., the wave functions in large systems under the OBC accumulate on the boundary [27–34], exceptional points [41–44], etc. The interplay of non-Hermiticity and the quasi-periodic system brings a new perspective for the localization phenomena [45–56]. Non-Hermiticity can affect the localization transition behavior, e.g., non-Hermiticity can destroy Anderson localization and lead to delocalization even in the 1D system, and it introduces a new scale and breaks down the one-parameter scaling, which is the central assumption of the conventional scaling theory of localization [57]. Furthermore, it has been demonstrated that non-Hermiticity can change the energy spectra of the disorder or the quasi-periodic system. A significant change of the energy spectra is the emergence of the imaginary parts, and the real-complex phase transition always appears accompanied by the localization transition [46, 48, 50, 53, and 58]. Very recently, the effect of the non-Hermiticity on the driven dynamics in a non-Hermitian AA model under the periodic boundary condition (PBC) has been studied [59]. It was found that the critical exponents for the non-Hermitian AA model under the PBC are different from those of the Hermitian AA model, and the driven dynamics of the localization–delocalization transition for different classes of initial states could be described by the KZS with the same set of critical exponents.

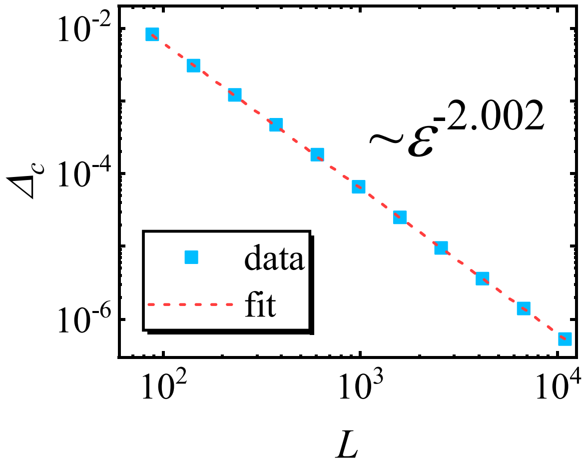

FIGURE 2
Energy gap between the ground and first excited states Δ_c as a function of the lattice size L. The power fit yields $\Delta_c \propto \varepsilon^{-2.002}$. Double-log scales are used. Here, $g = 0.5$, and the results are averaged for 100 choices of ϕ.

Although the driven dynamics of the non-Hermitian AA model under the PBC has been investigated, the driven dynamics of the non-Hermitian AA model under the OBC is still unknown. Since the skin effect, the non-Hermitian AA model undergoes a localization–skin effect transition under the OBC, which corresponds to a transition of the localization center of the wave functions from isolated sites to the boundary. Therefore, the behavior of the localization–skin effect transition under the OBC is different from that of the localization–delocalization transition under the PBC. Moreover, the energy spectrum under the OBC is different from that under the PBC [50]. Considering the effects of non-Hermiticity, it is interesting to investigate the driven dynamics of the non-Hermitian AA model under the OBC.

In the present paper, the static scaling behavior of the driven dynamics of the localization–skin effect transition in the non-Hermitian AA model under the OBC was studied. The non-Hermiticity of this model is induced by the non-reciprocal hopping [50]. Then, the static scaling behavior in the critical region of the localization–skin effect transition was studied, and the critical exponents were determined therein. Starting from the deep localized phase and slowly tuning the potential strength across the critical point, the driven dynamics in this model under the OBC were studied. It was shown that the driven dynamics of the localization–skin effect transition for the initial ground and excited states can be well described by the KZS with the same set of exponents. Finally, the dynamical emergence of the skin effect was observed, and the dynamics can be described by the KZS with the same set of exponents as well.

The rest of the paper is arranged as follows: the non-Hermitian AA model and phase diagram under the OBC are introduced in Section 2. The static scaling properties under the OBC are studied in Section 3, and the critical exponents are determined by the numerical study. Then, in Section 4, the driven dynamics are studied, and the KZS is numerically verified. A summary is given in Section 5.

2 The non-Hermitian AA model and phase diagram under the OBC

The Hamiltonian of the AA model is as follows [50]:

$$H = \sum_{i->j}^{L} \left(J_L c_j^{+} c_{j+1} + J_R c_{j+1}^{+} c_j \right) + \lambda \sum_{j}^{L} \cos\left[2\pi\left(\gamma j + \phi\right)\right] c_j^{\dagger} c_j, \quad (1)$$

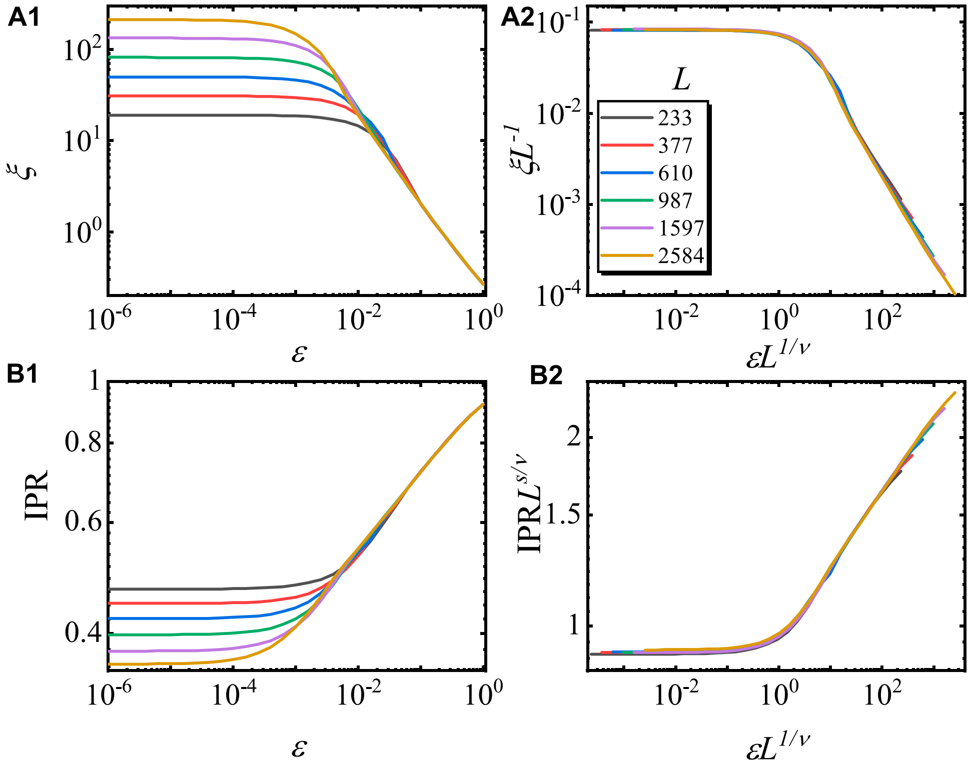

FIGURE 3
Finite scaling of ξ and IPR of the ground state in the localized phase. The curves of ξ versus ε before (A1) and after (A2) rescaling, according to Eq. 5 for different L values. The curves of the IPR versus ε before (B1) and after (B2) rescaling, according to Eq. 8 for different L values. Here, $g = 0.5$, $\varepsilon > 0$, and the model is in the localized phase region. Double-log scales are used, and the results are averaged for 100 choices of ϕ.

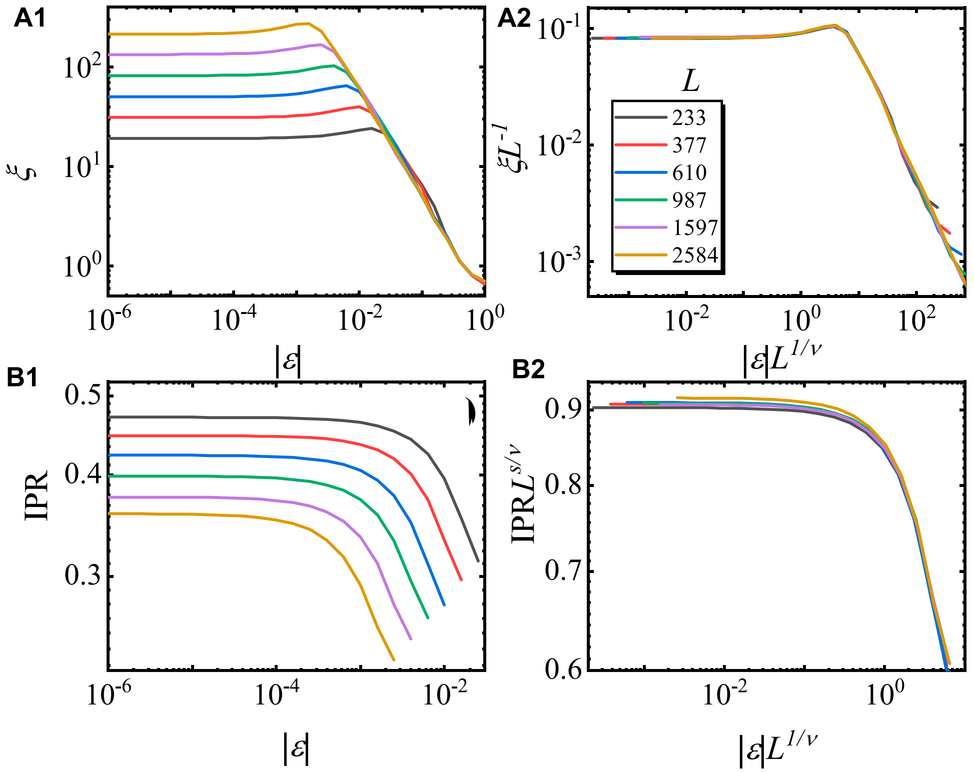

FIGURE 4
Finite scaling of ξ and IPR of the ground state in the skin effect phase. The curves of ξ versus $|\varepsilon|$ before (A1) and after (A2) rescaling, according to Eq. 5 for different L values. The curves of the IPR versus $|\varepsilon|$ before (B1) and after (B2) rescaling, according to Eq. 8 for different L values. Here, $g = 0.5$, $\varepsilon < 0$, and the model is in the skin effect phase region. Double-log scales are used, and the results are averaged for 100 choices of ϕ.

in which $c_j^\dagger$ (c_j) is the creation (annihilation) operator of the hard-core boson, $J_L = Je^{-g}$ and $J_R = Je^g$ are the asymmetry hopping amplitudes between the nearest neighboring (NN) sites, λ measures the amplitude of the quasi-periodic potential, $\gamma = (\sqrt{5} - 1)/2$ is an irrational number, and $\phi \in [0, 1)$ is the phase of the potential. In the following calculation, the OBC is imposed.

In Figure 1A, the phase diagram of the non-Hermitian AA model for $g > 0$ is plotted. It is shown that the model is in the localized phase when $\lambda > 2e^g$, while it is in the skin-effect phase when $\lambda < 2e^g$. At $\lambda = 2e^g$, the eigenstates of the system are all critical. Therefore, by varying λ through the critical point $\lambda_c = 2e^g$, the system undergoes a localization–skin effect phase transition under the OBC.

In different phases, the spatial distributions of the eigenstates show great different behaviors, which is an important characteristic feature in distinguishing these phases. Since the behavior of the spatial distributions of different eigenstates is similar to each other, the ground state is chosen as an example. As shown in Figure 1B, the spatial distribution of the ground states $|\Psi_g\rangle$ in different phases is plotted. In the localized phase, one finds that the wave function is localized on some isolated sites. However, in the skin effect phase, the wave function is localized on the boundary due to the non-Hermitian skin effect. The wave function is localized near the right side, but different from the skin effect, where the wave function is not localized on the boundary. Therefore, the localization–skin effect transition corresponds to a transition of the localization center from some isolated sites to the boundary.

3 Static critical properties in the critical region of localization–skin effect transition

3.1 Static scaling forms in the critical region

In this section, the static properties in the critical region of the localization–skin effect transition are studied, and the critical exponents for the localization–skin effect transition are examined by studying the static behaviors of the energy gap between the first excited state and the ground state Δ_c, localization length ξ, and inverse participation ratio (IPR). We found that the critical exponents for the localization–delocalization transition under the PBC are still applicable in the localization–skin effect transition.

As in the usual quantum criticality, the energy gap between the first excited state and the ground state at the critical point is

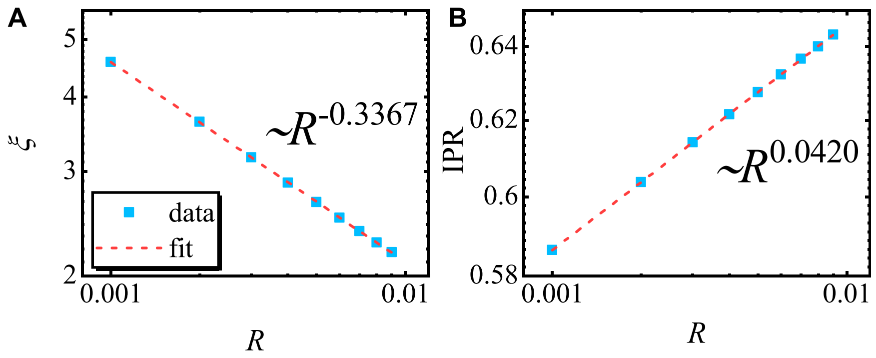

FIGURE 5
(A) ξ and **(B)** IPR at = 0 as a function of R. Here, we use g = 0.5 and L = 987. The results are averaged for 10 choices of ϕ.

usually used to characterize the localization–skin effect transition. According to finite-size scaling, the energy gap Δ_c should scale as follows:

$$\Delta_c \propto L^{-z}. \tag{2}$$

For the Hermitian AA model, z was determined as $z = 2.37$ [25], while $z = 2$ for the non-Hermitian AA model under the PBC [59].

The localization length ξ is defined as follows [25–59]:

$$\xi = \sqrt{\sum_{n>n_c}^{L} [(n-n_c)^2] P_n}, \tag{3}$$

in which P_n is the probability of the wave function at site n, and $n_c \equiv \sum nP_n$ is the localization center. Near a critical point, ξ scales with the distance to the critical point ε as follows:

$$\xi \propto \varepsilon^{-\nu}, \tag{4}$$

in which $\varepsilon = \lambda - \lambda_c$. Taken into account the finite-size scaling, the scaling form of ξ is given as follows:

$$\xi = L f_1 (\varepsilon L^{1/\nu}), \tag{5}$$

where f_1 is the scaling function for the static ξ. For the Hermitian AA model and non-Hermitian AA model under the PBC, ν is determined as $\nu = 1$ [25, 59, and 60].

The IPR is defined as follows [61 and 62]:

$$\mathrm{IPR} = \frac{\sum_{j=1}^{L} \| \Psi(j)\rangle|^4}{\sum_{j=1}^{L} \| \Psi(j)\rangle|^2}, \tag{6}$$

where $|\Psi(j)\rangle$ is the eigenvector. Under the OBC, the IPR shows a local minimum at the critical point, indicating the localization–skin effect transition [50]. Near the critical point, the IPR satisfies a scaling relation, shown as follows:

$$\mathrm{IPR} \propto \varepsilon^{s}. \tag{7}$$

Taken into account the finite-size scaling, the scaling form of the IPR is given as follows:

$$\mathrm{IPR} = L^{-s/\nu} f_2 (\varepsilon L^{1/\nu}), \tag{8}$$

in which f_2 is the scaling function for the static IPR. For the non-Hermitian AA model under the PBC, s is determined as $s = 0.1196$ [54 and 59].

3.2 Numerical results

By applying a finite-size scaling of Δ_c, the dynamical exponent z can be verified. The numerical results for Δ_c as a function of L are plotted in Figure 2. By a power-law fitting, one finds that $\Delta_c \propto L^{-2.002}$ with the exponent very close to $z = 2$, confirming that $z = 2$ is also applicable under the OBC.

In the localized phase, the Eqs 5– 8 are tested, and the ground state is taken as an example. As shown in Figure 3 (A1), we calculate the curves of ξ versus ε for different lattice sizes. After rescaling ξ as ξL^{-1} and ε as $\varepsilon L^{1/\nu}$ with $\nu = 1$, one finds that the rescaled curves match with each other very well, as plotted in Figure 3 (A2). In Figure 3 (B1), the curves of the IPR of the ground state versus ε for different lattice sizes are plotted. After rescaling the IPR as $\mathrm{IPR}L^{s/\nu}$ and ε as $\varepsilon L^{1/\nu}$ with $\nu = 1$ and $s = 0.1196$, the rescaled curves collapse onto each other.

Different from the non-Hermitian AA model under the PBC, ξ and IPR are still well defined under the OBC when $\lambda < 2e^{g}$. Therefore, the scaling functions of Eqs 5–8 are also verified in the skin effect phase. The numerical results are plotted in Figure 4. Figure 4 (A1) and (B1) show the ε dependence of ξ and IPR in the skin effect phase, respectively. After rescaling according to Eqs 5 and 8 with the same ν and s, we find that the rescaled curves collapse onto each other, as shown in Figure 4 (A2) and (B2).

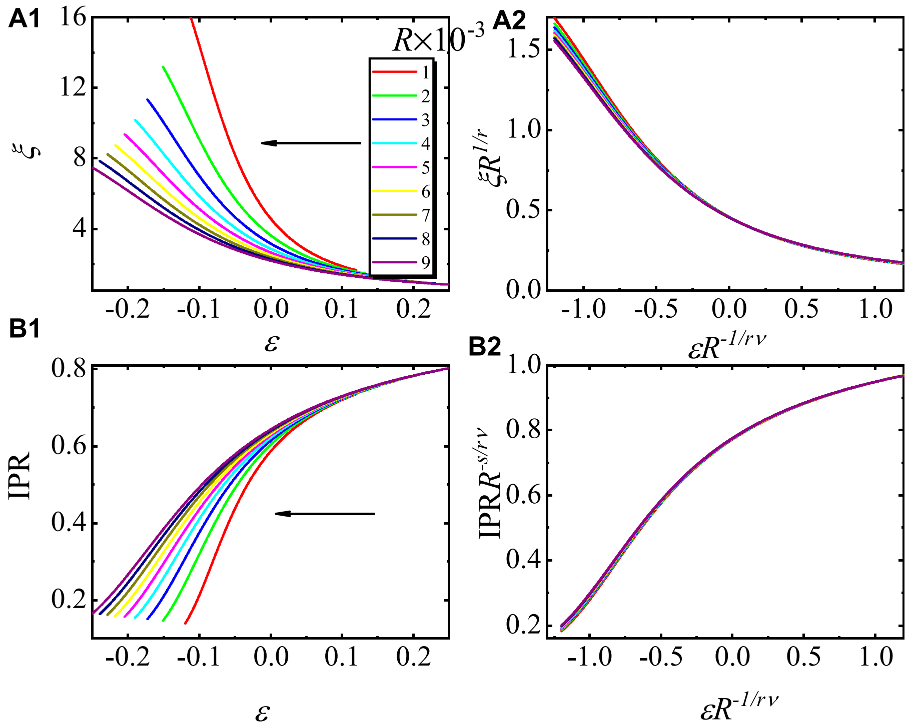

FIGURE 6
Driven dynamics with the initial ground state at $\varepsilon = 1$. (A1) Curves of ξ versus ε and (A2) the rescaled curves according to Eq. 10 for different R values. (B1) Curves of the IPR_n versus ε and (B2) the rescaled curves according to Eq. 11 for different R values. Here, we use $\varepsilon_0 = 1$, $g = 0.5$, and $L = 987$, and the results are averaged for 10 choices of ϕ. The arrows in (a1) and (b1) point to the direction of the changing ε.

These results confirm that the same set critical exponent of the non-Hermitian AA model under the PBC is applicable for the localization–skin effect transition. These exponents, z, ν, and s, are usually enough to determine the critical behavior in the localization–skin effect critical region.

4 Kibble–Zurek scaling in the localization–skin effect transition

4.1 General theory of the KZS

Here, we slowly vary ε across the critical point from an initial state in the localized phase. ε varies as follows:

$$\varepsilon = -Rt, \tag{9}$$

where R is the varying rate. We choose the initial time as $t_0 = -\varepsilon_0/R$. According to the KZS, when $|\varepsilon| > R^{1/\nu r}$ with $r = z{+}1/\nu$, the system can evolve adiabatically as the state has enough time to adjust to the change in the Hamiltonian. When $|\varepsilon| < R^{1/\nu r}$, the system enters the impulse region and ceases to evolve as a result of the critical point slowing down.

Around the critical point, the driven dynamics of ξ satisfy the KZS, which is given as follows:

$$\xi(\varepsilon, R) = R^{-1/r} g_1\left(\varepsilon R^{-1/r\nu}\right), \tag{10}$$

where g_1 is the scaling function for the driven dynamical ξ and $r = z{+}1/\nu$. The driven dynamics of the IPR of the nth eigenstate around the critical point satisfy the following:

$$\mathrm{IPR}(\varepsilon, R) = R^{s/r\nu} g_2\left(\varepsilon R^{-1/r\nu}\right), \tag{11}$$

where g_2 is the scaling function for the driven dynamical IPR.

It should be noted that the scaling functions Eqs 10 and 11 are suitable to describe the driven dynamics of the localization–delocalization phase transition under the PBC since the exponents are the same under the PBC and OBC. The full scaling form for a quantity, e.g., Eqs 10 and 11 for ξ and IPR, has also been proposed from different perspectives in classical and quantum phase transitions [25, 63–69]. In the recent study, such scaling forms have been generalized to study the non-equilibrium dynamics in the non-Hermitian systems under the PBC [42, 59, and 70]. In this work, we perform this full scaling form in the dynamical localization–skin effect transition in the non-Hermitian AA model under the OBC.

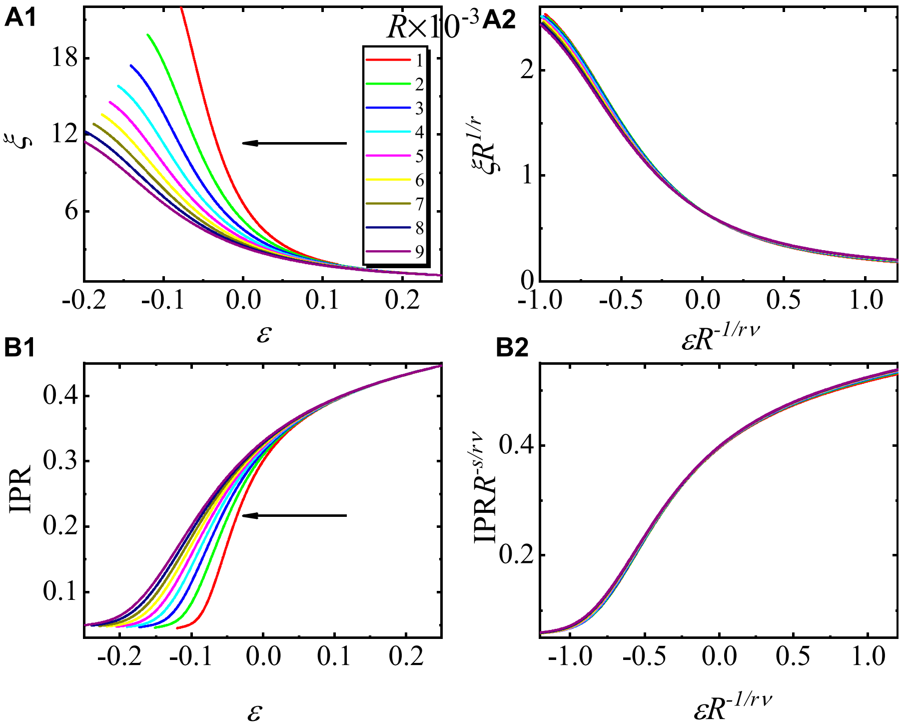

FIGURE 7
Driven dynamics with the initial 609th excited state at $\varepsilon = 1$. (A1) Curves of ξ versus ε, and (A2) the rescaled curves according to Eq. 10 for different R values. (B1) Curves of the IPR_n versus ε and (B2) the rescaled curves according to Eq. 11 for different R values. Here, we use $\varepsilon_0 = 1$, $g = 0.5$, and $L = 987$, and the results are averaged for 10 choices of ϕ. The arrows in (A1) and (B1) point to the direction of the changing ε.

4.2 Numerical results for the initial states deep in the localization phase

First, we verify the scaling function Eqs 10 and 11 with the initial state deep in the localized phase. We numerically solved the Schrodinger equation for the model (Eq. 1) under the OBC, and the finite difference method in the time direction is used. In the numerical calculation, the time interval is chosen as 10^{-3}.

According to Eqs 10 and 11, at $\varepsilon = 0$, ξ and IPR_n become the following:

$$\xi(\varepsilon = 0, R) \propto R^{-1/r}, \tag{12}$$

$$\mathrm{IPR}(\varepsilon = 0, R) \propto R^{s/r\nu}. \tag{13}$$

In Figure 5, we take the ground state at $\varepsilon_0 = 1$ as the initial state to test these predictions, where we plot the curves of $\xi_R(\varepsilon = 0, R)$ and $\mathrm{IPR}_n(\varepsilon = 0, R)$ as a function of R. The power-law fitting yields $\xi(\varepsilon = 0, R) \propto R^{-0.3367}$ and $\mathrm{IPR}(\varepsilon = 0, R) \propto R^{0.0420}$, which are consistent with the predictions in Eqs 12 and 13.

In Figure 6 (A1), the curves of ξ versus ε with the initial ground state at $\varepsilon = 1$ for different R values are plotted. After rescaling ξ and ε with R, according to Eq. 10, the rescaled curves collapse onto each other very well, as plotted in Figure 6 (A2). It confirms the scaling law of Eq. 10. The numerical results of the IPR versus ε and rescaled curves according to Eq. 11 are plotted in Figure 6 (B1) and (B2). The collapse in Figure 6 (B2) confirms the scaling function Eq. 11.

In addition to the initial ground state, the scaling functions of Eqs 10 and 11 are also verified for the excited states. The 609th excited state at $\varepsilon = 1$ is selected as the initial state. Figure 7 (A1) and (B1) show the evolution of ξ and IPR, respectively, for the 609th excited state. After the rescaling according to Eqs 10 and 11 with the same set of the critical exponents, we find the rescaled curves collapse onto each other, as shown in Figure 7 (A2) and (B2). These results confirm that the rescaling functions of Eqs 10 and 11 are applicable for the excited eigenstates.

4.3 Dynamical emergence of the skin effect

Since the critical exponents in the skin effect phase are identical to those in the localized phase, it is expected that the driven dynamics in the skin effect phase can also be described by the scaling functions of Eqs 10 and 11. To verify this prediction, we studied the driven dynamics with even smaller varying rates.

In Figure 8 (A1) and (B1), we calculate the curves of ξ and IPR versus ε for various R values. Here, we set the lattice size as

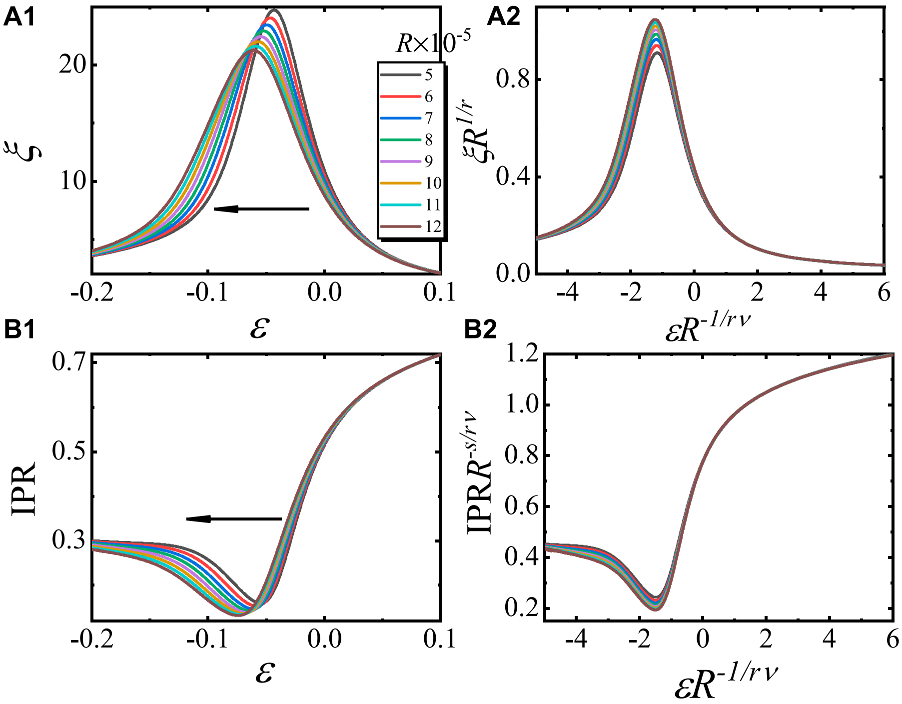

FIGURE 8
Dynamical emergence of the skin effect. (a1) Curves of ξ versus ε and (a2) the rescaled curves according to Eq. 10 for different R values. (b1) Curves of the IPR_n versus ε and (b2) the rescaled curves according to Eq. 11 for different R values. Here, we use $\varepsilon_0 = 1$, $g = 0.5$, and $L = 233$, and the results are averaged for 10 choices of ϕ. The arrows in (a1) and (b1) point to the direction of the changing ε.

$L = 233$; R values vary from 5×10^{-5} to 12×10^{-5}, which is small enough to observe the behavior of the dynamical emergence of the skin effect. The ground state at $\varepsilon = 1$ is chosen as the initial state. By rescaling ξ and ε as $\xi R^{1/r}$ and $\varepsilon R^{-1/r\nu}$, the rescaled curves collapse onto each other, as shown in Figure 8 (A2), confirming Eq. 10. As shown in Figure 8 (B1) and (B2), the curves of the IPR versus ε before and after rescaling according to Eq. 11 are plotted. We find that the rescaled curves, according to Eq. 11 with the same set of the critical exponents, collapse into a single curve. Furthermore, one finds that ξ shows a peak value and IPR shows a valley around $\varepsilon = 0$. Then, with the further decrease of ε, ξ decreases and IPR increases again. Such behaviors of ξ and IPR correspond to the dynamical emergence of the skin effect. These results confirm that Eqs 10 and 11 are still applicable in the dynamical emergence of the skin effect.

5 Summary

In summary, we have studied the static scaling behavior and the driven dynamics of the localization–skin effect transition in a non-Hermitian AA model under the OBC. By investigating the static behavior of ξ, IPR, and Δ_c, respectively, it is shown that the same set of critical exponents of ν, s, and z under the PBC are also applicable under the OBC. The driven dynamics of the localization–skin effect transition for different initial states are studied, and we find that the driven dynamics in both the initial ground and excited states can be described by the KZS with the same set of critical exponents. Then, the dynamical emergence of the skin effect is observed with an even small varying rate R, and it is shown that the dynamical emergence of the skin effect can also be described by the same scaling functions with the same set of critical exponents. Our present work generalizes the KZS to the localization–skin effect transition in non-Hermitian systems under the OBC.

Data availability statement

The raw data supporting the conclusion of this article will be made available by the authors, without undue reservation.

Author contributions

All authors contributed to the writing of the manuscript and to the interpretation of the results. L-JZ was responsible for the numerical methods adopted in the manuscript and original draft preparation; H-YW was responsible for conceptualization and formal analysis; and L-LH and QG were responsible for the numerical calculation.

Funding

L-JZ was supported by the National Natural Science Foundation of China (Grant no. 11704161), the Zhongwu Youth Innovation Talent Support Plan of Jiangsu University of Technology, and the China Postdoctoral Science Foundation (Grant no. 2021M691535).

Acknowledgments

The authors would like to thank A. Sinha and S. Yin for their helpful discussions.

Conflict of interest

The authors declare that the research was conducted in the absence of any commercial or financial relationships that could be construed as a potential conflict of interest.

Publisher's note

References

1. Aubry S, Andre G. Analyticity breaking and anderson localization in incommensurate lattices. *Ann Isr Phys. Soc.* (1980) 3:133.

2. Goblot V, Štrkalj A, Pernet N, Lado JL, Dorow C, Lemaître A, et al. Emergence of criticality through a cascade of delocalization transitions in quasiperiodic chains. *Nat Phys* (2020) 16:832–6. doi:10.1038/s41567-020-0908-7

3. Lüschen HP, Scherg S, Kohlert T, Schreiber M, Bordia P, Li X, et al. Single-particle mobility edge in a one-dimensional quasiperiodic optical lattice. *Phys Rev Lett* (2018) 120:160404. doi:10.1103/PhysRevLett.120.160404

4. Skipetrov SE, Sinha A. Time-dependent reflection at the localization transition. *Phys Rev B* (2018) 97:104202. doi:10.1103/PhysRevB.97.104202

5. Ganeshan S, Sun K, Das Sarma S. Topological zero-energy modes in gapless commensurate aubry-andré-harper models. *Phys Rev Lett* (2013) 110:180403. doi:10.1103/PhysRevLett.110.180403

6. Mastropietro V. Localization of interacting fermions in the aubry-andré model. *Phys Rev Lett* (2015) 115:180401. doi:10.1103/PhysRevLett.115.180401

7. Xu S, Li X, Hsu YT, Swingle B, Das Sarma S. Butterfly effect in interacting aubry-andre model: Thermalization, slow scrambling, and many-body localization. *Phys Rev Res* (2019) 1:032039. doi:10.1103/PhysRevResearch.1.032039

8. Das Sarma S, He S, Xie XC. Mobility edge in a model one-dimensional potential. *Phys Rev Lett* (1988) 61:2144–7. doi:10.1103/PhysRevLett.61.2144

9. Liu F, Ghosh S, Chong YD. Localization and adiabatic pumping in a generalized aubry-andré-harper model. *Phys Rev B* (2015) 91:014108. doi:10.1103/PhysRevB.91.014108

10. Thouless DJ. Bandwidths for a quasiperiodic tight-binding model. *Phys Rev B* (1983) 28:4272–6. doi:10.1103/PhysRevB.28.4272

11. Aulbach C, Wobst A, Ingold GL, Hänggi P, Varga I. Phase-space visualization of a metal–insulator transition. *New J Phys* (2004) 6:70. doi:10.1088/1367-2630/6/1/070

12. Wang Y, Cheng C, Liu XJ, Yu D. Many-body critical phase: Extended and nonthermal. *Phys Rev Lett* (2021) 126:080602. doi:10.1103/PhysRevLett.126.080602

13. Štrkalj A, Doggen EVH, Gornyi IV, Zilberberg O. Many-body localization in the interpolating aubry-andrè-fibonacci model. *Phys Rev Res* (2021) 3:033257. doi:10.1103/PhysRevResearch.3.033257

14. Zhang SX, Yao H. Universal properties of many-body localization transitions in quasiperiodic systems. *Phys Rev Lett* (2018) 121:206601. doi:10.1103/PhysRevLett.121.206601

15. Wang Y, Zhang JH, Li Y, Wu J, Liu W, Mei F, et al. Observation of interaction-induced mobility edge in an atomic aubry-andré wire. *Phys Rev Lett* (2022) 129:103401. doi:10.1103/PhysRevLett.129.103401

16. Dai CM, Zhang Y, Yi XX. Dynamical localization in non-hermitian quasicrystals. *Phys Rev A (Coll Park)* (2022) 105:022215. doi:10.1103/PhysRevA.105.022215

17. Zhou L. Floquet engineering of topological localization transitions and mobility edges in one-dimensional non-hermitian quasicrystals. *Phys Rev Res* (2021) 3:033184. doi:10.1103/PhysRevResearch.3.033184

18. Xu Z, Huangfu H, Zhang Y, Chen S. Dynamical observation of mobility edges in one-dimensional incommensurate optical lattices. *New J Phys* (2020) 22:013036. doi:10.1088/1367-2630/ab64b2

19. Xu Z, Chen S. Dynamical evolution in a one-dimensional incommensurate lattice with PT symmetry. *Phys Rev A (Coll Park)* (2021) 103:043325. doi:10.1103/PhysRevA.103.043325

20. Morales-Molina L, Doerner E, Danieli C, Flach S. Resonant extended states in driven quasiperiodic lattices: Aubry-andrè localization by design. *Phys Rev A (Coll Park)* (2014) 90:043630. doi:10.1103/PhysRevA.90.043630

21. Bairey E, Refael G, Lindner NH. Driving induced many-body localization. *Phys Rev B* (2017) 96:020201. doi:10.1103/PhysRevB.96.020201

22. Decker KSC, Karrasch C, Eisert J, Kennes DM. Floquet engineering topological many-body localized systems. *Phys Rev Lett* (2020) 124:190601. doi:10.1103/PhysRevLett.124.190601

23. Modak R, Rakshit D. Many-body dynamical phase transition in a quasiperiodic potential. *Phys Rev B* (2021) 103:224310. doi:10.1103/PhysRevB.103.224310

24. Yang C, Wang Y, Wang P, Gao X, Chen S. Dynamical signature of localization-delocalization transition in a one-dimensional incommensurate lattice. *Phys Rev B* (2017) 95:184201. doi:10.1103/PhysRevB.95.184201

25. Sinha A, Rams MM, Dziarmaga J. Kibble-zurek mechanism with a single particle: Dynamics of the localization-delocalization transition in the aubry-andré model. *Phys Rev B* (2019) 99:094203. doi:10.1103/PhysRevB.99.094203

26. Ashida Y, Gong Z, Ueda M. Non-hermitian physics. *Adv Phys X* (2021) 69:249–435. doi:10.1080/00018732.2021.1876991

27. Yao S, Wang Z. Edge states and topological invariants of non-hermitian systems. *Phys Rev Lett* (2018) 121:086803. doi:10.1103/PhysRevLett.121.086803

28. Song F, Yao S, Wang Z. Non-hermitian skin effect and chiral damping in open quantum systems. *Phys Rev Lett* (2019) 123:170401. doi:10.1103/PhysRevLett.123.170401

29. Okuma N, Kawabata K, Shiozaki K, Sato M. Topological origin of non-hermitian skin effects. *Phys Rev Lett* (2020) 124:086801. doi:10.1103/PhysRevLett.124.086801

30. Kawabata K, Sato M, Shiozaki K. Higher-order non-hermitian skin effect. *Phys Rev B* (2020) 102:205118. doi:10.1103/PhysRevB.102.205118

31. Borgnia DS, Kruchkov AJ, Slager RJ. Non-hermitian boundary modes and topology. *Phys Rev Lett* (2020) 124:056802. doi:10.1103/PhysRevLett.124.056802

32. Longhi S. Unraveling the non-hermitian skin effect in dissipative systems. *Phys Rev B* (2020) 102:201103. doi:10.1103/PhysRevB.102.201103

33. Fu Y, Hu J, Wan S. Non-hermitian second-order skin and topological modes. *Phys Rev B* (2021) 103:045420. doi:10.1103/PhysRevB.103.045420

34. Liu JS, Han YZ, Liu CS. A new way to construct topological invariants of non-hermitian systems with the non-hermitian skin effect. *Chin Phys B* (2020) 29: 010302. doi:10.1088/1674-1056/ab5937

35. Xue WT, Hu YM, Song F, Wang Z. Non-hermitian edge burst. *Phys Rev Lett* (2022) 128:120401. doi:10.1103/PhysRevLett.128.120401

36. El-Ganainy R, Makris KG, Khajavikhan M, Musslimani ZH, Rotter S, Christodoulides DN. Non-hermitian physics and pt symmetry. *Nat Phys* (2018) 14:11–9. doi:10.1038/nphys4323

37. Bender CM, Boettcher S. Real spectra in non-hermitian Hamiltonians having *PT* symmetry. *Phys Rev Lett* (1998) 80:5243–6. doi:10.1103/PhysRevLett.80.5243

38. Mostafazadeh A. Pseudo-hermiticity versus pt symmetry: The necessary condition for the reality of the spectrum of a non-hermitian Hamiltonian. *J Math Phys* (2001) 43:205–14. doi:10.1063/1.1418246

39. Zhang S, Jin L, Song Z. Topology of a parity–time symmetric non-hermitian rhombic lattice. *Chin Phys B* (2022) 31:010312. doi:10.1088/1674-1056/ac364a

40. Zhai LJ, Yin S. Out-of-time-ordered correlator in non-hermitian quantum systems. *Phys Rev B* (2020) 102:054303. doi:10.1103/PhysRevB.102.054303

41. Kawabata K, Bessho T, Sato M. Classification of exceptional points and non-hermitian topological semimetals. *Phys Rev Lett* (2019) 123:066405. doi:10.1103/PhysRevLett.123.066405

42. Yin S, Huang GY, Lo CY, Chen P. Kibble-zurek scaling in the yang-lee edge singularity. *Phys Rev Lett* (2017) 118:065701. doi:10.1103/PhysRevLett.118.065701

43. Dora B, Heyl M, Moessner R. The kibble-zurek mechanism at exceptional points. *Nat Commun* (2019) 10:2254. doi:10.1038/s41467-019-10048-9

44. Ding K, Ma G, Xiao M, Zhang ZQ, Chan CT. Emergence, coalescence, and topological properties of multiple exceptional points and their experimental realization. *Phys Rev X* (2016) 6:021007. doi:10.1103/PhysRevX.6.021007

45. Hatano N, Nelson DR. Non-hermitian delocalization and eigenfunctions. *Phys Rev B* (1998) 58:8384–90. doi:10.1103/PhysRevB.58.8384

46. Longhi S. Topological phase transition in non-hermitian quasicrystals. *Phys Rev Lett* (2019) 122:237601. doi:10.1103/PhysRevLett.122.237601

47. Longhi S. Metal-insulator phase transition in a non-hermitian aubry-andré-harper model. *Phys Rev B* (2019) 100:125157. doi:10.1103/PhysRevB.100.125157

48. Liu Y, Wang Y, Liu XJ, Zhou Q, Chen S. Exact mobility edges, PT-symmetry breaking, and skin effect in one-dimensional non-Hermitian quasicrystals. *Phys Rev B* (2021) 103:014203. doi:10.1103/PhysRevB.103.014203

49. Cai X. Localization and topological phase transitions in non-hermitian aubry-andré-harper models with *p*-wave pairing. *Phys Rev B* (2021) 103:214202. doi:10.1103/PhysRevB.103.214202

50. Jiang H, Lang LJ, Yang C, Zhu SL, Chen S. Interplay of non-hermitian skin effects and anderson localization in nonreciprocal quasiperiodic lattices. *Phys Rev B* (2019) 100:054301. doi:10.1103/PhysRevB.100.054301

51. Jazaeri A, Satija II. Localization transition in incommensurate non-hermitian systems. *Phys Rev E* (2001) 63:036222. doi:10.1103/PhysRevE.63.036222

52. Wang P, Jin L, Song Z. Non-hermitian phase transition and eigenstate localization induced by asymmetric coupling. *Phys Rev A (Coll Park)* (2019) 99: 062112. doi:10.1103/PhysRevA.99.062112

53. Zhai LJ, Yin S, Huang GY. Many-body localization in a non-hermitian quasiperiodic system. *Phys Rev B* (2020) 102:064206. doi:10.1103/PhysRevB.102.064206

54. Zhai LJ, Huang GY, Yin S. Cascade of the delocalization transition in a non-hermitian interpolating aubry-andré-fibonacci chain. *Phys Rev B* (2021) 104: 014202. doi:10.1103/PhysRevB.104.014202

55. Tang LZ, Zhang GQ, Zhang LF, Zhang DW. Localization and topological transitions in non-hermitian quasiperiodic lattices. *Phys Rev A (Coll Park)* (2021) 103:033325. doi:10.1103/PhysRevA.103.033325

56. Cai X. Localization and topological phase transitions in non-hermitian aubry-andré-harper models with *p*-wave pairing. *Phys Rev B* (2021) 103:214202. doi:10.1103/PhysRevB.103.214202

57. Kawabata K, Ryu S. Nonunitary scaling theory of non-hermitian localization. *Phys Rev Lett* (2021) 126:166801. doi:10.1103/PhysRevLett.126.166801

58. Hamazaki R, Kawabata K, Ueda M. Non-hermitian many-body localization. *Phys Rev Lett* (2019) 123:090603. doi:10.1103/PhysRevLett.123.090603

59. Zhai LJ, Huang GY, Yin S. Nonequilibrium dynamics of the localization-delocalization transition in the non-hermitian aubry-andré model. *Phys Rev B* (2022) 106:014204. doi:10.1103/PhysRevB.106.014204

60. Wei BB. Fidelity susceptibility in one-dimensional disordered lattice models. *Phys Rev A (Coll Park)* (2019) 99:042117. doi:10.1103/PhysRevA.99.042117

61. Bauer J, Chang TM, Skinner JL. Correlation length and inverse-participation-ratio exponents and multifractal structure for anderson localization. *Phys Rev B* (1990) 42:8121–4. doi:10.1103/PhysRevB.42.8121

62. Fyodorov YV, Mirlin AD. Analytical derivation of the scaling law for the inverse participation ratio in quasi-one-dimensional disordered systems. *Phys Rev Lett* (1992) 69:1093–6. doi:10.1103/PhysRevLett.69.1093

63. Monaco R, Mygind J, Rivers RJ. Zurek-kibble domain structures: The dynamics of spontaneous vortex formation in annular josephson tunnel junctions. *Phys Rev Lett* (2002) 89:080603. doi:10.1103/PhysRevLett.89.080603

64. Anglin JR, Zurek WH. Vortices in the wake of rapid bose-einstein condensation. *Phys Rev Lett* (1999) 83:1707–10. doi:10.1103/PhysRevLett.83.1707

65. Antunes ND, Gandra P, Rivers RJ. Is domain formation decided before or after the transition? *Phys Rev D* (2006) 73:125003. doi:10.1103/PhysRevD.73.125003

66. Dziarmaga J. Dynamics of a quantum phase transition: Exact solution of the quantum ising model. *Phys Rev Lett* (2005) 95:245701. doi:10.1103/PhysRevLett.95.245701

67. Damski B, Zurek WH. Dynamics of a quantum phase transition in a ferromagnetic bose-einstein condensate. *Phys Rev Lett* (2007) 99:130402. doi:10.1103/PhysRevLett.99.130402

68. Chandran A, Erez A, Gubser SS, Sondhi SL. Kibble-zurek problem: Universality and the scaling limit. *Phys Rev B* (2012) 86:064304. doi:10.1103/PhysRevB.86.064304

69. Tong X, Meng YM, Jiang X, Lee C, Neto GDDM, Gao X. Dynamics of a quantum phase transition in the aubry-andré-harper model with *p*-wave superconductivity. *Phys Rev B* (2021) 103:104202. doi:10.1103/PhysRevB.103.104202

70. Zhai LJ, Wang HY, Yin S. Hybridized kibble-zurek scaling in the driven critical dynamics across an overlapping critical region. *Phys Rev B* (2018) 97:134108. doi:10.1103/physrevb.97.134108

frontiers | Frontiers in Physics

TYPE Original Research
PUBLISHED 12 January 2023
DOI 10.3389/fphy.2023.1114719

OPEN ACCESS

EDITED BY
Yujun Zheng,
Shandong University, China

REVIEWED BY
Chuancun Shu,
Central South University, China
Emanuel De Lima,
Federal University of São Carlos, Brazil

*CORRESPONDENCE
Jin-Wei Hu,
✉ hujinww@163.com
Yong-Chang Han,
✉ ychan@dlut.edu.cn

SPECIALTY SECTION
This article was submitted to Atomic and Molecular Physics,
a section of the journal
Frontiers in Physics

RECEIVED 02 December 2022
ACCEPTED 04 January 2023
PUBLISHED 12 January 2023

CITATION
Zhang R, Hu J-W, Han Y-C, Fu B and Shundalau M (2023), Steering thermal photoassociation of magnesium atoms by two time-delayed femtosecond laser pulses.
Front. Phys. 11:1114719.
doi: 10.3389/fphy.2023.1114719

Steering thermal photoassociation of magnesium atoms by two time-delayed femtosecond laser pulses

Rong Zhang[1], Jin-Wei Hu[1,2]*, Yong-Chang Han[1,3]*, Bina Fu[4] and Maksim Shundalau[3,5,6]

[1]Department of Physics, Dalian University of Technology, Dalian, China, [2]Department of Physics, Shanxi Vocational University of Engineering and Technology, Jinzhong, China, [3]DUT-BSU Joint Institute, Dalian University of Technology, Dalian, China, [4]State Key Laboratory of Molecular Reaction Dynamics, Dalian Institute of Chemical Physics, Chinese Academy of Sciences, Dalian, China, [5]Physics Department, Belarusian State University, Minsk, Belarus, [6]Department of Information Engineering and Electrical and Applied Mathematics/DIEM, University of Salerno, Fisciano, Salerno, Italy

By solving the full-dimensional time-dependent Schrödinger equation with the thermal-random-phase wavepacket method, we investigate the photoassociation (PA) process of hot (1000 K) magnesium atoms induced by two time-delayed femtosecond laser pulses. Driven by the 840 nm fs laser pulses, the Mg_2 molecules can be formed on the four excited states, $(1)^1\Pi_g$, $(1)^1\Pi_u$, $(2)^1\Pi_u$, and $(2)^1\Sigma_u^+$, from the initial electronic ground state $X^1\Sigma_g^+$. It is found that the three-photon couplings between $X^1\Sigma_g^+$ and the three ungerade states [$(1)^1\Pi_u$ $(2)^1\Pi_u$, and $(2)^1\Sigma_u^+$], play dominant roles in the population transfer process. By scanning the pulse duration τ from 50 to 200 fs, and varying the delay time δt_0 from 0 to 2τ fs, we find that the final PA population is strongly dependent on the two parameters. For a given δt_0, the parameter τ can induce a significant variation (2 ~ 6.8 times) for the final PA population transfer, and for a given τ, one can also obtain a significant variation (2.7 ~ 3.5 times) of the final PA population by varying δt_0. Additionally, the dynamics of the coherently vibrational wavepackets of the four excited states are also influenced by the two parameters.

KEYWORDS

femtosecond (fs) laser, photoassociation, time-dependent schrodinger equation, thermal-random-phase wavepacket, multiphoton transition

1 Introduction

Through the interaction of the external laser fields with the colliding atoms, the molecular bond can be formed by absorbing or stimulated emitting one or several photons. This process is named as photoassociation (PA). PA has been studied extensively by using different laser pulses such as ultrashort laser pulses [1, 2], shaped laser pulses [3–5], pulse trains [6–8], *etc.* Shaped laser pulses are used in many PA experiments because of the advantages of the controlling of phase [9], amplitude [10, 11] and polarization [12]. Compared with ultrashort laser pulses with symmetric time profiles, the shaped laser pulses can enhance the PA transition efficiency in both the resonant and non-resonant spectral ranges [13, 14]. Zhang et al. employed a slowly-turned-on and rapidly-turned-off (STRT) laser pulse to achieve the PA process of the Cs_2 system [13]. The calculations indicated that the shaped STRT laser pulse has an obvious advantage over the unshaped pulses. The train of laser pulses is also a powerful way to transfer populations between different electronic states. Yang et al. investigated the effect of a train of ultrashort pulses on multiphoton transitions theoretically [6]. They found that the population accumulations are dependent on the relative phase between two adjacent pulses. It was proved that even higher PA efficiency can be achieved by using a train of STRT pulses [15]. They found that the population accumulations are dependent on the relative phase between two adjacent pulses. It was proved that even higher PA efficiency can be achieved by using a train of STRT pulses [16].

Many methods have been used to control the PA dynamics. Luc-Koenig et al. investigated the yield of molecules by using the theoretical framework of a Gaussian wavepacket as the initial state [16, 17]. Koch *et al.* found that molecules can be transferred directly from high-lying bound states to the ground vibrational level by using shaped femtosecond laser pulses [18]. de Lima et al. used a combination of two transition pathways to form molecules of the electronic ground state [19]. The first pathway is to use pump-dump time-delayed laser pulses to transfer populations to the electronic ground state. The second pathway applies a single far-infrared pulse to obtain electronic ground state molecules from free atoms directly. The interference between the pathways can be controlled by modifying the laser parameters, and the yields of the target ground state molecules can be enhanced.

With the development of laser techniques, researchers can achieve PA through ultrashort laser pulses such as femtosecond pulses. Ultrashort laser pulses are used to pump the free atom pairs to bound molecular states because of the broad bandwidth [20]. In previous studies, Salzmann et al. verified the PA of ultracold rubidium dimers using coherent femtosecond pulses and produced electronic excited rubidium molecules [2]. Merli et al. investigated the PA of ultracold rubidium atoms with shaped femtosecond laser pulses [4]. Vardi et al. calculated the radiative recombination of cold Na atoms by short laser pulses [21]. It was demonstrated that resonantly enhanced two-photon recombination of ultracold atoms is an efficient way to produce ultracold molecules.

Instead of forming ultracold molecules, PA also serves as another role in laser control of chemical reaction, i.e., the formation of chemical bonds in thermal atom gas. The PA of thermal atoms using femtosecond laser pulses and shaped pulses can lead to coherent control of thermal molecules [22, 23]. de Lima et al. used the non-perturbative laser pulse to produce molecules in a thermal atomic gas [24]. Levin et al. verified the coherent control of photoreactions in thermal conditions in experiment [25]. Wang et al. investigated the coherent control of the rovibrational dynamics of HF molecules by two-color pulses [26]. The population distributions oscillate with a period of π when the relative phase between the fundamental and the second-harmonic laser pulses varies.

In previous studies, many efforts have been devoted into the investigations of the effect of laser parameters, such as duration, amplitude, carrier envelope phase, etc., on PA process. And these laser pulse parameters are controllable and can also be used to enhance the PA efficiency in the pump-dump scheme [27]. Zhang et al. investigated the PA dynamics of Cs atoms system driven by a picosecond pulse with cubic phase modulation [28]. In the investigation of two-photon PA of ^{87}Rb atoms system, Kallush et al. found that a frequency-chirped pulse can enhance the molecular formation rate [29]. Zhang et al. used a modulated two-color laser field to steer the PA of ultracold Cs atoms in theory and control the PA dynamics through changing the phase of envelope and the period of the laser field [30]. Some researchers also used optimal control theory to obtain laser pulses in population transfer studies. For instances, the shaped laser pulses with minimum intensity proposed by the optimal control theory can transfer the highly excited Na$_2$ molecules to the ground vibrational level with a high efficiency of .99 [18]; and Ndong et al. used optimal control theory to drive the vibrational transfer from the dissociation limit to the vibrational ground state in the KRb system [31].

Compared to the single laser pulse, time-delayed pulses can introduce more various combination modes and be used in different ways in population transfer. There were reports on the formation of cold molecules by the PA process with consideration of the time delay of two laser pulses (see, e.g., Refs. [19, 24]). The dissociation process of the HD$^+$ molecule driven by two overlapping THz and infrared laser pulses was reported recently [32]. The effect of 2 picosecond pulses on the adiabatic population transfer of the LiH molecule was also reported [33]. However, there is few report on the influence of the pulses' delay time on the PA process in thermally hot atomic gas, except in Ref. [34].

Thus, we are motivated to investigate the influence of two time-delayed laser pulses on the PA process in thermally hot atomic gas. In this paper, the hot Mg atoms at 1000 K are taken as a model system, because it is a prototypical system for the study of PA processes in thermally hot atoms (see, e.g., Refs. [25, 34–36]). In thermal conditions, Mg$_2$ molecules can be produced through the multiphoton PA process by using chirped femtosecond laser pulses [25]. Hu et al. proposed a full-dimensional thermal-random-phase wavefunction method to simulate the thermal PA process including rovibrational couplings [35]. By using this method, the detailed population transfer dynamics has been revealed by employing the five-electronic-state model [36]. Here, we use the same five-electronic-state model as the one used in Ref. [36], yet we consider the interaction of two time-delayed femtosecond laser pulses with the system instead. At different delay times and pulse durations, we simulate the final populations of the four excited states and investigate the feasibility of control the thermal PA process by manipulating the combination of two pulses.

This paper is organized as follows: In Section 2, we briefly introduce the theory. In Section 3, we discuss the effect of the delay time and pulse duration on the population transfer of PA process of Mg atoms at 1000 K. In Section 4, the conclusions are summarized.

2 Theoretical approach

The initial thermal ensemble of the numerous rovibrational eigenfunctions $|n, j\rangle$ of the $X^1\Sigma_g^+$ state is described by the thermal-random-phase wavefunction method. For the details of this method with consideration of fully coupled rovibrational dynamics, one can refer to Ref. [35]. Here, we just briefly list the main equations and numerical parameters. The normalized initial thermal-random-phase wavefunction of the $X^1\Sigma_g^+$ state is expressed as,

$$\psi_1^k(R,\theta,t=0) = \frac{1}{\sqrt{Z}}\sum_{n,j}\sqrt{2j+1}e^{i\Theta_{n,j}^k}e^{-\frac{E_{n,j}}{2k_BT}}|n,j\rangle, \qquad (1)$$

where R is the internuclear distance and θ is the angle between the molecular axis and the z-axis of the space fix frame which is taken to be the polarization direction of the linear polarized laser pulses. $\Theta_{n,j}^k$ is the initial random phase of the $|n, j\rangle$ quantum eigenstate, with $k = 1, \ldots, N$ labeling different sets of random phases. n and j denote the translational

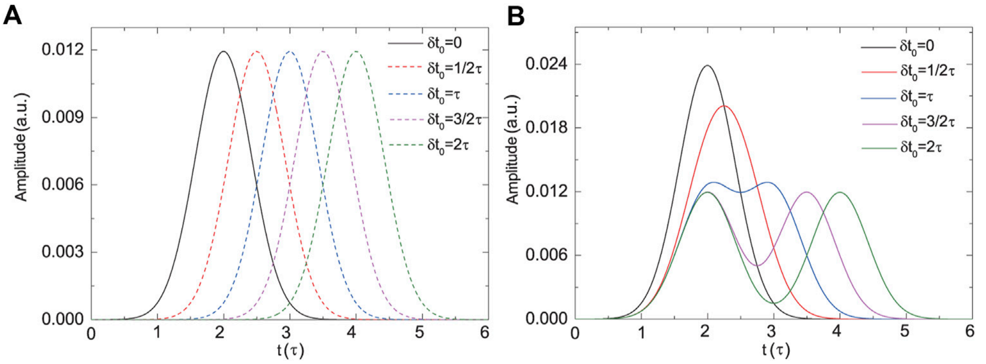

FIGURE 1
(A) The envelope functions of the two laser pulses at five different delay times, δt_0 = 0, 1/2τ, τ, 3/2τ and 2τ, respectively. The solid and dashed curves denote $f_1(t)$ and $f_2(t)$, respectively. **(B)** The total envelope function of the two laser pulses according to the five different delay times. Here, τ = 100 fs.

and rotational quantum numbers, respectively. $Z = \sum_{n,j}(2j+1)e^{-\frac{E_{n,j}}{k_B T}}$ is the normalization factor of the Boltzmann distribution. N different thermal-random-phase initial wavefunctions are then used as initial states for propagations, respectively. For a large number of N, the statistical average of the expectation values will converge.

The laser field used in this work consists of 2 femtosecond Gaussian pulses with the same wavelength of 840 nm and with a specific delay time between each other. The total electric field of the two laser pulses can be expressed as,

$$E(t) = \Sigma_i E_0 f_i(t) \cos\left[\omega_0 (t - t_{0i})\right], \quad i = 1, 2 \tag{2}$$

where t_{01} and t_{02} represent the central time of the two Gaussian pulses. We define $\delta t_0 = t_{02} - t_{01}$ as the delay time. $E_0 = 5 \times 10^{12}$ W/cm^2 is the peak amplitude of the two Gaussian pulses. $f_i(t) = \exp\left[-4\ln 2\,(t - t_{0i})^2/\tau^2\right]$ is the envelope function of the ith laser pulse. τ is the full width at half maximum (FWHM) denoting the pulse duration.

In this paper, we focus on the influences of the delay time δt_0 and the FWHM τ on the PA process. To compare the results with the variation of δt_0, we set τ = 100 fs to be the time unit to present δt_0. The envelope functions of the two pulses are shown in Figure 1A and the two pulses gradually separate from each other with the increase of δt_0 from 0 to 2τ. Figure 1B presents the sum of the envelopes of the two Gaussian pulses, i.e., the total envelope function $f_{\text{tot}}(t)$, for different δt_0.

The Hamiltonian that governs the propagation of the thermal-random-phase wavefunction is expressed as

$$\hat{H} = \begin{pmatrix} \hat{H}_1 + \omega_1^S & W_{12} & W_{13} & W_{14} & W_{15} \\ W_{12} & \hat{H}_2 + \omega_2^S & W_{23} & W_{24} & W_{25} \\ W_{13} & W_{23} & \hat{H}_3 + \omega_3^S & V_{34} & 0 \\ W_{14} & W_{24} & V_{34} & \hat{H}_4 + \omega_4^S & 0 \\ W_{15} & W_{25} & 0 & 0 & \hat{H}_5 \end{pmatrix} \tag{3}$$

where $\hat{H}_\xi = \hat{T} + \frac{\hat{L}^2}{2\mu R^2} + \hat{V}_\xi(R), \xi = 1, 2, 3, 4, 5$ is the nuclear rovibrational Hamiltonian in the absence of external fields for a given electronic state. ξ = 1, 2, 3, 4, 5 represent the states $X^1\Sigma_g^+$, $(1)^1\Pi_g$, $(1)^1\Pi_u$, $(2)^1\Pi_u$, and $(2)^1\Sigma_u^+$, respectively. And we use $|1\rangle$, $|2\rangle$, $|3\rangle$, $|4\rangle$, and $|5\rangle$ to simply represent these five states. $\hat{T}$, $\hat{L}$ and $\hat{V}_\xi$ represent the vibrational kinetic energy operator, angular momentum operator and the interaction potential of the two atoms, respectively. Note that the potential energy functions, $\hat{V}_3(R)$ and $\hat{V}_4(R)$, and the diabatic coupling, $\hat{V}_{34}(R)$, are in the diabatic representation which correspond to the $(1)^1\Pi_u$ and $(2)^1\Pi_u$ states in the adiabatic representation. μ is the reduced mass of the Mg$_2$ molecule. In Eq. (3), $\omega_\xi^S = -\frac{1}{4}E_0^2 f_{\text{tot}}^2(t)\sum_{j,j'}\epsilon_j\epsilon_{j'}\alpha_{jj'}^\xi \cos^2\theta$ is the dynamic Stark shift of the ξth electronic state. $\alpha_{jj'}^\xi$ represents the dynamic electronic polarizability. $W_{\xi\xi'}$ $(\xi \neq \xi')$ is the coupling of states $|\xi\rangle$ and $|\xi'\rangle$. In the two-photon rotating-wave approximation, $W_{12} = \frac{1}{4}E_0^2 f_{\text{tot}}^2(t)\sum_{j,j'}\epsilon_j\epsilon_{j'}M_{jj'}^{2\leftarrow 1}\cos^2\theta$ represents the two-photon coupling between states $|1\rangle$ and $|2\rangle$, where $M_{jj'}^{2\leftarrow 1}$ denotes the tensor element of the two-photon electric transition dipole moment [37]. $W_{\xi\xi'} = \mu_{\xi\xi'}(R)$ $E(t)\cos\theta$ $(\xi\xi' = 13, 14, 15, 23, 24)$ is the coupling *via* the transition dipole moment. W_{13}, W_{14} and W_{15} are the three-photon couplings and W_{23}, W_{24} and W_{25} are the one-photon couplings.

The five-state time-dependent Schrödinger equation of the Mg$_2$ system is shown as

$$i\frac{\partial}{\partial t}\begin{pmatrix} \psi_1^k(R,\theta,t) \\ \psi_2^k(R,\theta,t) \\ \psi_3^k(R,\theta,t) \\ \psi_4^k(R,\theta,t) \\ \psi_5^k(R,\theta,t) \end{pmatrix} = \hat{H}\begin{pmatrix} \psi_1^k(R,\theta,t) \\ \psi_2^k(R,\theta,t) \\ \psi_3^k(R,\theta,t) \\ \psi_4^k(R,\theta,t) \\ \psi_5^k(R,\theta,t) \end{pmatrix} \tag{4}$$

where $\psi_\xi^k(R,\theta,t)$ is the nuclear wavefunction of the $|\xi\rangle$ state for a given initial random-phase label k. The wavefunction can be divided into R- and θ-dependent parts, with the former expanded on a Fourier grid [38] and the latter expanded on a Legendre-Gauss quadrature grid [35].

We solve Eq. (4) by using the split-operator propagation method [39, 40]. At the critical time $t = t_f$ when the action of the laser pulses is over, the final population on the $|\xi\rangle$ state is calculated by statistically averaging over the expectation values of all thermal-random-phase wavefunctions,

$$P_\xi(t_f) = \frac{1}{N}\sum_{k=1}^{N}\int_R\int_\theta \left[\psi_\xi^k(R,\theta,t_f)\right]^*\psi_\xi^k(R,\theta,t_f)R^2\sin\theta\,\mathrm{d}\theta\,\mathrm{d}R. \tag{5}$$

Note that Eq. (5) is the integral over R and θ, and we can also obtain the population distribution along R at any given time t, i.e., the propagation of the radial wavepacket, by performing integral only over θ,

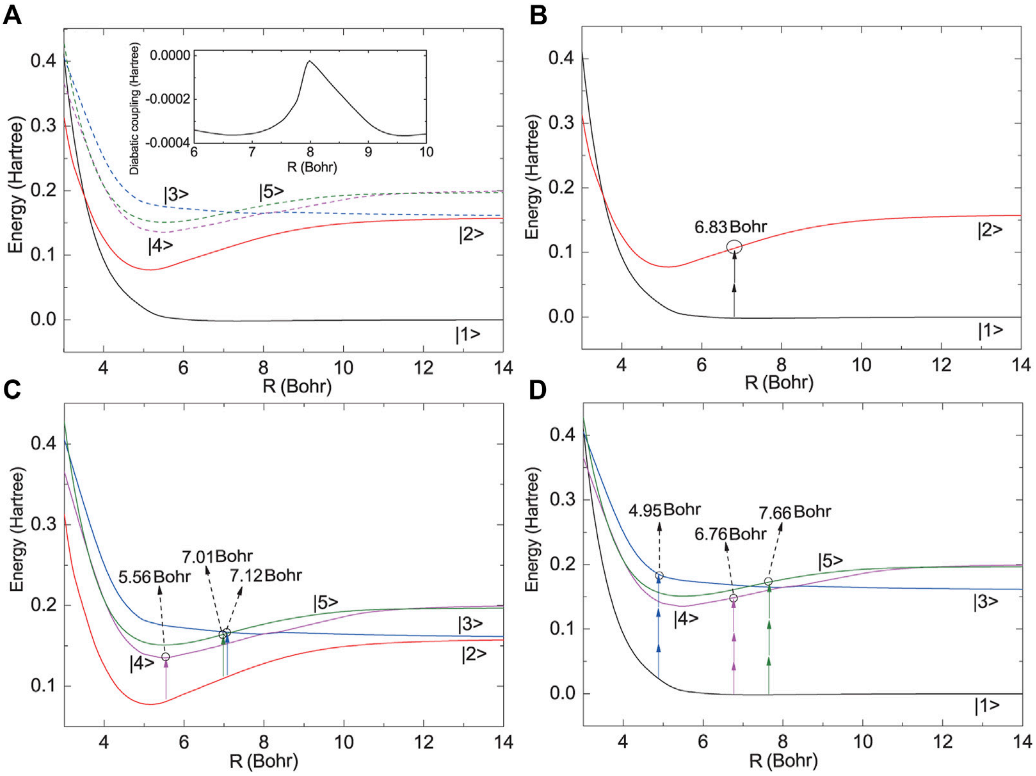

FIGURE 2
(A) The potential energy curves of the five-state-model of the Mg_2 system. The diabatic coupling between the $|3\rangle$ and $|4\rangle$ states is shown in the inset. **(B)** The two-photon coupling between the states $|1\rangle$ and $|2\rangle$. **(C)** The one-photon couplings between the states $|2\rangle$ and $|u\rangle$. **(D)** The three-photon couplings between the states $|1\rangle$ and $|u\rangle$. Here, u = 3, 4, 5.

$$P_\xi(R,t) = \frac{1}{N}\sum_{k=1}^{N}\int_\theta \left[\psi_\xi^k(R,\theta,t)\right]^* \psi_\xi^k(R,\theta,t)R^2 \sin\theta d\theta. \tag{6}$$

3 Results and discussions

The initial temperature of the colliding Mg atoms system is set to be 1000 K. The potential energy curves of the five relevant electronic states of the Mg_2 system are shown in Figure 2A. The relevant molecular datas, including the potentials, diabatic couplings, electric dipole moments, dynamic electronic polarizabilities, etc., are taken from Refs. [35, 37]. 1,024 and 250 grid points are used to express the radial range from 3 to 40 Bohr and the angular range from 0 to π, respectively. The time step is set to be .4 fs for the propagation of the wavepacket. These numerical parameters are kept the same as those used in Ref. [36] which have been checked to be able to provide the converged results.

Driven by the 840 nm laser field, these electronic states can interact with each other *via* one-, two- or three-photon couplings. The two-photon transition, which have been considered extensively in the PA process of the titled system (see, e.g., Refs. [25, 34–37]), can occur between the two gerade states, $|1\rangle$ and $|2\rangle$. As shown in Figure 2B, the energy difference between the two potentials at $R = 6.83$ Bohr exactly equals to the energy of two photons. The other higher excited states, are all ungerade states and energetically close with each other. Thus, we use $|u\rangle$ to denote the states $|3\rangle$, $|4\rangle$ and $|5\rangle$ states, for simplicity. Via the one-photon interaction, the gerade $|2\rangle$ state can couple with the ungerade $|u\rangle$ state. Due to the different shapes of the potential energy curves, the critical internuclear distance for one-photon resonance between the two potentials of $|2\rangle$ and $|u\rangle$ varies with u. As shown in Figure 2C, for $|2\rangle$ and $|4\rangle$, the one-photon resonance may probably occur at $R = 5.56$ Bohr, while for $|2\rangle$ and $|3\rangle$ (or $|5\rangle$), the one-photon resonance may probably occur in the vicinity of $R \sim 7$ Bohr. Recent theoretical calculations demonstrated that the three-photon transition from $|1\rangle$ to $|u\rangle$ may also play an important role in the PA process [35, 36]. In Figure 2D, we illustrate those critical internuclear separations at which the potential energy gaps between $|1\rangle$ to $|u\rangle$ equal to three-photon energy, which also present variance.

The above different kinds of coupling interactions can construct several transition pathways for PA. As demonstrated in Ref. [36], with the action of the 840 nm fs laser pulse, the direct two-photon transition from $|1\rangle$ to $|2\rangle$ is much weaker than the three-photon transition from $|1\rangle$ to $|u\rangle$, because the three-photon transition between the gerade and ungerade states is electric dipole allowed, while the two-photon transition between the two gerade states is electric dipole forbidden. Thus, the major population transfer path is considered to be $|1\rangle \overset{+3\hbar\omega}{\longrightarrow} |u\rangle \overset{-\hbar\omega}{\longrightarrow} |2\rangle$, corresponding to the schematic plot in Figure 3A.

In this paper, we mainly investigate the effect of the delay time δt_0 and the FWHM τ of the laser pulses on the populations of the four excited states. Thus, we divide our discussion into different cases: Case

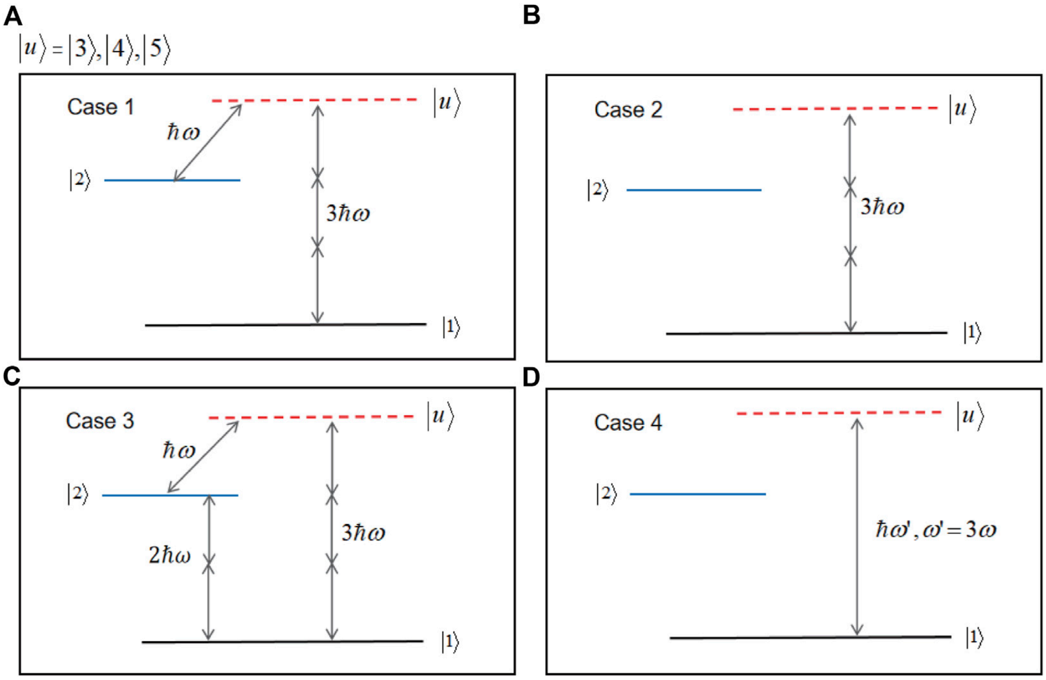

FIGURE 3
The four cases with the consideration of different coupling conditions. **(A)** Case 1: The one-photon coupling between $|2\rangle$ and $|u\rangle$ and the three-photon coupling between $|1\rangle$ and $|u\rangle$ are considered. **(B)** Case 2: Only the three-photon coupling between $|1\rangle$ and $|u\rangle$ is considered. **(C)** Case 3: All the one-, two- and three-photon couplings are taken into account. In Cases 1–3, the laser wavelength is 840 nm. **(D)** Case 4: The one-photon coupling between $|1\rangle$ and $|u\rangle$ is considered with the wavelength setting to be 280 nm.

1, corresponds to the major population transfer path, as shown in Figure 3A where the two-photon transition is neglected, and W_{12} in Eq. 3 is set to be zero in the propagating; Case 2, only the three-photon transition between $|1\rangle$ and $|u\rangle$ is considered, and W_{12}, W_{23}, W_{24} and W_{25} in Eq. 3 are all set to be zero; Case 3, all the possible couplings have been taken into account, and the propagating is performed with the full Hamiltonian as presented in Eq. 3; Case 4 denotes the transition from $|1\rangle$ to $|u\rangle$ *via* one-photon resonant coupling with the central frequency corresponding to 280 nm wavelength instead, and the Hamiltonian is formally the same as the one used for Case 2 except that the central frequency for W_{13}, W_{14} and W_{15} is changed accordingly. By comparing the calculation results of Cases 1 and 3, we can further confirm the major pathway for the PA process induced by the two time-delayed laser pulses. By comparing Cases 1 and 2, we can identify the enhancement of the one-photon coupling between $|2\rangle$ and $|u\rangle$ on the three-photon transition process. And by comparing Cases 1 and 4, we can demonstrate that the three-photon resonant transition and one-photon resonant transition depend on different laser-molecule interaction mechanism and that they behave differently with the laser parameters.

We first fix the FWHM of the two laser pulses to be $\tau = 100$ fs and the delay time $\delta t_0 = 0$ fs. Considering the major population transfer path, driven by the 840 nm laser pulses, i.e. Case 1, the formations and propagations of the radial wavepackets of the four excited states are shown in Figure 4. We can see that after the action of the laser pulses, the radial wavepackets oscillate periodically on the states $|2\rangle$, $|4\rangle$ and $|5\rangle$, respectively. This indicates that several certain vibrational levels have been populated on these specific electronic states. The oscillation period of the radial wavepacket of $|2\rangle$ is about 130 fs, which corresponds to a vibrational frequency of roughly 256 cm^{-1} which is quite comparable with the vibrational signal reported in experiment [34]. The radial wavepacket on $|3\rangle$ actually contains both the vibrational-bound and the continuous states.

In Case 1, the one- and three-photon couplings are taken into account. Here, we correlate the R position at which the radial wavepacket is initially formed, with the one at which two different electronic states resonate with each other. Since the three-photon coupling between $|u\rangle$ and $|1\rangle$ plays a major role in the population transfer process [36], we first concern about the wavepackets formed on the three ungerade excited states. In Figure 4B, during the action of the laser pulses (mainly from t = 150 to 250 fs), the radial wavepacket on the $|3\rangle$ is partly formed in the vicinity of $R \sim 5$ Bohr, which is right around the resonant position between the potentials of $|3\rangle$ and $|1\rangle$ marked in Figure 2D. The other parts of the radial wavepacket on the $|3\rangle$ are formed around $R \sim 6$, 7 Bohr and in the large R region of over 8 Bohr. This can be ascribed to the diabatic coupling between the $|3\rangle$ and $|4\rangle$ states. As shown in the inset plot in Figure 2A, the diabatic coupling can influence the wavefunctions of the $|3\rangle$ and $|4\rangle$ in the range from roughly 6 to 10 Bohr. Thus, although $|3\rangle$ and $|1\rangle$ are not quite resonant with each other in this R region, once $|4\rangle$ and $|1\rangle$ are resonant or near resonant, then the $|3\rangle$ state can be populated *via* diabatic coupling with the $|4\rangle$ state. As shown in Figure 4C, the corresponding radial wavepacket on the $|4\rangle$ state is initially in the R region from 6.5 to 8.5 Bohr which is in accordance with the above mentioned diabatic coupling region. Additionally, the resonance between the $|4\rangle$ and $|1\rangle$ states mainly occurs around 6.76 Bohr as

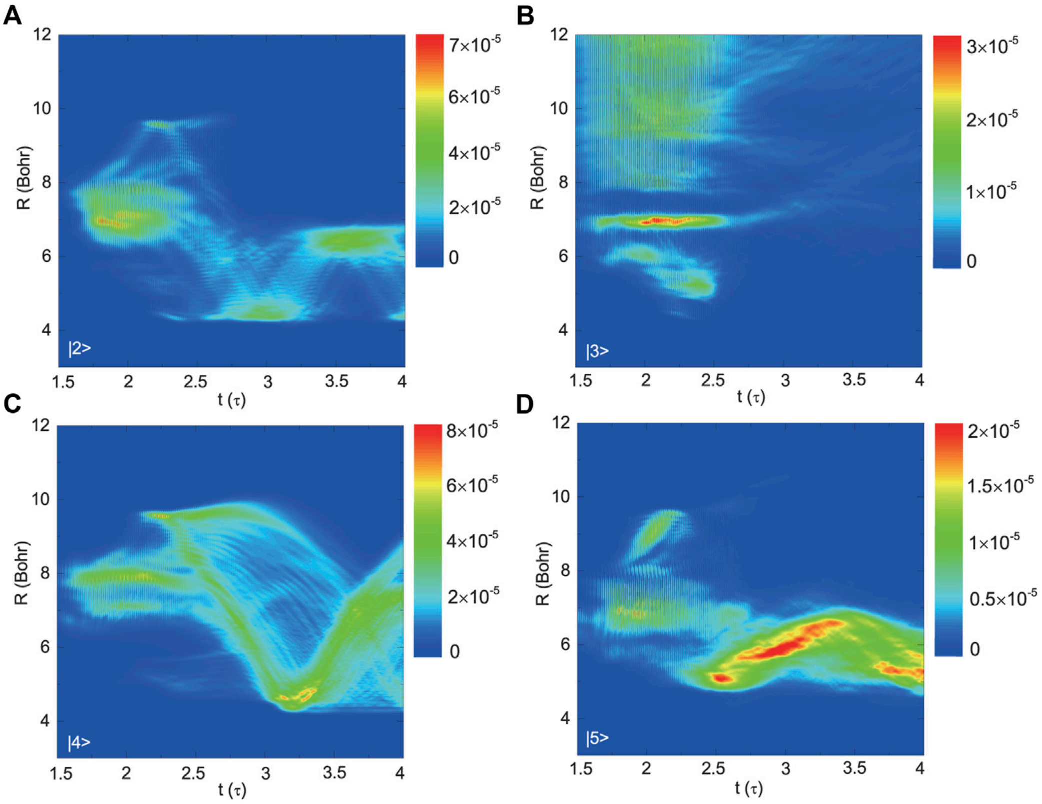

FIGURE 4
The propagations of the radial wavepackets for the four excited states, **(A)** $|2\rangle$, **(B)** $|3\rangle$, **(C)** $|4\rangle$, and **(D)** $|5\rangle$, in Case 1 with τ = 100 fs and δt_0 = 0.

shown in Figure 2D, which also falls in the diabatic coupling region between $|4\rangle$ and $|3\rangle$. Therefore, one can expect that the population is firstly transferred from $|1\rangle$ to $|4\rangle$ around 6.76 Bohr due to the three-photon resonance, and then redistributed between $|4\rangle$ and $|3\rangle$ in an even larger R region from 6 to 10 Bohr due to the diabatic coupling. Similarly, the radial wavepacket on $|5\rangle$ is initially formed around 7 Bohr at t = 200 fs when the peak of the laser pulse occurs, as shown in Figure 4D. This is consistent with the three-photon resonant position between $|5\rangle$ and $|1\rangle$ shown in Figure 2D.

The one-photon coupling between $|2\rangle$ and $|u\rangle$ can additionally enhance the population transfer process from $|1\rangle$ to $|u\rangle$. As shown in Figure 2C, in the vicinity of 7 Bohr, the one-photon coupling between $|2\rangle$ and $|5\rangle$ ($|3\rangle$) is strong. Thus, we can expect the three-photon transition from $|1\rangle$ to $|5\rangle$ ($|3\rangle$) may be enhanced around R ~ 7 Bohr. This can be verified from Figures 4B,D: When t varies from 200 to 250 fs, the distributions of the wavepackets on the $|5\rangle$ and $|3\rangle$ states have been enhanced around 7 Bohr. The similar circumstance occurs for the $|4\rangle$ state. As seen in Figure 4C, when t varies from 200 to 250 fs, there is an enhancement of the wavepacket around 5 Bohr which is consistent with the resonant position, R ~ 5.56 Bohr, between $|4\rangle$ and $|2\rangle$ shown in Figure 2C. The wavepacket on the $|2\rangle$ completely results from the one-photon coupling between $|2\rangle$ and $|u\rangle$, and consequently, it can be found to be initially localized around R ~ 5 and R ~ 7 Bohr, as shown in Figure 4A.

Here, the two laser pulses are set to coincide with each other in time, and we further discuss the influence of the delay time between the two pulses, δt_0, on the population transfer process. The thermally averaged final populations of the four excited states vary with δt_0 for different cases are shown in Figure 5, where τ is still fixed at 100 fs.

One aspect shown in Figure 5 is that the population transfer process is dominated by the three-photon resonant transition from $|1\rangle$ to $|u\rangle$ which can be enhanced by the one-photon resonant coupling between $|2\rangle$ and $|u\rangle$. Specifically, in Figure 5A, we compare the final populations of the four excited states in Case 1 (dashed line) with those in Case 3 (solid line). It can be found that the population variations with δt_0 in the two cases are almost the same. This illustrates that the two-photon coupling between $|1\rangle$ and $|2\rangle$ has little influence on the population transfer process, because Case 3 additionally includes the effect of two-photon coupling compared to Case 1. Figure 5B is then the comparison of the final populations of the four excited states between Case 1 (dashed line) and Case 2 (solid line). We can see that the final populations of the states $|2\rangle$, $|4\rangle$ and $|5\rangle$ in Case 1 are higher than those in Case 2, while that of the state $|3\rangle$ is not changed obviously from Case 1 to Case 2. This further indicates that the one-photon coupling between $|u\rangle$ and $|2\rangle$ can enhance three-photon transition from $|1\rangle$ to $|u\rangle$. These findings are consistent with the report in Ref. [36] based on the simulation of a single laser pulse action, and here we further extend it in the two time-delayed laser pulses condition.

The other aspect shown in Figure 5 is that the final populations of the four excited states can vary with δt_0 to different extent. In Figure 5B, in Case 2 where only the three-photon coupling between $|1\rangle$ and $|u\rangle$ is taken into account, P_3, P_4, and P_5 all decrease with the increase of δt_0 from 0 to 100 fs? However, the absolute value of P_5 is relatively small, which has

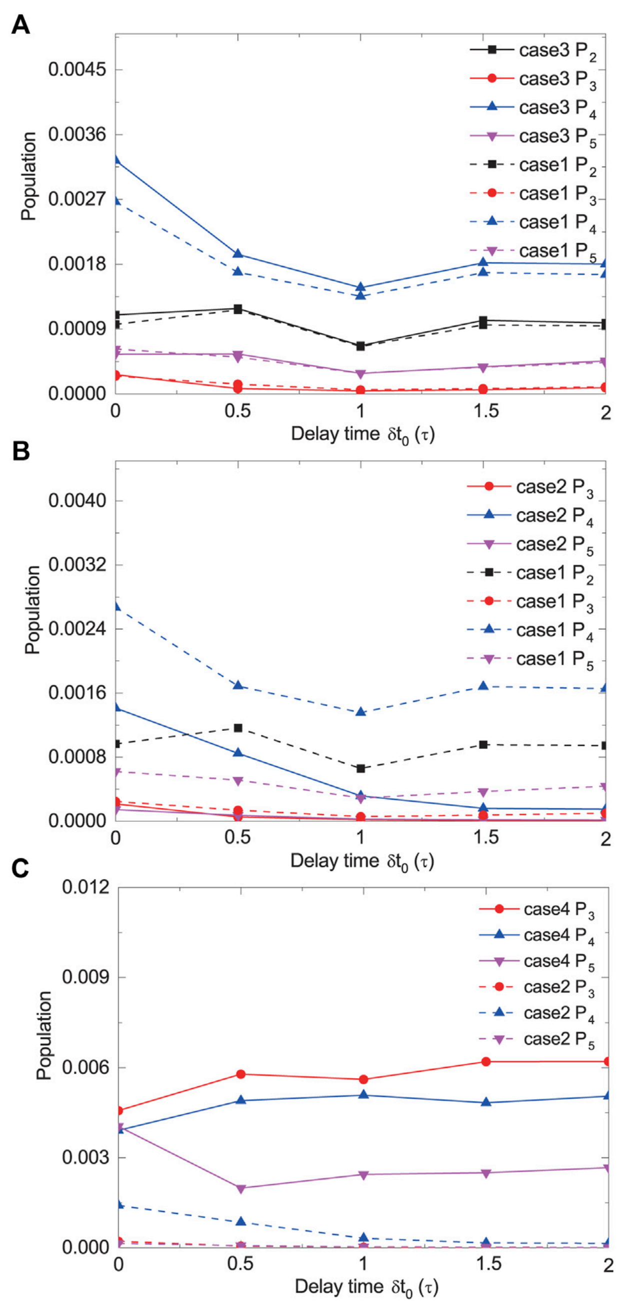

FIGURE 5
The comparisons of the final populations of the four excited states vary with δt_0 between **(A)** Case 1 and Case 3, **(B)** Case 1 and Case 2, **(C)** Case 2 and Case 4. Here, τ = 100 fs.

been enhanced significantly by the one-photon coupling between $|2\rangle$ and $|5\rangle$. Therefore, the variation of P_5 with δt_0 in Case 1, as the dashed pink line shown in Figure 5B, can not duplicate its behavior in Case 2. To understand why the three-photon resonant transition probability decreases with the increase of δt_0, we compare the final populations of the four excited states in Case 2 (dashed lines) with those in Case 4 (solid lines) in Figure 5C. Here, we find that in the $|1\rangle \rightarrow |u\rangle$ process, the resonance excitation of one-photon coupling is much higher than that of three-photon coupling. Moreover, the variation behavior of final population on a given state with δt_0 in Case 2 is totally different from the one in Case 4. This is because the one-photon resonance excitation mainly depends on the pulse shape and area of the laser field, while the multiple-photon resonance excitation more greatly relies on the peak intensity of the laser field [41, 42]. As shown in Figure 1B, the shape and area of the total pulse envelope vary with δt_0 which leads to the variations of P_3, P_4, and P_5 in Case 4; while the peak intensity of the laser field first decreases dramatically from δt_0 = 0 to 100 fs and then keeps almost unchanged from δt_0 = 100 to 200 fs, which is consistent with the variation behaviors of P_3, P_4, and P_5 in Case 2. Thus, the delay time between the pulses can be used as a good parameter for steering of the photoassociation process in the time area when the two pulses overlap with each other.

The FWHM of the laser pulse is another important laser parameter for steering molecular dynamics. To investigate its influence on the PA process, we first fix δt_0 = 0 and decrease FWHM τ from 100 to 50 fs. The propagation dynamics of the wavepackets on the four excited states in Case 1 are shown in Figure 6. Obviously, the wavepacket dynamics and its corresponding excitation probability vary from those in Figure 4. The pulse with short duration can form wavepackets with more concentrative localization and the vibrational periods also vary a little. For instance, the period for $|2\rangle$ decreases to roughly 100 fs which corresponds to an increase of the vibrational energy difference and suggests that some lower vibrational levels be populated. This can be ascribed to the relatively broader frequency domain of the τ = 50 fs pulse. Additionally, for the same peak intensity, the area of the τ = 50 fs pulse is smaller than that of the τ = 100 fs pulse. Thus, the final transition probability may also be influenced.

To further indicate the influence of τ and δt_0 on the PA efficiency, we calculate the total population of the four excited states as a function of the delay time for different FWHMs, with consideration of Case 3 including all one-, two-, and three-photon couplings. As shown in Figure 7, the four lines related to different τ present the similar behavior with the variation of the delay time. The total population first exhibits a relatively maximal value at δt_0 = 0, then decreases with the increase of the delay time from $\delta t_0 = 0$ to $\delta t_0 = \tau$, and finally tends to be steady when the delay time further increases from $\delta t_0 = \tau$ to $\delta t_0 = 2\tau$. This can be ascribed to the fact that the three-photon transition plays a dominant role in the PA process. And the three-photon transition heavily depends on the peak amplitude of the laser field. As shown in Figure 1, at $\delta t_0 = 0$, the peak amplitude of the laser field is the strongest, and it decreases with the increase of δt_0 and is unchanged when the two pulses separate from each other. Thus, it is good for us to use τ as the unit to define the delay time δt_0.

In Figure 7, it can be seen that the two parameters, τ and δt_0 both strongly influence the final PA populations. We note that at δt_0 = 0, the population for τ = 200 fs can reach .0073, while the one for τ = 50 fs decreases to roughly .0035. The former value is roughly 2 times larger than the latter one. At $\delta t_0 = 0.5\tau$, the total population for τ = 200 fs is roughly .0068, while the one for τ = 50 fs decreases to roughly .001. The former is about 6.8 times bigger than the latter. At $\delta t_0 = \tau$, the total population for τ = 200 fs is roughly .0041, while the one for τ = 50 fs decreases to roughly .002. At this point, the former is roughly 2 times greater than the latter. Thus, for a given δt_0, the parameter τ can induce a significant variation (2 ~ 6.8 times) for the population transfer of the PA process. Similarly, we can consider the influence of δt_0 on the total final population for a given τ. For τ = 200 fs, we can obtain the minimal total population of roughly .0027 at $\delta t_0 = 1.5\tau$, compared to the maximal one (roughly .0073) at δt_0 = 0. If we consider τ = 50 fs instead, the minimal value is roughly .001 at $\delta t_0 = 0.5\tau$, compared to the maximal one (roughly .0035) at δt_0 = 0. Thus, it is also a significant variation (2.7 ~ 3.5 times) which can be induced by δt_0.

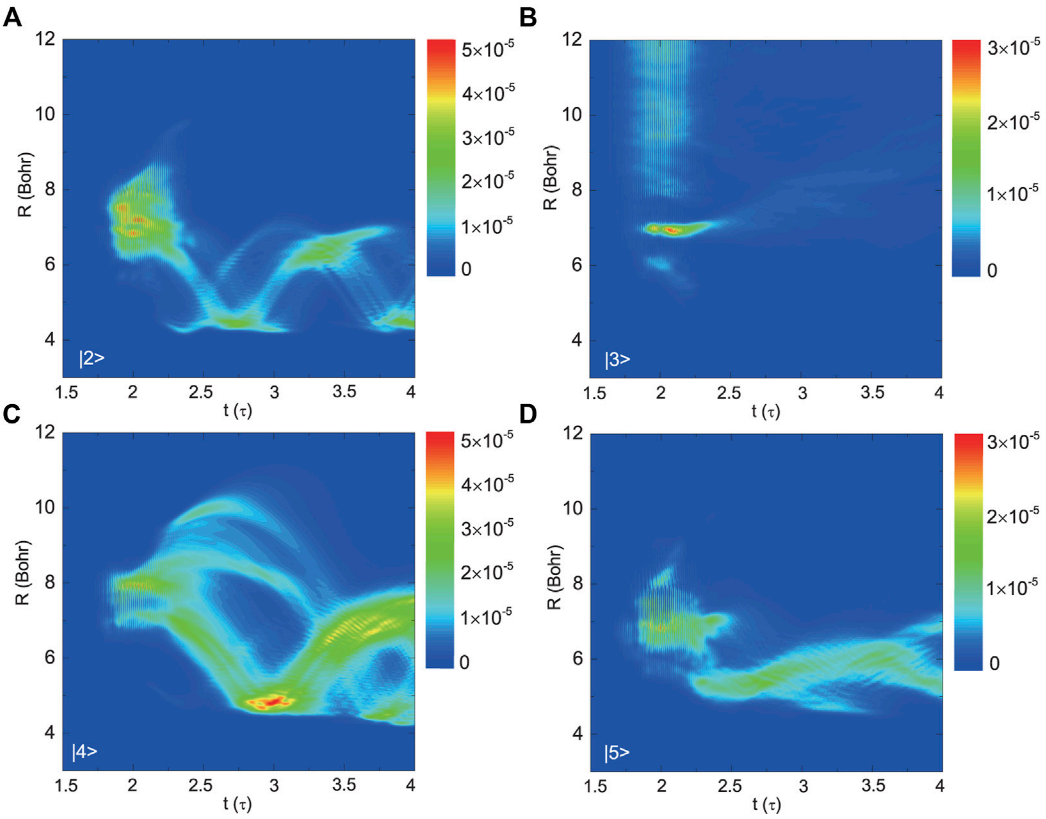

FIGURE 6
The propagations of the radial wavepackets for the four excited states, **(A)** |2⟩, **(B)** |3⟩, **(C)** |4⟩, and **(D)** |5⟩, in Case 1 with τ = 50 fs and δt_0 = 0.

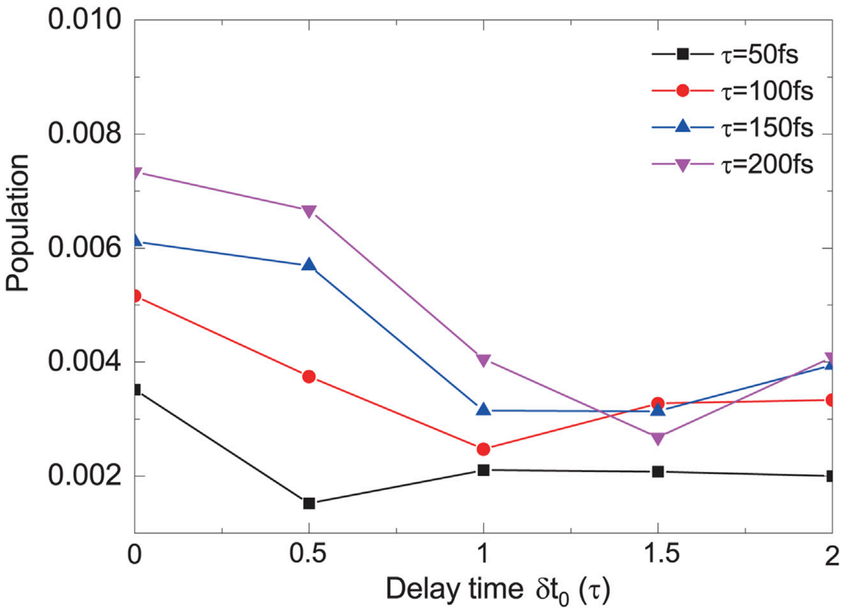

FIGURE 7
The total population of |2⟩, |3⟩, |4⟩ and |5⟩ as a function of the delay time in Case 3 for τ = 50, 100, 150, and 200 fs.

4 Conclusion

We have investigated theoretically the PA dynamics of hot Mg atoms induced by two time-delayed femtosecond laser pulses. In the typical five-electronic-state model, the molecules can be formed on the gerade excited state $(1)^1\Pi_g$ and the three ungerade higher excited states $(1)^1\Pi_u$, $(2)^1\Pi_u$, and $(2)^1\Sigma_u^+$ from the initial ground state $X^1\Sigma_g^+$. Driven by the 840 nm laser pulses, there are one-photon couplings between $(1)^1\Pi_g$ and the three ungerade excited states, two-photon coupling between $X^1\Sigma_g^+$ and $(1)^1\Pi_g$, and three-photon couplings between $X^1\Sigma_g^+$ and the three ungerade excited states. All these couplings are taken into account and it is found that the three-photon coupling plays a dominant role in the PA population transfer process. The three-photon transitions from the initial ground $X^1\Sigma_g^+$ state to the three ungerade higher excited states are strongly dependent on the peak intensity of the laser field. Thus, the pulse delay time δt_0 and the pulse duration τ can greatly influence the final PA populations. The total PA population of the four excited states is obtained with τ varying from 50 to 200 fs and δt_0 varying from 0 to 2τ. For a given δt_0, the parameter τ can induce a significant variation (2 ~ 6.8 times) for the final PA population, and for a given τ, one can also obtain a significant variation (2.7 ~ 3.5 times) of the final PA population by varying δt_0. Additionally, the dynamics of the coherent vibrational wavepackets on the four excited states are also influenced by the two parameters.

Data availability statement

The original contributions presented in the study are included in the article/supplementary material, further inquiries can be directed to the corresponding authors.

Author contributions

RZ performed research, analyzed data and wrote the paper; J-WH analyzed data and wrote the paper; Y-CH designed the research and wrote the paper; BF wrote the paper; MS wrote the paper.

Funding

The project is supported by the National Key R&D Program of China No. 2018YFA0306503; the National Natural Science Foundation of China under Grant Nos. 21873016, 12174044; International Cooperation Fund Project of DBJI No. ICR2105; the Fundamental Research Funds for the Central Universities (DUT21LK08).

Conflict of interest

The authors declare that the research was conducted in the absence of any commercial or financial relationships that could be construed as a potential conflict of interest.

Publisher's note

References

1. Londono BE, Derevianko A, Mahecha JE, Crubellier A, Luc-Koenig E. Femtosecond pulses and dynamics of molecular photoexcitation: RbCs example. *Phys Rev A* (2012) 85: 033419. doi:10.1103/PhysRevA.85.033419

2. Salzmann W, Mullins T, Eng J, Albert M, Wester R, Weidemüller M, et al. Coherent transients in the femtosecond photoassociation of ultracold molecules. *Phys Rev Lett* (2008) 100:233003. doi:10.1103/PhysRevLett.100.233003

3. Mullins T, Salzmann W, Götz S, Albert M, Eng J, Wester R, et al. Photoassociation and coherent transient dynamics in the interaction of ultracold rubidium atoms with shaped femtosecond pulses. I. Experiment. *Phys Rev A* (2009) 80:063416. doi:10.1103/PhysRevA.80.063416

4. Merli A, Eimer F, Weise F, Lindinger A, Salzmann W, Mullins T, et al. Photoassociation and coherent transient dynamics in the interaction of ultracold rubidium atoms with shaped femtosecond pulses. II. Theory. *Phys Rev A* (2009) 80: 063417. doi:10.1103/PhysRevA.80.063417

5. Salzmann W, Poschinger U, Wester R, Weidemüller M, Merli A, Weber SM, et al. Coherent control with shaped femtosecond laser pulses applied to ultracold molecules. *Phys Rev A* (2006) 73:023414. doi:10.1103/PhysRevA.73.023414

6. Yang WF, Gong SQ, Li RX, Xu ZZ. Coherent population accumulations of multiphoton transitions induced by an ultrashort pulse train in polar molecules. *Phys Rev A* (2006) 74:013407. doi:10.1103/PhysRevA.74.013407

7. Yang J, Chen MD, Shu CC, Hu WH, Cong SL. Rovibrational manipulation of molecular quantum state by a train of ultrashort pulses. *Chem Phys Lett* (2010) 491:156–9. doi:10.1016/j.cplett.2010.04.019

8. Ban T, Aumiler D, Vdović S, Vujičić N, Skenderović H, Pichler G. Coherent population dynamics in rubidium atoms excited by resonant 0π pulses. *Phys Rev A* (2009) 80:023425. doi:10.1103/PhysRevA.80.023425

9. Weiner AM, Leaird DE, Patel JS, Wullert JR. Programmable femtosecond pulse shaping by use of a multielement liquid-crystal phase modulator. *Opt Lett* (1990) 15:326. doi:10.1364/OL.15.000326

10. Wefers MM, Nelson KA. Programmable phase and amplitude femtosecond pulse shaping. *Opt Lett* (1993) 18:2032. doi:10.1364/OL.18.002032

11. Wefers MM, Nelson KA. Generation of high-fidelity programmable ultrafast optical waveforms. *Opt Lett* (1995) 20:1047. doi:10.1364/OL.20.001047

12. Brixner T, krampert G, Niklaus P, Gerber G. Generation and characterization of polarization-shaped femtosecond laser pulses. *Appl Phys B* (2002) 74:s133–44. doi:10.1007/s00340-002-0911-y

13. Zhang W, Huang Y, Xie T, Wang GR, Cong SL. Efficient photoassociation with a slowly-turned-on and rapidly-turned-off laser field. *Phys Rev A* (2010) 82:063411. doi:10.1103/PhysRevA.82.063411

14. Han YC, Hu JW, Wang BB. Thermal-average effects on photoassociation with a slowly-turned-on and rapidly-turned-off laser pulse. *Phys Rev A* (2018) 98:043420. doi:10.1103/PhysRevA.98.043420

15. Zhang W, Wang GR, Cong SL. Efficient photoassociation with a train of asymmetric laser pulses. *Phys Rev A* (2011) 83:045401. doi:10.1103/PhysRevA.83.045401

16. Luc-Koenig E, Kosloff R, Masnou-Seeuws F, Vatasescu M. Photoassociation of cold atoms with chirped laser pulses: Time-dependent calculations and analysis of the adiabatic transfer within a two-state model. *Phys Rev A* (2004) 70:033414. doi:10.1103/PhysRevA.70.033414

17. Luc-Koenig E, Vatasescu M, Masnou-Seeuws F. Optimizing the photoassociation of cold atoms by use of chirped laser pulses. *Eur Phys J D* (2004) 31:239–62. doi:10.1140/epjd/e2004-00161-8

18. Koch CP, Palao JP, Kosloff R, Masnou-Seeuws F. Stabilization of ultracold molecules using optimal control theory. *Phys Rev A* (2004) 70:013402. doi:10.1103/PhysRevA.70.013402

19. Lima EF. Coherent control of the formation of cold heteronuclear molecules by photoassociation. *Phys Rev A* (2017) 95:013411. doi:10.1103/PhysRevA.95.013411

20. Ulmanis J, Deiglmayr J, Repp M, Wester R, Weidemüller M. Ultracold molecules formed by photoassociation: Heteronuclear dimers, inelastic collisions, and interactions with ultrashort laser pulses. *Chem Rev* (2012) 112:4890–927. doi:10.1021/cr300215h

21. Vardi A, Abrashkevich D, Frishman E, Shapiro M. Theory of radiative recombination with strong laser pulses and the formation of ultracold molecules via stimulated photo-recombination of cold atoms. *J Chem Phys* (1997) 107:6166–74. doi:10.1063/1.474282

22. Tannor DJ, Rice SA. Control of selectivity of chemical reaction via control of wave packet evolution. *J Chem Phys* (1985) 83:5013–8. doi:10.1063/1.449767

23. Tannor DJ, Kosloff R, Rice SA. Coherent pulse sequence induced control of selectivity of reactions: Exact quantum mechanical calculations. *J Chem Phys* (1986) 85:5805–20. doi:10.1063/1.451542

24. Lima EF, Ho TS, Rabitz H. Laser-pulse photoassociation in a thermal gas of atoms. *Phys Rev A* (2008) 78:063417. doi:10.1103/PhysRevA.78.063417

25. Levin L, Skomorowski W, Rybak L, Kosloff R, Koch CP, Amitay Z. Coherent control of bond making. *Phys Rev Lett* (2015) 114:233003. doi:10.1103/PhysRevLett.114.233003

26. Wang R, Niu YY, Qiu MH, Han YC. Rovibrational population transfer in the ground state controlled by two coherent laser pulses. *Phys Rev A* (2015) 91:013401. doi:10.1103/PhysRevA.91.013401

27. Dulieu O, Raoult M, Tiemann E. Cold molecules: A chemistry kitchen for physicists. *J Phys B: Mol Opt Phys* (2006) 39:E01. doi:10.1088/0953-4075/39/19/E01

28. Zhang W, Xie T, Huang Y, Cong SL. Enhancing photoassociation efficiency by using a picosecond laser pulse with cubic-phase modulation. *Phys Rev A* (2011) 84:065406. doi:10.1103/PhysRevA.84.065406

29. Kallush S, Carini JL, Gould PL, Kosloff R. Directional quantum-controlled chemistry: Generating aligned ultracold molecules via photoassociation. *Phys Rev A* (2017) 96:053613. doi:10.1103/PhysRevA.96.053613

30. Zhang W, Zhao ZY, Xie T, Wang GR, Huang Y, Cong SL. Photoassociation dynamics driven by a modulated two-color laser field. *Phys Rev A* (2011) 84:053418. doi:10.1103/PhysRevA.84.053418

31. Ndong M, Koch CP. Vibrational stabilization of ultracold KRb molecules: A comparative study. *Phys Rev A* (2010) 82:043437. doi:10.1103/PhysRevA.82.043437

32. Wang R, Niu YY. Control of photodissociation of the molecular ion HD+ with two completely overlapping laser pulses. *Phys Lett A* (2021) 409:127515. doi:10.1016/j.physleta.2021.127515

33. Niu YY, Wang R. Adiabatic population transfer between electronic states of LiH molecule in two picosecond laser pulses. *AIP ADVANCES* (2018) 8:115003. doi:10.1063/1.5052465

34. Rybak L, Amaran S, Levin L, Tomza M, Moszynski R, Kosloff R, et al. Generating molecular rovibrational coherence by two-photon femtosecond photoassociation of thermally hot atoms. *Phys Rev Lett* (2011) 107:273001. doi:10.1103/PhysRevLett.107.273001

35. Hu JW, Han YC. Investigation of photoassociation with full-dimensional thermal-random-phase wavefunctions. *J Chem Phys* (2021) 155:064108. doi:10.1063/5.0059543

36. Hu JW, Yu J, Han YC. Multi-path effect in population transfer dynamics of the photoassociation of hot Mg atoms by a femtosecond laser pulse. *Chem Phys Lett* (2022) 792:139405. doi:10.1016/j.cplett.2022.139405

37. Amaran S, Kosloff R, Tomza M, Skomorowski W, Pawlowski F, Moszynski R, et al. Femtosecond two-photon photoassociation of hot magnesium atoms: A quantum dynamical study using thermal random phase wavefunctions. *J Chem Phys* (2013) 139:164124. doi:10.1063/1.4826350

38. Marston CC, Balint-Kurti GG. The Fourier grid Hamiltonian method for bound state eigenvalues and eigenfunctions. *J Chem Phys* (1989) 91:3571–6. doi:10.1063/1.456888

39. Feit MD, Fleck JA. Solution of the Schrödinger equation by a spectral method II: Vibrational energy levels of triatomic molecules. *J Chem Phys* (1983) 78:301–8. doi:10.1063/1.444501

40. Kosloff RA, Kosloff D. Fourier method solution for the time dependent SchrOdinger equation: A study of the reaction $H^+ + H^2$, D^++HD, and D^++H^2. *J Chem Phys* (1823) 79:1823–33. doi:10.1063/1.445959

41. Bergmann K, Theuer H, Shore BW. Coherent population transfer among quantum states of atoms and molecules. *Rev Mod Phys* (1998) 70:1003–25. doi:10.1103/RevModPhys.70.1003

42. Shore BW. *The theory of coherent atomic excitation*. New York: Wiley (1990).

Frontiers | Frontiers in Physics

TYPE Original Research
PUBLISHED 13 January 2023
DOI 10.3389/fphy.2022.1090973

EDITED BY
Libin Fu,
Graduate School of China Academy of Engineering Physics, China

REVIEWED BY
Arkajit Mandal,
Columbia University, United States
Yue Ban,
Basque Research and Technology Alliance (BRTA), Spain

*CORRESPONDENCE
H. D. Liu,
✉ liuhd100@nenu.edu.cn
H. Y. Sun,
✉ sunhy507@nenu.edu.cn

SPECIALTY SECTION
This article was submitted to Atomic and Molecular Physics,
a section of the journal
Frontiers in Physics

RECEIVED 06 November 2022
ACCEPTED 28 December 2022
PUBLISHED 13 January 2023

CITATION
Liu Y, Zhang YN, Liu HD and Sun HY (2023), Simulation of quantum shortcuts to adiabaticity by classical oscillators.
Front. Phys. 10:1090973.
doi: 10.3389/fphy.2022.1090973

Simulation of quantum shortcuts to adiabaticity by classical oscillators

Yang Liu[1], Y. N. Zhang[1,2], H. D. Liu[1]* and H. Y. Sun[1]*

[1]Center for Quantum Sciences and School of Physics, Northeast Normal University, Changchun, China,
[2]School of Science, Shenyang University of Technology, Shenyang, China

It is known that the dynamics and geometric phase of a quantum system can be simulated by classical coupled oscillators using the quantum–classical mapping method without loss of physics. In this work, we show that this method can also be used to simulate the schemes of quantum shortcuts to adiabaticity, which can quickly achieve the adiabatic effect through a non-adiabatic process. By mapping quantum systems by classical oscillators, two schemes, Berry's "transitionless quantum driving" and the Lewis–Riesenfeld invariant method, are simulated by a corresponding transitionless classical driving method, which keeps adiabatic phase trajectories and acquires Hannay's angle and the classical Lewis–Riesenfeld invariant method by manipulating the configurations of classical coupled oscillators. The classical shortcuts to adiabaticity for the two coupled classical oscillators, which is the classical version of a spin-1/2 in a magnetic field, is employed to illustrate our results and compared with quantum shortcuts-to-adiabaticity methods.

KEYWORDS

shortcut to adiabaticity, quantum–classical mapping, transitionless quantum driving, Lewis–Riesenfeld invariant, geometric phase

1 Introduction

Adiabatic processes of quantum systems have become a significant ingredient in quantum information processing for various practical purposes in metrology, interferometry, quantum computing, and control of chemical interaction [1–4]. Achieving state preparation or transferring the population with high fidelity *versus* parameter fluctuations should take a long time [5–7]. However, there are many instances where we need to speed these operations up to prevent them from suffering decoherence, noise, or losses [8, 9]. Therefore, proposing a way to speed up the adiabatic approaches has drawn considerable attention [10–13]. So far, a variety of techniques to implement shortcuts to adiabaticity (STA) have been proposed [5, 8, 14–21]. Notably, there is a shortcut passage algorithm proposed by Berry called "transitionless quantum driving" (TQD) [10]. This method accelerates adiabatic evolution in a hurry by designing a time-dependent interaction followed by the system exactly [10]. Moreover, Chen et al. put forward another method to accelerate the adiabatic passage using the Lewis–Riesenfeld (LR) invariant to keep the eigenstates of a Hamiltonian from a specified initial to the final configuration in an arbitrary time [8].

Not only STA techniques are developed in quantum systems but there are also dissipationless classical drivings in classical systems [20, 22–26]. Moreover, it is already known that a quantum system in a Hilbert space possesses a mathematically canonical classical Hamiltonian structure in the phase space [27–41]. For example, the structures of their phase spaces are usually regarded as the same [42, 43]. Classical and quantum mechanics can also be embedded in a unified formulation as a quantum–classical hybrid system [44]. There is a way to devote elements of quantum mechanics to classical mechanics, in which we can simulate the microscopic quantum behavior by a transition of the average value from a quantum system Hamiltonian into a classical system consisting of oscillators without losing any physics [45–55]. Therefore, it is possible to map and generalize adiabatic processes and STA for quantum systems to classical systems by the quantum–classical mapping method. As a matter of fact, we are inspired to ask if we can simulate the STA in quantum systems by classical oscillators. Based on this mapping and simulation, can it give specific classical schemes for quantum schemes for the STA as the dissipationless classical driving did? What is the relation between the quantum and classical STA?

In this paper, we first introduce the quantum–classical mapping and the relation between the Berry phase for the original quantum system and Hannay's angle for the mapped classical system in Section 2. In Section 3, we generalize and simulate the two kinds of STA methods, TQD and LR invariant-based methods, for quantum systems into the classical system through the quantum–classical mapping and construct a complete theoretical framework for both methods of achieving the STA in classical systems. On one hand, the TQD method which implements the STA by finding an additional Hamiltonian to drive the system can be simulated by adding an additional driving Hamiltonian to keep adiabatic phase trajectories and acquire Hannay's angle [23, 24]. On the other hand, the LR invariant method which keeps energy eigenstates from a specified initial to the final configuration can also be simulated by manipulating the configurations of classical coupled oscillators [20, 22]. To illustrate these two classical methods, we study the quantum–classical mapping and the two STA methods for a spin-1/2 in a magnetic field, which corresponds to two coupled classical oscillators in Section 4. Finally, we give a conclusion in Section 5.

2 Adiabatic evolution in quantum–classical mapping

We consider an N-level quantum system governed by Hamiltonian $\hat{H}(t)$; its dynamical evolution can be described by the following Schrödinger equation (see Appendix for details):

$$i\hbar \frac{d\psi_n(t)}{dt} = \frac{\partial H_C}{\partial \psi_n^\star}, \tag{1}$$

with the probability amplitudes ψ_n of the state $|\Psi\rangle = \sum_n \psi_n(t)|\psi_n\rangle$ on the bare basis $\{|\psi_n\rangle\}$ and the mean value energy $H_C(\boldsymbol{\psi}, \boldsymbol{\psi}^\star, t) = \langle \Psi|\hat{H}(t)|\Psi\rangle$, where $\boldsymbol{\psi}(\boldsymbol{t}) = (\psi_1(t), \ldots, \psi_n(t), \ldots, \psi_N(t))^T$. To study the adiabatic evolution of the system, it is convenient to transform the bare basis $\{|\psi_n\rangle\}$ into the adiabatic basis $\{|E_k(t)\rangle\}$, which consists of the time-dependent eigenstates $|E_k(t)\rangle$ of the Hamiltonian $\hat{H}(t)$. The amplitudes $\boldsymbol{\varphi}(\boldsymbol{t}) = [\varphi_1(t), \ldots, \varphi_n(t), \ldots, \varphi_N(t)]^T$ on the adiabatic basis are determined by $|\Psi\rangle = \sum_k \varphi_k(t)|E_k(t)\rangle$. These two bases can be connected by the unitary transformation given as follows:

$$\boldsymbol{\psi}(t) = \boldsymbol{U}(t)\boldsymbol{\varphi}(t), \tag{2}$$

with $U_{nk} = \langle \psi_n|E_k(t)\rangle$. By the adiabatic theorem, the probability $|\varphi_k(t)|^2$ remains unchanged in the adiabatic limit. The phase of the amplitudes φ_k accumulated *via* evolution includes a dynamic phase $\int E_k(t)dt$ and a Berry phase $\gamma_k = \int \langle E_k(t)|d_t E_k(t)\rangle dt$ [56].

This quantum adiabatic evolution can be equivalently mapped into a classical one without losing any physics [45, 46, 52]. If we decompose ψ_n into real and imaginary parts $\psi_n(t) = [q_n(t) + i p_n(t)]/\sqrt{2\hbar}$, the Schrödinger equation and its complex conjugate can be written as Hamilton canonical Eqs 46, 47, 53, shown as follows:

$$\dot{q}_n = \frac{\partial H_C}{\partial p_n}, \quad \dot{p}_n = -\frac{\partial H_C}{\partial q_n}. \tag{3}$$

The Hamiltonian $H_C(\boldsymbol{\psi}, \boldsymbol{\psi}^\star, t)$ can be transformed into $h(\boldsymbol{q}, \boldsymbol{p}, t)$, and the quantum dynamics in Eq. 1 can be represented by the classical evolution of the "position variable $\boldsymbol{q}(t)$" and "momentum variable $\boldsymbol{p}(t)$" in Eq. 3.

The adiabatic evolution of adiabatic states can also be mapped to a classical one. One can introduce a new pair of variables $(\boldsymbol{\theta}, \boldsymbol{I})$ corresponding to the amplitudes on the adiabatic basis by

$$\varphi_k(t) = \sqrt{\frac{I_k}{\hbar}} e^{-i\theta_k(t)} \tag{4}$$

and the Hamiltonian changes into [52]

$$H_C(\boldsymbol{\theta}, \boldsymbol{I}, t) = \sum_k E_k(t) I_k \Big/ \hbar + \frac{\partial S(\boldsymbol{q}, \boldsymbol{I}, t)}{\partial t}, \tag{5}$$

where $E_k(t)$ corresponds to the eigenvalues of the Hamiltonian $\hat{H}$, with corresponding eigenstates $|E_k(t)\rangle$. $S(\boldsymbol{q}, \boldsymbol{I}, t)$ is the generating function of the classical transformation $(\boldsymbol{q}(t), \boldsymbol{p}(t)) \rightarrow (\boldsymbol{\theta}(t), \boldsymbol{I})$

$$\begin{aligned} p_n(t) &= \sum_k \sqrt{2I_k}\{\cos\theta_k \mathrm{Im}[U_{nk}(t)] - \sin\theta_k \mathrm{Re}[U_{nk}(t)]\}, \\ q_n(t) &= \sum_k \sqrt{2I_k}\{\cos\theta_k \mathrm{Re}[U_{nk}(t)] + \sin\theta_k \mathrm{Im}[U_{nk}(t)]\} \end{aligned} \tag{6}$$

between the position–momentum variable and action–angle variable, which corresponds to the quantum unitary transformation $|E_k(t)\rangle = \sum_n U_{nk}(t)|\psi_n\rangle$ between the adiabatic basis and the bare basis. Under the adiabatic evolution, it has been proved that the two new variables $\boldsymbol{\theta}(t)$ and $\boldsymbol{I}$ satisfy the same canonical equations as the angle–action variables in classical mechanics [46], given as follows:

$$\dot{\theta}_k = E_k(t)/\hbar - \frac{\partial A_H(\boldsymbol{I}; t)}{\partial I_k}, \quad \dot{I}_k = 0. \tag{7}$$

Like the Berry phase, the adiabatic evolution will accumulate a dynamic angle $\int E_k(t)/\hbar dt$ and an additional angle onto the angle variable called Hannay's angle [57].

$$\Delta\theta_k(\boldsymbol{I}) = -\frac{\partial}{\partial I_k}\int A_H(\boldsymbol{I}; t), \tag{8}$$

where

$$\begin{aligned} A_H(\boldsymbol{I}; t) &= \langle \boldsymbol{p}(\boldsymbol{\theta}, \boldsymbol{I}; t)\partial_t \boldsymbol{q}(\boldsymbol{\theta}, \boldsymbol{I}; t)\rangle_\theta \\ &= \frac{1}{(2\pi)^N}\int d\theta \sum_n p_n(\boldsymbol{\theta}, \boldsymbol{I}; t)\partial_t q_n(\boldsymbol{\theta}, \boldsymbol{I}; t) \end{aligned} \tag{9}$$

is the angle connection for Hannay's angle [51]. The angular brackets $\langle \cdots \rangle_\theta$ denote the averaging over all angles $\boldsymbol{\theta}$ (this averaging process is called the averaging principle, which can be treated as the classical adiabatic approximation), and ∂_t is defined as $\partial_t F(t) = \frac{\partial F(t)}{\partial t}$. It can be proved that $A_H = \sum_k i I_k A_B(k; t)$ [52]. We note that $A_B(k; t)$ is nothing but a one-form for the Berry phase [51], and this means that Hannay's angle is exactly equal to the minus Berry phase of the original quantum system [48, 52], which is given as follows:

$$\Delta\theta_k(\boldsymbol{I}) = -\frac{\partial}{\partial I_k}\int A_H(\boldsymbol{I}; t) = -i\int A_B(k; t) = -\gamma_k. \tag{10}$$

So far, a quantum adiabatic evolution and its Berry phase can be perfectly mapped to a classical one and its Hannay's angle. Next, we will show that the two different methods for the quantum STA can also

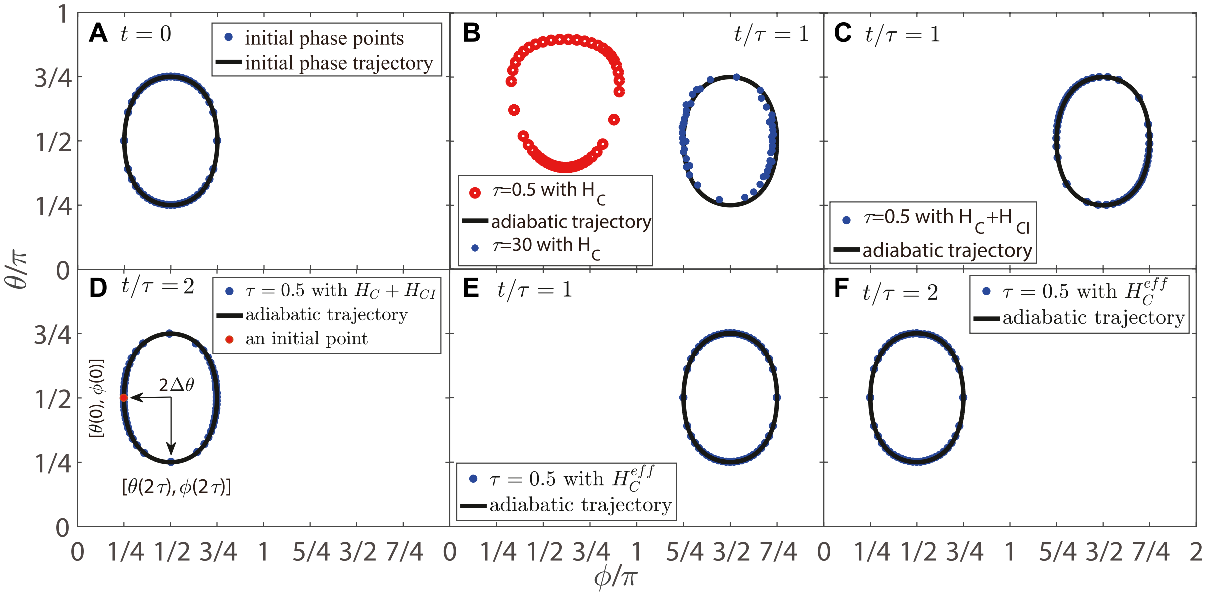

FIGURE 1
(A) Initial phase trajectory (solid line) and initial phase points (blue dots). **(B)** Final adiabatic trajectory (solid line) and final phase points driven by H_C when $t/\tau = 1$, $\tau = .5$ (red dot blanks) and $\tau = 30$ (blue dots). **(C)** Final adiabatic trajectory (solid line) and final phase points driven by $H_C + H_{CI}$, when $t/\tau = 1$ and $\tau = .5$ (blue dots). **(D)** Final adiabatic trajectory (solid line) and final phase points driven by $H_C + H_{CI}$, when $t/\tau = 2$ and $\tau = .5$ (blue dots). **(E)** Final adiabatic trajectory (solid line) and final phase points driven by H_I^{eff}, when $t/\tau = 1$ and $\tau = .5$ (blue dots). **(F)** Final adiabatic trajectory (solid line) and final phase points driven by H_I^{eff}, when $t/\tau = 2$ and $\tau = .5$ (blue dots).

be mapped to classical systems. It will not only connect the current methods for the classical STA to the quantum ones but also shed more light on the classical methods.

3 Shortcut to adiabaticity: From a quantum to classical system

3.1 Transitionless classical driving

We first discuss the transitionless tracking algorithm. For the non-adiabatic quantum driving, the quantum evolution cannot be restricted to an eigenstate, whatever the initial state is. According to the STA proposed by Berry, for the Hamiltonian $\hat{H}(t)$ we discussed in the previous section, if we want to keep no transitions between the eigenstates

$$|\varphi_n(t)\rangle = e^{i(\beta_n+\gamma_n)}|E_n(t)\rangle \tag{11}$$

of $\hat{H}(t)$ in the exact quantum evolution without the adiabatic approximation with the dynamic phase $\beta_n = -\frac{1}{\hbar}\int_0^t E_n(\tau)\mathrm{d}\tau$ and the geometric phase $\gamma_n = i\int_0^t \int \langle E_n(\tau)|\partial_\tau E_n(\tau)\rangle \mathrm{d}\tau$, we need an effective TQD Hamiltonian [10], given as follows:

$$\hat{H}_{eff} = \sum_n |E_n(t)\rangle E_n(t)\langle E_n(t)| + i\hbar \sum_n \left(|\partial_t E_n(t)\rangle\langle E_n(t)| - \langle E_n(t)|\partial_t E_n(t)\rangle |E_n(t)\rangle\langle E_n(t)|\right). \tag{12}$$

To drive state Eq. 11, the first sum in Eq. 12 is exactly the original Hamiltonian $\hat{H}(t)$ represented by the adiabatic basis, and the second sum contains two terms that cancel the transition between eigenstates and generate the accumulated Berry phase, respectively.

Similarly, for non-adiabatic classical driving, the evolution of the canonical coordinates $\boldsymbol{q}$ and $\boldsymbol{p}$ will also fail to keep the action variable $\boldsymbol{I}$ unchanged without the averaging principle, and their trajectories in the phase space will not follow adiabatic trajectories (see Figure 1B). Accordingly, the action variable $\boldsymbol{I}$ will be conserved in a classical evolution as long as the additional effects caused by the time-dependent canonical transformation are canceled. This means that if we want the Hamiltonian function driving the canonical variables as Eq. 7 without the average principle, the transitionless classical driving (TCD, no transition between action variables) Hamiltonian function can be written as follows [25]:

$$\begin{aligned} H_C^{eff}(\boldsymbol{I};t) &= H_C(\boldsymbol{I};\boldsymbol{\theta};t) + H_{CI}(\boldsymbol{I};\boldsymbol{\theta};t) \\ &= H_C(\boldsymbol{I};\boldsymbol{\theta};t) - \frac{\partial F}{\partial t} - A_H. \end{aligned} \tag{13}$$

With the quantum−classical mapping method we introduced in the last section, we can derive a more explicit form of the TCD Hamiltonian H_C^{eff} by averaging TQD Hamiltonian $\hat{H}_{eff}$ Eq. 12. After a straightforward derivation, we have

$$\begin{aligned} H_C^{eff} &= \langle\psi|\hat{H}_{eff}|\psi\rangle \\ &= \sum_n E_n|\varphi_n|^2 + i\hbar \sum_{n,m\neq n} \varphi_m^\star \varphi_n \langle E_m|\partial_t E_n\rangle \\ &= \sum_n I_n\omega_n - \sum_n \langle p_n(\boldsymbol{\theta},\boldsymbol{I};t)\partial_t q_n(\boldsymbol{\theta},\boldsymbol{I};t)\rangle_\theta \\ &\quad + \frac{1}{2}\sum_n \left[p_n(\boldsymbol{\theta},\boldsymbol{I};t)\partial_t q_n(\boldsymbol{\theta},\boldsymbol{I};t) - q_n(\boldsymbol{\theta},\boldsymbol{I};t)\partial_t p_n(\boldsymbol{\theta},\boldsymbol{I};t)\right] \\ &= \sum_n I_n\omega_n - \sum_n \partial_t\left[p_n(\boldsymbol{\theta},\boldsymbol{I};t)q_n(\boldsymbol{\theta},\boldsymbol{I};t)\right], \end{aligned} \tag{14}$$

where $\omega_n = E_n/\hbar$ and the angular brackets $\langle\cdots\rangle$ denote the averaging over all angle variables $\frac{1}{(2\pi)^N}\Pi_k^N \int_0^{2\pi} d\theta_k$. Comparing Eq. 13 with Eq. 9, the terms canceling the non-adiabatic evolution and generating Hannay's angle can be written as follows:

$$\begin{aligned}\frac{\partial F}{\partial t} &= -\frac{1}{2}\sum_n\left[q_n(\boldsymbol{\theta},\boldsymbol{I};t)\partial_t p_n(\boldsymbol{\theta},\boldsymbol{I};t) - p_n(\boldsymbol{\theta},\boldsymbol{I};t)\partial_t q_n(\boldsymbol{\theta},\boldsymbol{I};t)\right],\\ A_H &= \sum_n\langle p_n(\boldsymbol{\theta},\boldsymbol{I};t)\partial_t q_n(\boldsymbol{\theta},\boldsymbol{I};t)\rangle_\theta,\end{aligned} \tag{15}$$

respectively. Like the TQD, the choice of eigenfrequencies ω_n can be arbitrary and the geometric angles can be dropped for keeping the actions $\boldsymbol{I}$ conserved [10]. The simplest form of the Hamiltonian driving the canonical coordinates $\boldsymbol{q}$ and $\boldsymbol{p}$ with the conserved action $\boldsymbol{I}$ can be written as follows:

$$H_I^{eff} = \frac{1}{2}\sum_n\left[p_n(\boldsymbol{\theta},\boldsymbol{I};t)\partial_t q_n(\boldsymbol{\theta},\boldsymbol{I};t) - q_n(\boldsymbol{\theta},\boldsymbol{I};t)\partial_t p_n(\boldsymbol{\theta},\boldsymbol{I};t)\right]. \tag{16}$$

3.2 LR invariant-based scheme

A different approach to realize the quantum STA is based on the LR invariants [8, 58]. For the Hamiltonian $\hat{H}(t)$, a time-dependent invariant can be determined by

$$i\hbar\frac{\partial\hat{I}(t)}{\partial t} + \left[\hat{I}(t),\hat{H}(t)\right] = 0. \tag{17}$$

The eigenvalues λ_n of $\hat{I}(t)$ remain constant over time, and the time-dependent eigenstates $|\lambda_n(t)\rangle$ will accumulate an LR phase

$$\Omega_n(t) = \frac{1}{\hbar}\int_0^t\langle\lambda_n(\tau)|i\hbar\frac{\partial}{\partial\tau} - H(\tau)|\lambda_n(\tau)\rangle d\tau \tag{18}$$

via the dynamical evolution. By using the time-dependent unitary evolution operator

$$U = \sum_n e^{i\Omega_n(t)}|\lambda_n(t)\rangle\langle\lambda(0)|, \tag{19}$$

the Hamiltonian can be written as follows [8]:

$$\hat{H}_d \equiv i\hbar(\partial_t U)U^\dagger = -\hbar\sum_n|\lambda_n(t)\rangle\dot{\Omega}_n\langle\lambda_n(t)| + i\hbar\sum_n|\partial_t\lambda_n(t)\rangle\langle\lambda_n(t)|, \tag{20}$$

where the second term can be used to drive the eigenstates $|\lambda_n(t)\rangle$ of $\hat{I}(t)$ and generate the LR phase. Without loss of generality, the arbitrariness of choosing H_d can be fixed by the constrain $[\hat{I}(0),\hat{H}(0)] = 0$ and $[\hat{I}(t),\hat{H}(t)] = 0$ [8]. Invariant condition Eq. 17 can also be derived by comparing Eq. 20 with the original form of $\hat{H}(t)$. Therefore, one can design an evolution path from the initial Hamiltonian $\hat{H}(0)$ to the final one $\hat{H}(T)$ along one of the eigenstates $|\lambda_n(t)\rangle$ of $\hat{I}(t)$ to achieve the STA.

For a classical system, we can also find similar classical time-dependent invariants that satisfy

$$\dot{J}_k = \frac{\partial J_k(t)}{\partial t} + \{J_k(t), H_C(\boldsymbol{q},\boldsymbol{p};t)\} = 0. \tag{21}$$

By introducing a new pair of variables including the time-dependent invariants ($\boldsymbol{\xi}$, $\boldsymbol{J}$) (hereafter referred to as LR variables), we have the following canonical equations:

$$\dot{J}_k = -\frac{\partial G(\boldsymbol{\alpha},t)}{\partial\xi_k} = 0,\quad \dot{\xi}_k = \frac{\partial G(\boldsymbol{\alpha},t)}{\partial J_k}, \tag{22}$$

where $G(\boldsymbol{\xi}, t) = H_C(\boldsymbol{\xi}, \boldsymbol{J}, t) + S(\boldsymbol{\xi}, \boldsymbol{J}, t)$ is the Hamiltonian after a classical transformation $(\boldsymbol{q}(t), \boldsymbol{p}(t)) \rightarrow (\boldsymbol{\xi}(t), \boldsymbol{J})$ with the generating function $S(\boldsymbol{q}, \boldsymbol{I}, t)$. Since J_k are invariants, the Hamiltonian $G(\boldsymbol{\xi}, t)$ does not contain the angle variables ξ_k. The changes of angles then can be rewritten as follows:

$$\begin{aligned}\Delta\xi_k &= \int_0^T dt\left(\frac{\partial\langle H_C(\boldsymbol{\xi},\boldsymbol{J},t)\rangle_\xi}{\partial I_k} + \frac{\partial\langle S(\boldsymbol{\xi},\boldsymbol{J},t)\rangle_\xi}{\partial I_k}\right),\\ &= \int_0^T dt\left(\frac{\partial\bar{H}_C(\boldsymbol{J},t)}{\partial I_k} - \frac{\partial A_{LR}(\boldsymbol{J},t)}{\partial I_k}\right)\end{aligned} \tag{23}$$

with $\bar{H}_C(\boldsymbol{J},t) \equiv \langle H_C(\boldsymbol{\xi},\boldsymbol{J},t)\rangle_\xi$ and $A_{LR}(\boldsymbol{J},t) \equiv \sum_n\langle p_n(\boldsymbol{\xi},\boldsymbol{J},t)\partial_t q_n(\boldsymbol{\xi},\boldsymbol{J},t)\rangle_\xi$ which is similar to the dynamical part and geometrical part in the angle changes of the classical adiabatic evolution. The angular brackets $\langle\cdots\rangle_\xi$ denote an averaging over all LR angles $\boldsymbol{\xi}$. Note that these LR variables are generally not action–angle variables of H_C. However, we can set $\{J_k(0), H_C(0)\} = \{J_k(T), H_C(T)\} = 0$; the LR action variables J_k can, thus, be chosen as action variables that are related to the eigenfrequencies at initial time $t = 0$ and final time $t = T$. Similar to the quantum STA based on LR invariants, we can also design an evolution path from $H_C(0)$ to $H_C(T)$ with the invariants J_k, in which the initial action variables of H are equal to those in the final time.

To determine the specific form of the classical LR invariant-based scheme, we define the probabilities amplitudes d_k of $|\Psi\rangle = \sum_k d_k|\lambda_k\rangle$ on the LR basis $\{|\lambda_k\rangle\}$ as

$$d_k = \sqrt{\frac{J_k}{\hbar}}e^{-i\xi_k}, \tag{24}$$

using the quantum–classical mapping method. The canonical transformation ($\boldsymbol{q}$, $\boldsymbol{p}$) → ($\boldsymbol{\xi}$, $\boldsymbol{J}$) between position–momentum variables and LR variables can correspond to the quantum unitary transformation $|\lambda_k(t)\rangle = \sum_n U_{nk}(t)|\psi_n\rangle$ between the adiabatic basis and the bare basis given as follows:

$$\begin{aligned}p_n(t) &= \sum_k\sqrt{2J_k}\{\cos\xi_k\mathrm{Im}[U_{nk}(t)] - \sin\xi_k\mathrm{Re}[U_{nk}(t)]\},\\ q_n(t) &= \sum_k\sqrt{2J_k}\{\cos\xi_k\mathrm{Re}[U_{nk}(t)] + \sin\xi_k\mathrm{Im}[U_{nk}(t)]\}.\end{aligned} \tag{25}$$

Similar to the classical TQD scheme of the STA, the driving Hamiltonian should cancel the effect of the time-dependent transformation S and generate the angle $\Delta\xi_k$. By Eqs 13–23, we have

$$\begin{aligned}H_d &= \bar{H}_C(\boldsymbol{J},t) - A_{LR}(\boldsymbol{J},t) - \frac{\partial S}{\partial t}\\ &= \langle H_C(\boldsymbol{\xi},\boldsymbol{J},t)\rangle_\xi - \sum_n\langle p_n(\boldsymbol{\xi},\boldsymbol{J},t)\partial_t q_n(\boldsymbol{\xi},\boldsymbol{J},t)\rangle_\xi\\ &\quad+\frac{1}{2}\sum_n\left[p_n(\boldsymbol{\xi},\boldsymbol{J};t)\partial_t q_n(\boldsymbol{\xi},\boldsymbol{J};t) - q_n(\boldsymbol{\xi},\boldsymbol{J};t)\partial_t p_n(\boldsymbol{\xi},\boldsymbol{J};t)\right],\end{aligned} \tag{26}$$

with

$$\frac{\partial S}{\partial t} = -\frac{1}{2}\sum_n\left[p_n(\boldsymbol{\xi},\boldsymbol{J};t)\partial_t q_n(\boldsymbol{\xi},\boldsymbol{J};t) - q_n(\boldsymbol{\xi},\boldsymbol{J};t)\partial_t p_n(\boldsymbol{\xi},\boldsymbol{J};t)\right]. \tag{27}$$

According to the quantum–classical mapping, this classical Hamiltonian of LR invariants method is just the mean value of the quantum LR, given as follows:

$$H_d = \langle \psi | \hat{H}_d | \psi \rangle. \tag{28}$$

Therefore, the form of LR variables can be determined by equating H_d and H_C, and the boundary conditions are as follows:

$$\{J_k(0), H_C(0)\} = \{J_k(T), H_C(T)\} = 0. \tag{29}$$

On the contrary, we can design the classical Hamiltonian H_d from the evolution of LR variables to realize the classical LR invariant-based scheme.

4 Spin-1/2 in a magnetic field

To illustrate our results, we consider the adiabatic evolution and STA scheme for a simple two-level quantum system, i.e., a spin-half particle with the magnetic moment μ in an external magnetic field $\boldsymbol{B} = B(\sin\alpha\cos\beta,\ \sin\alpha\sin\beta,\ \cos\alpha)$. Its Hamiltonian reads

$$\begin{aligned}\hat{H} &= -\mu\hat{\boldsymbol{\sigma}}\cdot\boldsymbol{B} = -\mu B\begin{pmatrix}\cos\alpha & \sin\alpha e^{-i\beta}\\ \sin\alpha e^{i\beta} & -\cos\alpha\end{pmatrix}\\ &= -\mu B\left[\cos\alpha\left(|+\rangle\langle+| - |-\rangle\langle-|\right) + \sin\alpha\left(e^{-i\beta}|+\rangle\langle-| + e^{i\beta}|-\rangle\langle+|\right)\right],\end{aligned} \tag{30}$$

where $\hat{\boldsymbol{\sigma}} = (\hat{\sigma}_1, \hat{\sigma}_2, \hat{\sigma}_3)$ are Pauli matrices and $|\pm\rangle$ are the two spin eigenstates.

4.1 Transitionless classical driving

As we introduced in the previous section, if the two spin eigenstates $|\pm\rangle$ are chosen as the basis, the Hamiltonian in Eq. 30 can be mapped to the classical Hamiltonian of a coupled oscillator, given as follows:

$$\begin{aligned}h(\boldsymbol{p}, \boldsymbol{q}; \boldsymbol{B}) = -\frac{\mu B}{\hbar}\Big[\frac{1}{2}\left(p_2^2 + q_2^2 - p_1^2 - q_1^2\right)\cos\alpha\\ +\left(p_1 q_2 - p_2 q_1\right)\sin\alpha\sin\beta + \left(q_1 q_2 + p_1 p_2\right)\sin\alpha\cos\beta\Big],\end{aligned} \tag{31}$$

with $|\psi\rangle = \psi_1|-\rangle + \psi_2|+\rangle$ and $\psi_j = (q_j + ip_j)/\sqrt{2\hbar}$, $(j = 1, 2)$. The canonical variables $(\boldsymbol{q}, \boldsymbol{p})$ satisfy the normalization condition [46], shown as follows:

$$\sum_{j=1}^{2}\left(p_j^2 + q_j^2\right) = 2\hbar. \tag{32}$$

It is interesting to note that by defining a vector $\boldsymbol{S} = (S_1, S_2, S_3)$ with

$$\begin{cases} S_1 = \langle\sigma_1\rangle = \left(q_1 q_2 + p_1 p_2\right)/\hbar,\\ S_2 = \langle\sigma_2\rangle = \left(p_1 q_2 - p_2 q_1\right)/\hbar,\\ S_3 = \langle\sigma_3\rangle = \left(p_2^2 + q_2^2 - p_1^2 - q_1^2\right)/(2\hbar),\end{cases} \tag{33}$$

the Hamiltonian function can be written as follows:

$$h(\boldsymbol{S}; \mathbf{B}) = -\mu\boldsymbol{S}\cdot\mathbf{B}, \tag{34}$$

where the normalization condition of $\boldsymbol{S}$ is $S^2 \equiv S_1^2 + S_2^2 + S_3^2 = 1$, and their Poisson bracket has a relation with the quantum commutator, shown as follows [45]:

$$\left\{S_i, S_j\right\} = 2\varepsilon_{ijk}S_k\Big/\hbar = \frac{1}{i\hbar}\langle\psi|\left[\hat{\sigma}_i, \hat{\sigma}_j\right]|\psi\rangle. \tag{35}$$

We now move to calculate Hannay's angle. Since the Hamiltonian in Eq. 30 has two eigenstates,

$$\begin{aligned}|E_1\rangle &= \cos\frac{\alpha}{2}|+\rangle + \sin\frac{\alpha}{2}e^{i\beta}|-\rangle,\\ |E_2\rangle &= -\sin\frac{\alpha}{2}|+\rangle + \cos\frac{\alpha}{2}e^{i\beta}|-\rangle,\end{aligned} \tag{36}$$

with eigenenergies $-\mu B$ and μB, respectively. The canonical transformation $(\boldsymbol{q}, \boldsymbol{p}) \to (\boldsymbol{\theta}, \boldsymbol{I})$ and the mapped Hamiltonian function can be written as follows:

$$\begin{aligned}q_1 &= \sqrt{2I_1}\sin\frac{\alpha}{2}\cos(\beta - \theta_1) + \sqrt{2I_2}\cos\frac{\alpha}{2}\cos(\beta - \theta_2),\\ q_2 &= \sqrt{2I_1}\cos\frac{\alpha}{2}\cos\theta_1 - \sqrt{2I_2}\sin\frac{\alpha}{2}\cos\theta_2,\\ p_1 &= \sqrt{2I_1}\sin\frac{\alpha}{2}\sin(\beta - \theta_1) + \sqrt{2I_2}\cos\frac{\alpha}{2}\sin(\beta - \theta_2),\\ p_2 &= -\sqrt{2I_1}\cos\frac{\alpha}{2}\sin\theta_1 + \sqrt{2I_2}\sin\frac{\alpha}{2}\sin\theta_2,\\ \bar{h}(\boldsymbol{I}; \boldsymbol{B}) &= \mu B(I_2 - I_1)/\hbar.\end{aligned} \tag{37}$$

We can calculate the forms of variable $\boldsymbol{I}$ by the following:

$$\begin{aligned}I_1 &= \frac{\hbar}{2}(1 + \boldsymbol{S}\cdot\boldsymbol{b}),\\ I_2 &= \frac{\hbar}{2}(1 - \boldsymbol{S}\cdot\boldsymbol{b})\end{aligned} \tag{38}$$

with $\boldsymbol{q} = (q_1, q_2)$, $\boldsymbol{p} = (p_1, p_2)$, $\boldsymbol{\theta} = (\theta_1, \theta_2)$, $\boldsymbol{I} = (I_1, I_2)$, and $\boldsymbol{b} = \boldsymbol{B}/B$.

Therefore, we obtain the angle one-form by Eq. 9, given as follows:

$$A_H = -\frac{1}{2}(1 - \cos\alpha)\dot{\beta}I_1 - \frac{1}{2}(1 + \cos\alpha)\dot{\beta}I_2. \tag{39}$$

Hannay's angles can, thus, be obtained by Eq. 10, given as follows:

$$\begin{aligned}\Delta\theta_1 &= \oint\frac{1}{2}(1 - \cos\alpha)\dot{\beta}dt,\\ \Delta\theta_2 &= \oint\frac{1}{2}(1 + \cos\alpha)\dot{\beta}dt,\end{aligned} \tag{40}$$

which differ from the Berry phases in the original quantum Hamiltonian [58] only by a sign.

By Eq. 14, we have the following:

$$\begin{aligned}H_I^{eff} &= \frac{1}{2}\left[\left(-p_1^2 - q_1^2\right)\dot{\beta} + \left(p_1 q_2 - p_2 q_1\right)\cos\beta\dot{\alpha} - \left(p_1 p_2 + q_1 q_2\right)\sin\beta\dot{\alpha}\right]\\ &= \frac{\hbar}{2}\left[(S_3 - 1)\dot{\beta} + S_2\cos\beta\dot{\alpha} - S_1\sin\beta\dot{\alpha}\right],\end{aligned} \tag{41}$$

$$\begin{aligned}A_H &= -\frac{1}{2}(1 - \cos\alpha)I_1 - \frac{1}{2}(1 + \cos\alpha)I_2\\ &= -\frac{\hbar}{4}\left[(1 - \cos\alpha)(1 + \boldsymbol{S}\cdot\boldsymbol{b}) + (1 + \cos\alpha)(1 - \boldsymbol{S}\cdot\boldsymbol{b})\right]\\ &= -\frac{\hbar}{2}(1 - \cos\alpha\boldsymbol{S}\cdot\boldsymbol{b}).\end{aligned} \tag{42}$$

Therefore, we can get the TCD Hamiltonian function

$$\begin{aligned}H_{CI}(\boldsymbol{I}; \boldsymbol{\theta}; \boldsymbol{X}) &= \frac{\hbar}{2}\left[(S_3 - 1)\dot{\beta} + S_2\cos\beta\dot{\alpha} - S_1\sin\beta\dot{\alpha}\right] + \frac{\hbar}{2}(1 - \cos\alpha\boldsymbol{S}\cdot\boldsymbol{b})\dot{\beta}\\ &= \frac{\hbar}{2B^2}\boldsymbol{S}\cdot\left(\boldsymbol{B}\times\frac{\partial\boldsymbol{B}}{\partial t}\right),\end{aligned} \tag{43}$$

which takes a similar form as the counter-adiabatic driving Hamiltonian for spin-1/2 system Eq. 30. This means that the TCD scheme can be treated like a classical version of the TQD scheme by representing coordinate–momentum variables by the classical "spin" defined by Eq. 33.

We illustrate the evolution of the states through their trajectories in the phase space. The evolution of the points on phase trajectories can be determined by the dynamic equation of classical "spin," given as follows:

$$\dot{S}_i = \{S_i, H_C\} = \frac{-2\mu B}{\hbar}\varepsilon_{ijk}\left(b_j S_k - b_k S_j\right). \tag{44}$$

By defining $\theta = \arccos S_2$ and $\phi = \arctan S_2/S_1$, the dynamics of the original Hamiltonian H_C takes the following form:

$$\begin{aligned}\dot{\theta} &= \frac{-2\mu B}{\hbar}\sin\alpha\sin(\beta-\phi),\\ \dot{\phi} &= \frac{-2\mu B}{\hbar}\left[\cos\alpha - \frac{\sin\alpha\cos(\beta-\phi)}{\tan\theta}\right].\end{aligned} \tag{45}$$

The parameters of the magnetic field B are chosen as

$$\begin{aligned}\alpha &= \frac{\pi}{2} - \frac{\pi}{4}\sin\frac{\pi t}{\tau}, \quad & \beta &= \pi - \frac{\pi}{2}\cos\frac{\pi t}{\tau},\\ \dot{\alpha} &= -\frac{\pi^2}{4\tau}\cos\frac{\pi t}{\tau}, \quad & \dot{\beta} &= \frac{\pi^2}{2\tau}\sin\frac{\pi t}{\tau},\end{aligned} \tag{46}$$

and $\mu B/\hbar = -1$.

As shown in Figure 1B, the evolution of the canonical coordinates $\boldsymbol{p}$ and $\boldsymbol{q}$ will keep the action variable $\boldsymbol{I}$ almost unchanged, and their trajectories in the phase space will follow adiabatic trajectories when the frequency is slow.

For the TCD Hamiltonian $H_C + H_{CI}$, the effective magnetic field changes into the following:

$$\begin{aligned}\boldsymbol{B}_{eff} &= \boldsymbol{B} - \frac{\hbar}{2\mu}\left(\boldsymbol{b}\times\dot{\boldsymbol{b}}\right)\\ &= B\left\{\left[\sin\alpha\cos\beta + \frac{\hbar}{2\mu B}\left(\sin\beta\dot{\alpha} + \sin\alpha\cos\alpha\cos\beta\dot{\beta}\right)\right]\boldsymbol{i}\right.\\ &\quad \left.+\left[\sin\alpha\sin\beta - \frac{\hbar}{2\mu B}\left(\cos\beta\dot{\alpha} - \sin\alpha\cos\alpha\sin\beta\dot{\beta}\right)\right]\boldsymbol{j}+\left(\cos\alpha - \frac{\hbar}{2\mu B}\sin^2\alpha\dot{\beta}\right)\boldsymbol{k}\right\}.\end{aligned} \tag{47}$$

The dynamics of the TCD Hamiltonian can, thus, be written as follows:

$$\begin{aligned}\dot{\theta} &= \cos(\beta-\phi)\dot{\alpha} - \sin\alpha\sin(\beta-\phi)\left(\frac{2\mu B}{\hbar} + \cos\alpha\dot{\beta}\right),\\ \dot{\phi} &= -\frac{2\mu B}{\hbar}\cos\alpha + \sin^2\alpha\dot{\beta} + \frac{\sin\alpha\cos(\beta-\phi)(2\mu B/\hbar + \cos\alpha\dot{\beta}) + \sin(\beta-\phi)\dot{\alpha}}{\tan\theta}.\end{aligned} \tag{48}$$

To drive the eigenstates using $H_C + H_{CI}$, the evolution of the canonical coordinates $\boldsymbol{p}$ and $\boldsymbol{q}$ will keep action variables $\boldsymbol{I}$ unchanged, and their trajectories in the phase space will follow adiabatic trajectories no matter how fast the frequency is (see Figures 1C, D). By tracing the same phase points of the initial phase trajectory (see Figure 1A) and the final adiabatic trajectory, we can find that there is an angle of shift after an adiabatic evolution. Also, the angle of shift after a whole period is double that after half a period.

Moreover, for the simplest Hamiltonian Eq. 41 [dropping the constant term and the term generating the Hannay's angle Eq. 42], the dynamics of the simplest Hamiltonian H_I^{eff} is determined by the following:

$$\begin{aligned}\dot{\theta} &= \cos(\beta-\phi)\dot{\alpha},\\ \dot{\phi} &= \dot{\beta} + \frac{\sin(\beta-\phi)\dot{\alpha}}{\tan\theta}.\end{aligned} \tag{49}$$

It is easy to find that the adiabatic trajectories will remain unchanged after any period (see Figures 1E, F).

4.2 Classical LR invariant

In the approach of the LR invariant, the eigenstates of the LR invariant parallel to the eigenstates in Eq. 36 can be constructed as follows [8]:

$$\begin{aligned}|\lambda_1\rangle &= \cos\frac{\eta}{2}\,|+\rangle + \sin\frac{\eta}{2}e^{i\delta}|-\rangle,\\ |\lambda_2\rangle &= -\sin\frac{\eta}{2}\,|+\rangle + \cos\frac{\eta}{2}e^{i\delta}|-\rangle,\end{aligned} \tag{50}$$

and the LR invariant can be expressed as follows:

$$\hat{I}(t) = \frac{\hbar}{2}\Omega_0\begin{pmatrix}\cos\eta & \sin\eta e^{-i\delta}\\ \sin\eta e^{i\delta} & -\cos\eta\end{pmatrix}. \tag{51}$$

In the classical expression of the adiabatic process, without loss of generality, the time-dependent classical invariants can be designed by classical spin Eq. 33 as follows:

$$J_1 = \frac{\hbar}{2}\left(1 + \boldsymbol{S}\cdot\boldsymbol{b}'\right), \quad J_2 = \frac{\hbar}{2}\left(1 - \boldsymbol{S}\cdot\boldsymbol{b}'\right). \tag{52}$$

where $\boldsymbol{b}' = (\sin\eta\cos\delta, \sin\eta\sin\delta, \cos\eta)$ is the scaling factor with the parameters (η, δ).

The canonical transformation between position–momentum variables $(\boldsymbol{q}, \boldsymbol{p})$ and LR variables $(\boldsymbol{\xi}, \boldsymbol{J})$ can be written as follows:

$$\begin{aligned}q_1 &= \sqrt{2J_1}\sin\frac{\eta}{2}\cos(\delta-\xi_1) + \sqrt{2J_2}\cos\frac{\eta}{2}\cos(\delta-\xi_2),\\ q_2 &= \sqrt{2J_1}\cos\frac{\eta}{2}\cos\xi_1 - \sqrt{2J_2}\sin\frac{\eta}{2}\cos\xi_2,\\ p_1 &= \sqrt{2J_1}\sin\frac{\eta}{2}\sin(\delta-\xi_1) + \sqrt{2J_2}\cos\frac{\eta}{2}\sin(\delta-\xi_2),\\ p_2 &= -\sqrt{2J_1}\cos\frac{\eta}{2}\sin\xi_1 + \sqrt{2J_2}\sin\frac{\eta}{2}\sin\xi_2.\end{aligned} \tag{53}$$

After this canonical transformation, the Hamiltonian $h(\boldsymbol{q}, \boldsymbol{p}; \boldsymbol{B})$ becomes

$$\begin{aligned}G(\boldsymbol{J};\boldsymbol{B}) &= \bar{H}_C(\boldsymbol{J};\boldsymbol{B}) - A_{LR}(\boldsymbol{J};\boldsymbol{B})\\ &= \frac{\mu}{\hbar}\boldsymbol{B}\cdot\boldsymbol{b}'(J_2 - J_1) + \frac{1}{2}\left[J_1(1-\cos\eta) + J_2(1+\cos\eta)\right]\dot{\delta}.\end{aligned} \tag{54}$$

We can calculate LR angles accumulated *via* the evolution process by Eq. 23, given as follows:

$$\begin{aligned}\Delta\xi_1 &= \int dt\left[\frac{\mu}{\hbar}\boldsymbol{B}\cdot\boldsymbol{b}' - \frac{1}{2}(1+\cos\eta)\dot{\delta}\right],\\ \Delta\xi_2 &= \int dt\left[-\frac{\mu}{\hbar}\boldsymbol{B}\cdot\boldsymbol{b}' - \frac{1}{2}(1-\cos\eta)\dot{\delta}\right].\end{aligned} \tag{55}$$

According to Eq. 26, the driving Hamiltonian of the LR invariant-based scheme becomes

$$\begin{aligned}H_d &= \bar{H}_C(\boldsymbol{J},t) - A_{LR}(\boldsymbol{J},t) - \frac{\partial S}{\partial t}\\ &= \frac{\mu}{\hbar}\boldsymbol{B}\cdot\boldsymbol{b}(J_2 - J_1) + \left[\sin(\xi_1-\xi_2)\dot{\eta} - \cos(\xi_1-\xi_2)\ \sin\eta\dot{\delta}\right]\sqrt{J_1J_2},\\ &= S_3\left[-\mu\boldsymbol{B}\cdot\boldsymbol{b}'\cos\eta + \frac{\hbar}{2}\ \sin^2\eta\dot{\delta}\right] + S_1\left[-\mu\boldsymbol{B}\cdot\boldsymbol{b}'\sin\eta\cos\delta - \frac{\hbar}{2}\left(\sin\delta\dot{\eta} + \sin\eta\cos\eta\cos\delta\dot{\delta}\right)\right]\\ &\quad +S_2\left[-\mu\boldsymbol{B}\cdot\boldsymbol{b}'\sin\eta\sin\delta + \frac{\hbar}{2}\left(\cos\delta\dot{\eta} - \sin\eta\cos\eta\sin\delta\dot{\delta}\right)\right]\\ &= \boldsymbol{S}\cdot\boldsymbol{B}_d,\end{aligned} \tag{56}$$

where $\boldsymbol{B}_d = (\boldsymbol{B}\cdot\boldsymbol{b}')\boldsymbol{b}' - \frac{\hbar}{2\mu}\boldsymbol{b}'\times\dot{\boldsymbol{b}}'$. Comparing it with Eq. 34, the scaling factor $\boldsymbol{b}'$ satisfies the following:

$$\dot{\boldsymbol{b}}' = \frac{2\mu}{\hbar}\boldsymbol{b}'\times\boldsymbol{B}. \tag{57}$$

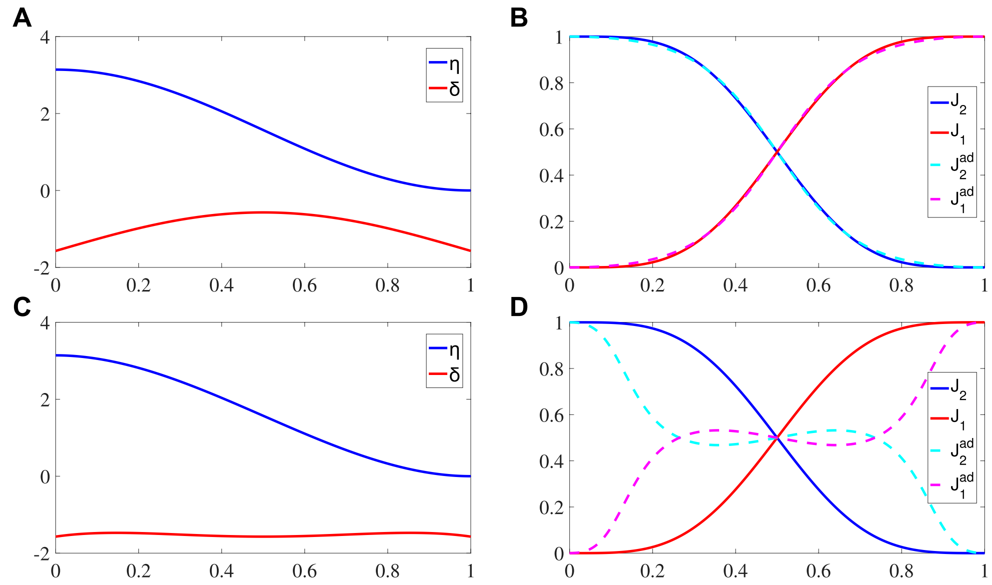

FIGURE 2
(A–C) Evolution of the parameters η (solid blue line) and δ (solid red line). **(B–D)** Time evolution of the action variables J_1 (solid red line), J_2 (solid blue line) driven by H_d, and adiabatic approximate invariants J_1^{ad} (dashed red line) and J_2^{ad} (dashed blue line) when t/τ = 1 and τ = .5.

The system invariant boundary conditions in Eq. 29 become

$$\dot{\boldsymbol{b}}'(0) = \dot{\boldsymbol{b}}'(T) = 0, \tag{58}$$

and the driving magnetic field in the Hamiltonian H can be chosen as

$$\boldsymbol{B} = -\frac{\hbar}{2\mu}\boldsymbol{b}' \times \dot{\boldsymbol{b}}' \tag{59}$$

to realize the evolution from initial energy eigenstates $|\lambda_n(0)\rangle$ to final energy eigenstates $|\lambda_n(T)\rangle$.

By equating Hamiltonian H_d Eq. 56 and $\bar{H}_C(\boldsymbol{J}, t)$, we can calculate these two pairs of parameters satisfying the following equation:

$$\begin{aligned} \dot{\delta} &= \frac{-2\mu B}{\hbar}\left[\cos\alpha + \sin\alpha\frac{\cos\eta}{\sin\eta}\cos(\beta-\delta)\right], \\ \dot{\eta} &= \frac{-2\mu B}{\hbar}\sin\alpha\sin(\beta-\delta). \end{aligned} \tag{60}$$

In particular, there is still arbitrariness in the choice of parameters η and δ. To illustrate the adiabatic evolution driven by Eq. 56, we make the invariants of the initial and final moments satisfy the boundary conditions and Eq. 60. For example, to transfer the state from the first oscillator with canonical variables q_1 and p_1 to the second oscillator with canonical variables q_2 and p_2, we can set $\dot{\eta}(0) = 0$, $\eta(0) = 0$, and $\eta(T) = \pi$ to satisfy the boundary conditions and chose a different scheme for δ.

To illustrate this result, we choose two different configurations of time-dependent parameters as shown in Figure 2. The first set of parameters

$$\begin{aligned} \eta &= \frac{\pi}{2} + \frac{\pi}{2}\cos\frac{\pi t}{\tau}, \\ \delta &= -\frac{\pi}{2} + \sin\frac{\pi t}{\tau} \end{aligned} \tag{61}$$

in Figure 2A which implements the adiabatic invariance of action variables can reproduce the evolution manipulated by the TQD Hamiltonian Eq. 43 as shown in Figure 2B. The action variables J_i exactly follow the adiabatic trajectories. The evolution of the phase trajectory is just like that in Figures 1A, E driven by H_C^{eff}. Similar to the fact that the TQD can be seen as one of the schemes for the inverse engineering based on the quantum LR invariant [59], the TCD which keeps the evolution exactly on the adiabatic trajectories in phase space of the classical Hamiltonian can be seen as one of the schemes for inverse engineering based on the classical LR invariant, which only needs the initial and final trajectories in the phase space matching adiabatic trajectories in the phase space of the classical Hamiltonian. Therefore, we can also design the classical Hamiltonian by different parameters to realize the classical LR invariant scheme. For example, the parameters

$$\begin{aligned} \eta &= \pi - 3\pi t^2 + 2\pi t^3, \\ \delta &= -\frac{\pi}{2} + \frac{\pi}{2}t - \frac{5\pi}{2}t^2 + 4\pi t^3 - 2\pi t^4 \end{aligned} \tag{62}$$

in Figure 2C can also realize the state transfer between the two oscillators with a nearly unchanged δ. Thus, the optional form of the parameters to implement the adiabatic invariance is not unique. These results can be perfectly related to the LR invariant method for the spin-1/2 system [59].

5 Conclusion

To sum up, we use the quantum–classical mapping method to simulate the two schemes of the STA, i.e., the TQD and quantum LR invariant method, by the classical system consisting of coupled oscillators. On one hand, for the TQD, which implements the STA by finding an additional Hamiltonian to drive the system, we derived the explicit form of an additional driving Hamiltonian to keep the evolution of adiabatic phase trajectories and acquire the Hannay's phase. This TCD method can perfectly simulate and match the TQD method. On the other hand, the Lewis–Riesenfeld invariant method, which keeps the energy eigenstates from a specified initial to the final configuration, can also be simulated by manipulating the configurations of classical coupled oscillators. Both of the approaches can accelerate the adiabatic process effectively under different circumstances and matches the quantum methods of the STA. These results prove that the protocol of the quantum–classical mapping can be used to generalize quantum schemes of the STA into the classical system. By this simulation, our theory could be expected to find applications of the STA for classical systems.

Data availability statement

The original contributions presented in the study are included in the article/Supplementary Material; further inquiries can be directed to the corresponding authors.

Author contributions

HL and HS initiated the idea. YL and HL wrote the main manuscript text. YL and YZ performed the calculations.

Funding

This work was supported by the National Natural Science Foundation of China (Contact Nos. 11875103 and 12147206).

Conflict of interest

Publisher's note

References

1. Li YC, Chen X. Shortcut to adiabatic population transfer in quantum three-level systems: Effective two-level problems and feasible counterdiabatic driving. *Phys Rev A* (2016) 94:063411. doi:10.1103/PhysRevA.94.063411

2. Král P, Thanopulos I, Shapiro M. ***Colloquium***: Coherently controlled adiabatic passage. *Rev Mod Phys* (2007) 79:53–77. doi:10.1103/RevModPhys.79.53

3. Saffman M, Walker TG, Mølmer K. Quantum information with rydberg atoms. *Rev Mod Phys* (2010) 82:2313–63. doi:10.1103/RevModPhys.82.2313

4. Vitanov NV, Rangelov AA, Shore BW, Bergmann K. Stimulated Raman adiabatic passage in physics, chemistry, and beyond. *Rev Mod Phys* (2017) 89:015006. doi:10.1103/RevModPhys.89.015006

5. Chen X, Ruschhaupt A, Schmidt S, del Campo A, Guéry-Odelin D, Muga JG. Fast optimal frictionless atom cooling in harmonic traps: Shortcut to adiabaticity. *Phys Rev Lett* (2010) 104:063002. doi:10.1103/PhysRevLett.104.063002

6. Longuet-Higgins HC, Öpik U, Pryce MHL, Sack RA. Studies of the jahn-teller effect. ii. the dynamical problem. *Proc R Soc A: Math Phys Eng Sci* (1958) 244 (1236):1–16. doi:10.1098/rspa.1958.0022

7. Pancharatnam S. Generalized theory of interference, and its applications. *Proc Indian Acad Sci A* (1956) 44:247–62. doi:10.1007/BF03046050

8. Chen X, Torrontegui E, Muga JG. Lewis-Riesenfeld invariants and transitionless quantum driving. *Phys Rev A* (2011) 83:062116. doi:10.1103/PhysRevA.83.062116

9. Rezek Y, Kosloff R. Irreversible performance of a quantum harmonic heat engine. *New J Phys* (2006) 8:83. doi:10.1088/1367-2630/8/5/083

10. Berry MV. Transitionless quantum driving. *J Phys A: Math Theor* (2009) 42:365303. doi:10.1088/1751-8113/42/36/365303

11. Ban Y, Chen X, Sherman EY, Muga JG. Fast and robust spin manipulation in a quantum dot by electric fields. *Phys Rev Lett* (2012) 109:206602. doi:10.1103/PhysRevLett.109.206602

12. Ban Y, Jiang LX, Li YC, Wang LJ, Chen X. Fast creation and transfer of coherence in triple quantum dots by using shortcuts to adiabaticity. *Opt Express* (2018) 26:31137–49. doi:10.1364/OE.26.031137

13. Chen X, Jiang RL, Li J, Ban Y, Sherman EY. Inverse engineering for fast transport and spin control of spin-orbit-coupled bose-einstein condensates in moving harmonic traps. *Phys Rev A* (2018) 97:013631. doi:10.1103/PhysRevA.97.013631

14. Zhang J, Shim JH, Niemeyer I, Taniguchi T, Teraji T, Abe H, et al. Experimental implementation of assisted quantum adiabatic passage in a single spin. *Phys Rev Lett* (2013) 110:240501. doi:10.1103/PhysRevLett.110.240501

15. del Campo A. Shortcuts to adiabaticity by counterdiabatic driving. *Phys Rev Lett* (2013) 111:100502. doi:10.1103/PhysRevLett.111.100502

16. del Campo A. Frictionless quantum quenches in ultracold gases: A quantum-dynamical microscope. *Phys Rev A* (2011) 84:031606. doi:10.1103/PhysRevA.84.031606

17. Chen YH, Shi ZC, Song J, Xia Y. Invariant-based inverse engineering for fluctuation transfer between membranes in an optomechanical cavity system. *Phys Rev A* (2018) 97:023841. doi:10.1103/PhysRevA.97.023841

18. Lu M, Xia Y, Shen LT, Song J, An NB. Shortcuts to adiabatic passage for population transfer and maximum entanglement creation between two atoms in a cavity. *Phys Rev A* (2014) 89:012326. doi:10.1103/PhysRevA.89.012326

19. Chen YH, Xia Y, Wu QC, Huang BH, Song J. Method for constructing shortcuts to adiabaticity by a substitute of counterdiabatic driving terms. *Phys Rev A* (2016) 93:052109. doi:10.1103/PhysRevA.93.052109

20. Deffner S, Jarzynski C, del Campo A. Classical and quantum shortcuts to adiabaticity for scale-invariant driving. *Phys Rev X* (2014) 4:021013. doi:10.1103/PhysRevX.4.021013

21. Chen X, Lizuain I, Ruschhaupt A, Guéry-Odelin D, Muga JG. Shortcut to adiabatic passage in two- and three-level atoms. *Phys Rev Lett* (2010) 105:123003. doi:10.1103/PhysRevLett.105.123003

22. Jarzynski C, Deffner S, Patra A, Subaşı Y. Fast forward to the classical adiabatic invariant. *Phys Rev E* (2017) 95:032122 (3). doi:10.1103/PhysRevE.95.032122

23. Okuyama M, Takahashi K. From classical nonlinear integrable systems to quantum shortcuts to adiabaticity. *Phys Rev Lett* (2016) 117:070401. doi:10.1103/PhysRevLett.117.070401

24. Jarzynski C. Generating shortcuts to adiabaticity in quantum and classical dynamics. *Phys Rev A* (2013) 88:040101. doi:10.1103/PhysRevA.88.040101

25. Deng J, Wang Q, Liu Z, Hänggi P, Gong J. Boosting work characteristics and overall heat-engine performance via shortcuts to adiabaticity: Quantum and classical systems. *Phys Rev E* (2013) 88:062122. doi:10.1103/PhysRevE.88.062122

26. Xiao G, Gong J. Suppression of work fluctuations by optimal control: An approach based on jarzynski's equality. *Phys Rev E* (2014) 90:052132. doi:10.1103/PhysRevE.90.052132

27. Olavo L. *Quantum mechanics as a classical theory; 2, relativistic theory*. Tech. Rep. quant-ph/9503021 (1995).

28. Arnold VI. Mathematical methods of classical mechanics. In: *Graduate texts in mathematics*, Vol. 60. New York, NY: Springer-Verlag (1978). doi:10.1007/978-1-4757-1693-1

29. Peres A, Terno DR. Hybrid classical-quantum dynamics. *Phys Rev A* (2001) 63:022101. doi:10.1103/PhysRevA.63.022101

30. Elze HT. Linear dynamics of quantum-classical hybrids. *Phys Rev A* (2012) 85:052109. doi:10.1103/PhysRevA.85.052109

31. Gil V, Salcedo LL. Canonical bracket in quantum-classical hybrid systems. *Phys Rev A* (2017) 95:012137. doi:10.1103/PhysRevA.95.012137

32. Kantner M, Mittnenzweig M, Koprucki T. Hybrid quantum-classical modeling of quantum dot devices. *Phys Rev B* (2017) 96:205301. doi:10.1103/PhysRevB.96.205301

33. Briggs JS, Eisfeld A. Equivalence of quantum and classical coherence in electronic energy transfer. *Phys Rev E* (2011) 83:051911. doi:10.1103/PhysRevE.83.051911

34. Briggs JS, Eisfeld A. Coherent quantum states from classical oscillator amplitudes. *Phys Rev A* (2012) 85:052111. doi:10.1103/PhysRevA.85.052111

35. Briggs JS, Eisfeld A. Quantum dynamics simulation with classical oscillators. *Phys Rev A* (2013) 88:062104. doi:10.1103/PhysRevA.88.062104

36. Briggs JS. Equivalent emergence of time dependence in classical and quantum mechanics. *Phys Rev A* (2015) 91:052119. doi:10.1103/PhysRevA.91.052119

37. Radonjić M, Prvanović S, Burić N. System of classical nonlinear oscillators as a coarse-grained quantum system. *Phys Rev A* (2011) 84:022103. doi:10.1103/PhysRevA.84.022103

38. Radonjić M, Prvanović S, Burić N. Hybrid quantum-classical models as constrained quantum systems. *Phys Rev A* (2012) 85:064101. doi:10.1103/PhysRevA.85.064101

39. Radonjić M, Prvanović S, Burić N. Emergence of classical behavior from the quantum spin. *Phys Rev A* (2012) 85:022117. doi:10.1103/PhysRevA.85.022117

40. Burić N, Popović DB, Radonjić M, Prvanović S. Orbits of hybrid systems as qualitative indicators of quantum dynamics. *Phys Lett A* (2014) 378 (16):1081–1084. doi:10.1016/j.physleta.2014.02.037

41. Arsenović D, Burić N, Popović DB, Radonjić M, Prvanović S. Positive-operator-valued measures in the Hamiltonian formulation of quantum mechanics. *Phys Rev A* (2015) 91:062114. doi:10.1103/PhysRevA.91.062114

42. Polchinski J. Weinberg's nonlinear quantum mechanics and the einstein-podolsky-rosen paradox. *Phys Rev Lett* (1991) 66:397–400. doi:10.1103/PhysRevLett.66.397

43. Chruściński D, Jamiołkowski A. Geometric phases in classical and quantum mechanics. In: *Progress in mathematical physics*, Vol. 36. Boston, MA: Springer Science and Business Media (2012). doi:10.1007/978-0-8176-8176-0

44. Zhang Q, Wu B. General approach to quantum-classical hybrid systems and geometric forces. *Phys Rev Lett* (2006) 97:190401. doi:10.1103/PhysRevLett.97.190401

45. Heslot A. Quantum mechanics as a classical theory. *Phys Rev D* (1985) 31:1341–8. doi:10.1103/PhysRevD.31.1341

46. Weinberg S. Testing quantum mechanics. *Ann Phys (N Y)* (1989) 194:336–86. doi:10.1016/0003-4916(89)90276-5

47. Weinberg S. Precision tests of quantum mechanics. *Phys Rev Lett* (1989) 62:485–8. doi:10.1103/PhysRevLett.62.485

48. Wu B, Liu J, Niu Q. Geometric phase for adiabatic evolutions of general quantum states. *Phys Rev Lett* (2005) 94:140402. doi:10.1103/PhysRevLett.94.140402

49. Zhang Q, Wu B. General approach to quantum-classical hybrid systems and geometric forces. *Phys Rev Lett* (2006) 97:190401. doi:10.1103/PhysRevLett.97.190401

50. Stone M. Born-oppenheimer approximation and the origin of wess-zumino terms: Some quantum-mechanical examples. *Phys Rev D* (1986) 33:1191–4. doi:10.1103/PhysRevD.33.1191

51. Gozzi E, Thacker WD. Classical adiabatic holonomy and its canonical structure. *Phys Rev D* (1987) 35:2398–406. doi:10.1103/physrevd.35.2398

52. Liu HD, Wu SL, Yi XX. Berry phase and hannay's angle in a quantum-classical hybrid system. *Phys Rev A* (2011) 83:062101. doi:10.1103/PhysRevA.83.062101

53. Heslot A. Quantum mechanics as a classical theory. *Phys Rev D* (1985) 31:1341–8. doi:10.1103/PhysRevD.31.1341

54. Strocchi F. Complex coordinates and quantum mechanics. *Rev Mod Phys* (1966) 38:36–40. doi:10.1103/RevModPhys.38.36

55. Dirac PAM, Bohr NHD. The quantum theory of the emission and absorption of radiation. *Proc R Soc Lond A* (1927) 114:243–65. doi:10.1098/rspa.1927.0039

56. Berry MV. Quantal phase factors accompanying adiabatic changes. *Proc R Soc Lond A* (1984) 392 (1802):45–57. The Royal Society London. doi:10.1098/rspa.1927.0039

57. Berry MV. Classical adiabatic angles and quantal adiabatic phase. *J Phys A: Math Gen* (1985) 18:15–27. doi:10.1088/0305-4470/18/1/012

58. Lewis HR, Jr, Riesenfeld W. An exact quantum theory of the time-dependent harmonic oscillator and of a charged particle in a time-dependent electromagnetic field. *J Math Phys* (1969) 10:1458–73. doi:10.1063/1.1664991

59. Chen X, Torrontegui E, Muga JG. Lewis-riesenfeld invariants and transitionless quantum driving. *Phys Rev A* (2011) 83:062116. doi:10.1103/PhysRevA.83.062116

Appendix: Derivation of the Schrödinger equation in the canonical form

The dynamical evolution of the N-level quantum system governed by the Hamiltonian $\hat{H}(t)$ can be described by the following Schrödinger equation:

$$i\hbar\partial_t|\Psi\rangle = \hat{H}(t)|\Psi\rangle, \tag{63}$$

which can be expanded by the quantum state $|\Psi\rangle = \sum\psi_n(t)|\psi_n\rangle$ as follows:

$$i\hbar\partial_t\left(\sum_n \psi_n(t)|\psi_n\rangle\right) = \hat{H}(t)|\Psi\rangle, \tag{64}$$

with the probability amplitudes ψ_n on the bare basis $\{|\psi_n\rangle\}$. Since $\{|\psi_n\rangle\}$ is a time-independent bare basis, Eq. 64 becomes

$$i\hbar d_t\psi_n(t)|\psi_n\rangle = \hat{H}(t)|\Psi\rangle. \tag{65}$$

Multiplying Eq. 65 by $\langle\psi_m|$, we have the following:

$$i\hbar d_t\psi_m(t) = \langle\psi_m|\hat{H}(t)|\Psi\rangle, \tag{66}$$

with $H_C(\psi,\psi^*,t) = \langle\Psi|\hat{H}(t)|\Psi\rangle = \sum_m\psi_m^*\langle m|\hat{H}(t)|\Psi\rangle$. Therefore, the Schrödinger equation in the canonical form can be written as follows:

$$i\hbar\frac{d\psi_m(t)}{dt} = \frac{\partial H_C}{\partial\psi_m^*}, \tag{67}$$

which is just the same as Eq. 1.

frontiers | Frontiers in Physics

TYPE Original Research
PUBLISHED 15 February 2023
DOI 10.3389/fphy.2023.1098170

OPEN ACCESS

EDITED BY
Huan Yang,
Shandong University, China

REVIEWED BY
Yonggang Peng,
School of Physics, Shandong University, China
Hsin-Yu Ko,
Cornell University, United States

*CORRESPONDENCE
Zhi Zhu,
✉ zhuzhi@usst.edu.cn
Yangmei Li,
✉ sunberry1211@hotmail.com

SPECIALTY SECTION
This article was submitted to Atomic and Molecular Physics,
a section of the journal
Frontiers in Physics

RECEIVED 14 November 2022
ACCEPTED 30 January 2023
PUBLISHED 15 February 2023

CITATION
Sun T, Wang L, Hu R, Li Y and Zhu Z (2023), Light controls edge functional groups to enhance membrane permeability.
Front. Phys. 11:1098170.
doi: 10.3389/fphy.2023.1098170

Light controls edge functional groups to enhance membrane permeability

Tingyu Sun[1], Lei Wang[1], Rengkai Hu[1], Yangmei Li[2]* and Zhi Zhu[1]*

[1]Key Laboratory of Optical Technology and Instrument for Medicine, Ministry of Education, College of Optical-Electrical and Computer Engineering, University of Shanghai for Science and Technology, Shanghai, China, [2]Innovation Laboratory of Terahertz Biophysics, National Innovation Institute of Defense Technology, Beijing, China

Functionalized membranes have high potential value in a broad range of practical applications, and the functional groups at the membrane edge play a vital role in the permeability of the membranes. Here, based on an edge-functionalized graphene oxide (GO) membrane model, we theoretically report that high-frequency terahertz stimulation at the frequency near 44.0 THz can significantly enhance the water permeability of the membrane by nearly five times. Its mechanism was revealed to be that the stimulation amplified the C-O stretching of the functional groups and suppressed other vibration modes of the groups. As a result, the modulation of edge functional groups brings down the energy barricade of the membrane and allows water molecules to penetrate the GO membrane more easily. These findings provide a new perspective for enhancing membrane permeability by modulating particular functional groups such as the carboxyl on the edge of the GO membrane.

KEYWORDS

graphene oxide, terahertz light, spectrum, permeation enhancement, absorption

Introduction

Membranes play an imperative role in life science and industrial applications, such as disease treatment and water purification [1, 2]. It is of important significance to understand and manipulate the transportation of water through membranes in many physical, chemical, biological, and technical applications. In different artificial and biological membranes, functional groups on the membrane determine the properties of the membrane and have a great influence on the permeability of water [3]. For example, as a two-dimensional (2D) material derived from graphene, GO has almost completely different properties from graphene [4, 5]. Compared to hydrophobic graphene, the polar oxygen-containing functional groups on the membrane make it hydrophilic and have different properties from graphene in many ways [6, 7]. GO membranes, as a feasible artificial membrane for water desalination and wastewater treatment [8–10], was first developed by Nair et al., and it was discovered that stacking GO film can selectively block the motion of non-aqueous solutions and allow water permeation through a unique pathway [11]. From then, many attempts to develop the application of GO membrane and methods to control the interlayer spacing of stacking GO have been discovered [12–15].

The interlayer spacing of the stacking GO membrane determines the ion and water permeation efficiency, a smaller interlayer spacing leads to better ion-sieving performance, while the flow rate of water decreases exponentially with the reduction in interlayer spacing [16–20]. The carboxyl group at the edge of the GO membrane is one of the major factors affecting the permeation of water molecules and other ions through the membrane due to the steric effect [21–24]. Previous attempts made to enhance the permeability of GO were mainly surface modification or reassembling [25, 26]. In contrast, THz electromagnetism (EM) stimulus is a novel and efficient approach. In recent years, the application of THz EM waves in biochemistry and the theoretical discussion on the interaction between light and matter are increasing gradually [27], starting from using an electric field, to enhance the water transport in nanochannels and gas dissolving in aqueous solutions [28, 29], to the application of terahertz-regulated dissolution of methane hydrate [30] or using THz wave to detect different materials and defects [31, 32]. Furthermore, in a biological system, THz stimuli can be applied to enhance the permeability of ion channels by directional interaction with functional groups [33–35] and even can be used to accelerate the DNA unwinding [36]. Biophotons at high-frequency THz range can also participate in the replication of DNA and neurotransmission [37, 38]. Previous research on THz–water interaction proves that THz wave can enhance the water permeability by changing the H-bond structure of one-dimensional (1D) and two-dimensional (2D) water in artificial membrane materials such as graphene and carbon tube [39–44]. As a 2D material sharing analogous behaviors with biological membranes, functional groups on GO membranes can also be stimulated with THz EM with high efficiency and directionally [45]. Inspired by the studies of THz light enhancing water transportation by interacting with matter and functional groups, we propose a light-based modulation method targeting edge functional groups to change the permeability of the GO membrane.

In this study, based on a special GO membrane model and primarily considering carboxyl groups on the edge of the membrane (Figure 1A), we uncovered the interaction between 44.0 THz EM wave and carboxyl, as well as the subsequent influence on the conformation of GO membrane water channels. The underlying mechanism is shown to be that THz EM stimuli can change the oscillation of carboxyl at the entrance and exit of the channel by affecting the carboxyl groups resonantly, thereby reducing the energy barrier for water molecules to enter and exit the GO membrane, thus improving the permeability of GO membranes by nearly five times.

Method

To explore the influence of THz EM stimulus on the dynamic properties of edge functional groups on a membrane and its subsequent effect on the conformation of the water channel and the permeability of the membrane, we designed a GO membrane model by stacking two sheets of GO in parallel with lengths, widths, and interlayer spacings of 3.42, 4.94, and 0.78 nm, respectively. Conventionally, the molecular structure of GO contains hydroxyl and epoxy functional groups on the basal plane and carboxyl grafted on the edges of the sheet, following the well-known Lerf–Klinowski model [46]. In our previous research, we studied the effect of the interaction between light and hydroxyl groups on the permeability of the GO membrane, while the epoxy shares a similar property with hydroxyl [45]. Relatively, the location of carboxyl groups exerts its effect on water permeation different from that of hydroxyl and epoxy groups, but it is an ideal model for studying the influence of edge functional groups on water permeation. Therefore, we focused on a pure carboxyl-functionalized GO membrane model to simplify the molecular dynamic simulation and the following data analysis. In order to

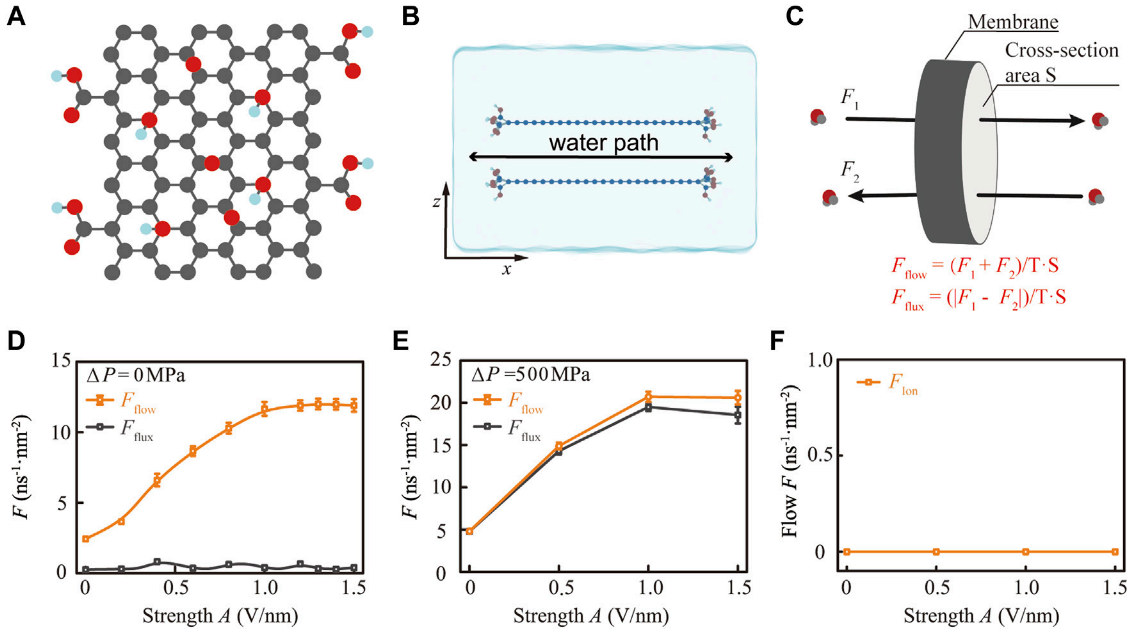

FIGURE 1
Electromagnetic (EM) stimulus at a specific frequency significantly enhances the permeability of the functionalized membrane for water. **(A)** Structural model of the normal GO plate. The gray, red, and cyan balls represent carbon, oxygen, and hydrogen atoms, respectively. **(B)** Schematic diagram of the GO membrane model by stacking two sheets of GO in parallel. **(C)** Schematic diagram for distinguishing water flow and flux, where flow and flux are the sum and difference of water molecules between the forward transport (F_1) and the backward transport (F_2), respectively. **(D)** Transition to a super permeation state of confined water modulated by 44.0 THz EM stimuli (orange curve) at different strengths (*A*) without the gradient field. **(E)** In the presence of a gradient field with a 500 MPa pressure difference, 44.0 THz EM stimulus enhances both the water flow and flux through the GO membrane. **(F)** EM stimulus did not enhance the permeability of ions due to the steric effect.

ensure that the water can be affected by the carboxyl on the path of permeating through the GO membrane, we grafted the carboxyl at the edge of the GO sheet with a certain space around 0.4–0.8 nm. The charge model for carboxyl was based on the carboxyl group in ASPH amino acid to ensure that the system was electrically neutral. The GO membrane was centered in the simulation box with side lengths of L_x = 5.75 nm, L_y = 5.11 nm, and L_z = 3.78 nm. Then, we filled the rest of the box with flexible SPCE-modelled water molecules [47–49]. Consequently, the size of the GO membrane model and the box ensures that the water molecules can only permeate through the GO membrane along the x-axis (Figure 1B; Supplementary Figure S1).

EM waves will be applied to the entire system at the beginning of the MD simulation. Since the electric component of EM waves dominates the interaction of the EM wave with small molecules at room temperature [40], an electric field $\boldsymbol{E}(t) = A \cdot \boldsymbol{u} \cdot \cos(\omega t + \varphi)$ was applied to simulate the EM wave, where A is the maximum amplitude of the electric field that determines the strength of the EM wave. The polarization direction of the wave was set to $\boldsymbol{u}$ = (1, 0, 0), which is parallel to the membrane plane. The frequency f of the EM wave relates to the angular frequency ω *via* the equation $f = \omega/2\pi$. Furthermore, to investigate the effect of hydrostatic pressure and THz stimuli together on the permeability of the membrane, we used the accelerated function of GROMACS to generate desired pressure difference (ΔP) [50]. F was applied to define the permeability of the GO membrane (Figure 1C), where F_1 and F_2 are the number of water molecules traversing forward and backward from one side of the membrane to the other along the x-axis, respectively. Furthermore, F_{flow} and F_{flux} are the sum and difference of F_1 and F_2 divided by the product of the simulation time and the cross-section area of the channel, respectively. Therefore, we use F_{flow} to describe the bidirectional permeability and F_{flux} to describe the unidirectional permeability of the membrane. To minimize the influence of temperature fluctuation on the simulation, a Nose–Hoover thermostat with a time constant for coupling of 0.2 ps was applied to maintain the average system temperature at 300 K with a fluctuation under 5 K (Supplementary Figure S2). More details of the simulation methods are shown in Supplementary Section S1.

Result and discussion

Under the effect of 44.0 THz EM, the GO membrane becomes more permeable to water molecules, but repellency to ions is maintained (Figures 1D–F). Evidently, the F_{flow} tends to increase non-linearly with increasing EM stimuli strength A under an equilibrium state, while the F_{flux} only fluctuates within a certain value without a substantial increase (Figure 1D). Under normal conditions without osmotic pressure and THz EM stimuli, the value of the F_{flow} and F_{flux} is around 2.42 ± 0.09 $\text{ns}^{-1}\cdot\text{nm}^{-2}$ and 0.25 ± 0.01 $\text{ns}^{-1}\cdot\text{nm}^{-2}$, respectively. With the stimuli of 44.0 THz EM, the F_{flow} will increase rapidly as A increases from 0.1 to 1.0 V/nm and remain in a super state with F_{flow} = 11.89 ± 0.44 $\text{ns}^{-1}\cdot\text{nm}^{-2}$ when $A \geq 1.0$ V/nm. In contrast, the F_{flux} fluctuated between 0.25 $\text{ns}^{-1}\cdot\text{nm}^{-2}$ and 0.65 $\text{ns}^{-1}\cdot\text{nm}^{-2}$ and does not increase with the stimulation of 44.0 THz EM. The reason behind this fact is that the values of F_1 and F_2 are close to each other under normal conditions, while the THz EM stimuli will boost up both F_1 and F_2, resulting in F_{flux} fluctuating within a certain range. However, if we applied 44.0 THz EM stimuli under a gradient field of ΔP = 500 MPa, both F_{flow} and F_{flux} will be excited to a super permeation state (Figure 1E). This is because the gradient field of ΔP = 500 MPa will boost up F_1 or F_2 depending on the direction of osmotic pressure, leading to a huge diverse between F_1 and F_2; thus, the value of F_{flow} and F_{flux} will be close to each other. Consequently, in the absence of THz EM stimuli, the osmotic pressure of ΔP = 500 MPa can enhance the permeability of the membrane in both F_{flow} and F_{flux} to 4.81 ± 0.31 $\text{ns}^{-1}\cdot\text{nm}^{-2}$ and 4.78 ± 0.29 $\text{ns}^{-1}\cdot\text{nm}^{-2}$, respectively. Subsequently, both F_{flow} and F_{flux} can increase by about four times under the stimulation of 44.0 THz EM with strength $A \geq 1.0$ V/nm, reaching the values of F_{flow} = 20.60 ± 0.99 $\text{ns}^{-1}\cdot\text{nm}^{-2}$ and F_{flux} = 19.54 ± 0.91 $\text{ns}^{-1}\cdot\text{nm}^{-2}$. This fact indicates that THz EM stimuli can enhance both the bidirectional and unidirectional permeability of the membrane with the presence of a gradient field.

Notably, we used higher osmotic pressure to make the phenomena more obvious. However, similar phenomena will occur in a lower gradient field, such as ΔP = 50 MPa (see details in Supplementary Figure S3; Supplementary Section S2). Neither gradient field nor THz EM can change the ion rejection of the membrane (Figure 1F). The GO membrane with an interlayer spacing of 0.78 nm has a strong steric effect on ions, which can refuse ions to enter the channel, as F_{Ion} remained 0 $\text{ns}^{-1}\cdot\text{nm}^{-2}$ at any stimuli strength A. In other words, 44.0 THz EM stimuli can enhance the water permeability of the membrane while keeping the ion rejection of the membrane unchanged.

In order to reveal the mechanism behind the phenomenon of the specific frequency of EM stimuli that can enhance the permeability of functionalized membranes, we focused on the vibration spectrum of carboxyl groups, which are essential for the permeation of water through the membranes. In the classical approximation, the absorption spectrum intensity (I) in terms of frequency can be calculated by using Fourier transform for the autocorrelation function of total charge current $\boldsymbol{J}(t) = \sum_i q_i \boldsymbol{v_i}(t)$ [44], where q_i and $\boldsymbol{v_i}$ represent the charge and velocity of the ith atom, respectively. The first principle of frequency selection is that the stimulation at a particular frequency can resonate with the vibration of functional groups on the membrane (see the frequency selection of other membrane models in Supplementary Figure S4). Furthermore, the stimulation at the selected frequency is weakly absorbed by the bulk water and confined water. As shown in Figure 2A, the carboxyl groups have characteristic peaks at 35.0 THz, 44.0 THz, and 112.0 THz, which correspond to the bending vibration of O-H and the stretching vibrations of C-O and O-H, respectively. They are far away from the prominent absorption peaks of bulk water and confined water, denoting that carboxyl can resonantly absorb the photon energy from the 35.0, 44.0, and 112.0 THz EM stimuli. The vibration modes of C-O and C=O show certain similarities.

To clarify the belonging of the frequency of 44.0 THz, we calculated the vibration of C-O and C=O separately and found out that the vibration of 44.0 THz is mainly contributed to the C-O stretching (Figure 2B). It is essentially in agreement with the result from the FT-IR measurement, indicating that the simulations are well calibrated. Among these characteristic frequencies, only 35.0 and 44.0 THz EM stimuli are able to enhance the permeability of the GO membrane, and the mechanism behind this enhancement is similar (the effect of 35.0 THz EM stimuli on the permeability of the membrane is shown in Supplementary Figure S5; Supplementary Section S4). Therefore, we will focus on 44.0 THz EM stimuli to uncover the mechanism behind this enhancement. From Figure 2C,

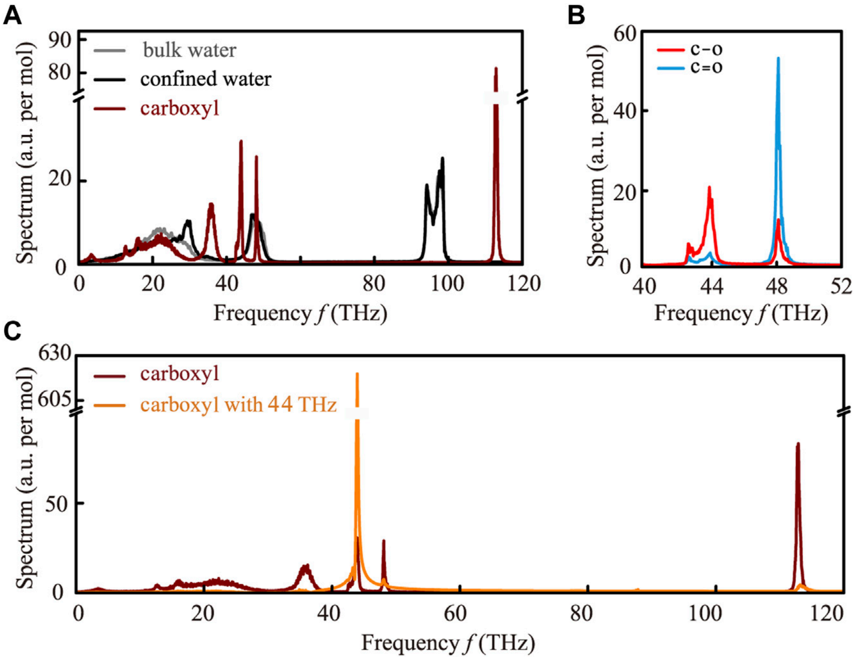

FIGURE 2
Mechanism behind the permeability enhancement of the membrane caused by EM stimuli at a specific frequency. **(A)** Vibrational spectra of bulk water (gray curve), confined water (black curve), and the carboxyl groups on the GO membrane (dark red curve). The vibrational models of carboxyl have characteristic frequencies centered at 35.0, 44.0, and 112.0 THz, respectively, which are far away from the prominent absorption peaks of bulk and confined waters. Consequently, carboxyl resonantly absorbs the photon energy of 35.0 and 44.0 THz EM stimuli, and its dynamical conformation is affected. **(B)** Composition detail of the vibrational spectra of carboxyl at the range of 40.0–52.0 THz. Distinctly, the vibration mode at 44.0 THz is mainly affected by the stretching vibration of the C-O bond. **(C)** Vibrational spectra of the carboxyl group before (dark red curve) and after (orange curve) the application of 44.0 THz stimulus.

we can clearly see that the vibration mode of the carboxyl group changes greatly after the application of 44.0 THz EM stimuli. Notably, the vibration mode with an intrinsic frequency of 44.0 THz is greatly enhanced by the corresponding stimuli, while other vibration modes had been reduced to a relatively weak state. In other words, due to the over-damping phenomenon caused by EM stimuli, all other vibration modes of carboxyl are suppressed, except for the vibration mode with an intrinsic frequency of 44.0 THz. As a result, the motion of the carboxyl group at the entrance of the water channel has changed dramatically under the influence of EM wave stimulation, which undoubtedly changes the permeability of the GO membrane.

Since the carboxyl group is located at the edge of the GO membrane and is hydrophilic, it tends to oscillate up and down in the direction perpendicular to the membrane plane under the attraction of water molecules around and the restriction of the carbon plate (Figure 3A). Figure 3B shows the trajectory of carboxyl in the absence and presence of THz EM stimuli. Evidently, the tendency of carboxyl to oscillate up and down has been suppressed after the application of 44 THz EM, confirming the conclusion of Figure 2C, and all vibration modes except C-O stretching have become weaker. Moreover, we can find that the oscillation period of carboxyl increases with the growth of the EM stimuli strength A (Figure 3C). Originally, it only takes 2.8 ns on average for carboxyl to complete a period of oscillating up and down, but as the stimuli strength A increases to 1.5 V/nm, the oscillation period increased to 8.6 ns on average. The dynamical change in carboxyl also changes the energy barrier for water molecules to permeate through the GO membrane. From Figure 3D, we can see the intermolecular interaction energy between the water molecule and the GO membrane. As the gateway for water molecules permeating through the membrane, carboxyl locates around 1.3 nm and 4.5 nm along the x-axis. Under normal circumstances, hydrophilic carboxyl will attract water molecules by forming H-bond with the interaction energy of $E_{\text{w-c}}$ = -24.0 kJ/mol, making it difficult for water molecules to enter or exit from the inside of the membrane. However, with the application of 44.0 THz EM stimuli, the dynamic conformation of carboxyl changes and the interaction energy $E_{\text{w-c}}$ reduces to -19.0 kJ/mol, making it less attractive to water and easier for water molecules to pass through. This fact leads to the conclusion that the movement change of carboxyl has a great influence on the membrane permeability due to its gateway location of water molecule transportation.

At last, it is worth noting that at the macroscopic level, the electric field required in an experiment to produce the dielectric breakdown of water is 0.07 V/nm. However, in classical molecular dynamics simulations, the electric field needed to affect the dynamic property of water significantly is almost 10 times greater than 0.07 V/nm. We did not observe the dielectric breakdown phenomenon in the simulation because the classical force field fixed the charge of atoms. This treatment just considered the orientation polarization and ignored the electron polarization. At the molecular level, dielectric breakdown is a bond-breaking process [51], and the electric field threshold to dissociate water molecules and sustain an ionic current

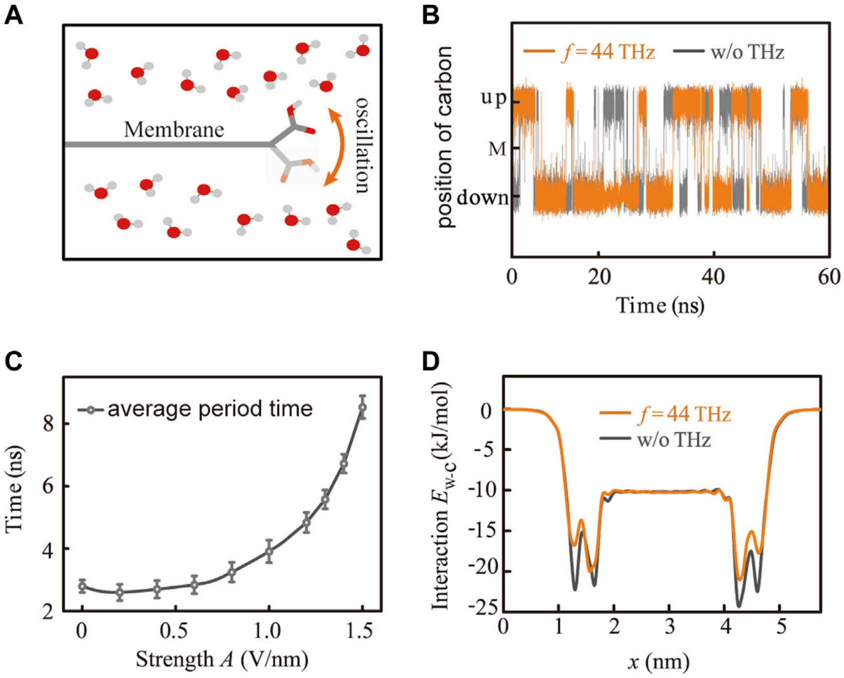

FIGURE 3
Effects of EM stimuli at the specific frequency on the movement of carboxyl. **(A)** Schematic diagram of movement for carboxyl on the edge of the membrane. **(B)** Dynamical conformation of carboxyl before (gray line) and after (orange line) the application of 44.0 THz stimuli, where the label M in the middle of the vertical axis represents the carbon plane of the GO membrane. **(C)** Average period time for the conformational change of carboxyl increases with the growth of stimuli strength of 44.0 THz.**(D)** Interaction energy $E_{w\text{-}c}$ between a water molecule and the membrane along the pathway of water molecules permeating through the membrane.

needs to be up to 3.5 V/nm [52]. Therefore, under this threshold, we can reveal the classical image rather than the quantum image of the influence of the external field on molecular orientation and vibration dynamics. Furthermore, in the simulation, thermal dissipation is based on the thermostat algorithm, while the water bath is used to control the system's temperature in the experiment. Although 44.0 THz is not the strongest absorption frequency band that water absorbs the EM stimulus, the local temperature will still rise if we irradiate the light on the water. Based on the continuous light source we applied in the simulation, the injected power from 44.0 THz EM stimulus to the unit volume of water is less than 0.6×10^{-9} W/nm^3 when $A < 1.5$ V/nm (see details in Supplementary Section S5). Therefore, to investigate the non-thermal effect of the enhancement of membrane permeability caused by light, the water bath needs to be designed to take away the injected energy in the process of the experiment as shown in the previous work [35].

Conclusion

In this work, we found that EM stimuli at a frequency of 44 THz can be resonantly absorbed by carboxyl groups at the edge position of the GO membrane, thereby changing the vibration mode and dynamic conformation of carboxyl groups. As a result, it reduced the energy barrier of water molecule transport and ultimately increased the permeability of the membrane by five times. It is worth noting that in various biological and artificial particle transport channels and membranes, the edge functional groups play an important role in screening molecules or ions. Therefore, our findings bring new insights into the study of biological channels and artificial membranes and provide a new approach to manipulating the transmembrane transport of water molecules and other particles in life science and industrial applications.

Data availability statement

The original contributions presented in the study are included in the article/Supplementary Material; further inquiries can be directed to the corresponding author.

Author contributions

Conceptualization, ZZ; Validation, LW; Investigation, TS and RH; Writing - original draft, TS; Writing - review and editing, YL and ZZ.

Funding

This work was supported by the National Key Research and Development Program of China (No. 2021YFA1200404), National Natural Science Foundation of China Projects (Nos T2241002, 12204547, and 11904231), and Innovation Laboratory of Terahertz

Biophysics and sponsored by Shanghai Sailing Program (No. 19YF1434100).

Acknowledgments

The authors also acknowledge the supercomputer support from Shanghai Snowlake Technology Co., Ltd.

Conflict of interest

The authors declare that the research was conducted in the absence of any commercial or financial relationships that could be construed as a potential conflict of interest.

Publisher's note

Supplementary material

The Supplementary Material for this article can be found online at: https://www.frontiersin.org/articles/10.3389/fphy.2023.1098170/full#supplementary-material

References

1. Koros WJ, Zhang C. Materials for next-generation molecularly selective synthetic membranes. *Nat Mater* (2017) 16(3):289–97. doi:10.1038/nmat4805

2. Feng L, Wu L, Qu X. New horizons for diagnostics and therapeutic applications of graphene and graphene oxide. *Adv Mater* (2013) 25(2):168–86. doi:10.1002/adma.201203229

3. Van der Bruggen B. Chemical modification of polyethersulfone nanofiltration membranes: A review. *J Appl Polym Sci* (2009) 114(1):630–42. doi:10.1002/app.30578

4. Zhu Y, Murali S, Cai W, Li X, Suk JW, Potts JR, et al. Graphene and graphene oxide: Synthesis, properties, and applications. *Adv Mater* (2010) 22(35):3906–24. doi:10.1002/adma.201001068

5. Dideikin AT, Vul AY. Graphene oxide and derivatives: The place in graphene family. *Front Phys* (2019) 6:149. doi:10.3389/fphy.2018.00149

6. Zhu Z, Guo HK, Jiang XK, Chen Y, Song B, Zhu Y, et al. Reversible hydrophobicity–hydrophilicity transition modulated by surface curvature. *J Phys Chem Lett* (2018) 9(9):2346–52. doi:10.1021/acs.jpclett.8b00749

7. Dreyer DR, Park S, Bielawski CW, Ruoff RS. The chemistry of graphene oxide. *Chem Soc Rev* (2010) 39(1):228–40. doi:10.1039/b917103g

8. Elimelech M, Phillip WA. The future of seawater desalination: Energy, technology, and the environment. *Science* (2011) 333(6043):712–7. doi:10.1126/science.1200488

9. Lonsdale HK. The growth of membrane technology. *J Membr Sci* (1982) 10(2-3):81–181. doi:10.1016/s0376-7388(00)81408-8

10. Li C, Yang J, Zhang L, Li S, Yuan Y, Xiao X, et al. Carbon-based membrane materials and applications in water and wastewater treatment: A review. *Environ Chem Lett* (2021) 19(2):1457–75. doi:10.1007/s10311-020-01112-8

11. Nair RR, Wu HA, Jayaram PN, Grigorieva IV, Geim AK. Unimpeded permeation of water through helium-leak–tight graphene-based membranes. *Science* (2012) 335(6067):442–4. doi:10.1126/science.1211694

12. Chen L, Shi G, Shen J, Peng B, Zhang B, Wang Y, et al. Ion sieving in graphene oxide membranes via cationic control of interlayer spacing. *Nature* (2017) 550(7676):380–3. doi:10.1038/nature24044

13. Han Y, Xu Z, Gao C. Ultrathin graphene nanofiltration membrane for water purification. *Adv Funct Mater* (2013) 23(29):3693–700. doi:10.1002/adfm.201202601

14. Hu M, Mi B. Enabling graphene oxide nanosheets as water separation membranes. *Environ Sci Technol* (2013) 47(8):3715–23. doi:10.1021/es400571g

15. Sun P, Zhu M, Wang K, Zhong M, Wei J, Wu D, et al. Selective ion penetration of graphene oxide membranes. *ACS Nano* (2013) 7(1):428–37. doi:10.1021/nn304471w

16. Devanathan R, Chase-Woods D, Shin Y, Gotthold DW. Molecular dynamics simulations reveal that water diffusion between graphene oxide layers is slow. *Sci Rep* (2016) 6(1):29484–8. doi:10.1038/srep29484

17. Abraham J, Vasu KS, Williams CD, Gopinadhan K, Su Y, Cherian CT, et al. Tunable sieving of ions using graphene oxide membranes. *Nat Nanotechnol* (2017) 12(6):546–50. doi:10.1038/nnano.2017.21

18. Chen B, Jiang H, Liu X, Hu X. Observation and analysis of water transport through graphene oxide interlamination. *J Phys Chem C* (2017) 121(2):1321–8. doi:10.1021/acs.jpcc.6b09753

19. Wei N, Peng X, Xu Z. Understanding water permeation in graphene oxide membranes. *ACS Appl Mater Inter* (2014) 6(8):5877–83. doi:10.1021/am500777b

20. Dai H, Xu Z, Yang X. Water permeation and ion rejection in layer-by-layer stacked graphene oxide nanochannels: A molecular dynamics simulation. *J Phys Chem C* (2016) 120(39):22585–96. doi:10.1021/acs.jpcc.6b05337

21. Liu S. Steric effect: A quantitative description from density functional theory. *J Chem Phys* (2007) 126(24):244103. doi:10.1063/1.2747247

22. Tsirelson VG, Stash AI, Liu S. Quantifying steric effect with experimental electron density. *J Chem Phys* (2010) 133(11):114110. doi:10.1063/1.3492377

23. Chen L, Moon JH, Ma X, Zhang L, Chen Q, Peng R, et al. High performance graphene oxide nanofiltration membrane prepared by electrospraying for wastewater purification. *Carbon* (2018) 130:487–94. doi:10.1016/j.carbon.2018.01.062

24. Liu S, Tong X, Chen Y, Crittenden J. Forward solute transport in forward osmosis using a freestanding graphene oxide membrane. *Environ Sci Technol* (2021) 55(9):6290–8. doi:10.1021/acs.est.0c08135

25. El Meragawi S, Akbari A, Hernandez S, Mirshekarloo MS, Bhattacharyya D, Tanksale A, et al. Enhanced permselective separation of per-fluorooctanoic acid in graphene oxide membranes by a simple PEI modification. *J Mater Chem A* (2020) 8(46):24800–11. doi:10.1039/d0ta06523d

26. Han Y, Jiang Y, Gao C. High-flux graphene oxide nanofiltration membrane intercalated by carbon nanotubes. *Acs Appl Mater Inter* (2015) 7(15):8147–55. doi:10.1021/acsami.5b00986

27. Wang P, Lou J, Fang G, Chang C. Progress on cutting-edge infrared-terahertz Biophysics. *IEEE Trans Microw Theor Tech.* (2022) 70(11):5117–40. doi:10.1109/tmtt.2022.3200333

28. Xie Z, Li Z, Li J, Kou J, Yao J, Fan J. Electric field-induced gas dissolving in aqueous solutions. *J Chem Phys* (2021) 154(2):024705. doi:10.1063/5.0037387

29. Zhang QL, Wu YX, Yang RY, Zhang JL, Wang RF. Effect of the direction of static electric fields on water transport through nanochannels. *Chem Phys Lett* (2021) 762:138139. doi:10.1016/j.cplett.2020.138139

30. Zhi Z, Shao-Dian Y, Tong-Chuan D, Zhao Y, Sun TY, Li YM. THz electromagnetic wave regulated dissolution of methane hydrate. *Acta Phys Sin-ch Ed* (2021) 70(24):248705. doi:10.7498/aps.70.20211779

31. Baxter HW, Worrall AA, Pang J, Chen R, Yang B. Volatile liquid detection by terahertz technologies[J]. *Front Phys* (2021) 9:639151. doi:10.3389/fphy.2021.639151

32. Zhenwei Z, Jing X, Rui J, Yinghong W, Hao G, Siyi H, et al. Terahertz non-destructive testing and imaging of high-voltage cables[J]. *Front Phys* (2022) 10:893145. doi:10.3389/fphy.2022.893145

33. Li Y, Chang C, Zhu Z, Sun L, Fan C. Terahertz wave enhances permeability of the voltage-gated calcium channel. *J Am Chem Soc* (2021) 143(11):4311–8. doi:10.1021/jacs.0c09401

34. Li Y, Zhu Z, Sun L, Xiang Z, Chang C, Fan C. Physicochemical insights on terahertz wave diminished side effects of drugs from slow dissociation. *ACS Nano* (2022) 16(5):8419–26. doi:10.1021/acsnano.2c02952

35. Liu X, Qiao Z, Chai Y, Zhu Z, Wu K, Ji W, et al. Nonthermal and reversible control of neuronal signaling and behavior by midinfrared stimulation. *Proc Natl Acad Sci U.S.A* (2021) 118(10):e2015685118. doi:10.1073/pnas.2015685118

36. Wu K, Qi C, Zhu Z, Wang C, Song B, Chang C. Terahertz wave accelerates DNA unwinding: A molecular dynamics simulation study. *J Phys Chem Lett* (2020) 11(17):7002–8. doi:10.1021/acs.jpclett.0c01850

37. Liu G, Chang C, Qiao Z, Wu K, Zhu Z, Cui G, et al. Myelin sheath as a dielectric waveguide for signal propagation in the mid-infrared to terahertz spectral range. *Adv Funct Mater* (2019) 29(7):1807862. doi:10.1002/adfm.201807862

38. Li N, Peng D, Zhang X, Shu Y, Zhang F, Jiang L, et al. Demonstration of biophoton-driven DNA replication via gold nanoparticle-distance modulated yield oscillation. *Nano Res* (2021) 14(1):40–5. doi:10.1007/s12274-020-2937-z

39. Guo YW, Qin JY, Hu JH, Cao JH, Zhu Z, Wang CL. Molecular rotation-caused autocorrelation behaviors of thermal noise in water. *Nucl Sci.Tech* (2020) 31(6):53–10. doi:10.1007/s41365-020-00767-w

40. Zhu Z, Chen C, Chang C, Song B. Terahertz-light induced structural transition and superpermeation of confined monolayer water. *ACS Photon* (2020) 8(3):781–6. doi:10.1021/acsphotonics.0c01336

41. Zhu J, Li H, Li X, Li J. Regulating evaporation of a water nanofilm by applying a terahertz alternating electric field. *J Chem Phys* (2022) 157(13):134707. doi:10.1063/5.0114551

42. Yang RY, Jiang WZ, Huo PY. Anisotropic energy absorption from mid-infrared laser pulses in constrained water systems. *J Mol Liq* (2022) 366:120286. doi:10.1016/j.molliq.2022.120286

43. Tong-Chuan D, Shao-Jian Y, Yon Z, Sun TY, Li YM, Zhu Z. Relationship between hydrogen bond network dynamics of water and its terahertz spectrum. *Acta Phys Sin-ch Ed* (2021) 70(24):248702. doi:10.7498/aps.70.20211731

44. Zhu Z, Chang C, Shu Y, Song B. Transition to a superpermeation phase of confined water induced by a terahertz electromagnetic wave. *J Phys Chem Lett* (2019) 11(1):256–62. doi:10.1021/acs.jpclett.9b03228

45. Sun T, Zhu Z. Light resonantly enhances the permeability of functionalized membranes. *J Membr Sci* (2022) 662:121026. doi:10.1016/j.memsci.2022.121026

46. Lerf A, He H, Forster M, Klinowski J. Structure of graphite oxide revisited. *J Phys Chem B* (1998) 102(23):4477–82. doi:10.1021/jp9731821

47. Toukan K, Rahman A. Molecular-dynamics study of atomic motions in water. *Phys Rev B* (1985) 31(5):2643–8. doi:10.1103/physrevb.31.2643

48. Berendsen HJC, Postma JPM, van Gunsteren WF, Hermans J. Interaction models for water in relation to protein hydration. In: Pullman B, editor. *Intermolecular forces.* Dordrecht: Reidel (1981). p. 331–342.

49. Berendsen HJC, Grigera JR, Straatsma TP. The missing term in effective pair potentials. *J Phys Chem* (1987) 91(24):6269–71. doi:10.1021/j100308a038

50. Zhu F, Tajkhorshid E, Schulten K. Pressure-induced water transport in membrane channels studied by molecular dynamics. *Biophys J* (2002) 83(1):154–60. doi:10.1016/s0006-3495(02)75157-6

51. Huang Z, Nomura K, Nakano A, Wang J. Molecular dynamics simulations of dielectric breakdown of lunar regolith: Implications for water ice formation on lunar surface. *Geophys Res Lett* (2021) 48(3):e2020GL091681. doi:10.1029/2020gl091681

52. Saitta AM, Saija F, Giaquinta PV. *Ab initio* molecular dynamics study of dissociation of water under an electric field. *Phys Rev Lett* (2012) 108(20):207801. doi:10.1103/physrevlett.108.207801

frontiers | Frontiers in Physics

TYPE Original Research
PUBLISHED 17 February 2023
DOI 10.3389/fphy.2023.1130225

OPEN ACCESS

EDITED BY
Libin Fu,
Graduate School of China Academy of Engineering Physics, China

REVIEWED BY
Ruifeng Lu,
Nanjing University of Science and Technology, China
Zhihao Lan,
University College London,
United Kingdom

*CORRESPONDENCE
Wen-Lei Zhao,
wlzhao@jxust.edu.cn

SPECIALTY SECTION
This article was submitted to Atomic and Molecular Physics,
a section of the journal
Frontiers in Physics

RECEIVED 23 December 2022
ACCEPTED 06 February 2023
PUBLISHED 17 February 2023

CITATION
Zhao W-L and Wang R-R (2023), Scaling laws of out-of-time-order correlators in a non-Hermitian kicked rotor model.
Front. Phys. 11:1130225.
doi: 10.3389/fphy.2023.1130225

Scaling laws of out-of-time-order correlators in a non-Hermitian kicked rotor model

Wen-Lei Zhao* and Ru-Ru Wang

School of Science, Jiangxi University of Science and Technology, Ganzhou, China

We investigate the dynamics of the out-of-time-order correlators (OTOCs) *via* a non-Hermitian extension of the quantum kicked rotor model, where the kicking potential satisfies $\mathcal{PT}$-symmetry. The spontaneous $\mathcal{PT}$-symmetry breaking emerges when the strength of the imaginary part of the kicking potential exceeds a threshold value. We find, both analytically and numerically, that in the broken phase of $\mathcal{PT}$ symmetry, the OTOCs rapidly saturate with time evolution. Interestingly, the late-time saturation value scales as a pow-law in the system size. The mechanism of such scaling law results from the interplay between the effects of the nonlocal operator in OTOCs and the time reversal induced by non-Hermitian-driven potential.

KEYWORDS

out-of-time-order correlators, PT-symmetry, kicked rotor system, information scrambling, quantum chaos

1 Introduction

In recent years, the out-of-time-order correlators (OTOCs) $C = -\langle[A(t),B]^2\rangle$ have attracted extensive attention in diverse fields of physics, ranging from quantum chaos [1,2] and quantum information [3] to black hole physics [4]. A fundamental concept in these fields is information scrambling, namely, the spread of information encoding in local degrees of freedoms over the entire system to be inaccessible by local measurement [5–7]. This progress is quantified by the growth of local operators with time evolution, due to which it will be no longer commutable with other operators, separated by a long distance [8,9]. The operator growth is dominated by the classical chaos in such a way that the rate of exponential growth of OTOCs is proportional to the classical Lyapunov exponent [10,11]. Nowadays, the OTOCs are being widely used to diagnose the many-body localization [12,13], quantum entanglement [14–16], quantum thermalization [17–19], and many-body chaos [20–22], hence promoting intensive investigations in the field of many-body physics [23,24]. Interestingly, experimental advances have observed both the quantum information scrambling and quantum phase transition by measuring the OTOCs in the system of the quantum circuit [25,26] and a nuclear magnetic resonance quantum simulator [27].

For $\mathcal{PT}$-symmetric systems, the dynamics of OTOCs signals the Yang–Lee edge singularity [28] of phase transition and shows the quantized response to external driven potential [29]. It is now widely accepted that the non-Hermiticity is a fundamental modification to conventional quantum mechanics [30–36] since many systems, such as optics propagation in the “gain-or-loss” medium [37–39], the electronics transport in the dissipative circuit [40–43], and cold atoms in the tailored magneto-optical trap [44–48], are described by a non-Hermitian theory. The extension of Floquet systems to non-Hermitian regimes uncovers rich understandings of physics [49–53]. For example, the scaling of the spontaneous $\mathcal{PT}$-symmetry breaking and its relation with classical chaos are revealed in a non-Hermitian chaotic system [54]. The ballistic energy diffusion [55] and quantized acceleration of momentum current [56] are reported in a $\mathcal{PT}$-symmetric kicked rotor (PTKR) model. The quantum kicked rotor (QKR) and its variants provide ideal platforms for investigating fundamental problems, such as the quantum transport in momentum-space lattice [57,58], the quantum-to-classical transition of chaotic systems [59,60], and the quantum thermalization in many-body systems [61]. The operator growth and chaotic information scrambling in different variations of QKR are still open issues and require urgent investigations.

In this context, we investigate, both analytically and numerically, the dynamics of OTOCs in a PTKR model, with focus on the broken phase of $\mathcal{PT}$ symmetry. We observed that the OTOCs rapidly saturate with time evolution. Interestingly, the saturation value is the power-law function of the dimension of the system, which demonstrates a kind of scaling-law of the OTOCs with the system size. The mechanism of such scaling law results from two aspects. One is that the action of the non-local operators constructing the OTOCs on the state leads to a power-law decayed distribution in momentum space. The other is that the non-Hermitian kicking potential induces the perfect time reversal of thequantum state in momentum space. Using the power-law decayed quantum state, we analytically obtain the scaling of OTOCs with the size of momentum space, for which the OTOCs is the power-law function of the dimension of the system. This demonstrates that the OTOCs unboundedly increase with the system size, revealing a kind of fast scrambling [62,63]. Our result sheds light on the Floquet engineering of the fast scramblers in the non-Hermitian map systems.

The paper is organized as follows. In Section 2, we show our model and the scaling-law of OTOCs. In Section 3, we present the theoretical analysis of the scaling law. Section 4 contains the conclusion and discussion.

2 Model and results

The Hamiltonian of a PTKR reads

$$H = \frac{p^2}{2} + V_K(\theta)\sum_{n=0}^{\infty}\delta(t-t_n), \tag{1}$$

with the kicking potential

$$V_K(\theta) = K[\cos(\theta) + i\lambda\sin(\theta)], \tag{2}$$

which satisfies the $\mathcal{PT}$ symmetry $V_K(\theta) = V_K^*(-\theta)$ [55]. Here, $p = -i\hbar_{\text{eff}}\partial/\partial\theta$ is the angular momentum operator and θ is the angle coordinate, which obey the communication relation $[\theta, p] = i\hbar_{\text{eff}}$ with $\hbar_{\text{eff}}$ the effective Planck constant. The parameters K and λ control the strength of the real and imaginary part of the kicking potential, respectively. The time t_n is integer, i.e., $t_n = 1, 2\ \ldots$, indicating the kicking number. All variables are properly scaled and thus in dimensionless units. The eigenequation of the angular momentum operator is $p|\phi_n\rangle = p_n|\phi_n\rangle$ with eigenstate $\langle\theta|\phi_n\rangle = e^{in\theta}/\sqrt{2\pi}$ and eigenvalue $p_n = n\hbar_{\text{eff}}$. On the basis of $|\phi_n\rangle$, an arbitrary quantum state can be expanded as $|\psi\rangle = \sum_{n=-\infty}^{\infty}\psi(p_n)|\phi_n\rangle$.

The evolution of the quantum state from t_j to t_{j+1} is given by $|\psi(t_{j+1})\rangle = U|\psi(t_j)\rangle$, where the Floquet operator U takes the form

$$U = \exp\left(-i\frac{p^2}{2\hbar_{\text{eff}}}\right)\exp\left[-i\frac{V_K(\theta)}{\hbar_{\text{eff}}}\right]. \tag{3}$$

In numerical simulations, one period evolution splits into two steps, namely, the kicking evolution $U_K(\theta) = \exp(-iV_K(\theta)/\hbar_{\text{eff}})$ and the free evolution $U_f(p_n) = \exp(-ip_n^2/2\hbar_{\text{eff}})$ [57–59]. At first, we construct the kicking evolution in angle coordinate space, $\psi'(\theta_l) = U_K(\theta_l)\psi(\theta_l, t_j)$ with discrete grids $\theta_l = -\pi + 2\pi l/N$ $(0 \le l < N)$ and $N = 2^m$. Then, the fast Fourier transform is used to realize the transformation of the state $|\psi'\rangle$ to momentum space yielding the state $\psi'(p_n)$ with $-N\hbar_{\text{eff}}/2 \le p_n \le (N-1)\hbar_{\text{eff}}/2$. Finally, we take the free evolution, i.e., $\psi(p_n, t_{j+1}) = U_f(p_n)\psi'(p_n)$. By repeating the same procedure, one can get the state $|\psi(t_n)\rangle$ at an arbitrary time. In the experiment, the PTKR model can be realized by an optical platform with a Fabry–Perot resonator consisting of two plane mirrors, one of which is equipped with a mixed-loss phase grating to mimic the periodic kicking sequence of PT-symmetric potential [55]. It is found that in the broken phase of PT-symmetry, the light propagation in the Fabry–Perot resonator demonstrates the unidirectional transport in frequency domain.

The eigenequation of the Floquet operator has the expression $U|\varphi_\varepsilon\rangle = e^{-i\varepsilon}|\varphi_\varepsilon\rangle$, where the eigenvalue ε is named as quasienergy. Intrinsically, the quasienergy of the PTKR model is complex, i.e., $\varepsilon = \varepsilon_r + i\varepsilon_i$, when the value λ exceeds a threshold value, i.e., $\lambda > \lambda_c$ [54,55], which is a signature of the spontaneous $\mathcal{PT}$-symmetry breaking of Floquet systems. Based on the relation $|\psi(t_n)\rangle = \sum_\varepsilon C_\varepsilon e^{-i\varepsilon_r t_n}e^{\varepsilon_i t_n}|\varepsilon_\varepsilon\rangle$, the norm $\mathcal{N} = \langle\psi(t_n)|\psi(t_n)\rangle$ exponentially increases with time for positive ε_i. We numerically investigate the time evolution of $\mathcal{N}$ for different λ. Figure 1A shows that for very small λ (e.g., $\lambda = 10^{-4}$), the norm remains at unity $\mathcal{N} = 1$ with the time evolution, which implies that $\varepsilon_i = 0$ and the system is in the unbroken phase of $\mathcal{PT}$ symmetry. Interestingly, for sufficiently large λ (e.g., $\lambda = 0.002$), the norm exponentially increases with time, i.e., $\mathcal{N} = e^{\gamma t}$, signaling the occurrence of the spontaneous $\mathcal{PT}$ symmetry breaking. The growth rate γ increases with the increase of λ. In order to quantify the phase transition point λ_c, we numerically investigate the time-averaged value of norm $\bar{\mathcal{N}} = \sum_{j=1}^{M}\mathcal{N}(t_j)/M$ for different values of λ. Our results show that for a specific $\hbar_{\text{eff}}$, the average value $\bar{\mathcal{N}}$ equals to unity for λ smaller than a critical value λ_c, beyond which the $\bar{\mathcal{N}}$ gradually increases (see Figure 1B). Moreover, the λ_c increases with the increase of $\hbar_{\text{eff}}$.

The OTOCs are defined as the average of the squared commutator, i.e., $C(t) = -\langle[A(t),B]^2\rangle$, where both operators $A(t) = U^\dagger(t)AU(t)$ and B are evaluated in the Heisenberg picture, and $\langle\cdots\rangle = \langle\psi(t_0)|\cdots|\psi(t_0)\rangle$ indicates the expectation value taken over the initial state $|\psi(t_0)\rangle$ [23]. It usually uses the thermal states for taking the average in the investigation of OTOCs of lattice systems. For the Floquet-driven system, however, there are no well-defined thermal states, as the temperature tends to be infinity as time evolves [64]. Without loss of generality, we choose a Gaussian wavepacket as an initial state, i.e., $\psi(\theta, 0) = (\sigma/\pi)^{1/4}\exp(-\sigma\theta^2/2)$ with $\sigma = 10$. We consider the case as $A = \theta$ and $B = p^m$ $(m \in \mathbb{N})$, hence $C(t) = -\langle[\theta(t), p^m]^2\rangle$.

Our main result is the scaling law of the late-time behavior of the OTOCs

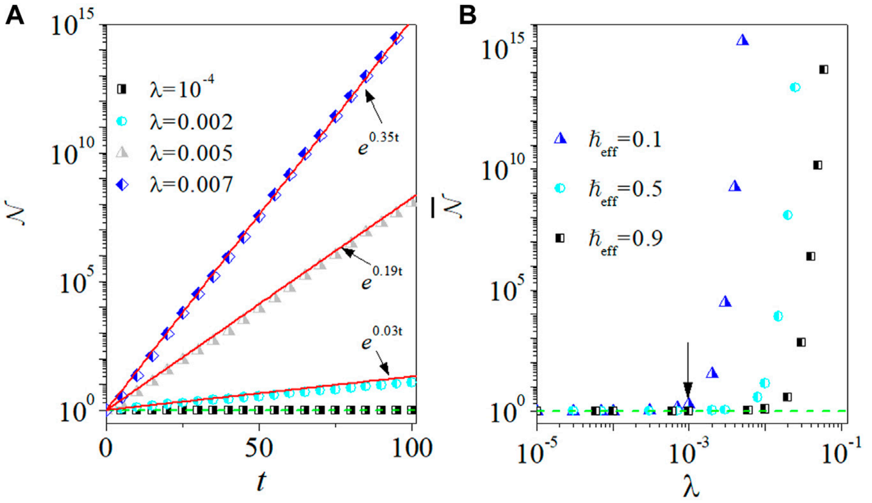

FIGURE 1
(A) Time dependence of $\mathcal{N}$ for $\hbar_{\rm eff}$ = 0.1 with $\lambda = 10^{-4}$ (squares), 0.002 (circles), 0.005 (triangles), and 0.007 (diamonds). Solid lines indicate the exponential fitting $\mathcal{N} = e^{\gamma t}$. **(B)** The average value $\bar{\mathcal{N}}$ *versus* λ with $\hbar_{\rm eff}$ = 0.1 (squares), 0.5 (circle), and 0.9 (triangles). Arrows mark the phase transition point λ_c for $\hbar_{\rm eff}$ = 0.1. Horizontal dashed lines in **(A,B)** denote $\mathcal{N} = 1$ and $\bar{\mathcal{N}} = 1$, respectively. The parameter is $K = 2\pi$.

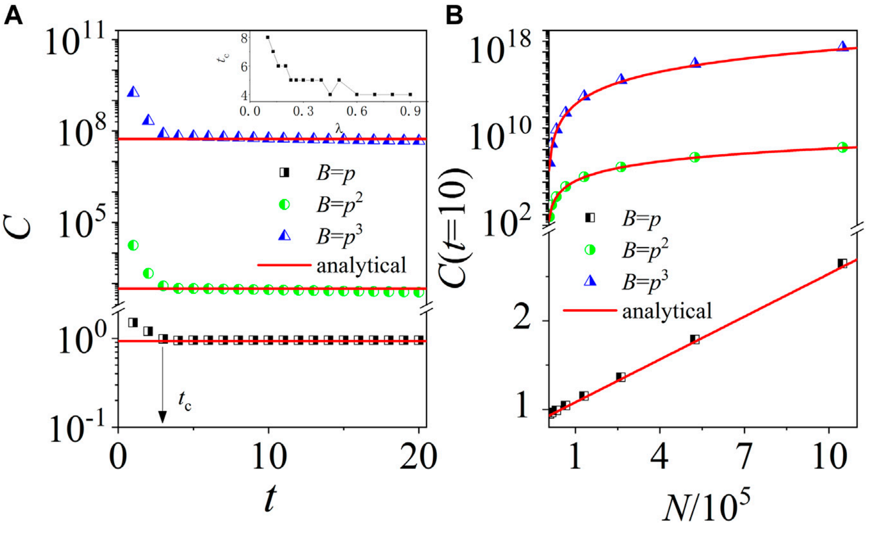

FIGURE 2
(A) Time dependence of $C(t)$ with $B = p$ (squares), p^2 (circles), and p^3 (triangles) with $N = 2^{13}$. The arrow marks the critical time t_c for $B = p$. Inset: Critical time t_c *versus* λ. **(B)** $C(t)$ at the time $t = t_{10}$ *versus* N. Solid lines in **(A,B)** denote our theoretical prediction in Eq. 4. The parameters are $K = 2\pi$, $\lambda = 0.9$, and $\hbar_{\rm eff}$ = 0.1.

$$C(t) \sim N^{2m-1}\theta_c^2, \tag{4}$$

where N is the dimension of the momentum space of the PTKR model, and $\theta_c = \pi/2$. This prediction is verified by numerical results in Figure 2. As an illustration, we consider m = 1, 2, and 3 in numerical simulations. Figure 2A shows that for a specific m, the $C(t)$ saturates rapidly as time evolves, which is in perfect agreement with our theoretical prediction in Eq. 4. The critical time for the saturation of C decreases with the increase of λ, until saturation (as shown in Figure 2A). In order to further confirm the scaling law of $C(t)$, we numerically investigate the C at a specific time for different values of N. Figure 2B shows that for $t = t_{10}$, the value of C increases in the power-law of N, which coincides with the theoretical prediction in Eq. 4. The scaling of $C(t)$ with dimensions of the system demonstrates that it diverges as $N \to \infty$, which is of interest in the study of fast scrambling [63]. We would like to mention that we previously found the scaling law for the OTOCs constructed by $A = \theta$ and $B = p$, in a Gross–Pitaevskii map system

[65]. Our present work explores the scaling law for $B = p^m$ with the arbitrary integer m; moreover, it extends the investigation to non-Hermitian systems, which is evidently a significant advance in the fields of operator growth in chaotic systems.

3 Theoretical analysis

3.1 Scaling law of the $C_1(t)$

Straightforward derivation yields the expression of OTOCs

$$C(t) = C_1(t) + C_2(t) - 2\mathrm{Re}[C_3(t)], \tag{5}$$

where the three terms in right side are defined by

$$C_1(t) = \langle \psi_R(t_0)|p^{2m}|\psi_R(t_0)\rangle, \tag{6}$$

$$C_2(t) = \langle \varphi_R(t_0)|\varphi_R(t_0)\rangle, \tag{7}$$

and

$$C_3(t) = \langle \psi_R(t_0)|p^m|\varphi_R(t_0)\rangle, \tag{8}$$

with $|\psi_R(t_0)\rangle = U^\dagger(t_n, t_0)\theta U(t_n, t_0)|\psi(t_0)\rangle$ and $|\varphi_R(t_0)\rangle = U^\dagger(t_n, t_0)\theta U(t_n, t_0)p^m|\psi(t_0)\rangle$.

To get the state $|\psi_R(t_0)\rangle$, one needs three steps: 1) forward evolution $t_0 \to t_n$, i.e., $|\psi(t_n)\rangle = U(t_n, t_0)|\psi(t_0)\rangle$; 2) action of the operator θ on $|\psi(t_n)\rangle$, i.e., $|\tilde{\psi}(t_n)\rangle = \theta|\psi(t_n)\rangle$; and 3) backward evolution $t_n \to t_0$, i.e., $|\psi_R(t_0)\rangle = U^\dagger(t_n, t_0)|\tilde{\psi}(t_n)\rangle$. $C_1(t_n)$ (see Eq. 6) is just the expectation value of the p^{2m} taken over the state $|\psi_R(t_0)\rangle$. For the numerical calculation of the state $|\varphi_R(t_0)\rangle$, one should first construct the operation of p^m on the initial state $|\psi(t_0)\rangle$, i.e., $|\varphi(t_0)\rangle = p^m|\psi(t_0)\rangle$. Then, forward evolution from t_0 to t_n yields the state $|\varphi(t_n)\rangle = U(t_n, t_0)|\varphi(t_0)\rangle$. At time $t = t_n$, the action of θ on the state $|\varphi(t_n)\rangle$ results in a new state $|\tilde{\varphi}(t_n)\rangle = \theta|\varphi(t_n)\rangle$, starting from which the time-reversal process $t_n \to t_0$ yields the state $|\varphi_R(t_0)\rangle = U^\dagger(t_n, t_0)|\tilde{\varphi}(t_n)\rangle$. The norm of $|\varphi_R(t_0)\rangle$ is just the $C_2(t_n)$ (see Eq. 7). As the two states $|\psi_R(t_0)\rangle$ and $|\varphi_R(t_0)\rangle$ are available at the end of time reversal, one can calculate the $C_3(t_n)$ according to Eq. 8.

It is known that in the $\mathcal{PT}$-symmetry breaking phase, the norm of quantum state $\mathcal{N}_\psi(t_n) = \langle \psi(t_n)|\psi(t_n)\rangle$ exponentially increases for both the forward and backward time evolutions. To eliminate the contribution of norm to OTOCs, it is necessary to take the normalization for the time-evolved state. Specifically, for the forward evolution $t_0 \to t_n$, we set the norm of the quantum state equals to that of the initial state, i.e., $\mathcal{N}_\psi(t_j) = \langle \psi(t_0)|\psi(t_0)\rangle$ with $0 \le j \le n$. The backward evolution starts from the time $t = t_n$ with the state $|\tilde{\psi}(t_n)\rangle$, whose norm $\mathcal{N}_{\tilde{\psi}}(t_n) = \langle \psi(t_n)|\theta^2|\psi(t_n)\rangle$ is expectation value of θ^2 with the state $|\psi(t_n)\rangle$. It is evident that the value of $\mathcal{N}_{\tilde{\psi}}(t_n)$ is important information encoded by the operation of θ on the state $|\psi(t_n)\rangle$. Based on this, we take the normalization of the quantum state in the backward evolution $t_n \to t_0$ in such a way that its norm equals to $\mathcal{N}_{\tilde{\psi}}(t_n)$, i.e., $\mathcal{N}_{\psi_R}(t_j) = \mathcal{N}_{\tilde{\psi}}(t_n)$. One can find that for both the forward and backward evolutions, the norm of a time-evolved state always equals that of the state which the time evolution starts from. The same procedure of normalization is applied in calculating $C_2(t_n)$. Therefore, we have the equivalence $\mathcal{N}_\varphi(t_j) = \langle \varphi(t_0)|\varphi(t_0)\rangle$ and $\mathcal{N}_{\varphi_R}(t_j) = \langle \tilde{\varphi}(t_n)|\tilde{\varphi}(t_n)\rangle$ $(0 \le j \le n)$ for the forward evolution and time reversal, respectively.

We rewrite the C_1 as

$$C_1(t) = \langle \psi_R(t_0)|p^{2m}|\psi_R(t_0)\rangle = \langle p^{2m}(t_0)\rangle_R \mathcal{N}_{\psi_R}(t_0), \tag{9}$$

where $\mathcal{N}_{\psi_R}(t_0) = \langle \psi_R(t_0)|\psi_R(t_0)\rangle$ is the norm of the quantum state $|\psi_R(t_0)\rangle$ and $\langle p^{2m}(t_0)\rangle_R = \langle \psi_R(t_0)|p^{2m}|\psi_R(t_0)\rangle / \mathcal{N}_{\psi_R}(t_0)$ indicates the exception value of p^{2m} of the state $|\psi_R(t_0)\rangle$ with the division of its norm. We numerically investigate both the forward and backward evolutions of the norm $\mathcal{N}$, and the mean values $\langle\theta\rangle$ and $\langle p\rangle$ for a specific time, e.g., $t = t_{10}$. It should be noted that we define the expectation value of observable Q as $\langle Q\rangle = \langle \psi(t)|Q|\psi(t)\rangle / \mathcal{N}(t)$ with $\mathcal{N}(t) = \langle \psi(t)|\psi(t)\rangle$. It is evident that such kind of definition eliminates the contribution of norm to mean value. Figure 3A shows that the norm is in unity during the forward time evolution (i.e., $t_0 \to t_{10}$) and remains at a fixed value, i.e., $\mathcal{N}_{\psi_R}(t_0) \approx \theta_c^2$ during the backward evolution (i.e., $t_{10} \to t_0$). For $t_0 \to t_{10}$, the value of norm equals to that of the normalized initial state, so $\mathcal{N}(t_j) = 1$. For the time reversal $t_{10} \to t_0$, our normalization procedure results in the equivalence $\mathcal{N}_{\psi_R}(t_j) = \langle \psi(t_n)|\theta^2|\psi(t_n)\rangle$. Interestingly, our numerical investigations in Figures 4A, C, E show that for the forward evolution, the initial Gaussian wavepacket rapidly moves to the position $\theta_c = \pi/2$; it should be noted that the initial Gaussian wavepacket has not moved to the position θ_c before t_4. This is the reason why $C(t)$ decays sharply before t_4. During the time reversal, it remains localized at θ_c with the width of distribution being much smaller than that of the state of forward evolution. Correspondingly, the mean value $\langle\theta\rangle$ has very slight differences with θ_c (see Figure 3A). Since the quantum state is extremely localized at θ_c, one can get the approximation

$$\mathcal{N}_{\psi_R}(t_0) = \langle \psi(t_n)|\theta^2|\psi(t_n)\rangle \approx \theta_c^2. \tag{10}$$

Figures 4B, D, F show the momentum distribution of the state during both forward and backward evolutions. For the forward evolution, the quantum state behaves like a soliton which moves to a positive direction in momentum space, resulting in the linear increase of the mean momentum, i.e., $\langle p\rangle = Kt$ (see Figure 3B). The mechanism of the directed acceleration has been unveiled in our previous investigations [29,56]. Intriguingly, at time $t = t_{10}$, the action of θ yields a state with a power-decayed shape, i.e., $|\psi_R(p, t_0)|^2 \propto (p - p_c)^{-2}$ (see Figure 4F). Most importantly, during the backward evolution, the quantum state still retains the power-law decayed shape, for which the center p_c decreases with time and almost overlaps with that of the state of the forward evolution. This clearly demonstrates a kind of time reversal of transport behavior in momentum space.

In the aspect of the mean momentum $\langle p\rangle$, we find that the value of $\langle p\rangle$ linearly decreases during the backward evolution and is in perfect symmetry with that of the forward evolution, which is a solid evidence of time reversal. In the end of the backward evolution, the quantum state $|\psi_R(t_0)\rangle$ is localized at the point $p = 0$ (see Figure 4B). By using the power-law distribution $|\psi_R(p, t_0)|^2 \sim p^{-2}$, it is straightforward to get the estimation of the expectation value of p^{2m}, i.e., $\langle p^{2m}\rangle_{\psi_R} = \int_{p_{-N/2}}^{p_{N/2}} p^{2m}|\psi_R(p, t_0)|^2 dp \propto N^{2m-1}$. Taking both $\langle p^{2m}\rangle_{\psi_R}$ and $\mathcal{N}_{\psi_R}(t_0)$ in Eq. 10 into Eq. 9 yields the relation

$$C_1(t) \propto N^{2m-1}\theta_c^2, \tag{11}$$

which is verified by our numerical results in Figure 5. As an illustration, we consider the cases with $m = 1$, 2, and 3. Our

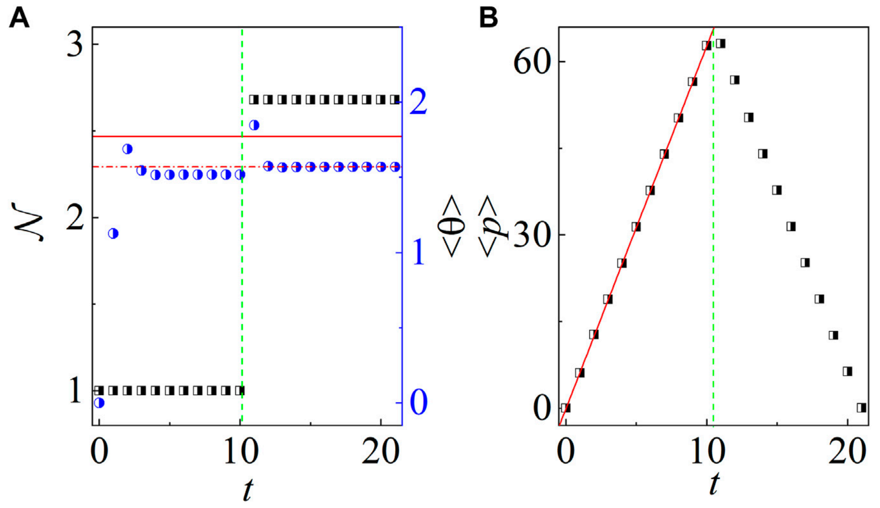

FIGURE 3
Time evolution of $\mathcal{N}$ **(A)**, $\langle\theta\rangle$ **(A)**, and $\langle p\rangle$ **(B)** with $t = t_{10}$. In **(A)**, solid and dash-dotted lines indicate $\mathcal{N} = \theta_c^2$ and $\langle\theta\rangle = \theta_c$ (= $\pi/2$), respectively. In **(B)**, solid line indicates $\langle p\rangle = Kt$. Green dashed lines in **(A,B)** are auxiliary lines. The parameters are the same as in Figure 2.

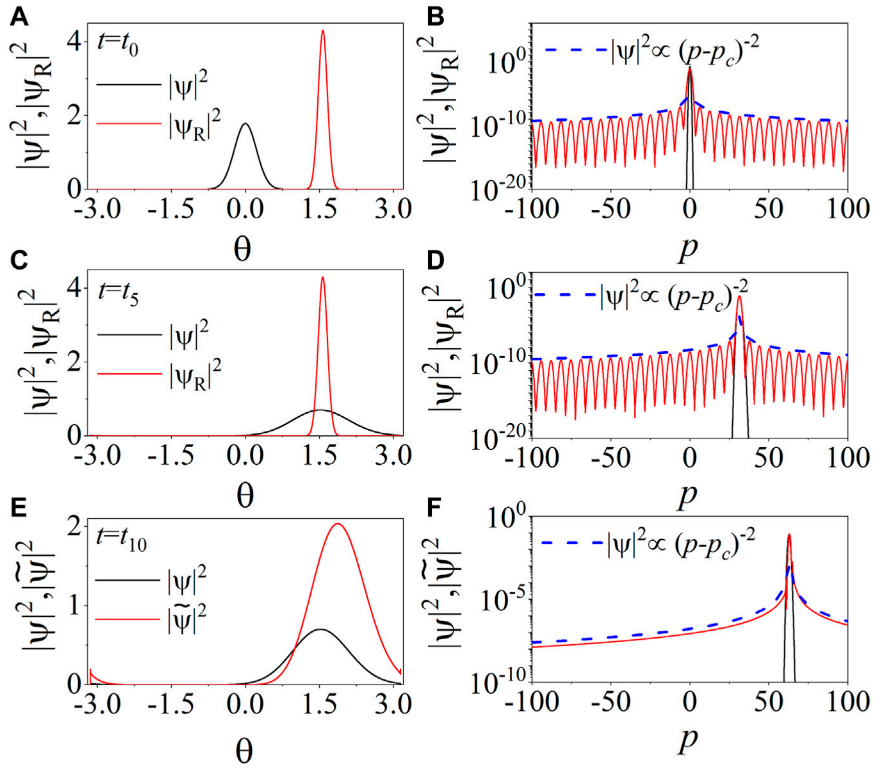

FIGURE 4
Distributions in real (left panels) and momentum (right panels) space. In **(A–D)**, black and red lines indicate the distribution of the states at the forward $|\psi(t_j)\rangle$ and backward $|\psi_R(t_j)\rangle$ evolution, respectively, with $t = t_0$ (top panels), $t = t_5$ (middle panels), and $t = t_{10}$ (bottom panels). In **(E–F)**, red and black lines indicate the distribution of the states $|\psi(t_{10})\rangle$ and $|\tilde{\psi}(t_{10})\rangle = \theta|\psi(t_{10})\rangle$. Blue dashed lines indicate the power-law decay $|\psi|^2 \propto (p - p_c)^{-2}$. The parameters are the same as in Figure 2.

numerical results of the late-time saturation values of C_1 are in good agreement with Eq. 11. It is now clear that the scaling of $C(t)$ with N originates from the power-law decay of the state $|\psi_R(t_0)\rangle$. The reason for the formation of power-law decayed wavefunction has been uncovered in Ref. 65.

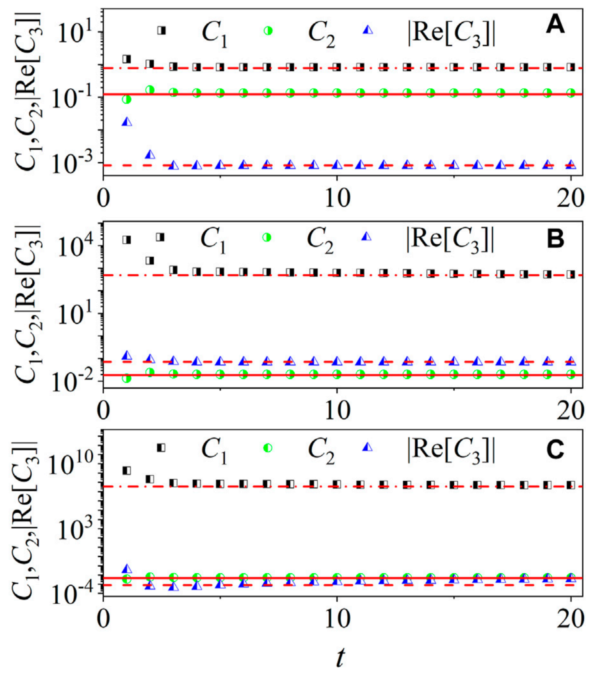

FIGURE 5
C_1 (squares), C_2 (circles), and $|\mathrm{Re}[C_3]|$ (triangles) *versus* time with $B = p$ **(A)**, p^2 **(B)**, and p^3 **(C)**. Dash-dotted, solid, and dashed lines indicate our theoretical prediction in Eq. 11 for C_1, Eq. 13 for C_2, and Eq. 15 for C_3, respectively. The parameters are the same as in Figure 2.

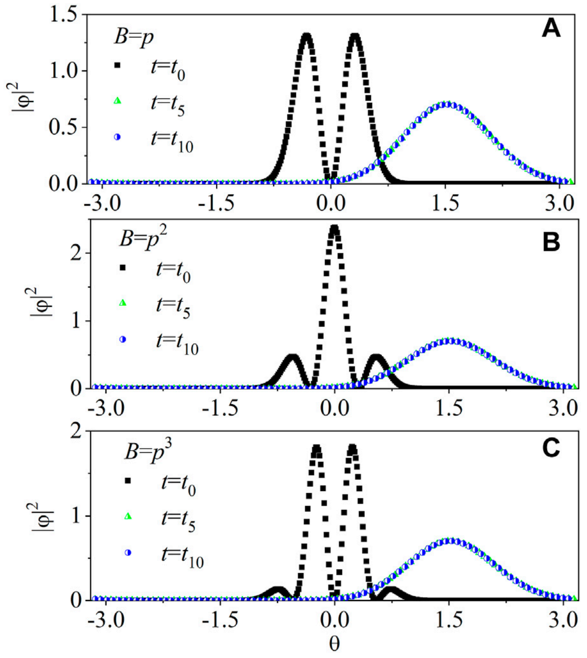

FIGURE 6
Probability density distributions in real space at the time $t = t_0$ (squares), t_5 (triangles), and t_{10} (circles) with $B = p$ **(A)**, p^2 **(B)**, and p^3 **(C)**. The parameters are the same as in Figure 2.

3.2 Analytical analysis of $C_2(t)$

We proceed to evaluate the time dependence of $C_2(t)$ in Eq. 7, which is just the norm of the state $|\varphi_R(t_0)\rangle$ at the end of backward evolution. According to our normalization procedure, the value of C_2 equals to the norm of the state $|\tilde{\varphi}(t_n)\rangle = \theta|\varphi(t_n)\rangle$, hence

$$C_2 = \langle\varphi(t_n)|\theta^2|\varphi(t_n)\rangle = \langle\theta^2\rangle\mathcal{N}_\varphi(t_n), \tag{12}$$

with $\mathcal{N}_\varphi(t_n) = \langle\varphi(t_n)|\varphi(t_n)\rangle$ and $\langle\theta^2\rangle = \langle\varphi(t_n)|\theta^2|\varphi(t_n)\rangle/\mathcal{N}(t_n)$. We numerically find that the state $|\varphi(t_n)\rangle$ is extremely localized at the position θ_c during the forward evolution (see Figure 6). Then, a rough estimation yields $\langle\theta^2\rangle \sim \theta_c^2$. The norm $\mathcal{N}_\varphi(t_n)$ equals that of the initial state $|\varphi(t_0)\rangle = p^m|\psi(t_0)\rangle$. By using the initial Gaussian wavepacket $\psi(p,t_0) = (1/\sigma\hbar_{\mathrm{eff}}^2\pi)^{1/4}\exp(-p^2/2\sigma\hbar_{\mathrm{eff}}^2)$, one can straightforwardly obtain

$$\mathcal{N}_\varphi(t_n) = \int_{-\infty}^{\infty} p^{2m}|\psi(p,t_0)|^2dp = \frac{(2m-1)!!}{2^m\alpha^m},$$

where $\alpha = 1/(\sigma\hbar^2)$ and $(\ldots)!!$ denote a double factorial. Taking both the $\langle\theta\rangle$ and $\mathcal{N}_\varphi(t_n)$ into Eq. 12 yields the late-time saturation value

$$C_2(t) \sim \theta_c^2\frac{(2m-1)!!}{2^m\alpha^m}, \tag{13}$$

which is in good agreement with our numerical results in Figure 5.

3.3 Scaling law of $C_3(t)$

The value of $C_3(t)$ depends on both the states $|\psi_R(t_0)\rangle$ and $|\varphi_R(t_0)\rangle$ (see Eq. 8). Figure 7 shows the probability density distributions of the two states in both the real space and momentum space. For comparison, the two states are normalized to unity. One can find the perfect consistence between $|\psi_R(t_0)\rangle$ and $|\varphi_R(t_0)\rangle$. Then, we roughly regard C_3 as the expectation value of the p^m taking over the state $\psi_R(t_0)$ or $\varphi_R(t_0)$, i.e., $C_3(t) \approx \langle p^m(t_0)\rangle_{\psi_R}\sqrt{\mathcal{N}_{\psi_R}(t_0)}\sqrt{\mathcal{N}_{\varphi_R}(t_0)}$, where according to aforementioned derivations $\mathcal{N}_{\psi_R}(t_0) = \theta_c^2$ and $\mathcal{N}_{\varphi_R}(t_0) = C_2(t)$. By using the power-law decayed wavepacket $|\psi_R(t_0)|^2 \propto p^{-2}$, one can obtain the estimation

$$\begin{aligned}\langle p^m(t_0)\rangle_{\psi_R} &\approx \int_{p_{-N/2}}^{p_{N/2}} p^m|\psi_R(p,t_0)|^2dp\\ &\sim \begin{cases}0 & \text{for odd } m,\\ N^{m-1} & \text{for even } m.\end{cases}\end{aligned}. \tag{14}$$

Accordingly, the C_3 is approximated as

$$C_3(t) \sim \begin{cases}0 & \text{for odd } m,\\ \eta N^{m-1} & \text{for even } m.\end{cases}. \tag{15}$$

with the prefactor $\eta \propto \theta_c^2[(2m-1)!!/2^m\alpha^m]^{\frac{1}{2}}$.

We numerically calculate the absolute value of the real part of C_3. Interestingly, our numerical results of $|\mathrm{Re}[C_3]|$ is in good agreement with the analytical prediction in Eq. 15 (see Figure 5), which proves the validity of our theoretical analysis. We further numerically investigate the $|\mathrm{Re}[C_3(t)]|$ at a specific time for different N. Figure 8 shows that for $B = p$, the value of $|\mathrm{Re}[C_3(t)]|$ is nearly zero with varying N, which is consistent with our theoretical prediction in Eq. 15. For $B = p^3$, the value of $|\mathrm{Re}[C_3(t)]|$ has slight difference with zero for large values of N, signaling the

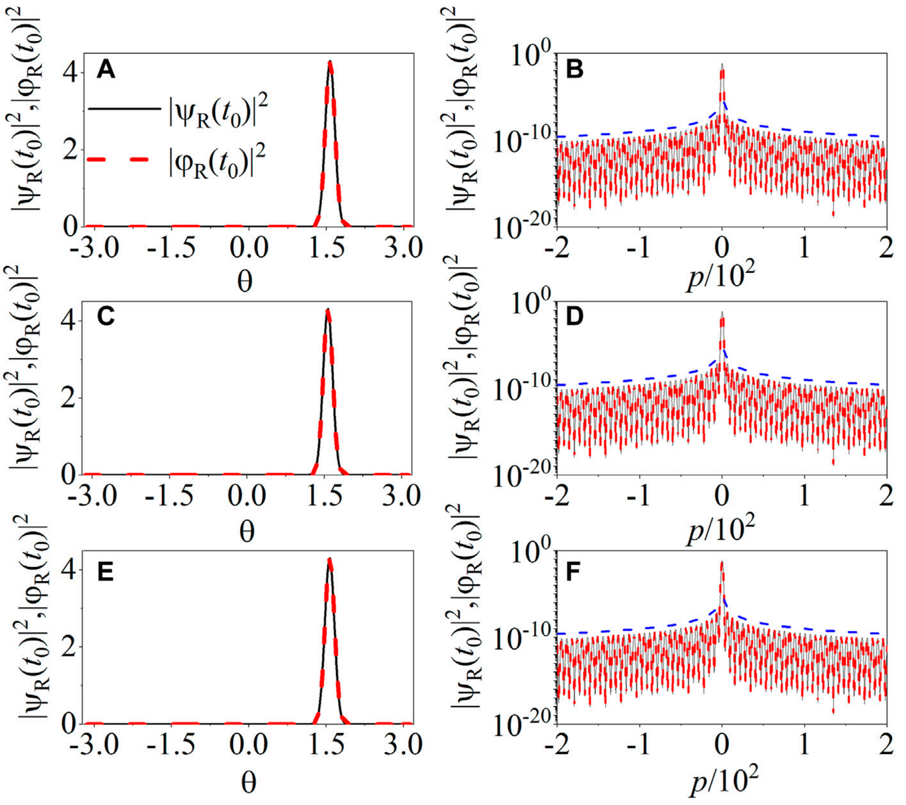

FIGURE 7
Comparison of the distribution of states $|\psi_R(t_0)\rangle$ (solid lines) and $|\varphi_R(t_0)\rangle$ (dashed lines) in real **(A, C, E)** and momentum space **(B, D, F)** with $B = p$ (top panels), p^2 (middle panels), and p^3 (bottom panels). Blue dashed lines in **(B, D, F)** indicate the power-law decay $|\psi_R(t_0)|^2$ ($|\varphi_R(t_0)|^2$) $\propto p^{-2}$. The parameters are the same as in Figure 2.

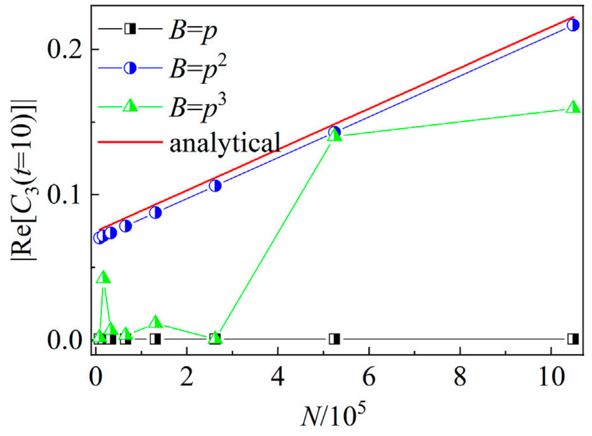

FIGURE 8
$|\mathrm{Re}\,[C_3(t)]|$ at the time $t = t_{10}$ *versus* N with $B = p$ (squares), p^2 (circles), and p^3 (triangles). Red solid line indicates our theoretical prediction in Eq. 15 with $\eta = 6.05 \times 10^{-7}$ for $B = p^2$. The parameters are the same as in Figure 2.

derivations with Eq. 15. This is due to the fact the quantum state $|\psi_R(t_0)|^2$ is not exactly symmetric around p. In order to quantify such asymmetry, we numerically investigate the difference of the sum of the probability between the positive and negative momentums $\Delta_\rho = \sum_{n=0}^{\frac{N}{2}-1} |\psi_R(t_0, p_n)|^2 - \sum_{n=-\frac{N}{2}}^{-1} |\psi_R(t_0, p_n)|^2$ and find that it is non-zero $\Delta_\rho = 0.13$. Interestingly, for $B = p^2$, the value of $|\mathrm{Re}\,[C_3(t)]|$ increases linearly with increasing N, which is clear evidence of the validity of our theoretical prediction.

4 Conclusion and discussion

In the present work, we investigate the dynamics of the $C(t) = -\langle[\theta(t), p^m]\rangle$ in a PTKR model. The spontaneous $\mathcal{PT}$-symmetry breaking is assured by the condition $\lambda > \lambda_c$. In the broken phase of $\mathcal{PT}$-symmetry, we find, both analytically and numerically, the scaling law of $C(t)$ with the dimension of the momentum space, i.e., $C(t) \sim N^{2m-1}\theta_c^2$. This demonstrates that the value of C increases unboundedly with N, which implies that the local perturbation can spread to the entire system very rapidly. In order to reveal the mechanism of the scaling, we make detailed investigations on both the forward and backward evolutions of the quantum state. Our investigations show that the action of θ on a quantum state leads to the formation of the power-law decayed momentum distribution $|\psi(p)|^2 \propto (p - p_c)^{-2}$. Interestingly, such a shape retains during the time reversal, in addition to the decrease of p_c to almost zero. Based on the power-law decayed state, we analytically derive the late-time saturation values of the three parts of the C, which is confirmed by numerical results.

In recent years, fruitful physics of quantum many-body systems, such as dynamical phase transition, many-body localization, and thermalization have received extensive studies. It is found that the energy conservation of chaotic systems leads to the scaling law of OTOCs, for which the late-time saturation of OTOCs scales as the inverse polynomial with the system size [66]. For chaotic systems with long-range interaction, the late-time saturation values of OTOCs obey the dynamical scaling law near the phase transition point [67]. Accordingly, our finding of the power-law scaling of OTOCs with the system size of the PTKR model serves as a new element of the quantum information scrambling in non-Hermitian map systems.

Data availability statement

The original contributions presented in the study are included in the article/Supplementary Material; further inquiries can be directed to the corresponding author.

Author contributions

W-LZ proposed ideas and revised the manuscript. R-RW conducted the numerical simulation and wrote the manuscript.

Funding

This work is supported by the National Natural Science Foundation of China (grant no. 12065009), the Science and Technology Planning Project of Jiangxi province (grant no. 20224ACB201006), and the Science and Technology Planning Project of Ganzhou City (grant no. 202101095077).

Conflict of interest

The authors declare that the research was conducted in the absence of any commercial or financial relationships that could be construed as a potential conflict of interest.

Publisher's note

References

1. Maldacena J, Shenker SH, Stanford D. A bound on chaos. *J High Energ Phys.* (2016) 08:106. doi:10.1007/jhep08(2016)106

2. Rozenbaum EB, Ganeshan S, Galitski V. Lyapunov exponent and out-of-time-ordered correlator's growth rate in a chaotic system. *Phys Rev Lett* (2017) 118:086801. doi:10.1103/physrevlett.118.086801

3. Harris J, Yan B, Sinitsyn NA. Benchmarking information scrambling. *Phys Rev Lett* (2022) 129:050602. doi:10.1103/physrevlett.129.050602

4. Hayden P, Preskill J. Black holes as mirrors: Quantum information in random subsystems. *J High Energ Phys.* (2007) 09:120. doi:10.1088/1126-6708/2007/09/120

5. Zanardi P, Anand N. Information scrambling and chaos in open quantum systems. *Phys Rev A* (2021) 103:062214. doi:10.1103/physreva.103.062214

6. Touil A, Deffner S. Information scrambling versus decoherence—two competing sinks for entropy. *PRX QUANTUM* (2021) 2:010306. doi:10.1103/prxquantum.2.010306

7. Prakash R, Lakshminarayan A. Scrambling in strongly chaotic weakly coupled bipartite systems: Universality beyond the Ehrenfest timescale. *Phys Rev B* (2020) 101: 121108. doi:10.1103/physrevb.101.121108

8. Zhou T, Xu S, Chen X, Guo A, Swingle B. Operator lé vy flight: Light cones in chaotic long-range interacting systems. *Phys Rev Lett* (2020) 124:180601. doi:10.1103/physrevlett.124.180601

9. Zhao SK, Ge ZY, Xiang Z, Xue GM, Zhao SP, Wang Z, et al. Probing operator spreading via Floquet engineering in a superconducting circuit. *Phys Rev Lett* (2022) 129:160602. doi:10.1103/physrevlett.129.160602

10. Yin C, Lucas A. Quantum operator growth bounds for kicked tops and semiclassical spin chains. *Phys Rev A* (2021) 103:042414. doi:10.1103/physreva.103.042414

11. Moudgalya S, Devakul T, Keyserlingk CV, Sondhi SL. Operator spreading in quantum maps. *Phys Rev B* (2019) 99:094312. doi:10.1103/physrevb.99.094312

12. Fan R, Zhang P, Shen H, Zhai H. Out-of-time-order correlation for many-body localization. *Sci Bull* (2017) 62(10):707–11. doi:10.1016/j.scib.2017.04.011

13. Smith A, Knolle J, Moessner R, Kovrizhin DL. Logarithmic spreading of out-of-time-ordered correlators without many-body localization. *Phys Rev Lett* (2019) 123: 086602. doi:10.1103/physrevlett.123.086602

14. Gärttner M, Hauke P, Rey AM. Relating out-of-time-order correlations to entanglement via multiple-quantum coherences. *Phys Rev Lett* (2018) 120:040402. doi:10.1103/physrevlett.120.040402

15. Keyserlingk CV, Rakovszky T, Pollmann F, Sondhi SL. Operator hydrodynamics, OTOCs, and entanglement growth in systems without conservation laws. *Phys Rev X* (2018) 8:021013. doi:10.1103/physrevx.8.021013

16. Lerose A, Pappalardi S. Bridging entanglement dynamics and chaos in semiclassical systems. *Phys Rev A* (2020) 102:032404. doi:10.1103/physreva.102.032404

17. Lewis-Swan RJ, Safavi-Naini A, Bollinger JJ, Rey AM. Unifying scrambling, thermalization and entanglement through measurement of fidelity out-of-time-order correlators in the Dicke model. *Nat Commun* (2019) 10:1581. doi:10.1038/s41467-019-09436-y

18. Zhu Q, Sun ZH, Gong M, Chen F, Zhang YR, Wu Y, et al. Observation of thermalization and information scrambling in a superconducting quantum processor. *Phys Rev Lett* (2022) 128:160502. doi:10.1103/physrevlett.128.160502

19. Balachandran V, Benenti G, Casati G, Poletti D. From the eigenstate thermalization hypothesis to algebraic relaxation of OTOCs in systems with conserved quantities. *Phys Rev B* (2021) 104:104306. doi:10.1103/physrevb.104.104306

20. Kobrin B, Yang Z, Kahanamoku-Meyer GD, Olund CT, Moore JE, Stanford D, et al. Many-body chaos in the sachdev-ye-kitaev model. *Phys Rev Lett* (2021) 126: 030602. doi:10.1103/physrevlett.126.030602

21. Borgonovi F, Izrailev FM, Santos LF. Timescales in the quench dynamics of many-body quantum systems: Participation ratio versus out-of-time ordered correlator. *Phys Rev E* (2019) 99:052143. doi:10.1103/physreve.99.052143

22. Xu S, Swingle B. *Scrambling dynamics and out-of-time ordered correlators in quantum many-body systems: A tutorial.* arXiv:2202.07060 quant-ph. (2022).

23. Heyl M, Pollmann F, Dóra B. Detecting equilibrium and dynamical quantum phase transitions in Ising chains via out-of-time-ordered correlators. *Phys Rev Lett* (2018) 121:016801. doi:10.1103/physrevlett.121.016801

24. Zamani S, Jafari R, Langari A. Out-of-time-order correlations and Floquet dynamical quantum phase transition. *Phys Rev B* (2022) 105:094304. doi:10.1103/physrevb.105.094304

25. Mi X, Roushan P, Quintana C, Mandra S, Marshall J, Neill C, et al. Information scrambling in quantum circuits. *Science* (2021) 374:1479–83. doi:10.1126/science.abg5029

26. Weinstein Z, Kelly SP, Marino J, Altman E. *Scrambling transition in a radiative random unitary circuit.* arXiv:2210.14242 quant-ph. (2022)

27. Nie X, Wei BB, Chen X, Zhang Z, Zhao X, Qiu C, et al. Experimental observation of equilibrium and dynamical quantum phase transitions via out-of-time-ordered correlators. *Phys Rev Lett* (2020) 124:250601. doi:10.1103/physrevlett.124.250601

28. Zhai LJ, Yin S. Out-of-time-ordered correlator in non-Hermitian quantum systems. *Phys Rev B* (2020) 102:054303. doi:10.1103/physrevb.102.054303

29. Zhao WL. Quantization of out-of-time-ordered correlators in non-Hermitian chaotic systems. *Phys Rev Res* (2022) 4:023004. doi:10.1103/physrevresearch.4.023004

30. Berry M. Physics of nonhermitian degeneracies. *Czech J Phys* (2004) 54:1039–47. doi:10.1023/b:cjop.0000044002.05657.04

31. Ashida Y, Gong Z, Ueda M. Non-Hermitian physics. *Adv Phys* (2020) 69:249–435. doi:10.1080/00018732.2021.1876991

32. Bender CM, Boettcher S. Real spectra in non-hermitian Hamiltonians HavingPTSymmetry. *Phys Rev Lett* (1998) 80:5243–6. doi:10.1103/physrevlett.80.5243

33. Bender CM, Brody DC, Jones HF. Complex extension of quantum mechanics. *Phys Rev Lett* (2002) 89:270401. doi:10.1103/physrevlett.89.270401

34. Zhao XM, Guo CX, Yang ML, Wang H, Liu WM, Kou SP. Anomalous non-Abelian statistics for non-Hermitian generalization of Majorana zero modes. *Phys Rev B* (2021) 104:214502. doi:10.1103/physrevb.104.214502

35. Yu ZF, Xue JK, Zhuang L, Zhao J, Liu WM. Non-Hermitian spectrum and multistability in exciton-polariton condensates. *Phys Rev B* (2021) 104:235408. doi:10.1103/physrevb.104.235408

36. Zhao XM, Guo CX, Kou SP, Zhuang L, Liu WM. Defective Majorana zero modes in a non-Hermitian Kitaev chain. *Phys Rev B* (2021) 104:205131. doi:10.1103/physrevb.104.205131

37. Pino JD, Slim JJ, Verhagen E. Non-Hermitian chiral phononics through optomechanically induced squeezing. *Nature (London)* (2022) 606:82–7. doi:10.1038/s41586-022-04609-0

38. El-Ganainy R, Makris KG, Khajavikhan M, Musslimani ZH, Rotter S, Christodoulides DN. Non-Hermitian physics and PT symmetry. *Nat Phys* (2018) 14:11–9. doi:10.1038/nphys4323

39. Xia S, Danieli C, Zhang Y, Zhao X, Lu H, Tang L, et al. Higher-order exceptional point and Landau–Zener Bloch oscillations in driven non-Hermitian photonic Lieb lattices. *APL Photon* (2021) 6:126106. doi:10.1063/5.0069633

40. Zhang Y, Xia S, Zhao X, Qin L, Feng X, Qi W, et al. Symmetry-protected third-order exceptional points in staggered flatband rhombic lattices. *Photon Res* (2023) 11(3): 225. doi:10.1364/PRJ.478167

41. Xiao Z, Li H, Kottos T, Al u A. Enhanced sensing and nondegraded thermal noise performance based on PT-symmetric electronic circuits with a sixth-order exceptional point. *Phys Rev Lett* (2019) 123:213901. doi:10.1103/physrevlett.123.213901

42. Chitsazi M, Li H, Ellis FM, Kottos T. Experimental realization of Floquet PT-symmetric systems {PT}}-Symmetric systems. *Phys Rev Lett* (2017) 119:093901. doi:10.1103/physrevlett.119.093901

43. Zou D, Chen T, He W, Bao J, Lee CH, Sun H, et al. Observation of hybrid higher-order skin-topological effect in non-Hermitian topolectrical circuits. *Nat Commun* (2021) 12:7201. doi:10.1038/s41467-021-26414-5

44. Kreibich M, Main J, Cartarius H, Wunner G. Tilted optical lattices with defects as realizations ofPTsymmetry in Bose-Einstein condensates. *Phys Rev A* (2016) 93:023624. doi:10.1103/physreva.93.023624

45. Keller C, Oberthaler MK, Abfalterer R, Bernet S, Schmiedmayer J, Zeilinger A. Tailored complex potentials and friedel's law in atom optics. *Phys Rev Lett* (1997) 79: 3327–30. doi:10.1103/physrevlett.79.3327

46. Li J, Harter AK, Liu J, Melo LD, Joglekar YN, Luo L. Observation of parity-time symmetry breaking transitions in a dissipative Floquet system of ultracold atoms. *Nat Commun* (2019) 10:855. doi:10.1038/s41467-019-08596-1

47. Xue Y, Hang C, He Y, Bai Z, Jiao Y, Huang G, et al. Experimental observation of partial parity-time symmetry and its phase transition with a laser-driven cesium atomic gas. *Phys Rev A* (2022) 105:053516. doi:10.1103/physreva.105.053516

48. Ren Z, Liu D, Zhao E, He C, Pak KK, Li J, et al. Chiral control of quantum states in non-Hermitian spin–orbit-coupled fermions. *Nat Phys* (2022) 18:385–9. doi:10.1038/s41567-021-01491-x

49. Zhou L, Han W. Driving-induced multiple PT-symmetry breaking transitions and reentrant localization transitions in non-Hermitian Floquet quasicrystals PT-symmetry breaking transitions and reentrant localization transitions in non-Hermitian Floquet quasicrystals. *Phys Rev B* (2022) 106:054307. doi:10.1103/physrevb.106.054307

50. Zhou L. Floquet engineering of topological localization transitions and mobility edges in one-dimensional non-Hermitian quasicrystals. *Phys Rev Res* (2021) 3:033184. doi:10.1103/physrevresearch.3.033184

51. Zhou L, Gu Y, Gong J. Dual topological characterization of non-Hermitian Floquet phases. *Phys Rev B* (2021) 103:L041404. doi:10.1103/physrevb.103.l041404

52. Zhang DJ, Wang Q, Gong J. Time-dependent PT-symmetric quantum mechanics in generic non-Hermitian systems-symmetric quantum mechanics in generic non-Hermitian systems. *Phys Rev A* (2019) 100:062121. doi:10.1103/physreva.100.062121

53. Longhi S. Oscillating potential well in the complex plane and the adiabatic theorem. *Phys Rev A* (2017) 96:042101. doi:10.1103/physreva.96.042101

54. West CT, Kottos T, Prosen T. PT-symmetric wave chaos. *Phys Rev Lett* (2010) 104: 054102. doi:10.1103/physrevlett.104.054102

55. Longhi S. Localization, quantum resonances, and ratchet acceleration in a periodically kickedPT-symmetric quantum rotator. *Phys Rev A* (2017) 95:012125. doi:10.1103/physreva.95.012125

56. Zhao WL, Wang J, Wang X, Tong P. Directed momentum current induced by the PT-symmetric driving. *Phys Rev E* (2019) 99:042201. doi:10.1103/physreve.99.042201

57. Santhanam MS, Paul S, Kannan JB. Quantum kicked rotor and its variants: Chaos, localization and beyond. *Phys Rep* (2022) 956:1–87. doi:10.1016/j.physrep.2022.01.002

58. Ho DYH, Gong J. Quantized adiabatic transport in momentum space. *Phys Rev Lett* (2012) 109:010601. doi:10.1103/physrevlett.109.010601

59. Gadway B, Reeves J, Krinner L, Schneble D. Evidence for a quantum-to-classical transition in a pair of coupled quantum rotors. *Phys Rev Lett* (2013) 110:190401. doi:10.1103/physrevlett.110.190401

60. Huang KQ, Zhao WL, Li Z. Effective protection of quantum coherence by a non-Hermitian driving potential. *Phys Rev A* (2021) 104:052405. doi:10.1103/physreva.104.052405

61. Vuatelet V, Rançon A. Effective thermalization of a many-body dynamically localized Bose gas. *Phys Rev A* (2021) 104:043302. doi:10.1103/physreva.104.043302

62. Belyansky R, Bienias P, Kharkov YA, Gorshkov AV, Swingle B. Minimal model for fast scrambling. *Phys Rev Lett* (2020) 125:130601. doi:10.1103/physrevlett.125.130601

63. Kuwahara T, Saito K. Absence of fast scrambling in thermodynamically stable long-range interacting systems. *Phys Rev Lett* (2021) 126:030604. doi:10.1103/physrevlett.126.030604

64. D'Alessio L, Rigol M. Long-time behavior of isolated periodically driven interacting lattice systems. *Phys Rev X* (2014) 4:041048. doi:10.1103/physrevx.4.041048

65. Zhao WL, Hu Y, Li Z, Wang Q. Super-exponential growth of out-of-time-ordered correlators. *Phys Rev B* (2021) 103:184311. doi:10.1103/physrevb.103.184311

66. Huang Y, Brandão FGSL, Zhang YL. Finite-size scaling of out-of-time-ordered correlators at late times. *Phys Rev Lett* (2019) 123:010601. doi:10.1103/physrevlett.123.010601

67. Wei BB, Sun G, Hwang MJ. Dynamical scaling laws of out-of-time-ordered correlators. *Phys Rev B* (2019) 100:195107. doi:10.1103/physrevb.100.195107

Frontiers in Physics

TYPE Original Research
PUBLISHED 10 March 2023
DOI 10.3389/fphy.2023.1098119

OPEN ACCESS

EDITED BY
Libin Fu,
Graduate School of China Academy of Engineering Physics, China

REVIEWED BY
Vinodkumar P. C.,
Sardar Patel University, India
Vaibhav Prabhudesai,
Tata Institute of Fundamental Research, India
Meishan Wang,
Ludong University, China

*CORRESPONDENCE
Yong Wu,
✉ wu_yong@iapcm.ac.cn
Ruifeng Lu,
✉ rflu@njust.edu.cn

SPECIALTY SECTION
This article was submitted to Atomic and Molecular Physics, a section of the journal Frontiers in Physics

RECEIVED 14 November 2022
ACCEPTED 21 February 2023
PUBLISHED 10 March 2023

CITATION
Peng Y, Hu X, Wu Y, Wang J, Lu R and Sisourat N (2023), Photodissociation of water molecule at short photon wavelengths: Dynamical studies.
Front. Phys. 11:1098119.
doi: 10.3389/fphy.2023.1098119

Photodissociation of water molecule at short photon wavelengths: Dynamical studies

Yigeng Peng[1,2,3], Xiaoqing Hu[2,3], Yong Wu[2,3]*, Jianguo Wang[2,3], Ruifeng Lu[1]* and Nicolas Sisourat[4]

[1]Department of Applied Physics, Nanjing University of Science and Technology, Nanjing, China, [2]Key Laboratory of Computational Physics, Institute of Applied Physics and Computational Mathematics, Beijing, China, [3]HEDPS, Center for Applied Physics and Technology, Peking University, Beijing, China, [4]Laboratoire de Chimie Physique–Mati`ere et Rayonnement, CNRS, Sorbonne Universités, Paris, France

In our last study [J. Phys. B At. Mol. Opt. Phys. 54, 125,102 (2021).], we reported the *ab initio* calculation of the full-dimensional potential energy surfaces of water molecule including 9 A′ and 9 A″ states in Cs symmetry. In this study, we performed additional non-adiabatic semi-classical studies based on the potential energy surfaces. Our simulation successfully repeated the near picosecond lifetime of the $\tilde{F}^1A'$ state measured by time resolved photo-electron spectra experiment [Chinese J. Chem. Phys. **32**, 53 (2019)]. We also determined the dissociation branching ratio including H + OH(X, A), H + H + O and H_2+O channels. In addition, the reaction path corresponding to H_2+O (^{1}S) channel is clearly marked out, which is found in recent free-electron laser experiment [Nat. Commun. **12**, 6,303 (2021)].

KEYWORDS

photodissociation, semi-classical, surface-hopping, potential energy surface, non-adiabatic dynamics

1 Introduction

With the development of vacuum ultra-violet free electron laser (VUV-FEL) light sources combined with time-sliced velocity-map imaging (TSVMI) [1] and time-resolved photo-electron spectroscopy (TRPES) technique [2], dynamical studies for the photochemistry process in molecules from highly excited electronic states have been performing for several years before [1, 3, 4]. Among small molecules, water had been extensively studied as an ideal polyatomic system. Interesting phenomena have been found for the photodissociation dynamics of highly-excited states of water, including the hot rotation of OH fragments in ground and excited states at special incident photon wavelengths [4, 5] the long-lived lifetime of $\tilde{F}$ and $\tilde{F}'$ states [6] and the high yield of the three-body H + H + O channel [7] at short wavelengths.

Despite the extensive experimental studies of the photodissociation of water molecule in highly-excited states, corresponding theoretical studies are relatively scarce due to the lack of the corresponding potential energy surfaces (PES). On the other hand, most theoretical studies focus on specific fragment quantum distributions such as the rovibronic [8] or the fine structures of OH radical [9], and few studies consist of all three channels of H + OH, H_2+O and H + H + O. In our latest work [10], we obtained the full dimensional potential energy surfaces with the combined multi configurational self-consistent field and multi reference single and double excitation configuration interaction method (MCSCF + MRDCI), nearly 99,000 geometries are considered which include all the three mentioned channels.

If we do not aim at studying quantum effects such as interference, energy resonant, or geometric phase, a semi-classical simulation of the nuclear motions is good enough to describe the reaction behavior with a lower computational cost. In this paper, based on our full-dimensional PESs, the photodissociation of water molecule with respect to the photon energy of 9–12 eV are studied with a semi-classical method, and the non-adiabatic transition is included using a Landau-Zener type approach near conical-intersections or avoid-crossings. It should be noted that, in the present study, only the states of $^1A'$ symmetry are taken into consideration because the ones with $^1A''$ symmetry are either long-lived [2, 6](second or higher $^1A''$) or lower than the energy range of interest ($\tilde{A}^1A'$, less than 8eV).

2 Theoretical method

The semi-classical simulation is performed by solving the Newton equations with the Verlet algorithm:

$$q(t+\Delta t) = 2q(t) - q(t-\Delta t) + \ddot{q}(t)\Delta t^2 \tag{1}$$

Here, q is the coordinate of an atom. The acceleration $\ddot{q}$ is determined from a finite difference on the PES with a multi-dimensional B-spline interpolation. Non-adiabatic process is considered using two main approximations—surface hopping and the Landau–Zener model [11, 12], which has been analyzed and tested in several conical intersection problems [13–15]. When the potential energy gap comes minimal along the classical trajectory, a non-adiabatic transition may occur. Considering a classical trajectory associated with the ith adiabatic surface, if at a critical time t_c, the energy gap function $Z_{ij}(q_c)$ between the ith and jth surfaces at the coordinate $\{q_c\}$ reaches a minimum, a transition from surface i to j can take place. The transition probability can be described by a Landau-Zener formula [11]:

$$P_{LZ} = exp\left(\frac{-\pi}{2\hbar}\sqrt{\frac{Z_{ij}(q_c)^3}{\frac{d^2}{dt^2}Z_{ij}(q(t))\,|_{t=t_c}}}\right) \tag{2}$$

During the simulation, such probability is compared with a pseudorandom number ξ within a uniform interval of [0,1]. If $\xi > P_{LZ}$ the trajectory stays on the current surface i. If $\xi < P_{LZ}$, the trajectory hops from the current surface i to the surface j, and the velocities are rescaled as:

$$\sum_\alpha \frac{1}{2}m_\alpha|\dot{q}_\alpha(t)|^2 + U_i(q_c) = \sum_\alpha \frac{1}{2}m_\alpha|\dot{q}_\alpha^{rs}(t)|^2 + U_j(q_c) \tag{3}$$

to ensure the energy conservation. The summation is over all nuclear with mass m_α. In our approach, only $j = i \pm 1$ are taken into consideration i.e. only the hopping between the adjacent surfaces are considered.

The initial geometry samplings are based on a Wigner distribution [16, 17] near the equilibrium geometry of the ground state $\tilde{X}^1A'$ at the ground vibrational state.

3 Results and discussion

3.1 The lifetime of state $\tilde{D}^1A'$ and $\tilde{F}^1A'$

We obtain the lifetime of state $\tilde{D}^1A'$ and $\tilde{F}^1A'$ by applying the simulation from each specific adiabatic surface. Thousands of trajectories are performed with different initial condition and then we can collect the numbers of undissociated trajectories at each time t as $N(t)$. Finally, the lifetime τ is obtained through an exponential fitting on $N(t)$ *versus* t as: $N(t) = N_0\,exp\,(-t/\tau)$.

The state $\tilde{D}^1A'$ is believed to be unstable due to the strong non-adiabatic coupling with the lower state of $\tilde{B}^1A'$ at the bending geometry. Several experimental studies have reported slightly diverging results. Steinkellner etal [18] obtained a value of 60 ± 50 fs with a large uncertainty using an ultrafast two-photon experiment in 2004. Then Yuan etal [19] estimated the lifetime of $\tilde{D}^1A'$ to be 13.5 fs from the bandwidth value of a two-photon spectrum. In the present study, as shown by Figure 1A, the dissociation lifetime for $\tilde{D}^1A'$ state is determined to be near 124 fs. The relatively short lifetime of 13.5 fs by Yuan etal [19] is within the lower limit of 60 ± 50 fs by Steinkellner etal [18] while the present value of 124 fs is near the upper limit of that. Present study may slightly overestimate the lifetime of $\tilde{D}^1A'$ state because other non-adiabatic processes (e.g. Coriolis couplings) may also lead to the dissociation thus reduce the dissociation lifetime. More theoretical and experimental works are required to accurately determine the lifetime of $\tilde{D}^1A'$ state. It should be noticed that, at the first 50 femtoseconds, the counts in Figure 1A is flat. This is caused by our simulation algorism: in first tens of femto-seconds, most trajectories cannot reach the defined dissociation conditions (e.g. OH bond length larger than a threshold value), so they are not regarded as ‘dissociated’.

The lifetime of $\tilde{F}^1A'$ state had been determined by Yang etal [6] to be as long as 1000 ± 300 fs using the time-resolved photo-electron spectroscopy (TRPES). They suggested a weak non-adiabatic traisition from $\tilde{F}^1A'$ to $\tilde{D}^1A'$, followed by dissociation from the $\tilde{D}^1A'$ surface as discussed above. However, in our last study [10], we suggested that the long lifetime should come from the long-time for symmetry-breaking process by analysing the PESs corresponding to such process. As shown in Figure 1B, the lifetime of $\tilde{F}^1A'$ is determined to be about 770 fs with our semi-classical simulation which is in good agreement with the TRPES results of Yang etal [6]. So our initial suggestions are well supported by the present simulation.

3.2 The channel ratio with respect to the incident photon energy

In previous theoretical studies, researchers mainly focus on part of the dissociation channels. e.g., for H + OH dissociation channel, Jiang etal [20] studied the rotational and vibrational distributions of the OH fragment, Zhou etal [8] studied the effect of spin-orbit couplings on the rotational distributions of OH fragment. For H_2+O channel, the only theoretical study was performed by van Harrevelt etal [21], in which the rotational and vibrational distributions of H_2 were obtained, a 10% ratio for the H_2+O channel was found which

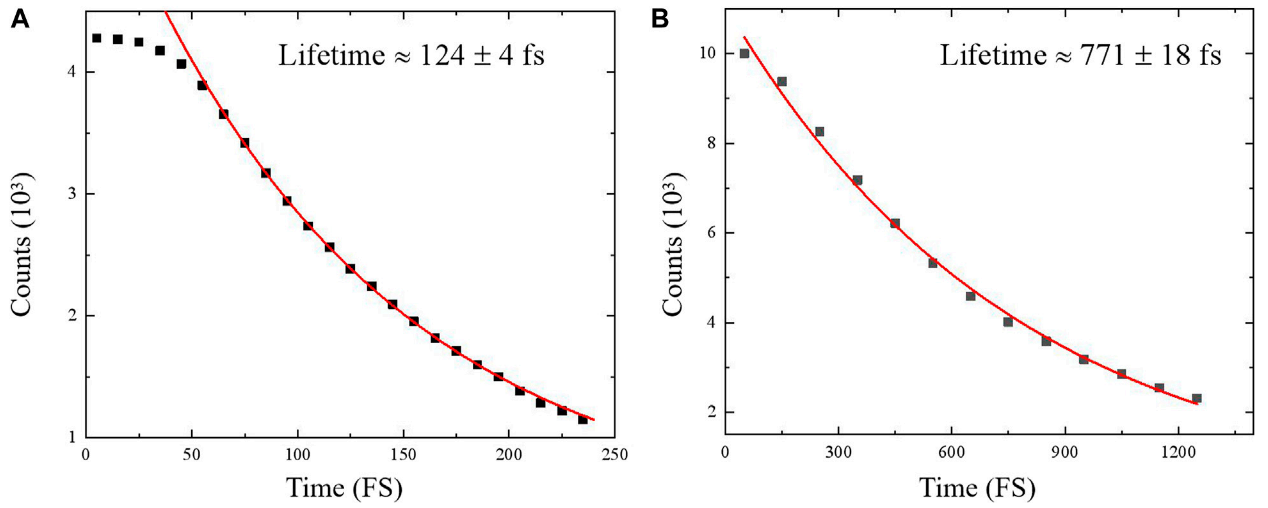

FIGURE 1
Number of undissociated trajectories *versus* simulation time of state $\tilde{D}^1A'$ (panel **(A)**) and $\tilde{F}^1A'$ (panel **(B)**). The lifetimes are obtained through a fitting procedure with an exponential function. Points are the simulated values and lines are the fitted curves. The uncertainties are due to the fitting procedure.

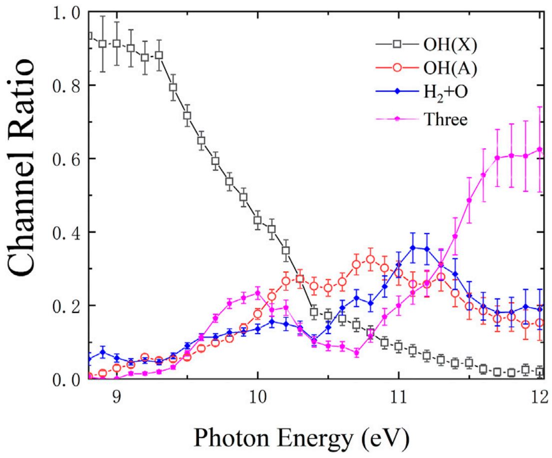

FIGURE 2
Branching ratio *versus* photon energy. OH(X) and OH(A) correspond to the H + OH channel with the OH fragment on ground and first excited states, respectively. "Three" correspond to the H + H + O channel. The error bars are determined from the statistical error of the number of the trajectories of each channel.

was in good accordance with earlier experimental results t [22]. For the three body channels, no specific theoretical studies are published. In a recent study, Chang etal [7] found a quite large ratio of the three-body channel at short wavelengths (near 100 nm, 12.34 eV).

Here we perform a simulation containing all three channels with the full-dimensional PESs obtained in our last work [10]. A key point is the determination of the initial surface. In the present study, we perform the simulation from all the excited $^1A'$ states and the numbers of the trajectories from each surface are determined as:

$$N_i \propto |D_{1i}(R_e)|^2 \big/ \omega_{1i}^2. \tag{4}$$

Here N_i is the number of the trajectories from the ith ($i > 1$) $^1A'$ surface, and $D_{1i}(R_e)$ and ω_{1i} are the transition dipole moments and vertical excitation energy at the equilibrium geometry from $^1A'$ to i^1A'. Such approximation is based on a vertical excitation from the ground state to the ith excitation state. Then the photon energy of each trajectory is determined as:

$$E_p = U_i(q(t=0)) + \sum\nolimits_\alpha \frac{1}{2} m_\alpha \left|\dot{q}_\alpha(t=0)\right|^2 - E_0 \tag{5}$$

E_p and E_0 are the photon energy and the zero-point energy of ground state, respectively. U_i is the PES of the ith surface. $q(t=0)$ and $\dot{q}_\alpha(t=0)$ correspond to the initial coordinates and velocities of each atom. Totally, hundreds of thousands of trajectories are performed, and the channel ratios are obtained and shown in Figure 2.

As shown in Figure 2, at low photon energy (near 9 eV), most trajectories lead to the H + OH(X) channel. As the photon energy increases the ratio of H + OH(X) channel reduces rapidly and the ratios of other channels rise. H + OH(A) channel corresponds to the dissociation on B^1A' surface: as the photon energy increases, the ratio of H + OH(A) channel rises to the maximum at near 10.7 eV. This may due to the fact that at higher photon energy, competition between three-body and H_2+O channel can take place. The H_2+O channel also rises with the photon energy increases from 9 eV and reaches the maximum at about 11.2 eV. It should be noted that, at about 10.2 eV, the H_2+O channel ratio is close to 10%, this is in good agreement with the ones presented by the theoretical results of van Harrevelt etal [21] and the experimental ones of Slanger etal [22]. The three-body dissociation of water molecule is an important way to generate the oxygen atom, and was discovered by both dissociative electron attachment [23] and photodissociation [7] experiments, but the mechanisms are different because the PESs of H_2O molecule and its anion are quite different. In present result, the ratio of three-body channel reaches the first maximum of about

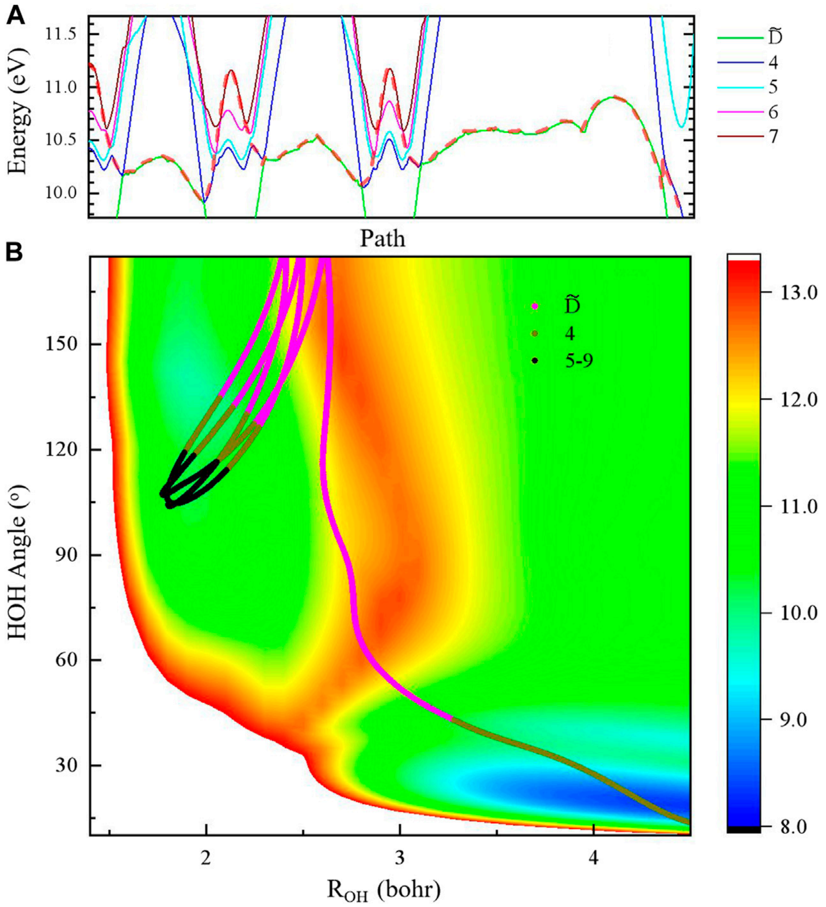

FIGURE 3
Reaction path corresponding to H_2+O (^{1}S) channel. In panel **(A)**, the adiabatic potential energies within the $^1A'$ symmetry along the reaction path is shown, the values corresponding to the trajectory is shown as a dashed line. In panel **(B)**, the symmetric ($R_{OH1} = R_{OH2}$) PES of $4^1A'$ in electron volts is shown, and the trajectory for the H_2+O (^{1}S) channel is shown in a multi-colored line, and each color correspond to an adiabatic surface shown by the legend. The color of the trajectory line depends on which adiabatic state the system is on during the reaction process. It should be noted that the horizonal axis correspond to the average length of the two OH bonds within this trajectory.

22% at near 10 eV, and reduces to below 10% at 10.6eV. Such reduction may come from the competition of the H + OH(A) and H_2+O channel. After that, the ratio of the three-body channel increases rapidly. A quite large value of 62% ± 12% of such channel is determined near 12 eV. In the recent experimental study by Chang etal [7], the ratios considering only H + OH and three-body channels are obtained, and a value of near 85% at 102 nm photon wavelength (12.15 eV) was presented. In present study, if we also exclude the H_2+O channel, the ratio of three-body channel can be determined as near 78% ± 15% at 12 eV. Such value is within the range of the experimental ones by Chang etal [7].

3.3 The H_2+O channel

In recent experimental work of Chang etal [3], the photo dissociation of water at wavelength ranging from 102.67 to 112.81 nm (10.99—12.08 eV), corresponding to the H_2+O channel, was studied. The H_2+O (^{1}S) channel was observed and the vibrationally excited H_2 molecule was mostly populated. This is surprising because the H_2+O (^{1}S) channels correspond to the fourth $1_{A'}$ surface at the asymptotic region and there exist a rather high energy barrier to overcome on this surface as shown in Figure 3B. In our last work [10] and the theoretical study in Chang etal [3], it was pointed out that the system can follow a non-adiabatic reaction path which corresponds to an avoid crossing zone between $\tilde{D}^1A'$ and 4th$^1A'$ (two OH bonds near 3.4 bohr and HOH angle near 45°), after such non-adiabatic transition, the system falls into a well which leads to the hot vibration of H_2 fragment. In present study, we also found few numbers of trajectories leading to the H_2+O (^{1}S) channel. A typical trajectory for the H_2+O (^{1}S) channel is shown in Figures 3A,B not only with the geometry movement but also the adiabatic state transition processes. Just as illustrated in our last study [10], the system oscillates for several cycles on the bending and symmetric stretching coordinates, but when the system transit to $\tilde{D}^1A'$ surface and the two OH bonds enlarge to near 2.6 bohr, at the HOH angle of 180°, the length of the two OH bonds will not shorten or elongate for a while and the system will keep staying at the $\tilde{D}^1A'$ surface. The main movement then is the contraction of HOH angle from 180 ° to near 60 °. Then the system moves to the avoid crossing between

$\tilde{D}^1A'$ and fourth $^1A'$ and transit to fourth $^1A'$ which leads to the H_2+O (^{1}S) channel.

4 Conclusion

By performing semi-classical simulation with Landau-Zener surface hopping approximation, the photo-dissociation dynamics of water molecule in high-lying states are studied. The lifetimes of $\tilde{D}^1A'$ and $\tilde{F}^1A'$ states are determined and found in good agreement with previous experiments. The dissociation channel ratio considering all three channels of H + OH, H_2+O and H + H + O within the photon energy from 9 to 12 eV are obtained. Good agreement is found between present ratio values and available experimental and theoretical ones. The H_2+O (^{1}S) channel is also found in the simulation and the corresponding reaction path is shown, which may help understanding such interesting reaction channel better. In future works, for deeper understanding of the dissociation mechanisms, more analysis of the reaction channels, and full-quantum mechanically studies including non-adiabatic coupling matrix elements and the wave-package propagation simulation should be performed.

Data availability statement

The original contributions presented in the study are included in the article/Supplementary Material, further inquiries can be directed to the corresponding author.

Author contributions

Conceptualization: YW, RL methodology: YP, NS investigation: YP, XH, visualization: YP, NS, XH supervision: YW, JW, RL writing—original draft: YP, NS writing—review and editing: YW, JW, RL.

Acknowledgments

Grants from the NSFC(Nos. 11934004,11904028) are acknowledged. We thank Dr K. Luo, Dr C. Yu., Dr J. W. Gao and Dr C. Z. Gao for helpful discussions. NS thanks the Institut de Chimie du CNRS for financial support.

Conflict of interest

The authors declare that the research was conducted in the absence of any commercial or financial relationships that could be construed as a potential conflict of interest.

Publisher's note

References

1. Chang Y, Yu S, Li Q, Yu Y, Wang H, Su S, et al. Tunable VUV photochemistry using vacuum ultraviolet free electron laser combined with H-atom Rydberg tagging time-of-flight spectroscopy. *Rev Sci Instrum* (2018) 89, 063113. doi:10.1063/1.5017757

2. He Z, Yang D, Chen Z, Yuan K, Dai D, Wu G, et al. An accidental resonance mediated predissociation pathway of water molecules excited to the electronic $\tilde{C}$ state. *Phys Chem Chem Phys* (2017) 19:29795–800. doi:10.1039/c7cp06286a

3. Chang Y, An F, Chen Z, Luo Z, Zhao Y, Hu X, et al. Vibrationally excited molecular hydrogen production from the water photochemistry. *Nat Commun* (2021) 12:6303. doi:10.1038/s41467-021-26599-9

4. Chang Y, Yu Y, Wang H, Hu X, Li Q, Yang J, et al. Hydroxyl super rotors from vacuum ultraviolet photodissociation of water. *Nat Commun* (2019) 10:1250. doi:10.1038/s41467-019-09176-z

5. Chang Y, An F, Li Q, Luo Z, Che L, Yang J, et al. Electronically excited OH super-rotors from water photodissociation by using vacuum ultraviolet free-electron laser pulses. *J Phys Chem Lett* (2020) 11:7617–23. doi:10.1021/acs.jpclett.0c02320

6. Yang D, Min Y, Chen Z, He Z, Chen Z, Yuan K, et al. Ultrafast dynamics of water molecules excited to electronic $\tilde{F}$ states: A time-resolved photoelectron spectroscopy study. *Chin J. Chem. Phys.* (2019) 32:53–8. doi:10.1063/1674-0068/cjcp1811243

7. Chang Y, Yu Y, An F, Luo Z, Quan D, Zhang X, et al. Three body photodissociation of the water molecule and its implications for prebiotic oxygen production. *Nat Commun* (2021) 12:2476. doi:10.1038/s41467-021-22824-7

8. Jiang B, Xie D, Guo H. State-to-state photodissociation dynamics of triatomic molecules: H_2O in the *B* band. *J Chem Phys* (2012) 136:034302. doi:10.1063/1.3676725

9. Zhou L, Xie D, Sun Z, Guo H. Product fine-structure resolved photodissociation dynamics: The A band of H_2O. *J Chem Phys* (2014) 140, 024310. doi:10.1063/1.4861230

10. Peng Y, Hu X, Wu Y, Wang J, Lu R, Sisourat N. Photodissociation dynamics of water molecule at short photon wavelengths: Full dimensional potential energy surface of rydberg states. *J Phys B: Mol Opt Phys* (2021) 54:125102. doi:10.1088/1361-6455/ac01ab

11. Belyaev AK, Lebedev OV. Nonadiabatic nuclear dynamics of atomic collisions based on branching classical trajectories. *Phys Rev A* (2011) 84, 014701. doi:10.1103/physreva.84.014701

12. Belyaev AK, Lasser C, Trigila G. Landau–Zener type surface hopping algorithms. *J Chem Phys* (2014) 140:224108. doi:10.1063/1.4882073

13. Kube S, Lasser C, Weber M. Monte Carlo sampling of Wigner functions and surface hopping quantum dynamics. *J Comput Phys* (2009) 228:1947–62. doi:10.1016/j.jcp.2008.11.016

14. Lasser C, Swart T. Single switch surface hopping for a model of pyrazine. *J Chem Phys* (2008) 129, 034302. doi:10.1063/1.2954019

15. Fermanian Kammerer C, Lasser C. Single switch surface hopping for molecular dynamics with transitions. *J Chem Phys* (2008) 128:144102. doi:10.1063/1.2888549

16. Schinke R. *Photodissociation dynamics*. Cambridge University Press (1993).

17. Dahl JP, Springborg M. The Morse oscillator in position space, momentum space, and phase space. *J Chem Phys* (1988) 88:4535–47. doi:10.1063/1.453761

18. Steinkellner O, Noack F, Ritze H-H, Radloff W, Hertel IV. Ultrafast predissociation dynamics of water molecules excited to the electronic $\tilde{C}$ and $\tilde{D}$ states. *J Chem Phys* (2004) 121:1765–70. doi:10.1063/1.1760732

19. Yuan K, Cheng L, Cheng Y, Guo Q, Dai D, Yang X. Two-photon photodissociation dynamics of H2O via the $\tilde{D}$ electronic state. *J Chem Phys* (2009) 131, 074301. doi:10.1063/1.3168398

20. Lin G-S-M, Zhou L, Xie D. Theoretical study of the state-to-state photodissociation dynamics of the vibrationally excited water molecule in the *B* band. *J Phys Chem A* (2014) 118:9220–7. doi:10.1021/jp503062s

21. van Harrevelt R, van Hemert MC. Quantum mechanical calculations for the $H_2O + h\nu \rightarrow O(^1D) + H_2$ photodissociation process. *J Phys Chem A* (2008) 112:3002–9. doi:10.1021/jp711857w

22. Slanger TG, Black G. Photodissociative channels at 1216 Å for H_2O, NH_3, and CH_4. *J Chem Phys* (1982) 77:2432–7. doi:10.1063/1.444111

23. Ram NB, Prabhudesai VS, Krishnakumar E. Resonances in dissociative electron attachment to water. *J Phys B: Mol Opt Phys* (2009) 42:225203. doi:10.1088/0953-4075/42/22/225203

frontiers | Frontiers in Physics

TYPE Original Research
PUBLISHED 23 March 2023
DOI 10.3389/fphy.2023.1106324

Sampling strategies for the Herman–Kluk propagator of the wavefunction

Fabian Kröninger[1]*, Caroline Lasser[2]* and Jiří J. L. Vaníček[1]*

[1]Laboratory of Theoretical Physical Chemistry, Institut des Sciences et Ingénierie Chimiques, Ecole Polytechnique Fédérale de Lausanne (EPFL), Lausanne, Switzerland, [2]Zentrum Mathematik, Technische Universität München, Munich, Germany

Check for updates

OPEN ACCESS

EDITED BY
Craig Martens,
University of California, Irvine,
United States

REVIEWED BY
Arkajit Mandal,
Columbia University, United States
Irene Burghardt,
Goethe University Frankfurt, Germany

*CORRESPONDENCE
Fabian Kröninger,
fabian.kroninger@epfl.ch
Caroline Lasser,
classer@ma.tum.de
Jiří J. L. Vaníček,
jiri.vanicek@epfl.ch

SPECIALTY SECTION
This article was submitted to Physical Chemistry and Chemical Physics, a section of the journal Frontiers in Physics

RECEIVED 23 November 2022
ACCEPTED 17 January 2023
PUBLISHED 23 March 2023

CITATION
Kröninger F, Lasser C and Vaníček JJL (2023), Sampling strategies for the Herman–Kluk propagator of the wavefunction.
Front. Phys. 11:1106324.
doi: 10.3389/fphy.2023.1106324

When the semiclassical Herman–Kluk propagator is used for evaluating quantum-mechanical observables or time-correlation functions, the initial conditions for the guiding trajectories are typically sampled from the Husimi density. Here, we employ this propagator to evolve the wavefunction itself. We investigate two grid-free strategies for the initial sampling of the Herman–Kluk propagator applied to the wavefunction and validate the resulting time-dependent wavefunctions evolved in harmonic and anharmonic potentials. In particular, we consider Monte Carlo quadratures based either on the initial Husimi density or on its square root as possible and most natural sampling densities. We prove analytical convergence error estimates and validate them with numerical experiments on the harmonic oscillator and on a series of Morse potentials with increasing anharmonicity. In all cases, sampling from the square root of Husimi density leads to faster convergence of the wavefunction.

KEYWORDS

quantum propagator, time-dependent semiclassical approximation, highly oscillatory integral, statistical convergence of Monte Carlo methods, mesh-free discretization

1 Introduction

Semiclassical initial value representation techniques [1, 2] have evolved into useful tools for calculations of the dynamics of atoms and molecules [3]. Frozen Gaussians and their superposition were introduced by Heller in 1981 [4] as an extension to the thawed Gaussian approximation [5] in order to capture non-linear spreading of the wavepackets. Herman and Kluk justified the frozen-Gaussian ansatz and introduced an improved approximation [6–8], now known as the Herman–Kluk propagator, which contains an additional prefactor that rigorously compensates for the fixed width of these frozen Gaussians and ensures unitarity of the time evolution in the stationary-phase limit [7]. The Herman–Kluk approximation keeps the trajectories of the individual Gaussians uncoupled, which sets it apart from the more accurate, but computationally more demanding approaches like the coupled coherent states [9] or the variational multi-configurational Gaussian method [10].

In the spirit of the semiclassical initial value representation, the Herman–Kluk propagator avoids the root search problem [2, 11]. Because of its high accuracy, this propagator belongs among the most successful semiclassical approximations [12–18] and has been derived in many different ways [9, 19–22]. There are observables, such as low-resolution vibronic spectra in mildly anharmonic systems, which can be well described by the more efficient thawed Gaussian approximation [23, 24] and other single-trajectory methods [25–30]. In chaotic and other systems, however, increased anharmonicity leads to wavepacket splitting and non-trivial interference effects. In such

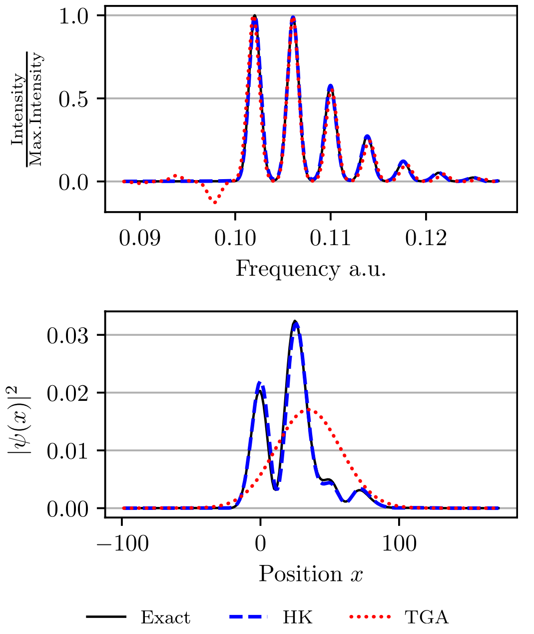

FIGURE 1
Upper panel: Spectra of a Morse potential evaluated using the exact quantum dynamics, Herman–Kluk (HK) propagator, and thawed Gaussian approximation (TGA). Both approximations yield accurate results. Lower panel: Position density at time $t \approx 392$ fs propagated in the same Morse potential. In contrast to the Herman–Kluk propagator, the thawed Gaussian approximation does not capture interference between faster and slower components of the wavepacket. For more details, see the last paragraph of Section 4.

situations, the single-trajectory methods break down, whereas the Herman–Kluk propagator often remains accurate and, at the least, provides a qualitatively correct insight (see, e.g., Figure 1). However, in its basic form, the Herman–Kluk propagator cannot describe non-adiabatic dynamics and quantum tunneling. To overcome this limitation, various extensions have been developed: For example, surface hopping Herman–Kluk initial value representation [31, 32] captures non-adiabatic dynamics, whereas higher-order semiclassical corrections to the Herman–Kluk propagator [33, 34] incorporate nuclear tunneling.

The multi-trajectory nature of the Herman–Kluk propagator is not only its advantage, but also its bottleneck. In particular, converged computations might require an extremely large number of trajectories. For this reason, several groups designed various methods, whose goal is reducing the number of trajectories required by the Herman–Kluk propagator. These include, e.g., Filinov filtering [13, 35–37], time-averaging [38–41], semiclassical interaction picture [42, 43], multiple-coherent states [44], hybrid dynamics [45–47], mixed quantum-semiclassical dynamics [48–50], and many others, which achieve the reduction in the number of trajectories by applying one of several possible further approximations.

Yet, the number of guiding trajectories can already be significantly reduced simply by choosing the sampling density of the initial conditions wisely. Although the acceleration of the convergence may be smaller than with the previously mentioned approximate methods, the advantage of this "purely numerical" approach based on improved exact sampling of the unaltered Herman–Kluk initial value representation is that the converged results agree exactly with the converged results of the original Herman–Kluk propagator. For this reason, an early numerical study [8] of the Herman–Kluk wavefunction employed the square root of the Husimi distribution as the sampling density of the initial state, whereas most calculations of observables, time-correlation functions, and wavepacket autocorrelation functions, i.e., quantities quadratic in the wavefunction, correctly employ sampling from the Husimi density [2, 51]. In contrast to observables and correlation functions, the Herman–Kluk wavefunction itself has not been studied much since the early papers [6, 8] and rigorous numerical analysis has been presented only recently [52, 53]. However, the choice of the optimal sampling density for the Herman–Kluk wavefunction itself has not been analyzed in detail.

The goal of this work is, therefore, to analyze the convergence of the Herman–Kluk wavefunction for different initial sampling strategies and to understand the convergence error as a function of time. Specifically, we investigate two mesh-free discretization approaches for the initial sampling—first analytically and then numerically on the examples of harmonic and Morse oscillators with increasing anharmonicity. In a follow-up paper, an analogous detailed analysis of the convergence of the norm, energy, and other expectation values will be presented.

The remainder of this paper is organized as follows. In the next section we briefly introduce the Herman–Kluk propagator and its components necessary for numerical computations. We define the initial sampling densities and specify the algorithm used for numerical experiments. In the main Section 3, we analyze the errors at the initial and final times due to the phase-space discretization. In particular, we prove that in the harmonic oscillator this error is a periodic function of time. Our numerical experiments in Section 4 confirm the theoretical error estimates and provide further insights into the anharmonic evolution generated by Morse potentials, which are not accessible to explicit analytical calculations.

2 Discretising the Herman–Kluk propagator

2.1 Herman–Kluk propagator

Evolution of a quantum state $|\psi(t)\rangle$ is governed by the time-dependent Schrödinger equation

$$i\hbar \frac{d}{dt}|\psi(t)\rangle = \hat{H}|\psi(t)\rangle, \ \ |\psi(0)\rangle = |\psi_0\rangle \tag{1}$$

where $\hbar$ is the reduced Planck constant and $\hat{H}$ is the Hamiltonian operator. Here, we assume the Hamiltonian to be the time-independent operator

$$\hat{H} = \frac{1}{2m}\hat{p}^T \cdot \hat{p} + V(\hat{q}), \tag{2}$$

where m is the mass (after mass-scaling coordinates), and q and p are D-dimensional position and momentum vectors. Under the usual regularity and growth assumptions on the potential energy function V, the spectral-theorem [54] provides for all times $t \in \mathbb{R}$ a well-defined unitary propagator

$$\hat{U}_t := \exp\left(-i\hat{H}t/\hbar\right), \tag{3}$$

in terms of which the solution of (1) can be expressed as

$$|\psi(t)\rangle = \hat{U}_t|\psi_0\rangle \tag{4}$$

for all square integrable initial data $\psi_0(x) = \langle x|\psi_0\rangle \in L^2(\mathbb{R}^D)$.

Solving the Schrödinger equation numerically is notoriously difficult for various reasons. With respect to the atomic scale, the nuclear mass is rather large, so that the presence of the factor m^{-1} in the kinetic energy operator induces highly oscillatory motion both with respect to time and space. More importantly, for most molecular systems the dimension D of the configuration space is so large that grid-based integration methods are very expensive if not infeasible. Therefore, one often resorts to mesh-free discretization methods or semiclassical approximations, both of which alleviate this "curse of dimensionality" at least partially.

The semiclassical Herman–Kluk propagator utilizes frozen Gaussian functions

$$\begin{aligned} g_z^\gamma(x) = &\left(\frac{\det\gamma}{\pi^D\hbar^D}\right)^{1/4} \\ &\times \exp\left\{-\left[(x-q)^T\cdot\gamma\cdot(x-q)/2 + ip^T\cdot(x-q)\right]/\hbar\right\} \end{aligned} \tag{5}$$

with a centre at the phase-space point $z = (q, p) \in \mathbb{R}^{2D}$ and with a fixed, real, symmetric, positive-definite width-matrix $\gamma \in \mathbb{R}^{D\times D}$. The frozen Gaussians $\{|g_z^\gamma\rangle: z \in \mathbb{R}^{2D}\}$ form an over-complete subset of the Hilbert space of square integrable functions. They have the striking property that any $|\psi\rangle \in L^2(\mathbb{R}^D)$ can be decomposed as [55]

$$|\psi\rangle = \int_{\mathbb{R}^{2D}} \langle g_z^\gamma|\psi\rangle |g_z^\gamma\rangle d\nu, \tag{6}$$

with the scaled phase-space measure $d\nu = dz/(2\pi\hbar)^D$. Using this decomposition for our solution of the time-dependent Schrödinger equation, we obtain

$$\hat{U}_t|\psi_0\rangle = \int_{\mathbb{R}^{2D}} \langle g_z^\gamma|\psi_0\rangle \hat{U}_t |g_z^\gamma\rangle \, d\nu. \tag{7}$$

Approximating the exact propagator $\hat{U}_t$ with the Herman–Kluk propagator

$$\hat{U}_t^{\mathrm{HK}} := \int_{\mathbb{R}^{2D}} R(t,z) e^{iS(t,z)/\hbar} |g_{z(t)}^\gamma\rangle\langle g_z^\gamma| d\nu \tag{8}$$

yields the Herman–Kluk wave function

$$\begin{aligned} |\psi^{\mathrm{HK}}(t)\rangle &:= \hat{U}_t^{\mathrm{HK}}|\psi_0\rangle \\ &= \int_{\mathbb{R}^{2D}} R(t,z) e^{iS(t,z)/\hbar} \langle g_z^\gamma|\psi_0\rangle |g_{z(t)}^\gamma\rangle d\nu. \end{aligned} \tag{9}$$

Here, $z(t) = (q(t), p(t))$ is the solution to the underlying classical Hamiltonian system

$$\dot{w} = J\cdot\nabla h(w), \;\; w(0) = z, \tag{10}$$

for the Hamiltonian function $h(q, p) = T(p) + V(q)$, where

$$J = \begin{pmatrix} 0 & \mathrm{Id}_D \\ -\mathrm{Id}_D & 0 \end{pmatrix} \in \mathbb{R}^{2D\times 2D} \tag{11}$$

is the standard symplectic matrix. S denotes the classical action integral

$$S(t,z) = \int_0^t \left[\frac{d}{d\tau} q(\tau)\cdot p(\tau) - h(z(\tau))\right] d\tau \tag{12}$$

which solves the initial value problem

$$\dot{S}(t,z) = T(p(t)) - V(q(t)), \;\; S(0,z) = 0, \tag{13}$$

for all $z = (q, p) \in \mathbb{R}^{2D}$. In (9), the Herman–Kluk prefactor

$$R(t,z) = 2^{-D/2}\cdot\det\left(M_{qq} + \gamma^{-1}\cdot M_{pp}\cdot\gamma - iM_{qp}\cdot\gamma + i\gamma^{-1}\cdot M_{pq}\right)^{1/2} \tag{14}$$

depends on the matrices

$$M_{\alpha\beta} = \partial\alpha_t/\partial\beta_0 \in \mathbb{R}^{D\times D} \quad (\alpha,\beta \in \{q,p\}), \tag{15}$$

i.e., the four $D \times D$ block components of the $2D \times 2D$ stability matrix M. Stability matrix, defined as the Jacobian $M(t) = \partial z(t)/\partial z$ of the flow map, is the solution to the variational equation

$$\dot{M}(t) = J\cdot\mathrm{Hess}\; h(z(t))\cdot M(t), \;\; M(0) = \mathrm{Id}_{2D}, \tag{16}$$

with Hess h the Hessian of the Hamiltonian function h.

The Herman–Kluk approximation (9) has been mathematically justified in different works [53, 56–58]. It has been shown that the exactly evolved quantum state is approximated by the Herman–Kluk state (9) with an error of the order of $\hbar$. More precisely,

$$\sup_{t\in[0,T]} \||\psi(t)\rangle - |\psi^{\mathrm{HK}}(t)\rangle\|_{L^2} \le C(T)\hbar, \tag{17}$$

for all initial data $|\psi_0\rangle$ of norm one, where $T > 0$ is a fixed time and $C(T) > 0$ is a constant independent of $\hbar$ and independent of $|\psi_0\rangle$. If the potential is at most quadratic, then the approximation is exact [53]. For the expectation value of an observable $\hat{A}$, the error of the Herman–Kluk approximation can be pessimistically estimated as

$$\langle\psi(t)|\hat{A}|\psi(t)\rangle = \langle\psi^{\mathrm{HK}}(t)|\hat{A}|\psi^{\mathrm{HK}}(t)\rangle + \mathcal{O}(\hbar), \tag{18}$$

by using the triangle inequality. In particular, this gives an upper bound for the error of the squared norm (if $\hat{A} = \hat{I}$) or energy (if $\hat{A} = \hat{H}$). However, this coarse estimate is potentially not sharp, since it cannot account for error cancellation due to oscillation.

2.2 Discretisation

Evolving the wavefunction (9) with the Herman–Kluk propagator requires evaluating an integral over the phase space $\mathbb{R}^{2D}$ and the overlap of the initial state with a frozen Gaussian. Furthermore, the algorithm needs to propagate the trajectories $z(t) = (q(t), p(t))$, the classical action $S(t, z)$, and the Herman–Kluk prefactor $R(t, z)$ according to Hamilton's equations of motion for all chosen quadrature points $z \in \mathbb{R}^{2D}$. The latter can be achieved using symplectic integration methods to preserve also the symplectic structure of the classical Hamiltonian system. Due to the curse of dimensionality, for high D the integral on $\mathbb{R}^{2D}$ must be evaluated using mesh-free discretization, such as Monte Carlo methods [59].

To evaluate the Herman–Kluk wavefunction (9) by Monte Carlo sampling, we rewrite the integral from Eq. 9 as

$$|\psi^{\mathrm{HK}}(t)\rangle = \langle r(z)|\phi(t,z)\rangle\rangle_{\rho(z)}, \tag{19}$$

where we introduced the notation

$$\begin{aligned}\langle|\psi(t,z)\rangle\rangle_{\rho(z)} &:= \int_{\mathbb{R}^{2D}}|\psi(t,z)\rangle\, d\mu\\ &= \int_{\mathbb{R}^{2D}}|\psi(t,z)\rangle\rho(z)\, d\nu\end{aligned} \tag{20}$$

for the phase-space average of $|\psi(t,z)\rangle$ with respect to a probability measure μ with density $\rho(z) = d\mu/d\nu$ and defined a time-dependent state

$$|\phi(t,z)\rangle := R(t,z)e^{iS(t,z)/\hbar}|g^{\gamma}_{z(t)}\rangle, \tag{21}$$

i.e., a propagated frozen Gaussian multiplied by the Herman–Kluk and phase prefactors, and a time-independent function

$$r(z) := \langle g^{\gamma}_{z}|\psi_0\rangle\ \rho(z)^{-1}. \tag{22}$$

The Monte Carlo estimator is then given by

$$|\psi_N(t)\rangle = \frac{1}{N}\sum_{j=1}^{N}|\psi(t,z_j)\rangle, \tag{23}$$

where $\psi(t, z_j)$ is the state obtained from initial condition z_j and $z_1, z_2, \ldots, z_N$ are sampled from probability density $\rho(z)$.

As for any importance sampling, there are infinitely many ways to decompose the time-independent part of the phase-space integrand in Eq. 9 into the product $\langle g^{\gamma}_{z}|\psi_0\rangle = r(z)\rho(z)$ of a prefactor r with a normalized sampling density ρ. If one computes observables and correlation functions, which are quadratic in the initial state, $\rho(z)$ is typically taken to be the Husimi probability density

$$\rho_{\mathrm{H}}(z) := |\langle g^{\gamma}_{z}|\psi_0\rangle|^2 \tag{24}$$

of the initial state $|\psi_0\rangle$. For Husimi distribution, the prefactor $r(z)$ becomes

$$r_{\mathrm{H}}(z) = \langle\psi_0|g^{\gamma}_{z}\rangle^{-1}. \tag{25}$$

However, since the wavefunction evolved with the Herman–Kluk propagator is first- and not second-order in $|\psi_0\rangle$, it is natural to also test the square root of the Husimi density and to consider the probability density

$$\tilde{\rho}(z) := \frac{|\langle g^{\gamma}_{z}|\psi_0\rangle|}{\int_{\mathbb{R}^{2D}}|\langle g^{\gamma}_{w}|\psi_0\rangle|d\nu} \tag{26}$$

with a bounded prefactor

$$\tilde{r}(z) := \langle g^{\gamma}_{z}|\psi_0\rangle\ \tilde{\rho}(z)^{-1}. \tag{27}$$

Indeed, in their early paper [8], Kluk et al. used this "square-root" approach for computing the Herman–Kluk wavefunction and mentioned that it was "especially appealing because it [was] a well defined, non-arbitrary way of choosing the basis [. . .]." In the following, we shall show that the square-root approach is indeed optimal, but the number of samples still suffers from an exponential dependence on the dimension.

The two probability densities $\rho_{\mathrm{H}}(z)$ and $\tilde{\rho}(z)$ can now be used to compute the phase-space integral by Monte Carlo integration. To sum up, we have two cases, in which we evaluate $|\psi^{\mathrm{HK}}(t)\rangle$ either as

$$|\psi^{\mathrm{HK}}(t)\rangle = \langle r_{\mathrm{H}}(z)|\phi(t,z)\rangle\rangle_{\rho_{\mathrm{H}}(z)} \qquad \text{(Case H)}$$

or as

$$|\psi^{\mathrm{HK}}(t)\rangle = \langle \tilde{r}(z)|\phi(t,z)\rangle\rangle_{\tilde{\rho}(z)}. \qquad \text{(Case sqrt} - \text{H)}$$

In general, the integral over $\mathbb{R}^D$ defining the overlap of the initial wavefunction with a Gaussian has to be computed by numerical quadrature. However, for important specific cases analytical formulas are available. If the initial wavefunction is a Gaussian wavepacket $|\psi_0\rangle = |g^{\gamma}_{z_0}\rangle$ centred at some phase-space point $z_0 = (q_0, p_0) \in \mathbb{R}^{2D}$, then

$$\begin{aligned}\langle g^{\gamma}_{z}|\psi_0\rangle_{L^2(\mathbb{R}^D)} = \exp&\left[-\frac{1}{4\hbar}(z-z_0)^T\cdot\Sigma_0\cdot(z-z_0)\right]\\ &\cdot\exp\left[\frac{i}{2\hbar}(p+p_0)^T\cdot(q-q_0)\right],\end{aligned} \tag{28}$$

where $\Sigma_0 := \begin{pmatrix}\gamma & 0\\ 0 & \gamma^{-1}\end{pmatrix}$ is the matrix containing the width parameters of the initial coherent state. Then, the Husimi density is given by

$$\rho_{\mathrm{H}}(z) = \exp\left[-\frac{1}{2\hbar}(z-z_0)^T\cdot\Sigma_0\cdot(z-z_0)\right], \tag{29}$$

whereas the second approach provides the density

$$\tilde{\rho}(z) = 2^{-D}\exp\left[-\frac{1}{4\hbar}(z-z_0)^T\cdot\Sigma_0\cdot(z-z_0)\right] \tag{30}$$

and prefactor

$$\tilde{r}(z) = 2^{D}\exp\left[\frac{i}{2\hbar}(p+p_0)^T\cdot(q-q_0)\right]. \tag{31}$$

2.3 Summary of the numerical algorithm

Taking into account all the previous considerations, we slightly extend the natural numerical algorithm (described, e.g., Section 4 of Ref. [52]) for finding the Herman–Kluk approximation to the wavefunction at time t.

Algorithm 1: (Herman–Kluk propagation)

1. Draw independent samples $z_1, \ldots, z_N \in \mathbb{R}^{2D}$ from a distribution with density $\rho_{\mathrm{H}}(z)$ or $\tilde{\rho}(z)$ given by Eqs. 29 and 30.
2. For all $j \in \{0, 1, \ldots, N\}$:
    2.1 Set initial values $z(0) = z_j$, $M(0) = \mathrm{Id}_{2D}$ and $S(0) = 0$.
    2.2 Compute approximate solutions to Eqs. 10, 13 and 16 up to time t with a symplectic integration method [60] based on the Störmer–Verlet scheme [61, 62].
    2.3 Compute the Herman–Kluk prefactor $R(t, z_j)$ from $M(t)$ while choosing the correct branch of the complex square root [63], which guarantees continuity of $R(t, z_j)$ as a function of t.

3. Calculate $|\psi_N(t)\rangle$ by means of formula (23) with $|\psi(t, z_j)\rangle$ replaced with either

$$|\psi_{\mathrm{H}}(t,z_j)\rangle = r_{\mathrm{H}}(z_j)R(t,z_j)e^{iS\left(t,z_j\right)/\hbar}|g^{\gamma}_{z_j(t)}\rangle \tag{32}$$

or

$$|\tilde{\psi}(t,z_j)\rangle = \tilde{r}(z_j)R(t,z_j)e^{iS\left(t,z_j\right)/\hbar}|g^{\gamma}_{z_j(t)}\rangle, \tag{33}$$

where $r_{\mathrm{H}}(z_j)$ and $\tilde{r}(z_j)$ are given by Eqs. 25, 28 and 31.

We note that Eqs. 10, 13 and 16 can be evaluated simultaneously with a single numerical integrator. To increase the accuracy of the time integration one can use higher-order composition methods [64, 65]. They increase the order of the time integrator, but also its numerical cost. A higher-order time integrator is not necessarily useful since the phase-space error occurring from the Monte Carlo quadrature usually dominates the time integration error.

3 Phase space error analysis

Algorithm 1 relies on the discretisation of the phase-space integrals and of the system of ordinary differential equations. Here we focus only on the phase-space discretisation error. A similar, but less formal phase-space error analysis was applied to various algorithms for computing fidelity and classical correlation functions [66–69].

3.1 Moments of the integrand

To assess the accuracy of the Monte Carlo estimator (23), we examine the moments of the two different integrands: $|\psi_{\mathrm{H}}(t)\rangle$ and $|\tilde{\psi}(t)\rangle$. First, we observe that for any $s > 0$,

$$\mathbb{E}\left[\|\tilde{\psi}(t)\|^s\right] = \int_{\mathbb{R}^{2D}} |R(t,z)|^s \, |\tilde{r}(z)|^s \, d\tilde{\mu}(z) < \infty, \tag{34}$$

since $\tilde{r}(z)$ and the Herman–Kluk prefactor $R(t, z)$ are both bounded functions. For a discussion of the boundedness of $R(t, z)$, see Section 1 of the Supplementary Material. In contrast,

$$\begin{aligned}\mathbb{E}\left[\|\psi_{\mathrm{H}}(t)\|^s\right] &= \int_{\mathbb{R}^{2D}} |R(t,z)|^s \, |r_{\mathrm{H}}(z)|^s \, d\mu_{\mathrm{H}}(z) \\ &= \int_{\mathbb{R}^{2D}} |R(t,z)|^s \, |\langle g_z^\gamma | \psi_0\rangle|^{2-s} \, d\nu\end{aligned} \tag{35}$$

ceases to be finite for $s \geq 2$. However, both integrands have a finite first moment, so that the strong law of large numbers (Theorem 2.4.1 in Ref. [70]) provides convergence of the estimator,

$$|\psi_N(t)\rangle \to |\psi^{\mathrm{HK}}(t)\rangle \quad \text{as } N \to \infty, \tag{36}$$

with probability one. Divergence of the second moment for (Case H) does not violate convergence of the estimator, but results in a slightly worse convergence rate than the one for (Case sqrt-H). Numerical results in Section 4 confirm this expectation. This shows that the initial sampling density has to be chosen carefully.

3.2 Mean squared error

For (Case sqrt-H) the second moment is finite, so that the mean squared error of the Monte Carlo estimator (23) is well-defined and satisfies

$$\mathbb{E}\left[\||\psi_N(t)\rangle - |\psi^{\mathrm{HK}}(t)\rangle\|^2\right] = \frac{\mathbb{V}[|\tilde{\psi}(t)\rangle]}{N}, \tag{37}$$

where the expectation value and the variance are with respect to the density $\tilde{\rho}(z)$. Moreover (see also [52]),

$$\begin{aligned}\mathbb{V}[|\tilde{\psi}(t)\rangle] &= \int_{\mathbb{R}^{2D}} \||\tilde{\psi}(t)\rangle - \mathbb{E}[|\tilde{\psi}(t)\rangle]\|^2 \, d\tilde{\mu}(z) \\ &= \int_{\mathbb{R}^{2D}} |R(t,z)|^2 \, |\tilde{r}(z)|^2 \, d\tilde{\mu}(z) - \||\psi^{\mathrm{HK}}(t)\rangle\|^2.\end{aligned} \tag{38}$$

In the special case of an initial Gaussian initial wavepacket $|\psi_0\rangle = |g_{z_0}^\gamma\rangle$, this simplifies to

$$\mathbb{V}[|\tilde{\psi}(t)\rangle] = 4^D \int_{\mathbb{R}^{2D}} |R(t,z)|^2 \, d\tilde{\mu}(z) - \||\psi^{\mathrm{HK}}(t)\rangle\|^2, \tag{39}$$

and at initial time $t = 0$ we obtain

$$\mathbb{V}[|\tilde{\psi}(0)\rangle] = 4^D - 1, \tag{40}$$

since the Herman–Kluk prefactor satisfies $R(0, z) = 1$.

For a more general assessment of the variance, numerical experiments in Section 4 consider the error between the approximations with N and $2N$ samples. By the linearity of the expectation value and the triangle inequality, this error can be estimated by

$$\begin{aligned}&\mathbb{E}\left[\||\psi_N(t)\rangle - |\psi_{2N}(t)\rangle\|^2\right] \\ &\leq \mathbb{E}\left[\||\psi_N(t)\rangle - |\psi^{\mathrm{HK}}(t)\rangle\|^2\right] + \mathbb{E}\left[\||\psi^{\mathrm{HK}}(t)\rangle - |\psi_{2N}(t)\rangle\|^2\right] \\ &= \frac{3}{2}\frac{\mathbb{V}[|\psi(t)\rangle]}{N}.\end{aligned} \tag{41}$$

Note that Eq. 37 gives only the expected convergence error, i.e., the convergence error averaged over infinitely many independent simulations, each using N trajectories. The actual convergence error for any specific simulation with N trajectories may deviate from this analytical estimate substantially due to statistical noise. Nevertheless, in Section 2 of the Supplementary Material, we explain how Eq. 37 can also provide a rigorous lower bound and asymptotic estimate of the number of trajectories needed for convergence of a single simulation.

3.3 Other sampling densities

For the special case of an initial Gaussian wavepacket $|\psi_0\rangle = |g_{z_0}^\gamma\rangle$, the two proposed sampling densities $\rho_{\mathrm{H}}(z)$ and $\tilde{\rho}(z)$ belong to a family of normal distributions with probability density functions

$$\rho_a(z) = \left(\frac{2}{a}\right)^D \exp\left[-\frac{1}{a\hbar}(z - z_0)^T \cdot \Sigma_0 \cdot (z - z_0)\right] \tag{42}$$

with $a \geq 2$. In the spirit of importance sampling, the Herman–Kluk wavefunction can accordingly be written as a phase-space average

$$|\psi^{\mathrm{HK}}(t)\rangle = \langle|\psi_a(t,z)\rangle\rangle_{\rho_a(z)}. \tag{43}$$

At time $t = 0$, the norm of the integrand satisfies

$$\||\psi_a(0,z)\rangle\| = \left(\frac{a}{2}\right)^D \exp\left[-\left(\frac{a-4}{4a\hbar}\right)(z - z_0)^T \cdot \Sigma_0 \cdot (z - z_0)\right], \tag{44}$$

which implies for the variance

$$\begin{aligned}\mathbb{V}[|\psi_a(0)\rangle] &= \left(\frac{a}{4\pi\hbar}\right)^D \int_{\mathbb{R}^{2d}} \exp\left[-\left(\frac{a-2}{2a\hbar}\right)|z|^2\right] dz - 1 \\ &= \left(\frac{a^2}{2(a-2)}\right)^D - 1.\end{aligned} \tag{45}$$

For $a > 2$, the function $a \mapsto a^2/(2a - 4)$ attains its minimum at $a = 4$, which corresponds to the sampling density $\tilde{\rho}$. In other words, (Case sqrt-H) is optimal as far as the mean squared error is concerned. Nevertheless, even this optimal sampling results in an unfavorable exponential growth with the number of dimensions D.

3.4 Harmonic motion

The one-dimensional harmonic oscillator

$$\hat{H} = -\frac{\hbar^2}{2m}\frac{d^2}{dx^2} + \frac{m\omega^2}{2}x^2 \tag{46}$$

is one of the rare examples for which explicit expressions for the solution of the Schrödinger equation and for the Herman–Kluk prefactor exist. For an initial Gaussian wavepacket $|\psi_0\rangle = |g^{\gamma}_{z_0}\rangle$ with position and momentum $q_0, p_0 \in \mathbb{R}$, the exact wavefunction is given by [71]

$$\psi_{\mathrm{ex}}(x,t) = \exp\left\{\frac{i}{\hbar}\left[\frac{\alpha_t}{2}(x-q_t)^2 + p_t(x-q_t) + \beta_t\right]\right\}, \tag{47}$$

where

$$\alpha_t = b\frac{\alpha_0\cos(\omega t) - b\sin(\omega t)}{b\cos(\omega t) + \alpha_0\sin(\omega t)}, \tag{48}$$

$$q_t = q_0\cos(\omega t) + \frac{p_0}{b}\sin(\omega t), \tag{49}$$

$$p_t = p_0\cos(\omega t) - bq_0\sin(\omega t)\ \text{and} \tag{50}$$

$$\beta_t = \beta_0 + \frac{1}{2}\left[q_t p_t - q_0 p_0 + i\hbar\ln\left(\frac{z_t}{b}\right)\right] \tag{51}$$

with the abbreviations $z_t = b\cos(\omega t) + \alpha_0\sin(\omega t)$, $\alpha_0 = i\gamma$, and $b = m\omega$. Here, β_0 includes the normalization constant for the wavefunction at time $t = 0$. The classical action is given by

$$S(t,q_0,p_0) = \frac{1}{2}\sin(\omega t)\left[\left(\frac{p_0^2}{b} - bq_0^2\right)\cos(\omega t) - q_0 p_0\sin(\omega t)\right]. \tag{52}$$

The four components of stability matrix M can be obtained, from their definition (15), by differentiating expressions for q_t and p_t with respect to q_0 and p_0, namely,

$$M(t) = \begin{pmatrix} \cos(\omega t) & b^{-1}\sin(\omega t) \\ -b\sin(\omega t) & \cos(\omega t) \end{pmatrix}. \tag{53}$$

The Herman–Kluk prefactor satisfies

$$R(t) = \left\{\frac{1}{2}\left[2\cos\omega t - i\sin(\omega t)\left(\frac{\gamma}{b} + \frac{b}{\gamma}\right)\right]\right\}^{1/2}, \tag{54}$$

so that the variance (38) can be written as

$$\mathbb{V}[|\tilde{\psi}(t)\rangle] = 2\left[4\cos^2(\omega t) + \left(\frac{\gamma}{b} + \frac{b}{\gamma}\right)^2\sin^2(\omega t)\right]^{1/2} - 1. \tag{55}$$

This implies that for (Case sqrt-H) applied to a harmonic oscillator, the mean squared error of our Monte Carlo estimator oscillates with a period of π/ω between

$$3 \le \mathbb{V}[|\tilde{\psi}(t)\rangle] \le 2\left(\frac{\gamma}{m\omega} + \frac{m\omega}{\gamma}\right) - 1. \tag{56}$$

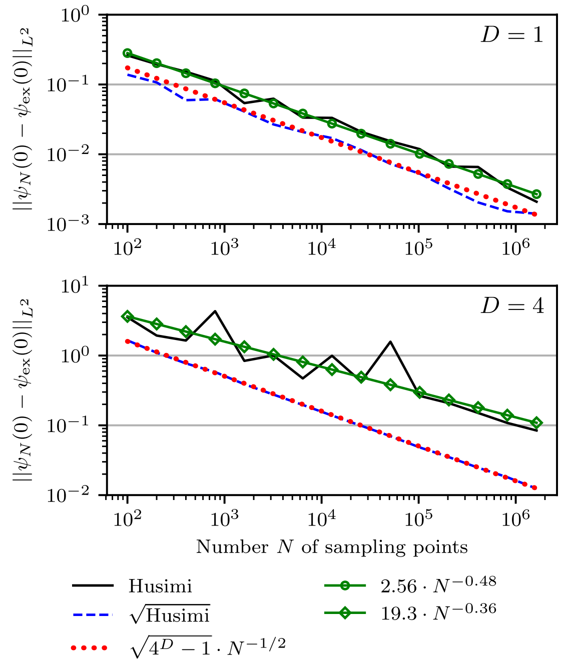

FIGURE 2

Sampling error of the initial wavefunction in one (upper panel) and four (lower panel) dimensions as a function of the number N of Monte Carlo points. The plot displays the error for sampling from the Husimi density (Case H) and its approximated convergence (marked lines) as well as the error for sampling from the square root of the Husimi density (Case sqrt-H) and its analytical error estimation (dotted line).

4 Numerical examples

In this section, we complement our previous theoretical results with numerical examples. We start by examining how the performance of Algorithm 1 depends on the method to discretise the phase space. We explore the time dependence of the variance of the Monte Carlo estimator in one dimension in a harmonic oscillator as well as in a series of increasingly anharmonic Morse potentials. The Monte Carlo integration is tested by averaging over N independent, identically distributed samples of initial conditions. We approximate its convergence rate by assuming a power law

$$F(N) = cN^{-s} \tag{57}$$

dependence of the mean statistical error on the number of samples N. The prefactor c and order s of convergence are determined by the linear fit (in the least-squares sense) of the logarithm of Eq. 57 to the dependence of the logarithm of the statistical error on the logarithm of N.

Throughout our numerical examples, we work in atomic units ($\hbar = 1$), mass-scaled coordinates and with an initial state that is a Gaussian wavepacket with phase-space centre $z_0 \in \mathbb{R}^{2D}$.

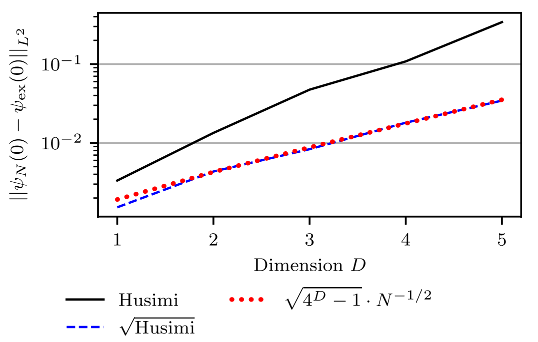

FIGURE 3
Dependence of the sampling error of the initial wavefunction on dimension D for $N = 100 \cdot 2^{13} \approx 8 \cdot 10^5$ points sampled from either the Husimi density (Case H) or its square root (Case sqrt-H). The analytical error estimate for the latter sampling is shown by the dotted line.

4.1 Initial phase-space error

We start by considering a spherical initial Gaussian wavepacket $|\psi_{\text{ex}}(0)\rangle = |g_{z_0}^{\gamma}\rangle$ with a width parameter $\gamma = 2\text{Id}_D$ in one and four dimensions. For $D = 1$, it is centred at $z_0 = (-1, 0)$ and for $D = 4$, at $z_0 = -(1, 1, 1, 1, 0, 0, 0, 0)$. Figure 2 shows the L^2-distance

$$\||\psi_N(0)\rangle - |\psi_{\text{ex}}(0)\rangle\|_{L^2} \tag{58}$$

of the Monte Carlo estimators for (Case H) and (Case sqrt-H) from the exact wavefunction at initial time as a function of the number of Monte Carlo quadrature points. We can immediately see that the analytical prediction (40) of the mean squared error (37) of (Case sqrt-H) is fulfilled. For (Case H), the curve-fitting approximation (57) provided $(c, s) = (2.56, -0.48)$ for $D = 1$ and $(c, s) = (19.3, -0.36)$ for $D = 4$. It shows that both cases converge to the correct result and that (Case sqrt-H) performs slightly better than (Case H). Additionally, Figure 3 displays the L^2-distance of the estimators for both cases from the exact wavefunction at initial time as a function of the dimension D. Each wavefunction was approximated with $N \approx 8 \cdot 10^5$ trajectories. The analytical prediction (40) for (Case sqrt-H) is realized. Moreover, the error for (Case H) increases faster with D.

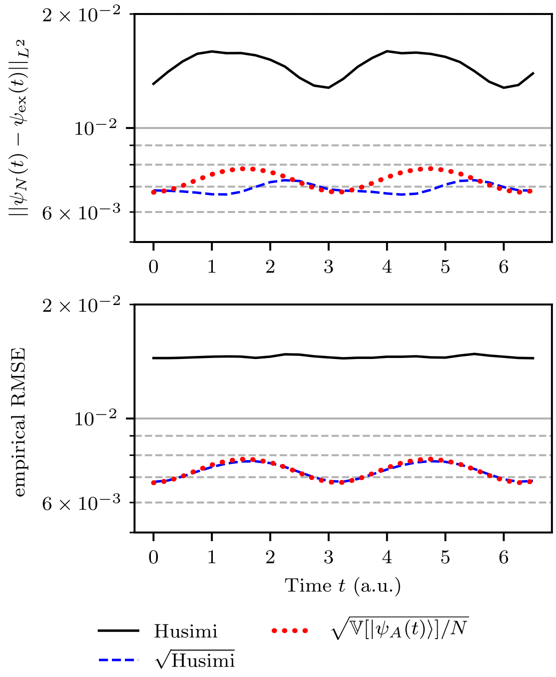

FIGURE 4
Time dependence of the sampling error of the Herman–Kluk wavefunction propagated in a harmonic oscillator. The upper panel is produced by one run with $N = 2^{16} = 65{,}536$ trajectories, whereas the lower panel is produced by $K = 100$ independent runs, each with $N = 2^{16} = 65{,}536$ trajectories, and averaging the square of the error over the K runs. The analytical error estimate for the sampling from the square root of the Husimi density (Case sqrt-H) is shown with the dotted line.

4.2 Harmonic potential

To analyze the effect of dynamics on the convergence, let us consider a harmonic potential $V(x) = x^2/2$ in one dimension and explore the dynamics for one full oscillation period. The initial Gaussian wavepacket is still localized in $z_0 = (-1, 0)$ with width $\gamma = 2$. In Figure 4, we compare the exact wavefunction (47) with the numerical realization of the Herman–Kluk propagator which uses the exact solution to $q(t)$, $p(t)$, $S(t, z)$ and $R(t, z)$ stated in Eqs 49, 50, 52, 54. Since the Herman–Kluk propagator is exact for harmonic motion and since we supply exact classical trajectories, the observed numerical error is only due to the Monte Carlo integration. The upper panel of Figure 4 shows the time dependence of the L^2-error

$$\||\psi_N(t)\rangle - |\psi_{\text{ex}}(t)\rangle\|_{L^2}, \tag{59}$$

where the semiclassical wavefunctions were generated using $N = 2^{16}$ trajectories. Sampling from the square root of the Husimi density (Case sqrt-H) results in approximately twice smaller error than sampling from the Husimi density itself. For (Case sqrt-H), the figure also displays the analytical error estimate derived in (55), which matches the numerical error up to small statistical noise. To remove this statistical noise and to match the analytical estimate (55) more accurately, in the lower panel of Figure 4 we plot the empirical root mean square error (RMSE) [59] S_{100}, where

$$S_K := \frac{1}{K}\sum_{j=1}^{K} \||\psi_N^{(j)}(t)\rangle - |\psi_{\text{ex}}(t)\rangle\|^2, \tag{60}$$

K is an integer number of independent simulations (indexed by j) and each $\psi_N^{(j)}$ was itself approximated using N independent samples. One can see that

$$\mathbb{E}[S_K] = \mathbb{E}\left[\||\psi_N(t)\rangle - |\psi_{\text{ex}}(t)\rangle\|^2\right] = \frac{\mathbb{V}[|\tilde{\psi}(t)\rangle]}{N}. \tag{61}$$

For $K = 1$, one obtains the result represented in the upper panel of Figure 4. For $K \to \infty$, due to the strong law of large numbers, S_K

converges almost surely to its expectation value and hence to the analytical error estimate.

The lower panel of Figure 4 shows the empirical RMSE computed with $K = 100$ and $N = 2^{16}$. For (Case sqrt-H), it coincides almost perfectly with the analytical prediction. We note that the error reaches its maximum whenever the wavefunction passes through the bottom of the potential and its minimum when the wavefunction arrives at the turning points. Even though this analysis makes only sense for finite variance, the figure also displays the empirical RMSE for (Case H), which is nearly constant. Both panels show a qualitatively similar error evolution for (Case H), however, at a magnitude that is considerably larger than the error for (Case sqrt-H).

4.3 Morse potential

To investigate the convergence of the Herman–Kluk wavefunction in anharmonic systems, we consider dynamics generated by a less and more anharmonic Morse potentials. The parameters were taken from [29]. Our initial state is a Gaussian wavepacket with zero initial position and momentum $(q_0, p_0) = (0, 0)$, and with a width parameter $\gamma = 0.00456$ a.u. ≈ 1000 cm^{-1}. The Morse potential

$$V(x) = V_{\mathrm{eq}} + D_e\left[1 - e^{-a\left(x - q_{\mathrm{eq}}\right)}\right]^2 \tag{62}$$

is characterized by the dissociation energy D_e, decay parameter a, and the position q_{eq} and energy V_{eq} of the minimum. We considered two Morse potentials, both with $V_{\mathrm{eq}} = 0.1$ and $q_{\mathrm{eq}} = 20.95$ a.u., but with different values of a and D_e. The latter two parameters, however, were chosen so that the global harmonic potential fitted to the Morse potential at q_{eq} had the same frequency

$$\omega_{\mathrm{eq}} = \sqrt{V''\left(q_{\mathrm{eq}}\right)} = \sqrt{2D_e a^2} = 0.0041 \ \text{a.u.} \approx 900 \ \text{cm}^{-1} \tag{63}$$

for the two Morse potentials. The anharmonicity of the potentials was conveniently controlled with the dimensionless parameter

$$\chi = \hbar\frac{\omega_{\mathrm{eq}}}{4D_e}, \tag{64}$$

which is also reflected in the bound energy levels [71]

$$E_n = \hbar\omega_{\mathrm{eq}}\left[\left(n + \frac{1}{2}\right) - \chi\left(n + \frac{1}{2}\right)^2\right] \tag{65}$$

of a Morse oscillator. Then D_e and a are given by

$$\begin{aligned} D_e &= \hbar\frac{\omega_{\mathrm{eq}}}{4\chi}, \\ a &= \sqrt{2\frac{\omega_{\mathrm{eq}}\chi}{\hbar}}. \end{aligned} \tag{66}$$

We choose two different values

$$\chi = 0.005 \quad \text{and} \quad \chi = 0.01 \tag{67}$$

of anharmonicity and compare the Herman–Kluk propagation with a grid-based reference quantum calculation obtained by the Fourier-split method [72], which is second-order accurate with respect to the time step. The position grid was set from $x = -200$ to 1500 with 4096 equidistant points for $\chi = 0.005$ and from $x = -200$ to 10,000 with 16,384 equidistant points for $\chi = 0.01$. The larger grid for $\chi = 0.01$ was required to capture oscillations of the wavefunctions in the tail region, which are due to the increased anharmonicity. For the time propagation of the Herman–Kluk wavefunction, we used a second order Størmer-Verlet scheme with step size $\Delta t = 8$ a.u. ≈ 0.194 fs.

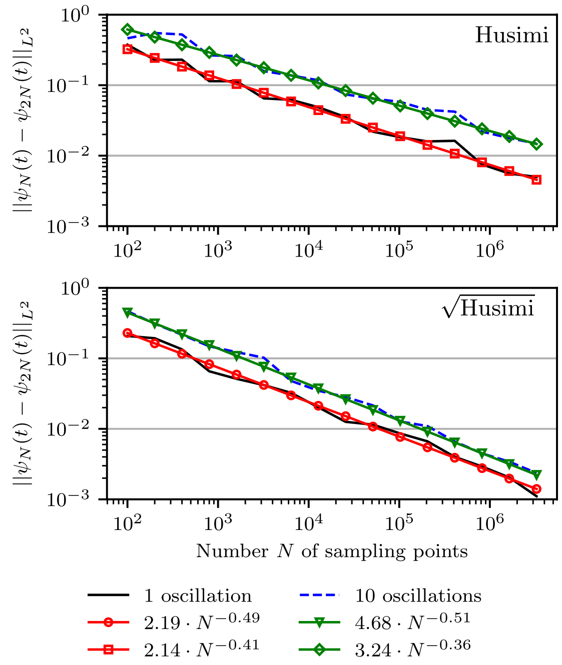

FIGURE 5
Sampling error between the Herman–Kluk wavefunctions obtained with N and $2N$ Monte Carlo quadrature points as a function of N. The wavefunctions are calculated in a Morse potential with anharmonicity parameter $\chi = 0.005$ after approximately one (solid line) or ten oscillations (dashed line). The upper panel shows both errors and their approximated convergence rates for (Case H). Similarly, (Case sqrt-H) is displayed in the lower panel.

Because the Herman–Kluk approximation is not exact in a Morse potential, to separate the statistical convergence error from the semiclassical error of the fully converged Herman–Kluk approximation, in Figure 5 we show the L^2-error

$$\|\psi_N(t) - \psi_{2N}(t)\| \tag{68}$$

between the Herman–Kluk wavefunctions calculated with N and $2N$ trajectories as a function of N. Both wavefunctions were propagated in a Morse potential with anharmonicity $\chi = 0.005$. Each panel includes the error for the fixed time t after approximately one oscillation (196 time steps) and ten oscillations (1960 time steps). In addition, the convergence rates for both sampling schemes were fitted to the same power law (57). We observe that sampling from the square root of the Husimi density (Case sqrt-H), shown in the lower panel, performs better than sampling from the Husimi density (Case H), displayed in the upper panel.

Figure 6 shows the analogous results obtained in a Morse potential with a larger anharmonicity parameter $\chi = 0.01$. Here, we display the wavefunctions after 202 and 2020 time steps, which are approximately the times after the first and tenth oscillations. As expected for anharmonic evolution, the error after ten oscillations is worse than after one oscillation.

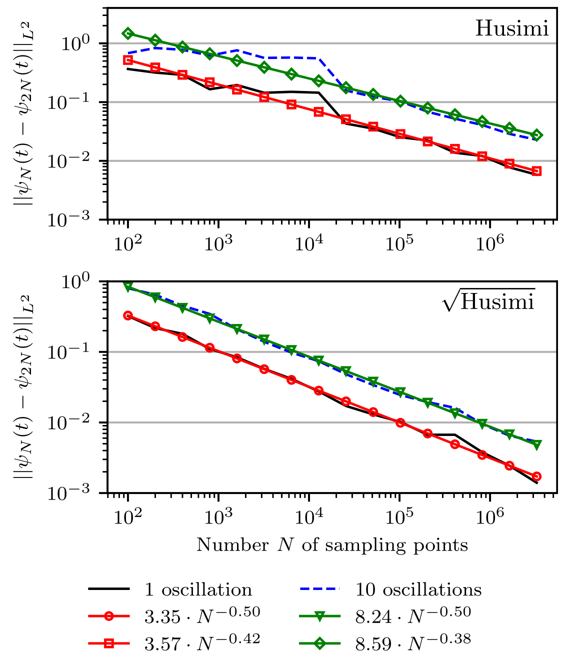

FIGURE 6
Same as Figure 5, except that the anharmonicity parameter of the Morse potential was increased to χ = 0.01.

TABLE 1 Summary of convergence rates for (Case sqrt-H) and (Case H) at initial time, in a harmonic oscillator and in two Morse potentials after one and ten oscillations.

	(Case sqrt-H)	(Case H)
Initial time		
$D = 1$	$\sqrt{(4^D - 1)} \cdot N^{-1/2}$	$2.56 \cdot N^{-0.48}$
$D = 4$	$\sqrt{(4^D - 1)} \cdot N^{-1/2}$	$19.3 \cdot N^{-0.36}$
Harmonic potential	$\mathbb{V}[\|\tilde{\psi}(t)\rangle]^{1/2} \cdot N^{-1/2}$ with variance from (55)	
Morse pot.: χ = 0.005		
1 oscillation	$2.19 \cdot N^{-0.49}$	$2.14 \cdot N^{-0.41}$
10 oscillations	$4.68 \cdot N^{-0.51}$	$3.24 \cdot N^{-0.36}$
Morse pot.: χ = 0.01		
1 oscillation	$3.35 \cdot N^{-0.50}$	$3.57 \cdot N^{-0.42}$
10 oscillations	$8.24 \cdot N^{-0.50}$	$8.59 \cdot N^{-0.38}$

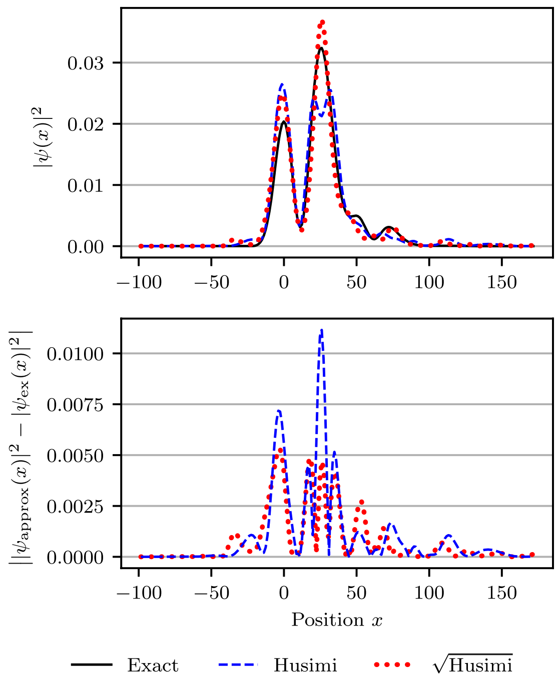

FIGURE 7
Position probability densities (upper panel) and their absolute errors (lower panel) in a Morse potential with χ = 0.01 after 10 oscillations (2020 time steps ≈ 392 fs). Position probability densities of the Herman–Kluk approximation for (Case H) and (Case sqrt-H) were computed with N = 800 trajectories.

Increased anharmonicity also increases the error in comparison to Figure 5. Again, the sampling from the square root of the Husimi density (Case sqrt-H) has consistently a lower error than (Case H).

To complement the abstract convergence study of the L^2-error, in the upper panels of Figures 7 and 8, we compare the more intuitive position probability densities of the “exact” quantum grid-based solution with those of (Case H) and (Case sqrt-H). Both figures were obtained in a Morse potential with anharmonicity parameter $\chi = 0.01$ at a time after ten oscillations. The difference lies in the number of trajectories used. The less converged results in Figure 7 were obtained with only N = 800 trajectories, whereas the fully converged results in Figure 8 employed $N = 100 \cdot 2^{14}$ trajectories. The lower panels of the two figures display the absolute errors of the position density for the two cases, measured with respect to the “exact” grid-based position density. The two panels of Figure 7 confirm again that sampling from the square root of Husimi density (Case sqrt-H) results in faster convergence than sampling from the Husimi density (Case sqrt-H). The upper panel of Figure 8 shows that in the numerically converged regime, the Herman–Kluk propagator approximates the exact solution in this system very well, regardless whether one samples from the Husimi density or its square root. The fact that results are numerically converged is confirmed in the lower panel of Figure 8, where the errors of (Case H) and (Case sqrt-H) are approximately the same, which implies that the common remaining error is the error of the Herman–Kluk approximation and not the phase-space discretization error.

Analytical expressions and numerical fits to the convergence rates for all studied systems are summarized in Table 1.

Finally, we note that Figure 1 in the Introduction was based, as Figure 8, on the Morse potential with anharmonicity parameter $\chi = 0.01$ and Herman–Kluk calculations used $N = 100 \cdot 2^{14}$ trajectories. For the computation of the position density, we used the more efficient (Case

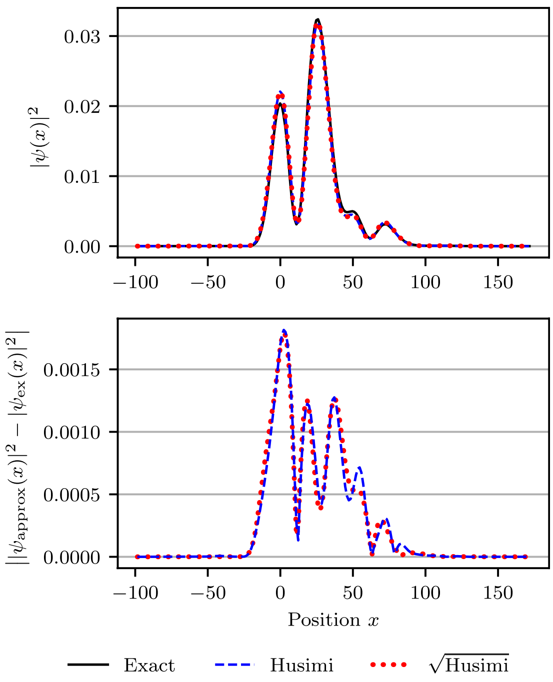

FIGURE 8
Same as Figure 7, except that the results were computed with $N = 100 \cdot 2^{14} \approx 1.6 \cdot 10^6$ trajectories and, therefore, are converged.

sqrt-H). The spectra in the upper panel were obtained by the Fourier transform of the wavepacket autocorrelation function; the Herman–Kluk autocorrelation function was computed by sampling from the Husimi density (Case H), because it gives the exact result (=1) at $t = 0$ regardless of the number of trajectories and, therefore, converges faster at short times.

5 Conclusion and outlook

We compared two different sampling strategies for evaluating the semiclassical wavefunction evolved with the Herman–Kluk propagator. For the initial phase-space sampling, we either used the Husimi density (Case H) or its square root (Case sqrt-H). We showed that the square root sampling produces a Monte Carlo integrand with finite second moment, while the Husimi sampling comes with an undesirable infinite second moment. The numerical experiments for the harmonic oscillator and two Morse oscillators with different extents of anharmonicity confirm that the infinite second moment results in a slower convergence of the Monte Carlo estimator. Therefore, we recommend the square root approach (Case sqrt-H) whenever the Herman–Kluk propagator is used directly for approximating the quantum-mechanical wavefunction and the L^2-error of the wavefunction approximation is the relevant accuracy measure. However, we explicitly verified that at initial time the square root density's second moment, even though it is finite, has an unfavorable, exponential dependence on the dimension, possibly leading to a large number of trajectories required for a reasonably accurate wavefunction.

Although the wavefunction is a central object in quantum mechanics, one is often interested directly in observables, which can be computed as expectation values. It is clearly inefficient to compute expectation values, such as energy or squared norm, with the Herman–Kluk propagator by computing the wave function first. A follow-up paper, in which an analysis similar to that presented here will be applied to the autocorrelation function as well as to the expectation values is in preparation. In particular, the approach to expectation values proposed in [52] will be analysed in detail. Our present analysis and sampling approaches could, in principle, help increase the efficiency of any Gaussian-based method, although it is difficult to predict the possible implications that the coupling between different Gaussians present in Gaussian basis methods [9, 10] might have for the choice of the optimal sampling density.

Data availability statement

The raw data supporting the conclusion of this article will be made available by the authors, without undue reservation.

Author contributions

All authors have contributed to the design and execution of the research and to the writing of the manuscript. FK performed all numerical calculations and prepared all figures.

Acknowledgments

The authors acknowledge financial support from the European Research Council (ERC) under the European Union's Horizon 2020 Research and Innovation Programme (Grant Agreement No. 683069–MOLEQULE) and from the EPFL.

Conflict of interest

The authors declare that the research was conducted in the absence of any commercial or financial relationships that could be construed as a potential conflict of interest.

Publisher's note

Supplementary Material

The Supplementary Material for this article can be found online at: https://www.frontiersin.org/articles/10.3389/fphy.2023.1106324/full#supplementary-material

References

1. Miller WH. Classical S matrix: Numerical application to inelastic collisions. *J Chem Phys* (1970) 53:3578–87. doi:10.1063/1.1674535

2. Miller WH. The semiclassical initial value representation: A potentially practical way for adding quantum effects to classical molecular dynamics simulations. *J Phys Chem A* (2001) 105:2942–55. doi:10.1021/jp003712k

3. Heller EJ. *The semiclassical way to dynamics and spectroscopy*. Princeton, NJ: Princeton University Press (2018).

4. Heller EJ. Frozen Gaussians: A very simple semiclassical approximation. *J Chem Phys* (1981) 75:2923–31. doi:10.1063/1.442382

5. Heller EJ. Time-dependent approach to semiclassical dynamics. *J Chem Phys* (1975) 62:1544–55. doi:10.1063/1.430620

6. Herman MF, Kluk E. A semiclasical justification for the use of non-spreading wavepackets in dynamics calculations. *Chem Phys* (1984) 91:27–34. doi:10.1016/0301-0104(84)80039-7

7. Herman MF. Time reversal and unitarity in the frozen Gaussian approximation for semiclassical scattering. *J Chem Phys* (1986) 85:2069–76. doi:10.1063/1.451150

8. Kluk E, Herman MF, Davis HL. Comparison of the propagation of semiclassical frozen Gaussian wave functions with quantum propagation for a highly excited anharmonic oscillator. *J Chem Phys* (1986) 84:326–34. doi:10.1063/1.450142

9. Shalashilin DV, Child MS. The phase space ccs approach to quantum and semiclassical molecular dynamics for high-dimensional systems. *Chem Phys* (2004) 304:103–20. doi:10.1016/j.chemphys.2004.06.013

10. Richings G, Polyak I, Spinlove K, Worth G, Burghardt I, Lasorne B. Quantum dynamics simulations using Gaussian wavepackets: The vmcg method. *Int Rev Phys Chem* (2015) 34:269–308. doi:10.1080/0144235X.2015.1051354

11. Kay KG. Semiclassical initial value treatments of atoms and molecules. *Annu Rev Phys Chem* (2005) 56:255–80. doi:10.1146/annurev.physchem.56.092503.141257

12. Kay KG. Numerical study of semiclassical initial value methods for dynamics. *J Chem Phys* (1994) 100:4432–45. doi:10.1063/1.466273

13. Walton AR, Manolopoulos DE. A new semiclassical initial value method for franck-condon spectra. *Mol Phys* (1996) 87:961–78. doi:10.1080/00268979600100651

14. Garashchuk S, Tannor D. Wave packet correlation function approach to H2(v)+H→H+H2(v′): Semiclassical implementation. *Chem Phys Lett* (1996) 262: 477–85. doi:10.1016/0009-2614(96)01111-6

15. Thoss M, Wang H. Semiclassical description of molecular dynamics based on initial-value representation methods. *Annu Rev Phys Chem* (2004) 55:299–332. doi:10.1146/annurev.physchem.55.091602.094429

16. Spanner M, Batista VS, Brumer P. Is the filinov integral conditioning technique useful in semiclassical initial value representation methods? *J Chem Phys* (2005) 122: 084111. doi:10.1063/1.1854634

17. Tatchen J, Pollak E. Semiclassical on-the-fly computation of the $S_0 \rightarrow S_1$ absorption spectrum of formaldehyde. *J Chem Phys* (2009) 130:041103. doi:10.1063/1.3074100

18. Ceotto M, Atahan S, Shim S, Tantardini GF, Aspuru-Guzik A. First-principles semiclassical initial value representation molecular dynamics. *Phys Chem Chem Phys* (2009) 11:3861–7. doi:10.1039/B820785B

19. Kay KG. Integral expressions for the semiclassical time-dependent propagator. *J Chem Phys* (1994) 100:4377–92. doi:10.1063/1.466320

20. Miller WH. On the relation between the semiclassical initial value representation and an exact quantum expansion in time-dependent coherent states. *J Phys Chem B* (2002) 106:8132–5. doi:10.1021/jp020500+

21. Miller WH. An alternate derivation of the Herman–Kluk (coherent state) semiclassical initial value representation of the time evolution operator. *Mol Phys* (2002) 100:397–400. doi:10.1080/00268970110069029

22. Deshpande SA, Ezra GS. On the derivation of the herman–kluk propagator. *J Phys A* (2006) 39:5067–78. doi:10.1088/0305-4470/39/18/020

23. Tannor DJ, Heller EJ. Polyatomic Raman scattering for general harmonic potentials. *J Chem Phys* (1982) 77:202–18. doi:10.1063/1.443643

24. Begušić T, Roulet J, Vaníček J. On-the-fly *ab initio* semiclassical evaluation of time-resolved electronic spectra. *J Chem Phys* (2018) 149:244115. doi:10.1063/1.5054586

25. Hagedorn GA. Semiclassical quantum mechanics. I. The $\hbar \rightarrow 0$ limit for coherent states. *Commun Math Phys* (1980) 71:77–93. doi:10.1007/bf01230088

26. Lee SY, Heller EJ. Exact time-dependent wave packet propagation: Application to the photodissociation of methyl iodide. *J Chem Phys* (1982) 76:3035–44. doi:10.1063/1.443342

27. Hagedorn GA. Raising and lowering operators for semiclassical wave packets. *Ann Phys (Ny)* (1998) 269:77–104. doi:10.1006/aphy.1998.5843

28. Coalson RD, Karplus M. Multidimensional variational Gaussian wave packet dynamics with application to photodissociation spectroscopy. *J Chem Phys* (1990) 93: 3919–30. doi:10.1063/1.458778

29. Begušić T, Cordova M, Vaníček J. Single-Hessian thawed Gaussian approximation. *J Chem Phys* (2019) 150:154117. doi:10.1063/1.5090122

30. Prlj A, Begušić T, Zhang ZT, Fish GC, Wehrle M, Zimmermann T, et al. Semiclassical approach to photophysics beyond kasha's rule and vibronic spectroscopy beyond the condon approximation. The case of azulene. *J Chem Theor Comput.* (2020) 16:2617–26. doi:10.1021/acs.jctc.0c00079

31. Wu Y, Herman MF. Nonadiabatic surface hopping herman-kluk semiclassical initial value representation method revisited: Applications to tully's three model systems. *J Chem Phys* (2005) 123:144106. doi:10.1063/1.2049251

32. Wu Y, Herman MF. A justification for a nonadiabatic surface hopping herman-kluk semiclassical initial value representation of the time evolution operator. *J Chem Phys* (2006) 125:154116. doi:10.1063/1.2358352

33. Hochman G, Kay KG. Tunneling by a semiclassical initial value method with higher order corrections. *J Phys A* (2008) 41:385303. doi:10.1088/1751-8113/41/38/385303

34. Hochman G, Kay KG. Tunneling in two-dimensional systems using a higher-order herman–kluk approximation. *J Chem Phys* (2009) 130:061104. doi:10.1063/1.3079544

35. Filinov VS. Calculation of the feynman integrals by means of the Monte Carlo method. *Nucl Phys B* (1986) 271:717–25. doi:10.1016/S0550-3213(86)80034-7

36. Makri N, Miller WH. Monte Carlo integration with oscillatory integrands: Implications for feynman path integration in real time. *Chem Phys Lett* (1987) 139: 10–4. doi:10.1016/0009-2614(87)80142-2

37. Makri N, Miller WH. Monte Carlo path integration for the real time propagator. *J Chem Phys* (1988) 89:2170–7. doi:10.1063/1.455061

38. Elran Y, Kay KG. Improving the efficiency of the herman–kluk propagator by time integration. *J Chem Phys* (1999) 110:3653–9. doi:10.1063/1.478255

39. Kaledin AL, Miller WH. Time averaging the semiclassical initial value representation for the calculation of vibrational energy levels. *J Chem Phys* (2003) 118:7174–82. doi:10.1063/1.1562158

40. Buchholz M, Grossmann F, Ceotto M. Mixed semiclassical initial value representation time-averaging propagator for spectroscopic calculations. *J Chem Phys* (2016) 144:094102. doi:10.1063/1.4942536

41. Buchholz M, Grossmann F, Ceotto M. Simplified approach to the mixed time-averaging semiclassical initial value representation for the calculation of dense vibrational spectra. *J Chem Phys* (2018) 148:114107. doi:10.1063/1.5020144

42. Shao J, Makri N. Forward-backward semiclassical dynamics in the interaction representation. *J Chem Phys* (2000) 113:3681–5. doi:10.1063/1.1287823

43. Petersen J, Pollak E. Semiclassical initial value representation for the quantum propagator in the heisenberg interaction representation. *J Chem Phys* (2015) 143: 224114. doi:10.1063/1.4936922

44. Ceotto M, Atahan S, Tantardini GF, Aspuru-Guzik A. Multiple coherent states for first-principles semiclassical initial value representation molecular dynamics. *J Chem Phys* (2009) 130:234113. doi:10.1063/1.3155062

45. Grossmann F. A semiclassical hybrid approach to many particle quantum dynamics. *J Chem Phys* (2006) 125:014111. doi:10.1063/1.2213255

46. Goletz CM, Grossmann F. Decoherence and dissipation in a molecular system coupled to an environment: An application of semiclassical hybrid dynamics. *J Chem Phys* (2009) 130:244107. doi:10.1063/1.3157162

47. Grossmann F. A semiclassical hybrid approach to linear response functions for infrared spectroscopy. *Phys Scr T* (2016) 91:044004. doi:10.1088/0031-8949/91/4/044004

48. Antipov SV, Ye Z, Ananth N. Dynamically consistent method for mixed quantum-classical simulations: A semiclassical approach. *J Chem Phys* (2015) 142: 184102. doi:10.1063/1.4919667

49. Church MS, Antipov SV, Ananth N. Validating and implementing modified filinov phase filtration in semiclassical dynamics. *J Chem Phys* (2017) 146:234104. doi:10.1063/1.4986645

50. Malpathak S, Church MS, Ananth N. A semiclassical framework for mixed quantum classical dynamics. *J Phys Chem A* (2022) 126:6359–75. doi:10.1021/acs.jpca.2c03467

51. Pollak E, Upadhyayula S, Liu J. Coherent state representation of thermal correlation functions with applications to rate theory. *J Chem Phys* (2022) 156: 244101. doi:10.1063/5.0088163

52. Lasser C, Sattlegger D. Discretising the herman-kluk propagator. *Numerische Mathematik* (2017) 137:119–57. doi:10.1007/s00211-017-0871-0

53. Lasser C, Lubich C. Computing quantum dynamics in the semiclassical regime. *Acta Numerica* (2020) 29:229–401. doi:10.1017/S0962492920000033

54. Hall BC. *Quantum theory for mathematicians*. New York: Springer (2013). doi:10.1007/978-1-4614-7116-5

55. Martinez A. *An introduction to semiclassical and microlocal analysis*. New York: Springer-Verlag (2002).

56. Kay KG. The herman–kluk approximation: Derivation and semiclassical corrections. *Chem Phys* (2006) 322:3–12. doi:10.1016/j.chemphys.2005.06.019

57. Swart T, Rousse V. A mathematical justification for the herman-kluk propagator. *Commun Math Phys* (2008) 286:725–50. doi:10.1007/s00220-008-0681-4

58. Robert D. On the herman–kluk semiclassical approximation. *Rev Math Phys* (2010) 22:1123–45. doi:10.1142/s0129055x1000417x

59. Caflisch RE. Monte Carlo and quasi-Monte Carlo methods. *Acta Numerica* (1998) 7:1–49. doi:10.1017/S0962492900002804

60. Brewer ML, Hulme JS, Manolopoulos DE. Semiclassical dynamics in up to 15 coupled vibrational degrees of freedom. *J Chem Phys* (1997) 106:4832–9. doi:10.1063/1.473532

61. Hairer E, Lubich C, Wanner G. *Geometric numerical integration: Structure-preserving algorithms for ordinary differential equations*. New York: Springer Berlin Heidelberg (2006).

62. Hairer E, Lubich C, Wanner G. Geometric numerical integration illustrated by the Størmer-Verlet method. *Acta Numerica* (2003) 12:399–450. doi:10.1017/S0962492902000144

63. Stewart I, Tall D. *Complex analysis*. Cambridge, United Kingdom: Cambridge University Press (2018). doi:10.1017/9781108505468

64. Kahan W, Li RC. Composition constants for raising the orders of unconventional schemes for ordinary differential equations. *Math Comput* (1997) 66:1089–99. doi:10.1090/s0025-5718-97-00873-9

65. Suzuki M. General theory of higher-order decomposition of exponential operators and symplectic integrators. *Phys Lett A* (1992) 165:387–95. doi:10.1016/0375-9601(92)90335-J

66. Vaníček J. Dephasing representation of quantum fidelity for general pure and mixed states. *Phys Rev E* (2006) 73:046204. doi:10.1103/PhysRevE.73.046204

67. Mollica C, Vaníček J. Beating the efficiency of both quantum and classical simulations with a semiclassical method. *Phys Rev Lett* (2011) 107:214101. doi:10.1103/PhysRevLett.107.214101

68. Mollica C, Zimmermann T, Vaníček J. Efficient sampling avoids the exponential wall in classical simulations of fidelity. *Phys Rev E* (2011) 84:066205. doi:10.1103/PhysRevE.84.066205

69. Zimmermann T, Vaníček J. Role of sampling in evaluating classical time autocorrelation functions. *J Chem Phys* (2013) 139:104105. doi:10.1063/1.4820420

70. Durrett R. *Probability: Theory and examples*. Cambridge, United Kingdom: Cambridge University Press (2019). doi:10.1017/9781108591034

71. Tannor DJ. *Introduction to quantum mechanics: A time-dependent perspective*. Sausalito: University Science Books (2007).

72. Feit MD, Fleck JA, Jr. Solution of the Schrödinger equation by a spectral method ii: Vibrational energy levels of triatomic molecules. *J Chem Phys* (1983) 78:301–8. doi:10.1063/1.444501

73. Dyke P. *An introduction to laplace transforms and fourier series*. London: Springer London (2013). doi:10.1007/978-1-4471-6395-4

Frontiers in
Physics

Investigates complex questions in physics to understand the nature of the physical world

Addresses the biggest questions in physics, from macro to micro, and from theoretical to experimental and applied physics.

Discover the latest Research Topics

See more →

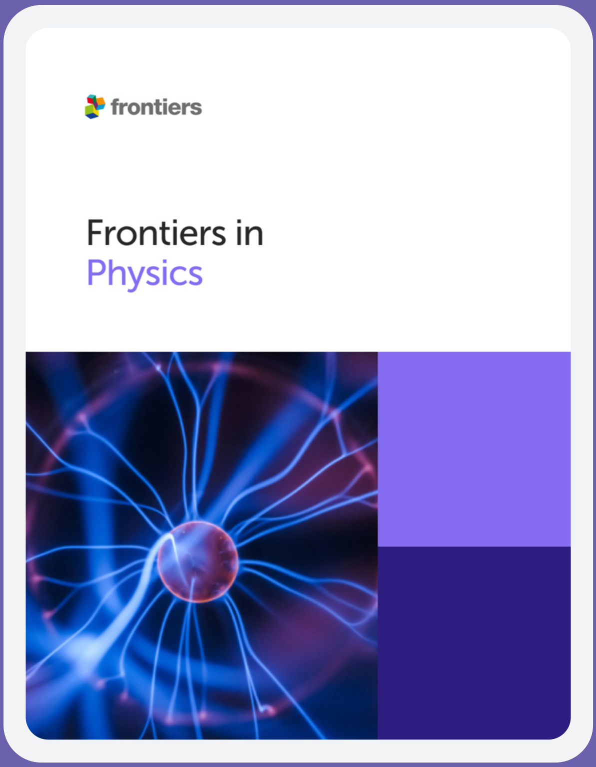

Frontiers

Avenue du Tribunal-Fédéral 34
1005 Lausanne, Switzerland
frontiersin.org

Contact us

+41 (0)21 510 17 00
frontiersin.org/about/contact